INDIRECT STUDIES OF ASTROPHYSICAL RADIATIVE CAPTURE REACTIONS

A Dissertation

by

EAMES A. BENNETT

Submitted to the Office of Graduate and Professional Studies of
Texas A&M University
in partial fulfillment of the requirements for the degree of

DOCTOR OF PHILOSOPHY

Co-Chairs of Committee,	Gregory Christian
	Grigory Rogachev
Committee Members,	Aaron Couture
	Jeremy Holt
	Sherry Yennello
Head of Department,	Grigory Rogachev

December 2020

Major Subject: Physics & Astronomy

ABSTRACT

The first study in this work focuses on the ^{23}Mg(p,γ)^{24}Al reaction. Although several resonances may contribute to the overall rate at novae temperatures, the resonance at $\sim$ 475 keV is thought to be dominant. The strength of this resonance has been directly measured using a radioactive ^{23}Mg beam impinging on a windowless H_2 gas target using the DRAGON facility at TRIUMF; however, recent high-precision ^{24}Al mass measurements have called this result into question. An indirect measurement of the proton width using the ^{23}Na(d,p)^{24}Na reaction in inverse kinematics has been performed to study the mirror state of the $\sim$ 475 keV resonance in ^{24}Na. A measurement of the spectroscopic factor of the 2512 keV state in ^{24}Na is also presented. These results are discussed with a focus on previous theory calculations and experimental results.

The second study attempts to probe the photon strength function in ^{58}Fe. The photon strength function can provide insight into the properties of nuclei that are difficult to directly measure. In particular, Hauser-Feshbach reaction models typically use this statistical quantity to describe electromagnetic coupling. By constraining this theoretical input, a more accurate understanding of a given nucleus can be attained. This quantity may also be useful in making inferences about other neutron capture reactions. An analysis of multi-step gamma cascades from individual resonances from the ^{57}Fe(n,γ)^{58}Fe reaction is presented. Comparisons of this experimental data to gamma-cascades simulated by DICEBOX is shown, and constraints on the photons strength function are proposed.

DEDICATION

This thesis work is dedicated to Dr. Donald V. Bennett and Dr. Eve M. Bennett. I am so fortunate to have you both as parents and, more importantly, as friends. None of this would have been possible without you.

ACKNOWLEDGMENTS

I would like to express my sincere gratitude to Dr. Greg Christian for welcoming me into his young group and directing my research. His enthusiasm for research has made it a pleasure to work with him over the past four years.

Additional thanks go to Dr. Shuya Ota for all his support through this dissertation and the many comprehensive conversations we have had together. I also would like to thank Dr. Jack Bishop and Dr. Cody Parker, both of whom provided guidance and support throughout my academic career. I would also like to thank Dr. Cathleen Fry for teaching me the ropes on DANCE and for helping to make LANL such a welcoming environment.

Special thanks goes to Dr. Antti Saastamoinen and Dr. Ryan Wilkinson for the long nights in the counting room getting TIARA for Texas off the ground. I am also deeply appreciative of all the help the Cyclotron Institute support staff, the Cyclotron Operations Group, and the machine shop staff have provided over the years.

My gratitude is owed to all the members of P-27 at Los Alamos National Laboratory, especially Dr. Chris Prokop, Dr. Jack Winkelbauer, and Dr. Shea Mosby for their invaluable technical and scientific insight.

I would like to express my gratitude towards Prof. Grigory V. Rogachev, Prof. Jeremy Holt, and Prof. Sherry Yennello for serving on my committee and providing invaluable feedback on this work.

To all those who have been there with me through this journey: thank you. In particular, I need to thank Dr. Jaymes Farrell, Michael Roosa, Derek Anderson, Lauren Aldoroty, Tarini Konchady, and Dr. Sriteja Upadhyayula, all of whom have made graduate school infinitely more enjoyable. Additionally, I would be remiss not to thank the many people outside of academia who helped make Texas home; specifically Michael Pincus, Charles Arnold, Omar Nuñez, Michael Krutak, and Brooks Bixler.

None of this would have been possible without my family. To my parents, Don and Kyla,

and my sister Denali, thank you so much for always believing in me. And of course, thanks goes to my dog, Bee, for her loyal companionship.

Finally, I am deeply indebted to Dr. Aaron Couture for all the counsel and wisdom he has provided in the short time we have known each other. His mentorship has been invaluable in navigating my final year of graduate school and the transition into the next chapter of my career. It has been an honor to work with such a phenomenal scientist and a genuinely compassionate human being.

CONTRIBUTORS AND FUNDING SOURCES

Contributors

This work was supported by a dissertation committee consisting of Professor Greg Christian (chair), Professor Grigory V. Rogachev (co-chair), and Professor Jeremy Holt of the Department of Physics and Astronomy as well as Professor Sherry Yennello of the Department of Chemistry and Dr. Aaron Couture of Los Alamos National Laboratory.

The data presented in Part I was taken with help from members of the TIARA for Texas collaboration, including Professor Wilton Catford, Professor Gavin Lotay, Dr. Adrien Matta, Dr. Ryan Wilkinson, and Sam Hallam of the University of Surrey. The data analyzed for Part II was provided by Dr. Christopher Prokop and Dr. Aaron Couture of Los Alamos National Laboratory. The analysis shown in Chapter 9 was conducted with guidance from Dr. Milan Krtička of the Charles University at Prague and Dr. Aaron Couture of Los Alamos National Laboratory.

All other work conducted for the dissertation was completed by the student independently.

Funding Sources

Graduate study was supported by teaching and research assistantships from the Cyclotron Institute and Texas A&M University. The work presented in this dissertation was funded in part by the U.S. Department of Energy, Office of Science, award No. DE-FG02-93ER4077 as well as the US National Nuclear Security Administration, award No. DE-NA0003841

TABLE OF CONTENTS

Page

LIST OF FIGURES

FIGURE Page

LIST OF TABLES

TABLE Page

1. INTRODUCTION

1.1 Nuclear Astrophysics

From the very cradle of civilization, humans have looked up at the stars and sought to comprehend their place among them. Early cultures viewed the sky as a palace of the gods, tracking the motion of stars and planets while simultaneously weaving them into the fabric of their culture. As societies developed, the ebb and flow of these celestial bodies intertwined with the earth below: calendars designed around the movement of the sun and moon told farmers when to reap and when to sow, routes across seemingly endless bodies of water were plotted by starlight, and the fundamental laws of the Universe were teased out of the motion of the planets. Time and time again, history shows that astronomy is inextricably linked to the advancement of human civilization.

As humanity's understanding of the Universe improved, questions as to its origin and future began to emerge. It wasn't until the twentieth century, however, that researchers started to unravel the beginnings of the cosmos in a meaningful way. Observations made by Edwin Hubble and other astronomers seemed to suggest that the Universe was stretching and expanding. The Big Bang theory, proposed in 1931 by Georges Lemaître, suggested that the Universe emerged from an infinitely dense point containing all matter and energy observed today [1]. This "hypothesis of the primeval atom" was the catalyst for the theory of Big Bang nucleosynthesis. Proposed by Ralph Alpher and George Gamow, the theory predicted the evolution of light elements beyond hydrogen by the Big Bang [2]. However, this theory failed to explain the existence of heavier elements in the Universe. The solution to this issue originated from Hans Bethe (who was whimsically included on Alpher and Gamow's paper), when he elucidated the nuclear mechanisms that allow for fusion in stars [3]. Subsequent work by many scientists, perhaps most famously the B^2FH paper [4], formalized the underpinnings of stellar nucleosynthesis.

Prying into the heart of stars to better understand the origin of elements remains a key problem in nuclear physics into the twenty-first century. As stellar evolution directly dictates the abundance of elements observed in the Universe as well as Galactic chemical abundances, a firm understanding of the reactions that occur within these stellar furnaces is required. However, recreating the extremes of a stellar environment in the lab remains as a key challenge in reducing uncertainties on the nuclear data required to reconstruct complex reaction networks. Only a small fraction of all astrophysically relevant reactions can be directly measured in a laboratory environment. Even then, it is often necessary to perform experiments at relatively high energies and then extrapolate the results to lower stellar energies, introducing significant uncertainties in the results. Technical limitations also prevent certain reactions from being studied. Certain radioactive beams or targets cannot be produced in sufficient quantity or with high enough purity. Certain resonances that are strongly populated in the lab can overwhelm resonances of astrophysical interest. In these cases, it is often necessary to explore indirect methods of probing reaction parameters.

1.1.1 Indirect Experimental Methods in Nuclear Physics

Over the past several decades, a number of indirect techniques have been developed to overcome some of these previously mentioned limitations. Broadly speaking, these techniques use a nuclear reaction that's accessible in the laboratory to constrain a related reaction of astrophysical interest. Then, utilizing appropriate components of nuclear theory, properties of the accessible reaction are related to the desired reaction. These theoretical elements are typically nuclear structure parameters, so this approach requires robust theoretical underpinnings to accurately relate parameters between reactions.

As an exhaustive explanation of all possible indirect experimental techniques is not the goal of this dissertation, specific methods relevant to the presented work are discussed in Chapter 2 and Chapter 6, and indirect methods are discussed more broadly in Chapter 3.

1.2 Thesis Structure

This dissertation is broken into two parts, each describing a separate experiment utilizing indirect techniques to probe astrophysically relevant processes.

The first part of this work focuses on constraining the astrophysical ^{23}Mg(p,γ)^{24}Al reaction rate through a measurement of the ^{23}Na(d,p)^{24}Na reaction. Chapter 2 provides a brief overview of the astrophysical motivation for the work and the indirect technique utilized to investigate the reaction of interest. Chapter 3 builds a conceptual framework around the theory of transfer reactions and stellar reaction rates. Chapter 4 describes the experimental setup used for the work (TIARA for Texas) and the basic function behind each of the primary detectors. The analysis of the results from the ^{23}Na(d,p)^{24}Na experiment are presented in Chapter 5.

The second part of this dissertation focuses on the study of the photon strength function in ^{58}Fe using the ^{57}Fe(n,γ)^{58}Fe reaction. Chapter 6 motivates the work by explaining the importance of ^{60}Fe in astronomy and astrophysics and describes how the study of ^{58}Fe can be used to benchmark a new indirect experimental method. Chapter 7 constructs the statistical nucleus and the fundamental concepts behind the photon strength function. Chapter 8 introduces the Detector for Advanced Neutron Capture Experiments (DANCE) as well as the Los Alamos Neutron Science Center, where the experiment was performed. The results of the ^{57}Fe(n,γ)^{58}Fe experiment as well as the resulting constraints on its photon strength function are presented in Chapter 9. Finally, Chapter 10 provides a brief summary of the work performed and the results found in this dissertation.

2. THE ASTROPHYSICAL ^{23}Mg(p,γ)^{24}Al REACTION RATE

2.1 Explosive Stellar Burning

While the process of stellar burning typically balances the gravity of the star's own mass against the energy created by nuclear fusion [5], certain edge cases exist that result in continued nucleosynthesis outside of hydrostatic equilibrium. Runaway thermonuclear reactions create environments at the extremes of temperature and density, giving rise to explosive nuclear burning and providing entry to reaction channels that would not otherwise be accessible. In particular, radioactive nuclear species prone to β-decay are produced in sufficient quantity and survive long enough to participate in a different reaction before they have a chance to β-decay [6]. As this process generally creates a diversity of elements and isotopes, it is thought to play a significant role in determining elemental abundances in galaxies.

This work focuses on the process of rapid proton capture (rp-process), in which proton-rich nuclei are created in rapid succession via the bombardment of stable nuclei by protons. As this process occurs on the order of seconds, radioactive nuclei with significantly longer half-lives can be produced that, when observed decaying after ejection, can inform how the products are mixed into the interstellar medium [6].

2.1.1 Classical Novae

A classical nova typically occurs in a binary system between a white dwarf and an accreting main sequence star. An accretion disc forms around the white dwarf and, as relatively small amounts of matter fall from the accretion disc onto the surface of the white dwarf, thermonuclear runaway occurs. The course of the runaway is determined by a number of factors, primarily the amount of matter deposited onto the surface of the white dwarf and the degeneracy of the matter. Partially degenerate matter will burn and remain on the surface, however, if the matter is sufficiently degenerate, it will trigger a complete mass ejection.

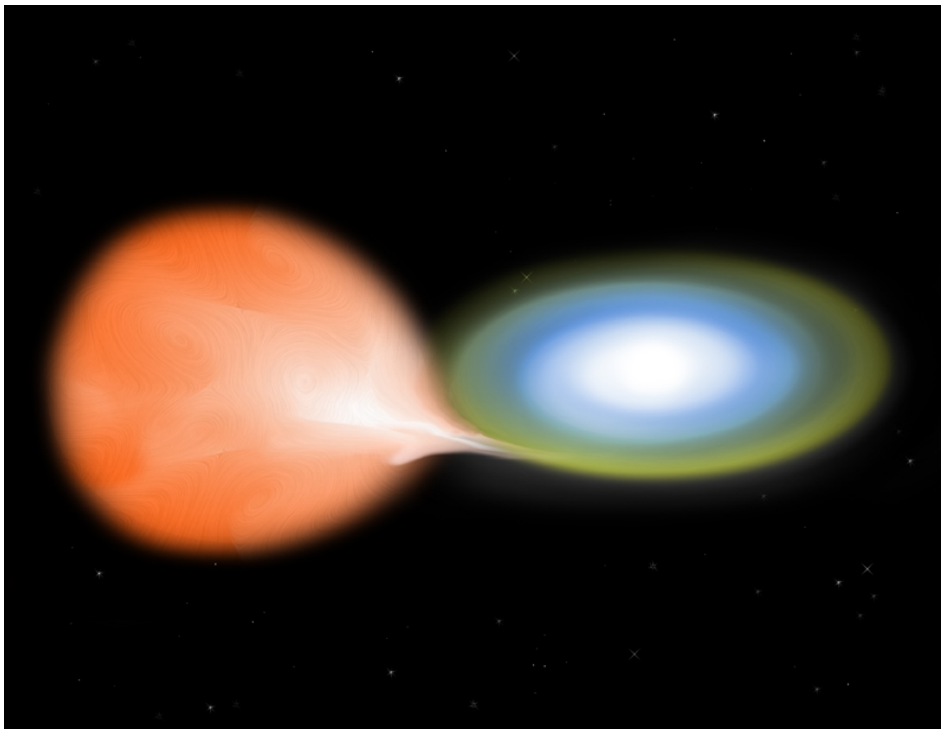

Figure 2.1: An artist's interpretation of a classical nova. In this image, the red companion star is ceding matter into the accretion disc around its white dwarf partner. Reprinted with permission from [8].

These conditions can reach stellar temperatures of up to 0.5 gigaKelvin (GK) and will occur over 100-200 seconds [6].

From an orbital perspective, this process begins when the main sequence star has filled its Roche lobe, the maximum radius at which matter is still gravitationally bound to the star. At this point, matter from the star is transferred to the dwarf star via the system's inner Lagrangian point [6]. The material will then begin to orbit the dwarf, creating the aforementioned accretion disc [7]. As the reaction proceeds, the two stars will drift apart in order to conserve angular momentum and the entire event ends. An artist's interpretation of a classical nova can be seen in Figure 2.1.

Classical novae are a periodic event as the binary system is not destroyed after the process completes [5]. For a single system, a classical nova may occur once every 10^3-10^5 years [6]. The Galactic nova rate, however, is approximately 40 per year. This means classical novae

may be one of the most significant contributors to the chemical evolution of the Galaxy [9].

2.1.2 X-ray Bursts

X-ray bursts are extremely similar to classical nova, but differ in that the primary star in an X-ray burst is a neutron star. Other than this, the companion star is still a main sequence star that transfers some of its mass beyond its Roche lobe, through the inner Lagrange point, and can form an accretion disc around the primary star. As neutron stars have a significantly larger gravity than white dwarfs, the accreted matter has a higher energy when it reaches the surface of the neutron star. Subsequently, stellar temperatures in excess of 1 GK can be achieved [6]. These higher temperatures enable elements up to tellurium to be formed during X-ray bursts [10].

There are two types of X-ray bursts, which are classified by the frequency of their outbursts. Type I X-ray bursts have much lower frequencies, occurring with periods on the order hours, days, or weeks. Type II X-ray bursts are rapid events with periods on the order of seconds to minutes, with some sources producing as many as several thousand bursts in a single day [11].

2.2 The ^{23}Mg(p,γ)^{24}Al Reaction

The modeling of nuclear reaction networks formed during explosive nuclear burning is a complex topic that depends on access to high quality nuclear data. Even relatively small uncertainties can lead to significant variations in model predictions [12, 13]. One study performed by Iliadis *et al* varied the reaction rate of over 175 different nuclear reactions within their uncertainties and examined the effect on the abundance of 142 different isotopes under $A = 40$. These simulations were performed for classical novae using a number of different nova models and conditions. The results identified reactions that required further study to reduce uncertainty in calculated elemental abundances [14]. Having access to accurate reaction rates is therefore an important component of investigating these astrophysical phenomena.

The ^{23}Mg(p,γ)^{24}Al reaction was one of the reactions identified as important classical novae, though it also appears to play a role in X-ray bursts. In classical novae, it provides an escape from the Ne-Na cycle via the proton capture reaction on ^{23}Mg at low stellar temperatures (< 1 GK). This reaction outpaces the β decay reaction favored at lower temperatures (< 0.1 GK) [15, 16]. The ^{24}Al generated by this proton capture reaction quickly decays into ^{24}Mg and allows entrance into the Mg-Al cycle [17]. This may contribute to the synthesis of other elements produced in classical novae, such as silicon, sulfur, and argon [15]. This reaction also impacts the production of important long-lived gamma-emitters ^{22}Na and ^{26}Al [14]. Additionally, in type I X-ray bursts, recent work indicates this reaction plays a role in determining the composition of the burst ashes based on simulations performed using a single zone X-ray burst model. Variations on this reaction rate showed fluctuations up to a factor of two in the abundance of nuclei that composed a significant mass fraction of the burst ashes [12].

The ^{23}Mg(p,γ)^{24}Al reaction has attracted significant attention over the past two decades. A series of shell model studies established the initial energies and strengths of important resonances. Shell model calculations placed the first resonance energy at about $E_r \sim 475$ keV with a resonance strength between 25 and 27 meV. A second resonance at $E_r \sim 663$ keV was identified; however, the studies disagreed on the resonance strength by over a factor of two [15, 19]. However, for classical nova, the resonant energy at ~ 475 keV appears to be the dominant contributor to the reaction rate at stellar temperatures of 0.2-0.4 GK [15].

As this reaction populates proton unbound states in ^{24}Al, it prompted a series of (^{3}He,t) experiments to establish the spins and level energies of states in ^{24}Al. While there was some variations, the experiments suggested the reaction populated a 3^+ resonance between 2328 keV and 2369 keV [20, 21, 22]. In 2008, a fusion-evaporation experiment at Gammasphere found the energy level to be $E_x = 2345.1 \pm 1.4$ keV, placing the resonance energy at $E_r = 473 \pm 3$ keV [18]. The experiment performed in-beam gamma-ray spectroscopy on the ^{24}Al nucleus and established the most precise measurement to date.

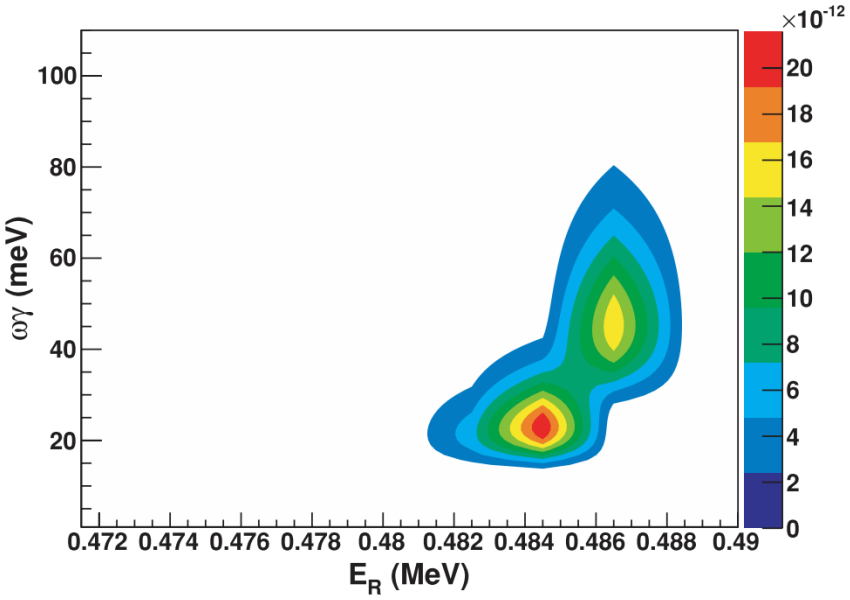

Figure 2.2: The probability distribution function from the direct measurement of the ^{23}Mg(p,γ)^{24}Al reaction performed at DRAGON. The reaction, which occurred towards the rear of the gas chamber, shows two clear maxima that may be potential correlations between resonance energy and resonance strength. Reprinted with permission from [18].

Following the Gammasphere measurement, the first direct measurement of the ^{23}Mg(p,γ)^{24}Al reaction was performed utilizing the DRAGON facility at TRIUMF. A ^{23}Mg beam was impinged on a hydrogen gas target and the reaction was measured using bismuth germanate (BGO) detector array. However, due to uncertainties in the resonance energy, the reaction occurred far upstream of the center of the gas target. This resulted in a double-peaked probability contour, shown in Figure 2.2, with different predicted resonance energies and strengths. The authors selected the higher probability peak and reported a resonance energy of $485.7^{+1.3}_{-1.8}$ keV and a resonance strength of 38^{+21}_{-15} meV [18], which were in tentative agreement with previous shell model calculations [15, 19].

The resonance energy value obtained by the DRAGON experiment also agreed with the Gammasphere measurement, which had been revised to $E_r = 482 \pm 2.0$ keV after a more precise Q-value was determined [23]. However, the uncertainties in the position of the

resonance within the extended gas target limit the reliability of the DRAGON measurement. After a 2015 precision study of the mass of ^{24}Al, a revised resonance energy based on the Gammasphere measurement established $E_r = 480.8 \pm 1.4$ keV [16]. While a subsequent re-calibration of the magnetic constant used to measure the beam energy at DRAGON did lower the resonance energy to $E_r = 485.0^{+1.3}_{-1.8}$ keV [24], this remains a 2σ deviation from the value taken from the revised value from the Gammasphere measurement. To lend insight to the properties of this resonance, a measurement of its proton width—a key parameter in determining the resonance strength—was taken by populating the mirror state of the ~ 475 keV resonance of ^{24}Al using the ^{23}Na(d,p)^{24}Na reaction.

2.3 The ^{23}Na(d,p)^{24}Na Reaction

The ^{23}Na(d,p)^{24}Na reaction is a stable beam reaction in which a sodium nucleus absorbs a deuteron and emits a proton in a direct, single-step process. This particular study was performed in inverse kinematics, where the sodium beam was impinged on a deuterated carbon target and the resulting proton was measured at backward lab angles. Previous studies of the ^{23}Na(d,p)^{24}Na reaction will be discussed in Chapter 5, however, it is a well-documented reaction. This made it an ideal candidate to commission the new TIARA for Texas (T4T) experimental setup, which will be described in detail in Chapter 4. As the eventual goal for T4T is to perform transfer reactions in inverse kinematics using exotic beams, commissioning the setup with a series of stable beam experiments served to validate the capabilities of the detector array.

As stated previously, ^{24}Na is the mirror nucleus of ^{24}Al. This means that some nuclear structure between the nuclei is similar, and thus the neutron-rich sodium nucleus can provide insight to its neutron-deficient mirror. The details of these similarities are described below.

2.3.1 Mirror Nuclei

A mirror nucleus simply means that the number of neutrons and protons is reversed. So, for example, ^{24}Na has $Z = 11$ and $N = 13$ while its mirror nucleus ^{24}Al has $Z = 13$ and

$N = 11$. As the strong nuclear force is felt equally by protons and neutrons, and given that it is the dominant force within the nucleus, this means that both nuclei have a common nuclear structure. While there are limits to the similarities between mirror nuclei, well-established corrections can be made for the Coulomb contributions from the differing nuclei and the treatment works well for light nuclei.

A common nuclear structure between nuclei implies the existence of mirror analogue states, where the nucleon wave functions are the same save for the number of neutrons and protons. Properties from states in one nucleus can be applied to analogue states in the mirror nucleus. This means that states that would be difficult to measure in laboratory in one nucleus may have a mirror state that can be measured more easily. This is particularly important in astrophysical reactions, where unbound states in the nucleus of interest often have mirror states that are bound.

In the present work, the ^{23}Na(d,p)^{24}Na reaction has been utilized to study the ^{23}Mg(p,γ)^{24}Al reaction. The 2512 keV state in ^{24}Na is the mirror state of the 2349 keV state in ^{24}Al, the state populated by the $\sim$ 475 keV resonance in the aforementioned proton-capture reaction [15]. Previous studies have used the spectroscopic factors from mirror states to estimate reaction parameters of astrophysical interest [25] and these values are expected to agree within 20% for light nuclei [26].

In essence, this means the $\sim$ 475 keV resonance in ^{24}Al can be probed indirectly by populating the analogue resonance in ^{24}Na. This allows us to infer properties of the astrophysically relevant reaction, the details of which will be covered in Chapter 5.

3. THEORY OF STELLAR NUCLEOSYNTHESIS

3.1 Theoretical Overview

Understanding the nucleosynthesis of elements requires a functional knowledge of the thermonuclear reactions that occur in a stellar environment and the physics that govern these processes. This chapter discusses the general principles of thermonuclear reactions in a stellar environment, physics of narrow resonances, some methods for determining resonance parameters through indirect means, and techniques for using transfer reactions as a method of studying narrow resonances. The theoretical models used to compare to experimental results are also discussed.

The aim of this chapter is to establish a conceptual framework for understanding the contents of this thesis rather than to provide an exhaustive treatment of nuclear reactions and astrophysics. A significant portion of this chapter is based on Christian Iliadis' textbook "Nuclear Physics of Stars" as well as G.R. Satchler's "Introduction to Nuclear Reactions", and omits some of the more rigorous proofs for the sake of brevity.

3.2 General Properties of Thermonuclear Reaction Rates

A nuclear reaction is often expressed in terms of the incoming and outgoing particles. For the simple case of a single projectile a incident on a target nucleus X producing a daughter nucleus Y and an ejectile b, the reaction can be written as

$$a + X \rightarrow Y + b \tag{3.1}$$

or, more commonly,

$$X(a, b)Y\,. \tag{3.2}$$

The energy released during this reaction is given by the reaction Q value. The Q value can be calculated using the rest masses of the particles involved in the reaction and is expressed

as

$$Q = (m_X + m_a)c^2 - (m_Y + m_b)c^2 \tag{3.3}$$

where m_X and m_a are the rest masses of the particles in the entrance channel, and m_Y and m_b are the rest masses of the particles in the exit channel. The Q value provides insight into the energetics of the reaction. A reaction with a negative Q value is endothermic, requiring external energy to be added to the entrance channel for the reaction to occur. If the Q value of the reaction is positive, the reaction is exothermic and an excess of energy exists in the exit channel after the reaction occurs [27]. This excess energy generally appears in the kinetic energy of the daughters. Additionally, both exothermic and endothermic reactions can populate excited states of the daughter nucleus. Generally, an exothermic reaction that populates excited states can then be expressed as

$$Q_{ex} = (m_X + m_a)c^2 - (m_Y^* + m_b)c^2 = Q - E_{ex} \tag{3.4}$$

where $m_Y^* c^2$ is the mass energy of the excited nucleus, Q_{ex} is the observed Q value of the reaction, Q is the Q value of the reaction with the daughter nucleus in the ground state, and E_{ex} is the excitation energy above the ground state. The latter can be written as

$$E_{ex} = (m_Y^* - m_Y)c^2 \,. \tag{3.5}$$

Another useful quantity for understanding thermonuclear reactions is the energy required to liberate a single nucleon from the nucleus. These values are referred to as separation energies and are expressed as S_p for the proton separation energy and S_n for the neutron separation energy. The difference in the binding energy between the nuclei before and after separation determines the separation energy and can be calculated as

$$S_p = \left[M\left({}^{A-1}_{Z-1}X_N\right) - M\left({}^{A}_{Z}X_N\right) + m_p\right] c^2 \tag{3.6}$$

$$S_n = \left[M\left({}^{A-1}_{Z}X_{N-1}\right) - M\left({}^{A}_{Z}X_{N}\right) + m_n\right]c^2 \tag{3.7}$$

where ${}^{A}_{Z}X_N$ is the standard way of expressing a nucleus X of mass number A, atomic number Z, neutron number N, m_p is the mass of the proton, and m_n is the mass of the neutron. The function $M(...)$ denotes taking the mass of that nucleus [27].

There are a number of important astrophysical reactions that can be expressed using the formalism laid out in Equation 3.2. Radiative proton capture, written as $X(p,\gamma)Y$, is particularly important for explosive stellar phenomena like classical novae or x-ray bursts [28]. Neutron capture, generally $X(n,\gamma)Y$, is also an important reaction for the formation of heavy elements in neutron capture processes such as the r-process and s-process. This will be discussed in further detail in Chapter 6.

3.3 Cross Sections and Reaction Rates in a Stellar Environment

While Q values quantify the energetics of a nuclear reaction on a reaction-by-reaction basis, in stellar astrophysics it is valuable to understand the total energy liberated by all reactions taking place in a given unit volume. Assessing this requires the introduction of two additional quantities: the nuclear cross section, and the velocity distribution of particles in the volume. The nuclear cross section expresses the probability that two unique nuclei will react. Specifically, the ratio of nuclear reactions per unit time (N_R/t) to the product of the incident particle flux (N_b/tA) and the number of target nuclei (N_a), is written as

$$\sigma = \frac{N_R/t}{\left[N_b/(tA)\right]N_a} \tag{3.8}$$

where A is the cross-sectional area and t is a unit of time. Nuclear cross sections generally depend on the relative velocity of the reactants, so $\sigma = \sigma(v)$ [29].

The rate of nuclear reactions can be written as a product of the flux of the projectile particles and the effective reaction area for a given volume. Rearranging Equation 3.8 with

this in mind yields

$$\frac{N_R}{tV} = \sigma \frac{N_a}{V} v \frac{N_b}{V} \,. \tag{3.9}$$

For simplicity of notation, the rate of nuclear reactions can be expressed as $\frac{N_R}{tV} \equiv R_{ab}$. Assuming the incident and target particles have a rest mass greater than zero and remembering the nuclear cross section is dependent on the relative velocity of the system, Equation 3.9 can be rewritten as

$$R_{ab} = N_a N_b v \sigma(v) \tag{3.10}$$

where $N_a \equiv N_a/V$ and $N_b \equiv N_b/V$ are the number densities in units of particles per volume.

Since a stellar plasma at thermodynamic equilibrium will have particles with a range of different velocities, the relative velocity of two interacting particles can be expressed using a probability distribution. This function $P(v)$ obeys the normal properties of a probability distribution and thus allows us to express Equation 3.10 as

$$R_{ab} = N_a N_b \int_0^\infty v P(v) \sigma(v) dv = N_a N_b \langle \sigma v \rangle_{ab} \tag{3.11}$$

where $N_a N_b$ is the total number density of non-identical interacting particles and $\langle \sigma v \rangle_{ab}$ is the reaction rate per particle pair [29]. For a large number of identical particles, the number density would be $N_a^2/2$ allowing us to generalize the expression for the reaction rate as

$$R_{ab} = \frac{N_a N_b \langle \sigma v \rangle_{ab}}{1 + \delta_{ab}} \tag{3.12}$$

where δ_{ab} is the Kronecker delta.

However, when considering reactions taking place in a stellar environment, it is often more useful to state the reaction rate in terms of observable characteristics of the star. In this case, combining the nuclear physics information in Equation 3.12 results in

$$r_{ab} = \frac{N_A \langle \sigma v \rangle_{ab}}{1 + \delta_{ab}} \tag{3.13}$$

where N_A is Avogadro's number and r_{ab} is expressed in terms of $\mathrm{cm^3 mol^{-1} s^{-1}}$ [5]. Next, considering that particles in a stellar gas are non-degenerate and generally move at non-relativistic speeds, the velocity distribution of particles undergoing nuclear reactions in the gas can be accurately described by a Maxwell-Boltzmann distribution. Written first as a function of velocity and then as a function of energy, this results in a probability distribution

$$P(v)dv = 4\pi v^2 \left(\frac{\mu}{4\pi kT}\right)^{3/2} e^{-\frac{\mu v^2}{2kT}} dv \tag{3.14}$$

$$= P(E)dE \tag{3.15}$$

$$= \frac{2}{\sqrt{\pi}} \frac{1}{(kT)^{3/2}} \sqrt{E} e^{-\frac{E}{kT}} dE\,, \tag{3.16}$$

where μ is the reduced mass of the two particles, T is the stellar temperature, and k is the Boltzmann constant. With this in mind, the per particle reaction rate can now be expressed as

$$\langle \sigma v \rangle = \int_0^\infty P(v)\sigma(v) v dv \tag{3.17}$$

$$= \int_0^\infty P(E)\sigma(E) v dE \tag{3.18}$$

$$= \left(\frac{8}{\pi\mu}\right)^{1/2} \frac{1}{(kT)^{3/2}} \int_0^\infty \sigma(E) E e^{-\frac{E}{kT}} dE\,, \tag{3.19}$$

where $\sigma(E)$ is the energy-dependent cross section [29]. Since this quantity varies for different particles, the exact expression will depend upon the reaction mechanism involved. This is discussed in further detail in the following sections.

3.4 Thermonuclear Reaction Rates

Solutions to Equation 3.19 depend on how well-behaved $\sigma(E)$ is, and whether the integral in the expression for $\langle \sigma v \rangle$ can be solved numerically or analytically. Generally, it is preferable to solve the integral analytically as it can then be extrapolated to different energy regions allowing for an improved estimate of the reaction rate. Additionally, in cases where the energy

dependent cross section is unknown, a numerical solution is impossible. However, when the energy dependence of a cross section has been determined experimentally or theoretically, a numerical solution can be deployed. For cross sections with complex energy dependence, a numerical solution may be the only approach that yields a functional result [29]. The following section will broadly examine the analytical cases.

A large number of thermonuclear reactions fall into one of two categories: cross sections that vary smoothly with energy (non-resonant cross sections), and cross sections that change rapidly close to a certain energy (resonant cross sections). The non-resonant case will be discussed for charged and neutral particles, and the resonant case will be treated for narrow-resonance reaction rates.

3.4.1 Non-resonant Charged-Particle-Induced Reactions

As stated previously, cross sections can vary drastically with energy and can make analytical solutions difficult. In order to minimize energy dependence when extrapolating cross sections to different energy regimes, it is helpful to introduce the concept of the astrophysical S-factor. Denoted as $S(E)$, this allows the energy-dependent cross section to be rewritten as

$$\sigma(E) = \frac{1}{E} e^{-2\pi\eta} S(E) \tag{3.20}$$

where $e^{-2\pi\eta}$ is the Gamow factor. The Gamow factor describes the probability of an s-wave particle to tunnel through the Coulomb barrier and is defined as

$$e^{-2\pi\eta} \equiv \exp\left(-\frac{2\pi}{\hbar}\sqrt{\frac{\mu c^2}{2E}} Z_a Z_b e^2\right) \tag{3.21}$$

where η is the Sommerfeld parameter, Z_a and Z_b are the atomic numbers of the particles involved in the reaction, e is the charge of the electron, and μ is the reduced mass of the system.

The astrophysical S-factor is useful in that it removes the $1/E$ dependence and the

transmission probability from the energy-dependent cross section. Substituting Equation 3.20 into Equation 3.19 yields

$$\langle \sigma v \rangle = \left(\frac{8}{\pi\mu}\right)^{1/2} \frac{1}{(kT)^{3/2}} \int_0^\infty e^{-2\pi\eta} S(E) e^{-\frac{E}{kT}} dE \tag{3.22}$$

$$= \left(\frac{8}{\pi\mu}\right)^{1/2} \frac{1}{(kT)^{3/2}} \int_0^\infty \exp\left(-\frac{2\pi}{\hbar}\sqrt{\frac{\mu c^2}{2E}} Z_a Z_b e^2\right) S(E) e^{-\frac{E}{kT}} dE \tag{3.23}$$

where the parameters of the Gamow and Sommerfeld factors are the same as above. Since $S(E)$ varies smoothly with energy for non-resonant reactions, the primary energy dependence will come from the other terms. It is clear that at low energies the contribution from the Maxwell-Boltzmann distribution will dominate. However, at high energies, the Gamow factor becomes the dominant contribution to the reaction rate. Convolving these two factors maximizes the integrand at a point where the product of both factors is maximized. This is illustrated in Figure 3.1 for a ^{12}C(α,γ)^{16}O reaction. The point where the convolved terms are maximized, denoted as E_0, is the Gamow peak, and is found by solving the first derivative of the integrand

$$0 = \frac{d}{dE}\left(-\frac{2\pi}{\hbar}\sqrt{\frac{\mu}{2E}} Z_a Z_b e^2 - \frac{E}{kT}\right)_{E=E_0} \tag{3.24}$$

$$\frac{1}{kT} = \frac{\pi}{\hbar}\sqrt{\frac{\mu}{2}} \frac{1}{E_0^{3/2}} Z_a Z_b e^2 \tag{3.25}$$

$$E_0 = \left[\left(\frac{\pi}{\hbar}\right)^2 \left(Z_a Z_b e^2\right)^2 \frac{\mu}{2} (kT)^2\right]^{1/3} . \tag{3.26}$$

This energy represents the most effective energy for non-resonant nuclear reactions to occur in a stellar plasma at a given temperature [29]. The characteristics of the Gamow peak can be reasonably approximated with a Gaussian function. With this in mind, the width of the Gamow peak (ΔE_0) is found by ensuring the second derivatives match at E_0. The width of the Gamow peak varies primarily with temperature and Coulomb barrier, with higher temperatures and larger-Z nuclei having a greater peak width. This relatively narrow range

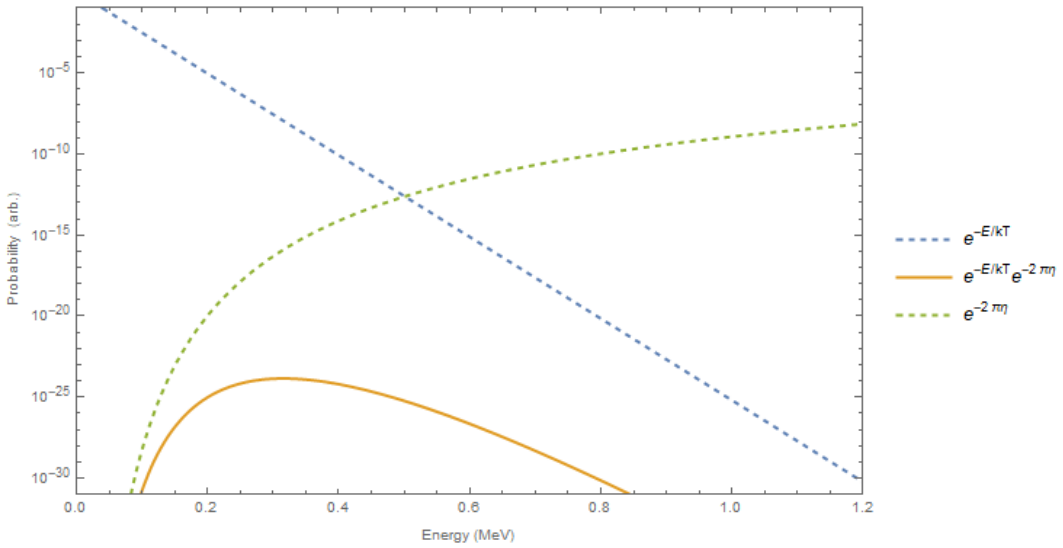

Figure 3.1: Relative probability and Gamow peak for a non-resonant charged particle reaction. The Maxwell-Boltzmann distribution, denoted as $e^{-E/kT}$, and the Gamow factor, denoted as $e^{-2\pi\eta}$, shown for a ^{12}C(α,γ)^{16}O reaction at 0.2 gigakelvin (GK). The Gamow peak, shown as $e^{-E/kT}e^{-2\pi\eta}$, is depicted with a solid orange line.

of energies where the reaction is most likely to occur is referred to as the Gamow window.

Using the above simplifications, an analytic form of the non-resonant reaction rate at the Gamow peak can now be written as

$$\langle \sigma v \rangle = \left(\frac{2}{\mu}\right)^{1/2} \frac{\Delta E_0}{(kT)^{3/2}} S(E_0) e^{-\frac{3E_0}{kT}} \tag{3.27}$$

for smoothly varying, uncomplicated forms of the astrophysical S-factor. In reality, however, the S-factor can vary sharply within the Gamow window. It is here that a separate analytical approach is required to properly treat this behavior, an approach that is covered in Section 3.4.3.

3.4.2 Non-resonant Neutron-Induced Reactions

Events involving neutral particles are generally simpler to treat in that there is no Coulomb barrier for the incident particle to overcome. In a stellar environment, neutrons tend to thermalize quickly and take on a Maxwell-Boltzmann velocity distribution. Neutrons

can then be captured by nuclei in the plasma, typically via an (n,γ) radiative capture reaction. These reactions are most likely to take place at the peak of the velocity distribution, given as

$$v_T = \sqrt{\frac{2kT}{\mu}} \tag{3.28}$$

where v_T is the velocity of the particle at thermal energies. For s-wave neutrons ($\ell = 0$) at thermal velocities, the reaction cross section varies inversely with energy such that

$$\sigma \sim \frac{1}{v_T} \sim \frac{1}{\sqrt{E_T}} \tag{3.29}$$

where v_T and E_T are the velocity and energy at thermal energies, respectively. While emission of charged particles from the exit channel of neutron-induced reactions will vary the transmission probability, for high Q-value reactions this relationship holds for (n,p) and (n,α) reactions. Using this $\sigma \sim 1/v$ relationship enables us to set the astrophysical S-factor to $S \equiv \sigma v$, setting it constant. We can now rewrite the reaction rate as

$$N_A\langle\sigma v\rangle = N_A \int_0^\infty vP(v)\sigma(v)dv = N_A\sigma v = N_A S = \text{constant}. \tag{3.30}$$

This relationship implies that the reaction rate is independent of temperature; however, the $1/v$ relationship does not hold in all cases. This relationship breaks down as neutron energies increase, as different reaction channels become energetically available, or as higher partial waves contribute to the neutron cross section [29].

In the case of increased partial wave contribution the relationship between the cross section and the velocity can be rewritten as

$$\sigma_\ell \sim \frac{1}{v^2}\Gamma_\ell \tag{3.31}$$

where ℓ is the orbital angular momentum of the state, and Γ is the partial width of the state. Partial widths are an important component of the Breit-Wigner formulas and will be

covered in more detail in Section 3.4.3. However, so long as the neutron separation energy remains well above the neutron kinetic energy, this can be simplified to

$$\Gamma_\ell(E) \sim E^{\ell+1/2} \tag{3.32}$$

yielding the relationships

$$\sigma_\ell \sim \frac{1}{v}, v, v^3 \tag{3.33}$$

$$\sigma_\ell \sim E^{-1/2}, E^{1/2}, E^{3/2} \tag{3.34}$$

for $\ell = 0, 1, 2$, respectively. Using Equation 3.34, the partial-wave-dependent non-resonant neutral particle reaction rate can be rewritten as

$$N_A\langle\sigma v\rangle = \left(\frac{8}{\pi\mu}\right)^{1/2} \frac{N_A}{(kT)^{3/2}} \int_0^\infty E\sigma(E)e^{-E/kT}dE \sim \int_0^\infty E^{\ell+1/2}e^{-E/kT}dE \tag{3.35}$$

where the integrand $E^{\ell+1/2}e^{-E/kT}$ represents the most energetically favorable window for these reactions to occur [29]. This reaction rate can be seen in Figure 3.2 for different values of orbital angular momentum.

Many neutron-induced reactions, especially neutron capture reactions, report the reaction rate in terms of the Maxwellian-averaged cross section. With this in mind, the reaction rate can now be expressed as

$$N_A\langle\sigma v\rangle = N_A\langle\sigma\rangle_T v_T = N_A \frac{4}{v_T\sqrt{\pi}} \int_0^\infty v\sigma(v) \left(\frac{v}{v_t}\right)^2 e^{-(v/v_T)^2}dv \tag{3.36}$$

where v_T is the thermal velocity, and $\langle\sigma\rangle_T$ is the Maxwellian-averaged cross section at thermal velocity. Using the relationship established in Equation 3.30 for s-wave neutrons, this reduces

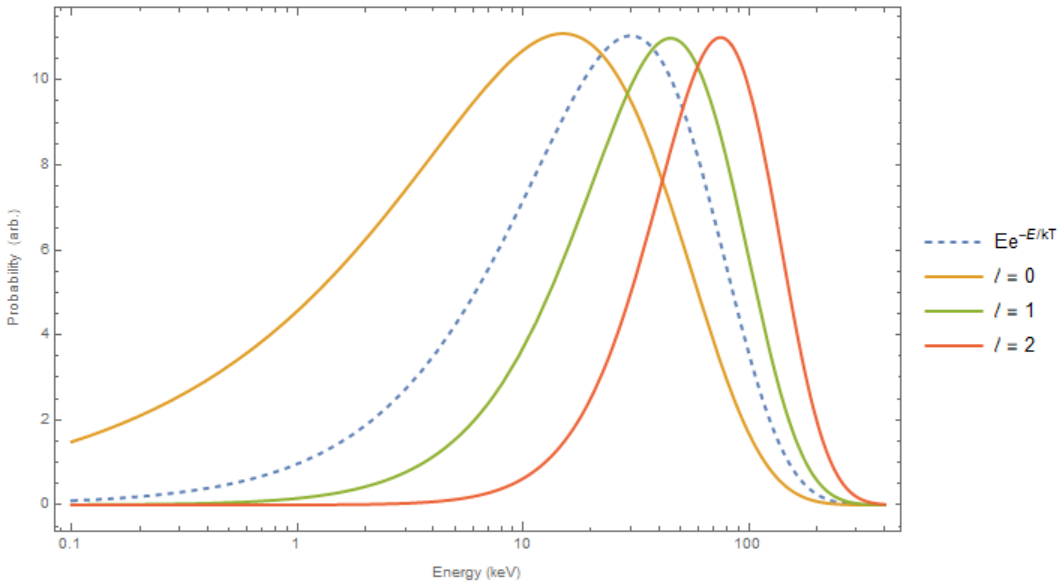

Figure 3.2: A plot of the relative probability versus neutron energy for a non-resonant neutral particle reaction. The above plot depicts relative probability of a reaction versus neutron energy for a neutral-particle non-resonant reaction. This plot shows the energy window for reactions with different angular momentum transfer in a stellar environment of $kT = 30$ keV. The Maxwell-Boltzmann distribution, denoted as $e^{-E/kT}$, is included for comparison.

the reaction rate to

$$N_A\langle\sigma\rangle_T v_T = N_A \frac{4}{v_T\sqrt{\pi}} v_T\sigma(v_T)\int_0^\infty \left(\frac{v}{v_t}\right)^2 e^{-(v/v_T)^2} dv = N_A v_T \sigma(v_T) \tag{3.37}$$

implying the Maxwellian-averaged cross section is the same as the cross section measured at thermal velocities. Other relationships, such as those established in Equation 3.34, can be substituted directly into the above equation. These estimates provide reasonable approximations; however, in practice the reaction cross section often must be measured experimentally for a range of neutron energies and integrated numerically [30].

3.4.3 Narrow-resonance Reactions

Unlike non-resonant reactions where the astrophysical S-factor varies smoothly, narrow-resonance reactions have S-factors that change sharply over small energy regions. Considering Equation 3.1 again, this reaction is treated as a two-step process with clearly separated

incoming and outgoing particles. Instead, imagining this process in three steps would make this equation

$$a + X \rightarrow Z^* \rightarrow Y + b \tag{3.38}$$

where Z^* is an intermediate compound nucleus in an excited state [31]. In this interpretation, the compound nucleus can be treated as a many-body system with a number of virtual states. Narrow-resonance reactions occur when the center-of-mass energy of the reaction corresponds with a virtual state in the compound nucleus. In addition to the energy requirement, the intrinsic angular momentum of the incident and target particles ($\vec{J_a}$ and $\vec{J_X}$, respectively) must be equal to the angular momentum of the virtual state ($\vec{J}$) such that

$$\vec{J} = \vec{J_X} + \vec{J_a} + \vec{L} \tag{3.39}$$

where $\vec{L}$ is the relative angular momentum between the two particles.

An excited state in the compound nucleus with positive energy is inherently particle unbound. As such, the state can be treated as a single particle in a potential and the energy-dependent cross section is given by the Breit-Wigner formula. For the above reaction, the cross section can be written

$$\sigma_{BW}(E) = \frac{\lambda^2}{4\pi} \frac{2J+1}{(J_X+1)(2J_a+1)} (1+\delta_{Xa}) \frac{\Gamma_i \Gamma_j}{(E_r - E)^2 + \Gamma^2/4} \tag{3.40}$$

where J_X is the spin of the target, J_a is the spin of the projectile, J and E_r are the spin and energy of the state in the compound nucleus, λ is the wave number, Γ_i and Γ_j are the partial widths of the entrance and exit reaction channels, and Γ is the total resonance width [29]. The total resonance width is calculated by summing all energetically allowed decay partial widths

$$\Gamma = \sum_{i=1}^{n} \Gamma_i \,. \tag{3.41}$$

To avoid confusion, the wave number can be substituted with the de Broglie wavelength such

that $\lambda = 2\pi\hbar/\sqrt{2\mu E}$. The Kronecker delta is included from Equation 3.10 to account for identical particles in the entrance channel.

The reaction rate for a narrow-resonance reaction can now be written as

$$N_A\langle\sigma v\rangle = N_A\left(\frac{8}{\pi\mu}\right)^{1/2}\frac{N_A}{(kT)^{3/2}}\int_0^\infty E\sigma_{BW}(E)e^{-E/kT}dE \tag{3.42}$$

$$= N_A\frac{\sqrt{2\pi}\hbar^2}{(\mu kT)^{3/2}}\omega\int_0^\infty \frac{\Gamma_i\Gamma_j}{(E_r-E)^2+\Gamma^2/4}e^{-E/kT}dE \tag{3.43}$$

where ω is defined as

$$\omega \equiv \frac{(2J+1)(1+\delta_{Xa})}{(J_X+1)(2J_a+1)} \tag{3.44}$$

and therefore contains all the relevant spin information. This expression can be further simplified by assuming the resonance is narrow enough such that the partial widths and the Maxwell-Boltzmann factor will not vary over the width of the resonance. In this case, these values can simply replaced by their value at the resonance energy E_r. This yields

$$N_A\langle\sigma v\rangle = N_A\frac{\sqrt{2\pi}\hbar^2}{(\mu kT)^{3/2}}e^{-E_r/kT}\omega\frac{\Gamma_i\Gamma_j}{\Gamma}2\int_0^\infty \frac{\Gamma/2}{(E_r-E)^2+\Gamma^2/4}dE \tag{3.45}$$

$$= N_A\frac{\sqrt{2\pi}\hbar^2}{(\mu kT)^{3/2}}e^{-E_r/kT}\omega\frac{\Gamma_i\Gamma_j}{\Gamma}2\pi \tag{3.46}$$

$$= N_A\left(\frac{2\pi}{\mu kT}\right)^{3/2}\hbar^2 e^{-E_r/kT}\omega\gamma \tag{3.47}$$

where $\omega\gamma$ is defined as

$$\omega\gamma \equiv \omega\frac{\Gamma_i\Gamma_j}{\Gamma}\,. \tag{3.48}$$

This quantity $\omega\gamma$ is commonly referred to as the resonance strength and is proportional to the area under the resonance cross section. In the case where more than one resonance contributes to a reaction rate, the reaction rate can be determined by summing over each

contributing resonance. This would make Equation 3.47

$$N_A\langle\sigma v\rangle = N_A\left(\frac{2\pi}{\mu kT}\right)^{3/2}\hbar^2\sum_{i=1}^{n}e^{-E_i/kT}(\omega\gamma)_i \tag{3.49}$$

where n is the number contributing resonances [9].

3.5 Indirect Measurements of Resonance Properties

From Equation 3.47 it is clear that the two most important properties of a resonance are the resonance energy (E_r) and the resonance strength ($\omega\gamma$). The preferred method of measuring these resonance properties is by taking direct measurements with the isotope of interest, with a beam energy that matched the resonance energy in the center of mass frame. For short-lived radioactive isotopes, this involves producing a radioactive ion beam, and for long-lived radioactive isotopes this often involves creating a radioactive target or, less frequently, a long-lived radioactive beam. Directly measuring the cross section of a given reaction by constructing a yield curve allows for the resonant energy and strength to be extracted.

Take for example the direct measurement that was discussed in Chapter 2. The experiment was performed at the Detector of Recoils And Gamma rays Of Nuclear reactions (DRAGON) detector at TRIUMF in Vancouver, BC utilizing an exotic isotope separator and accelerator to generate and deliver radioactive isotope beams to a gas target [32]. The incident beam impinges upon an extended (12.3 cm) gas target, and, after losing energy in the target volume, can induce the radiative capture of the gas. Measuring the position of the reaction in the target provides a direct measurement of the resonance energy. The resonance strength is obtained by counting the number of generated recoils per incident beam particle [18, 33].

However, technological limitations often restrict the number of reactions that can be studied via direct methods. Often in the case of radioactive isotopes, the target or beam of interest is too difficult to generate and integrate into an experiment. In other cases, a reso-

nance of interest is very weak, which either makes it difficult to separate from background or impossible to measure in a reasonable length of time. Indirect methods of measuring resonance parameters provide an alternative way of determining resonance energies and critical properties. A number of techniques exist including Coulomb dissociation, the Trojan Horse method, as well as measurement of the asymptotic normalization coefficients and spectroscopic factors [34, 35, 36]. For the purposes of this thesis, focus will be given to utilizing transfer reactions to extract relevant resonance parameters from spectroscopic factors.

3.5.1 Indirect Measurements using Transfer Reactions

Consider the case of a proton radiative capture $X(p,\gamma)Y$, where the only available reaction channels are the proton channel Γ_p and the gamma channel Γ_γ. Equation 3.48 can now be expressed as

$$\omega\gamma = \omega\frac{\Gamma_p\Gamma_\gamma}{\Gamma} = \frac{2J+1}{(2J_X+1)(2J_p+1)}\frac{\Gamma_p\Gamma_\gamma}{(\Gamma_p+\Gamma_\gamma)} \tag{3.50}$$

where J_X and J_p are the spins of the target nucleus and proton, respectively. The resonance strength can therefore be constrained by measuring any of these individual values. For example, if the spins of the target, particle, and populated state are known, measuring the partial widths of the resonance allows for the resonant strength to be calculated. This calculation is made even easier if one partial width dominates the resonance strength.

Consider the case in which particle emission is the dominant form of decay. This would imply that $\Gamma_p \gg \Gamma_\gamma$, making the resonance strength

$$\omega\gamma = \omega\frac{\Gamma_p\Gamma_\gamma}{(\Gamma_p+\Gamma_\gamma)} \approx \omega\frac{\Gamma_p\Gamma_\gamma}{\Gamma_p} = \omega\Gamma_\gamma\,. \tag{3.51}$$

This indicates that the resonance strength depends primarily on the gamma partial width. Often the gamma partial width is measured by measuring the lifetimes of the resonant state of interest. In the case of a dominant proton partial width, however, the states are proton-unbound by nature and thus decay preferentially via proton emission, making measurements of the gamma lifetime difficult. Estimates of the gamma partial width can be made by using

the gamma partial width from analogue states in the mirror nucleus. This requires correction for the energy differences between analogue states that arise from the Coulomb barrier, but are otherwise a very close approximation [9].

The alternative case, where $\Gamma_\gamma \gg \Gamma_p$ and the nucleus decays primarily via gamma emission, results in a resonance strength given by

$$\omega\gamma = \omega\frac{\Gamma_p\Gamma_\gamma}{(\Gamma_p + \Gamma_\gamma)} \approx \omega\frac{\Gamma_p\Gamma_\gamma}{\Gamma_\gamma} = \omega\Gamma_p\,. \tag{3.52}$$

Contrary to the previous scenario, this now implies that the resonant strength depends primarily on the proton width. We can substitute the proton width as

$$\Gamma_p = C^2S \cdot \Gamma_{sp} \tag{3.53}$$

where C^2S is the spectroscopic factor Γ_{sp} is the single-particle partial width of the state. Effectively, the spectroscopic factor is a dimensionless ratio that describes how strongly the measured resonance behaves like a pure single-particle resonance. The single-particle partial width is given by

$$\Gamma_{sp} = \frac{2\hbar^2 P_C}{mR^2}\theta_{sp}^2\,, \tag{3.54}$$

where m is the mass of the particle, R is the nuclear radius, P_C is the penetration factor, and θ_{sp} is the dimensionless single-particle reduced width [29]. Both the spectroscopic factor and the single-particle reduced width will be described in more detail in Section 3.5.2.

To constrain resonance parameters using transfer reactions, it is clear that a number of variables must be known: the spins of the incident and outgoing particles, the single-particle reduced width, and the spectroscopic factor. For the purpose of this work, the spectroscopic factor is the important experimentally measured quantity as all other quantities have been experimentally determined or can be derived from theory.

3.5.2 Theoretical Models of Transfer Reactions

A transfer reaction can be generalized as a reaction in which a number of nucleons are transferred into or out of a target nucleus. In order to construct a theoretical basis to treat these reactions, a model of the nucleus must first be established. This model must competently treat both the energy levels which incident particles can populate as well as the nuclear orbitals of given states. The nuclear shell model can adequately provide both of these pieces of information, as it describes a nucleus as a series of shells populated by protons and neutrons. This model is similar to the Bohr model of the atom, which describes electron orbitals around the nucleus as a series of well-defined shells.

3.5.2.1 The Nuclear Shell Model

Nuclear shells differ from atomic shells in a number of ways, chiefly in that nuclear shells must account for nucleon-nucleon interactions. This is further complicated by the presence of two different nuclear particles in the nucleus, as well as the fact that there is no heavy center of force for nucleons. Despite these problems, the nuclear shell model does provide insight as well as a theoretical underpinning, which allows for a better understanding of nuclear reactions.

Briefly, the nuclear shell model can be constructed by first solving the Schrödinger equation in three dimensions for a given potential, written generally as

$$\left(\frac{-\hbar^2}{2m}\Delta^2 + V(r)\right)\Phi(r) = E\Phi(r)\,. \tag{3.55}$$

In this equation $V(r)$ is a spherically symmetric potential, r is the radius, E is the energy eigenvalue, $\Phi(r)$ is the wave function of a single nucleon, and m is the mass of the nucleon. Solving this equation provides the quantized energy levels of a given nucleus. The energy levels found from this equation are particularly sensitive to the nuclear potential. One of the

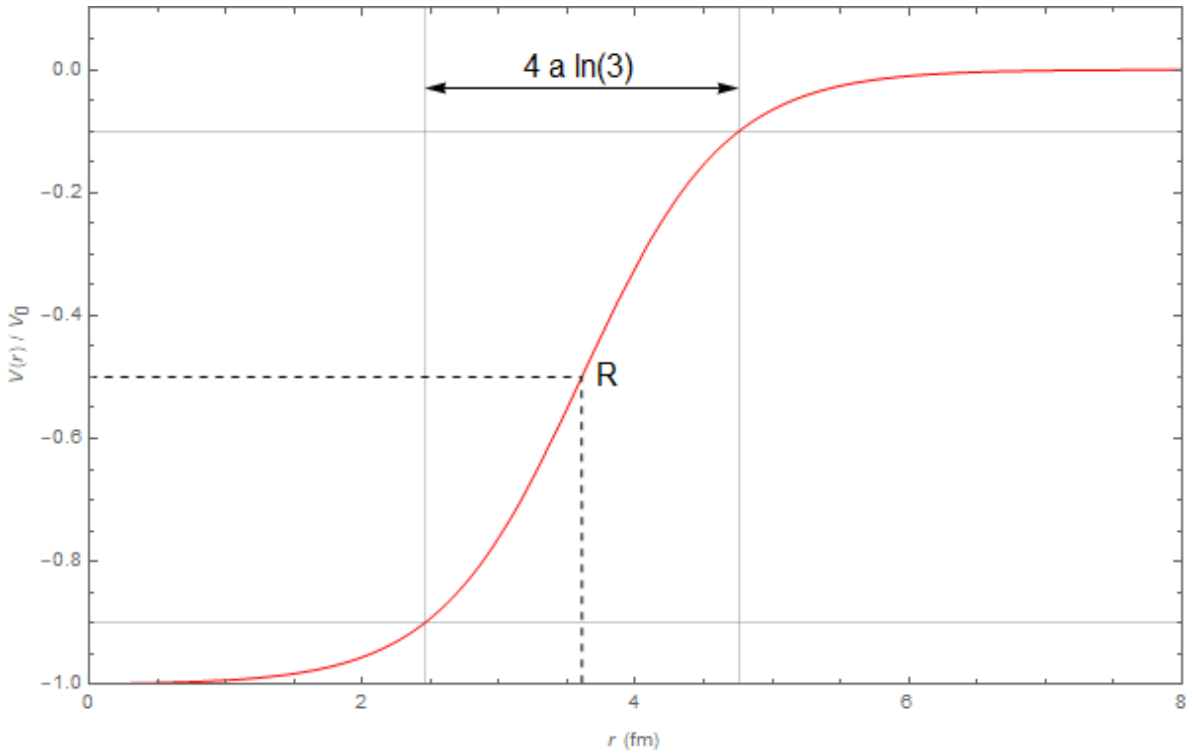

Figure 3.3: The Woods-Saxon Potential, a semi-realistic form of the nuclear potential. The value $4a\ln(3)$ represents the area in which the nuclear potential varies from $0.9V_0$ to $0.1V_0$ and R is the mean nuclear radius [27].

most commonly assumed nuclear potentials is the Woods-Saxon potential, given as

$$V(r) = \frac{-V_0}{1 + e^{\frac{r-R}{a}}} \tag{3.56}$$

where V_0 is the potential radius, R is the mean nuclear radius, and a is a constant that describes the diffuseness of the nuclear surface. Figure 3.3 depicts this potential for an arbitrary nucleus. On its own, this potential mirrors experimentally observed data for the first several nuclear shells. However, for larger nuclei, additional modifications must be considered.

In order to replicate behavior observed in higher-order shells, a spin-orbit coupling term must be added to the potential. First proposed in 1949 by Mayer [37], Haxel, Jensen, and

Suess [38], the introduced term

$$-V_{so}(r) = -\vec{\ell} \cdot \vec{s} \tag{3.57}$$

allowed for the nuclear shell model to account for the coupling between the intrinsic spin s and the orbital angular momentum ℓ of the nucleus. When the $\vec{\ell}$ and $\vec{s}$ vectors oppose one-another, the binding energy of nucleus decreases while the overall binding energy increases when they are parallel. This change in the overall binding energy dependent on spin causes the quantized energy levels to split, causing spin-orbit splitting of energy-degenerate orbitals and thus accounts for all experimentally observed shell closures in nuclei on and near stability [27]. Each shell model orbital is defined by the principle quantum number n, the orbital angular momentum ℓ, and the total spin J of the nucleons in that orbital.

3.5.2.2 Single-nucleon Transfer Reactions

The shell model of the nucleus, at its extreme, stipulates that single-particle states of paired or unpaired nucleons define the behavior of the nucleus as a whole. Thus, single-nucleon transfer reactions are frequently used to probe the shell-model structure of the nucleus [39]. These reactions are direct reactions that generally occur at the very periphery of the surface of the nucleus, such that beam and target particles do not form a compound nucleus. The nucleon transferred during these reactions tends to preferentially populate single-particle states, or states that can be generally described as a nuclear core with a single nucleon orbiting in a well-defined shell-model orbital [40].

A number of stripping and pickup reactions fall under the category of single-nucleon transfer. Taking the specific case of a (d,p) reaction, however, Equation 3.2 can be rewritten as

$$X(d,p)Y = X(d,p)\,[X+n] \tag{3.58}$$

since the daughter nucleus simply picks up a neutron relative to the target nucleus. The cross section is proportional to the overlap of the initial and final state wave functions, or in this case the overlap in the X and $X+n$ systems. As the final state is assumed to be single-

particle in nature, the observed experimental cross section can appear lower when compared to the theoretical approximation. This occurs when the experimentally populated state is not purely single-particle and the single-particle strength is spread over several different states. As discussed earlier, the spectroscopic factor is used to quantify how strongly a state behaves like its theoretical single-particle analogue, and can therefore be determined with the equation

$$C^2S = \frac{\sigma_{exp}}{\sigma_{th}} \tag{3.59}$$

where σ_{exp} is the experimentally observed cross section, and σ_{th} is the cross section predicted by theory.

It is worth considering that the experimental and theoretical cross section will vary depending upon the angle at which it is observed. This behavior is characterized by the differential cross section, or angular distribution $\frac{d\sigma}{d\Omega}$, and can be related to the total cross section as

$$\sigma = \oint_{4\pi} \frac{d\sigma}{d\Omega} d\Omega = \int_0^{\pi} \int_0^{2\pi} \frac{d\sigma}{d\Omega} \sin\theta d\theta d\phi \tag{3.60}$$

where Ω is the solid angle. While the shape of the angular distribution depends on a number of different factors, the primary contributor is the angular momentum transferred during the reaction. Different quantities of angular momentum transfer can drastically vary the shape of the angular distribution due to angular momentum conservation during the reaction. By comparing experimental data to theoretical predictions of the angular distribution, inferences about a particular state's angular momentum can be made and its spin an parity can be confidently constrained [40].

3.5.2.3 The Plane Wave Born Approximation

As discussed previously, the theoretical cross section can be obtained by comparing the overlap in the initial and final state wave functions. The simplest method of doing this is via the plane wave Born approximation (PWBA). This method makes several simplifying assumptions, such as taking the nucleus to be a simple spherically symmetric weak scattering

potential and modeling the wave functions of the incoming and outgoing particles as plane waves. The differential cross section of our (d,p) reaction can be written as

$$\frac{d\sigma_\beta}{d\Omega} = \frac{\mu_\alpha \mu_\beta}{\left(2\pi\hbar^2\right)^2} \frac{k_\beta}{k_\alpha} |T|^2 \tag{3.61}$$

where α is the incoming channel $X + d$, β is the outgoing channel $[X + n] + p$, μ is the reduced mass of each channel, k is the momentum, and T is the transmission amplitude. The transmission amplitude is then roughly given by

$$T = \int \psi_{[X+n]} \psi_p \, e^{i\vec{k_\beta} \cdot \vec{r_\beta}} \, V \, \psi_X \psi_d \, e^{i\vec{k_\alpha} \cdot \vec{r_\alpha}} \, d\tau \tag{3.62}$$

where ψ_i is the wave function of each nucleus, V is the spherically symmetric scattering potential, $e^{i\vec{k_i} \cdot \vec{r_i}}$ are the plane waves, and τ represents all the variables to be integrated over. This equation can be solved analytically via a partial wave expansion [39], yielding

$$T \approx \sum_\ell C_\ell j_\ell(qR) \tag{3.63}$$

where C_ℓ are Clebsch-Gordon coefficients determined by the contributions of various values of angular momentum ℓ, j_ℓ is the spherical Bessel function, R is the nuclear radius, and is the difference in momentum given by

$$q = k_\alpha - k_\beta \, . \tag{3.64}$$

For single-particle states with only one value of ℓ, this means that the differential cross section is proportional to the square of the spherical Bessel function. From this relationship, the PWBA can accurately predict the shape of the differential cross section. However, it fails to accurately predict experimental cross sections.

3.5.2.4 The Distorted Wave Born Approximation

In order to begin to reproduce experimental cross sections, effects from inelastic scattering and absorption into other exit channels must be assessed. These factors are considered by the distorted wave Born approximation (DWBA). As its name implies, the plane waves utilized by the PWBA are replaced by distorted waves that account for scattering effects

$$\chi(\vec{k},\vec{r}) = e^{i\vec{k}\cdot\vec{r}} + \psi_{\text{scatt}} \tag{3.65}$$

where ψ_{scatt} contains the scattering wave function. Additionally, the simple scattering potential is replaced by an optical potential, a more complex function comprised of terms modeling the Woods-Saxon potential, the absorption of incoming waves into non-elastic reaction channels, spin-orbit coupling, and the Coulomb barrier [27]. These terms are constrained by taking experimental data from similar nuclei in the appropriate energy regime and fitting the model to match [39]. With this in mind, the transmission amplitude is given by

$$T = \iint \chi^{(-)}(\vec{k_\beta},\vec{r_\beta})\langle p,[X+n]|V|d,X\rangle\chi^{(+)}(\vec{k_\alpha},\vec{r_\alpha})d\vec{r_\alpha}\vec{r_\beta} \tag{3.66}$$

where the nuclear matrix element $\langle p,[X+n]|V|d,X\rangle$ is a function of $\vec{r_\alpha}$ and $\vec{r_\beta}$. The solution to this equation is no longer a simple analytic expression and solving often requires numerical integration [39]. However, what is lost in simplicity is made up for in accuracy, as the DWBA has proven to be an exceptionally powerful tool for analyzing direct reactions. A number of computer codes have been developed to aid in the analysis of experimental transfer reactions, including TWOFNR [41] and FRESCO [42].

A further extension of the DWBA specifically for (d,p) reactions involves including interaction effects between the deuteron's constituent nucleons. As the deuteron is only weakly bound with a binding energy of about 2.2 MeV, the breakup of the deuteron makes a significant contribution to the incoming wave function. Functionally, this means treating the two-

body system of projectile and target as a three-body system including the target, deuteron neutron, and deuteron proton. One solution to this, proposed by Johnson and Soper [43], treats the two-body neutron and proton system as a fixed system with a zero-range interaction determined by the neutron-proton interaction. This approach, referred to as the adiabatic distorted wave approximation (ADWA), is an almost identical calculation to DWBA formulations, so reaction codes can be easily modified to perform ADWA calculations [40].

4. TIARA FOR TEXAS

4.1 Experimental Overview

The experiment was conducted at the Texas A&M University Cyclotron Institute in November 2016 using the Transfer and Inelastic All-angle Reaction Array (TIARA), a compact silicon-detector array designed to study direct reactions in inverse kinematics. A beam of ^{23}Na was accelerated by the K150 cyclotron to 10 AMeV. This beam was then impinged on a 500 μg·cm^{-2} thick deuterated polythene (CD_2) target placed at the center of TIARA. Excited states of ^{24}Na, populated via the ^{23}Na(d,p)^{24}Na reaction, were identified using light-ejectile protons detected in the TIARA silicon-detector array [44]. Further resolving power was attained by isolating gamma rays generated by the reaction in the four segmented high-purity germanium detectors surrounding the target position. Heavy-recoil particles were separated using the MDM-2 spectrometer and then measured using the Oxford detector [45, 46].

Differential cross-sections with respect to scattering angle were constructed for astrophysically-relevant excited states that allowed for the extraction of spectroscopic factors. The experiment served as one of several commissioning experiments for the TIARA for Texas (T4T) collaboration and acted as a proof of principle for several proposed radioactive-ion beam experiments. The experimental setup is described in this section, while the detailed operation of each detector is described in the following sections.

4.1.1 Beam production

The stable beam of ^{23}Na was produced by feeding sodium atoms into an electron-cyclotron resonance ion source (ECRIS). The Texas A&M ECRIS uses a combination of neodynium-iron-boron permanent magnets and conventional water-cooled copper electromagnets to contain a plasma field of high-energy electrons [47]. These electrons collide with the sodium atoms injected into the ECRIS and liberate atomic electrons. Once the sodium are stripped

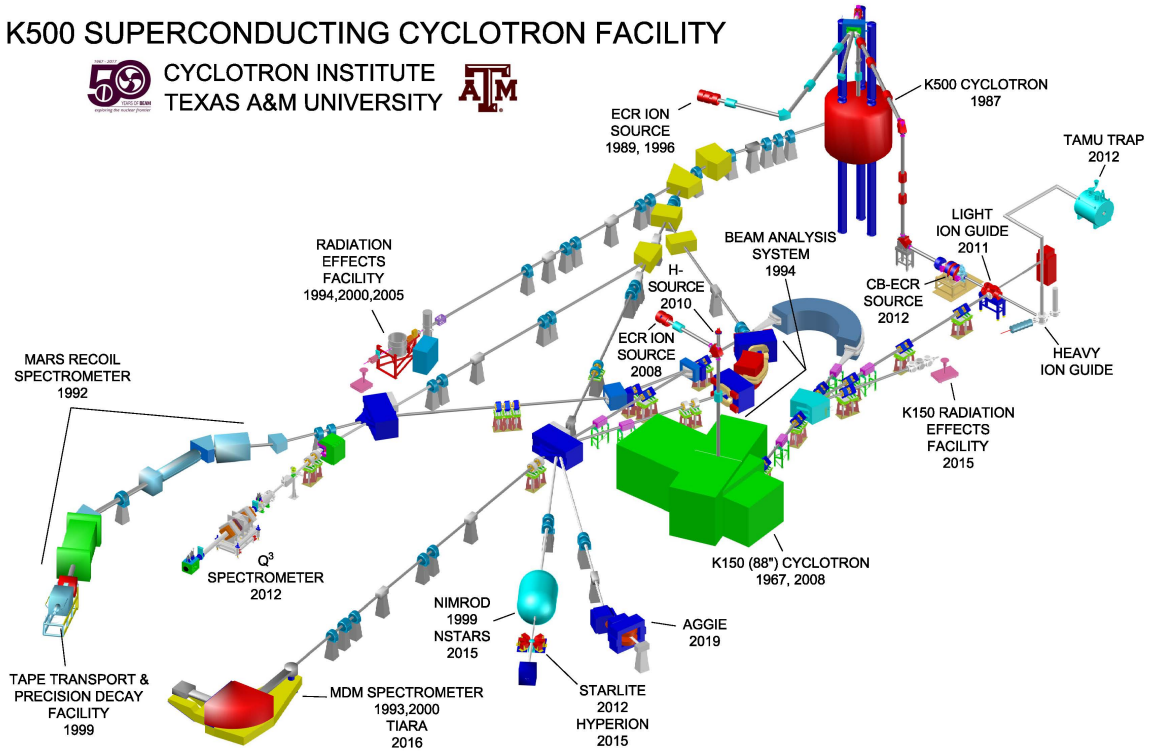

Figure 4.1: A figure showing the Cyclotron Institute accelerators and beam line. The Cyclotron Institute consists of two cyclotrons, the K500 and the K150, as well as five experimental halls and numerous experimental setups. This image is accurate as of Fall 2019.

down to their $^{23}Na^{8+}$ charge state, they are extracted from the ECRIS and injected into the K150 cyclotron. This particle accelerator, based off of the design of the original Berkeley 88-inch cyclotron [48], was recently recommissioned as part of a facility upgrade project to generate re-accelerated rare isotope beams. The traditional electromagnet cyclotron accelerated the sodium ions up to 10 AMeV before extraction. The beam was then purified using a large-diameter analyzing magnet and sent to the experimental setup located in Cave 3. In this study, the final delivered beam arrived at 10 AMeV at a rate of approximately $1{\times}10^{8}$ particles per second. An image of the Cyclotron Institute is shown in Figure 4.1.

4.1.2 Silicon Detectors

The Transfer and Inelastic All-angle Reaction Array (TIARA) is a compact silicon-detector array designed to study direct reactions in inverse kinematics. Housed in an aluminum vacuum chamber, up to three silicon arrays can run simultaneously allowing TIARA to cover lab angles between 4° and 170° [44]. A diagram of TIARA is shown in Figure 4.2. In the present study TIARA utilized only two silicon arrays, the HyBall and Barrel.

4.1.2.1 HyBall

The first array, a backward annular silicon-detector (commonly referred to as the HyBall), consists of six wedges of 400 μg thick double-sided silicon-strip detectors. Each wedge is divided up into sixteen rings covering the θ_{lab} angles between 137° and 169.4° (each strip covering roughly 2°) as well as eight sectors covering the radial angles. This segmentation allows each combination of ring and sector to act as a pixel, giving TIARA the ability to resolve both the energy and position of a particle. The energy resolution of the HyBall is

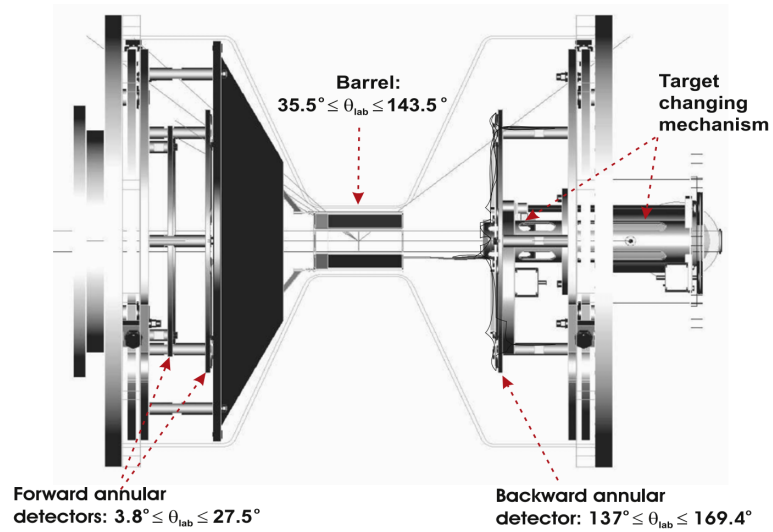

Figure 4.2: A schematic of TIARA showing the effective lab angles it covers. This diagram shows the different detectors TIARA is capable of supporting as well as the effective lab angles each detector covers. For this experiment, only the backward annular silicon-detector (HyBall) and the Barrel were used. Reprinted with permission from [44].

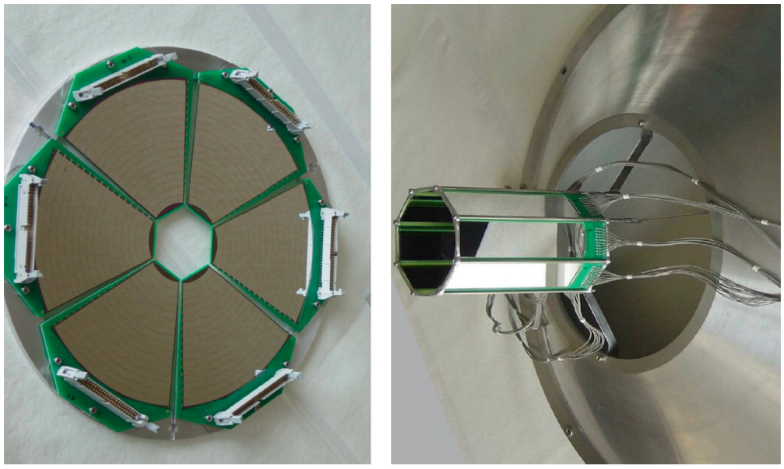

Figure 4.3: Pictures of the HyBall and Barrel detectors. (*LEFT*) The HyBall detector with its six wedges and (*RIGHT*) the Barrel mounted on the wok. Reprinted with permission from [44].

dependent upon the energy of the incident particle, but for a 5.5 MeV alpha particle the detector has an energy resolution of roughly 70 keV (FWHM) [44].

4.1.2.2 Barrel

The second telescope, referred to as the Barrel, consists of eight silicon-detectors arranged in an octagon around the target position. The Barrel covers the θ_{lab} angles between 35.5° and 143.5° and consists of an inner and outer layer. The Inner and Outer Barrel both consist of eight silicon-strip detectors subdivided into four sections, allowing the Barrel to capture both position and energy information.

The Inner Barrel utilizes four resistive silicon-strips for each of the eight detectors. These strips are approximately 400 μm thick, have an active area of 94.8 mm × 22.6 mm, and measure 5.65 mm wide [44]. In principle, a resistive silicon-strip detector reads signals from opposite ends of the detector area simultaneously. It is then possible to use the ratio of charge collected at either end to determine where a particle hit on the detector. Using resistive silicon-strips necessitates the use of far fewer channels at the expense of reduced energy and position resolution. Due to the electronic noise inherent in the detectors the

Inner Barrel has higher energy thresholds and, while the energy and position resolution is dependent on the energy of the deposited particle, can measure a 5.5 MeV alpha particle with a nominal position resolution of 1.0 mm and a nominal energy resolution of 140 keV (FWHM) [49].

The Outer Barrel is almost twice as thick as the Inner Barrel and is designed to tag energetic particles that manage to punch through the Inner Barrel. Since position information is collected from the Inner Barrel, the Outer Barrel collects only energy information. The energy resolution for one strip of the Barrel is roughly 70 keV (FWHM) for a 5.5 MeV alpha particle [44]. During a number of the commissioning experiments the Outer Barrel was inoperable and as such will not be discussed in any further detail in this work. Both the HyBall and the Barrel are shown in Figure 4.3.

4.1.3 High-purity Germanium Detectors

The vacuum chamber of TIARA is designed such that four HPGe detectors can be placed within 50-55 mm of the target position. The walls of the vacuum chamber are thinner around the target position, allowing for less attenuation of gamma rays in this region. This allows for a maximum photopeak efficiency of approximately 15% at 1 MeV [40].

The experimental setup utilized four segmented HPGe detectors from the Hyperion array [50] mounted on a custom-designed frame around TIARA's target position. Each detector consisted of a germanium crystal electronically segmented into four crystal volumes with a square face measuring 50 mm $\times$ 50 mm and a depth of 80 mm. Each crystal was also separated into three segment volumes running perpendicular to the beam. The segmentation is demonstrated in Figure 4.4. This segmentation allowed for a position to be attained for each individual gamma ray and for a Doppler correction to be applied to the gamma ray's energy, a process described in Chapter 5. The four HPGe detectors were positioned perpendicular to the beam at approximate azimuthal angles of 45° 135° 225° and 315° and at a distance of between 50 mm and 55 mm from the center of the target. This provided maximum coverage around the target position and contributed to our relatively-high photopeak efficiency. A

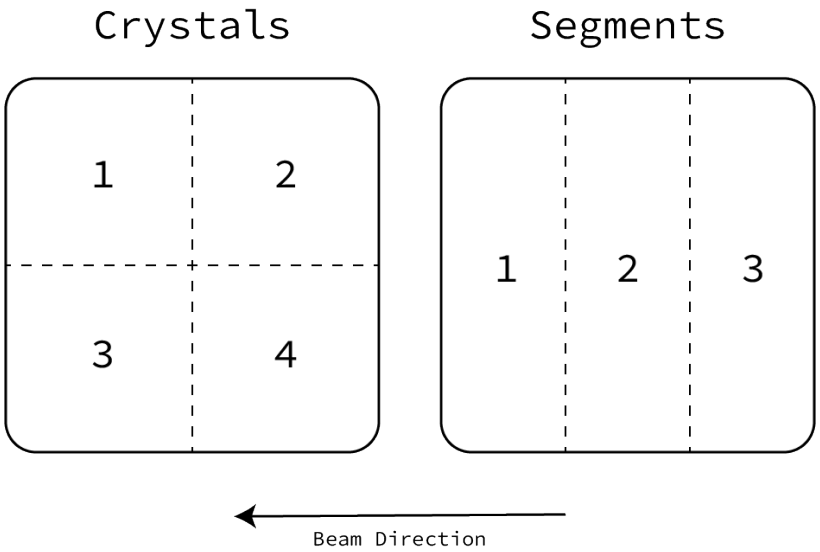

Figure 4.4: Diagram showing the segmentation of the HPGe detectors. This diagram shows the electronically segmented volumes of the HPGe detectors. Each detector volume is segmented into both crystals and segments, however these are shown separately to avoid confusion.

schematic of this setup is shown in Figure 4.5.

4.1.4 MDM and Oxford Detector

The Oxford MDM-2 magnetic spectrometer and the Oxford detector were first developed and brought online in 1983 at the University of Oxford [45] and were later transferred to the Texas A&M Cyclotron Institute. The spectrometer was installed in Cave 3 and the Oxford detector underwent a number of upgrades over the years [51, 46], ultimately resulting in the experimental setup utilized during the TIARA for Texas campaigns and described below.

4.1.4.1 MDM-2 Spectrometer

The Multipole-Dipole-Multipole (MDM) magnetic spectrometer, located just downstream of TIARA, consists of several magnetic elements: a sextupole at the entrance, two multipoles at the entrance and exit, and a gradient-field dipole. With a radius of 1.6 m, the MDM is capable of bending a mass energy product of up to 315 MeV amu and a resolving power ($E/\Delta E$) of about 3000. Additionally, the spectrometer is capable of accepting a maximum

solid angle of up to 8 msr and an energy ratio ($E_{\max}/E_{\min}$) of up to 1.31 [45]. The acceptance of the MDM is defined by a series of $\pm 2^{\circ}$ slits in the x- and y-directions situated at the entrance of the magnet. At the exit of the MDM, a Faraday cup and a large metal plate, referred to as the blocker, were affixed to a set of servo motors that allowed them to be moved in and out of the focal plane.

The primary function of the MDM was to separate unreacted ^{23}Na from the ^{24}Na heavy-recoils. Due to their difference in respective magnetic rigidity, the unreacted beam was tuned such that the majority of the particles hit the blocker before passing into the Oxford detector. The remaining beam accepted into the Oxford detector appeared to be the ^{24}Na heavy-recoils.

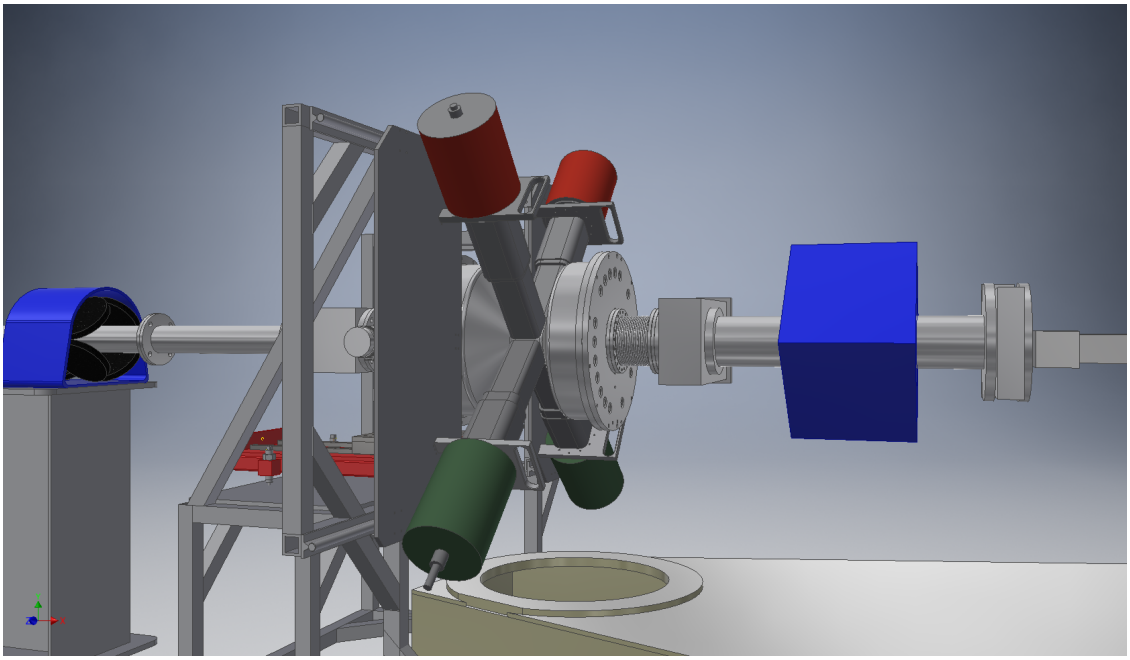

Figure 4.5: Orthographic view of the HPGe detectors around the TIARA chamber. Specifically, this diagram shows the HPGe detectors arranged around the TIARA chamber. The detectors were mounted on large, sliding metal plates that allowed them to move away from the chamber for disassembly or target changes.

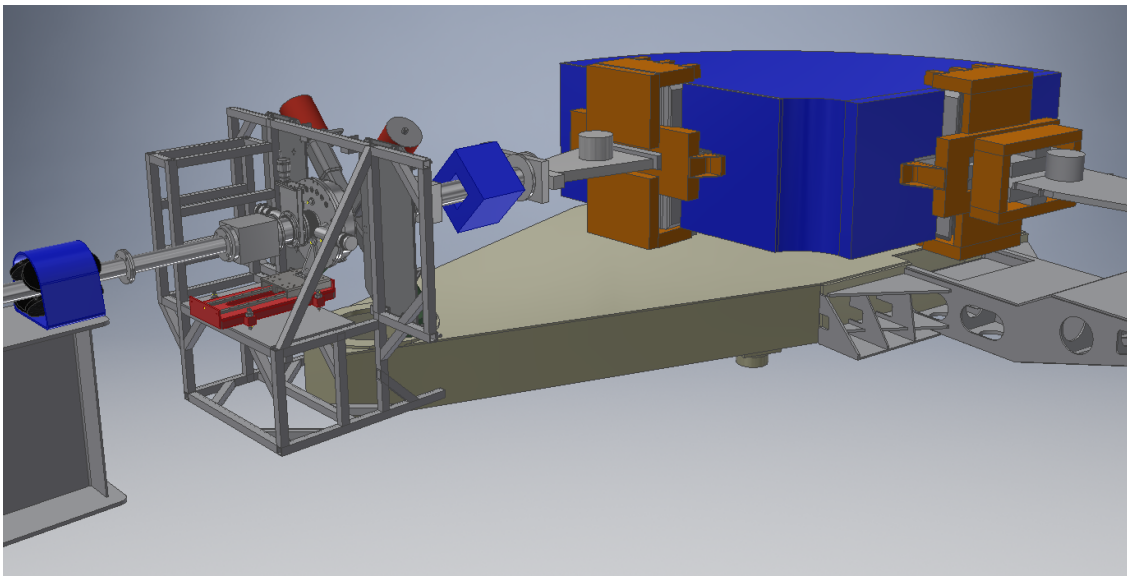

Figure 4.6: Orthographic view of the MDM-2 magnetic spectrometer. In this image, the dipole is pictured in blue while the entrance and exit multipoles are pictured in orange.

4.1.4.2 Oxford Detector

The Oxford detector, located directly behind the MDM, is a gas-filled ionization chamber that functions as a *E-dE* detector. The detector uses a number of different techniques to measure energy loss as the particle passes through the gas as well as the position of the particle as it passes through the detector. It consists of a cathode, two anodes, four resistive proportional-counting wires, a MICROMEGAS plate [52], and a Frisch grid. A schematic of these elements is shown in Figure 4.7.

After exiting the MDM, particles enter the Oxford detector through a 25 μm thick Mylar window. This window acts as a barrier, isolating the isobutane gas inside the detector from the vacuum in the MDM. While the Oxford detector is capable of holding pressures up to more than 200 Torr, the present study maintained pressure in the chamber at about 40 Torr for the first half of the experiment and 30 Torr for the second half of the experiment. Once inside the chamber, particles begin to slow down and liberate electrons from the gas. These electrons, guided by the electric field, drift towards the four proportional-counting wires.

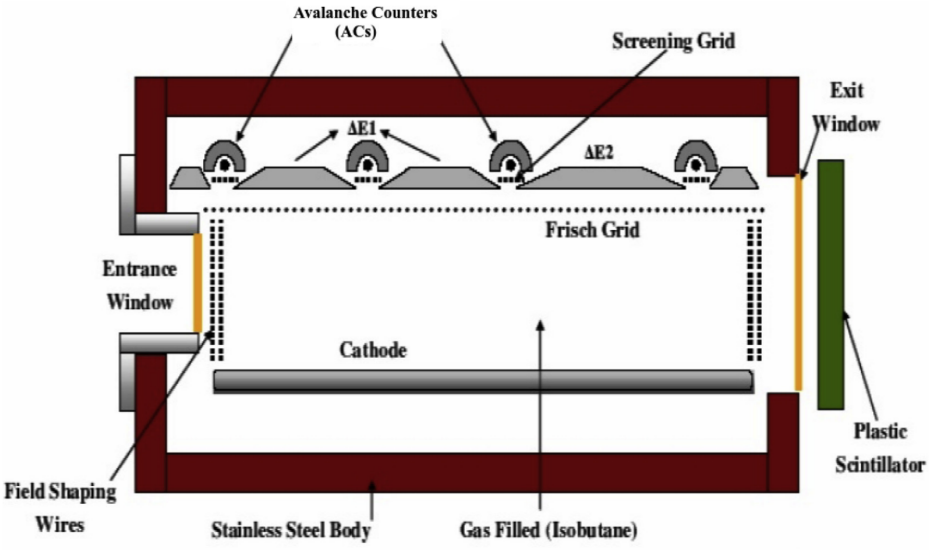

Figure 4.7: A schematic of the Oxford detector. The Oxford detector is comprised of a cathode, two anodes, four resistive proportional-counting wires, a MICROMEGAS plate, and a Frisch grid. All of these elements can be seen in this cross-section of the detector. Reprinted with permission from [46].

Each wire is oriented parallel to the focal plane and each wire is spaced 16 cm from its nearest neighbor. The wires acted as pickups for the electrons, creating a signal measured at each end of the wire. By comparing relative signals at each end of the wire, a position is deduced. Furthermore, the wires can be used as a rudimentary measurement of the beam rate [51].

The energy-loss measurement is made by the two anodes and the MICROMEGAS plate. The two anodes collect the free electrons liberated from the isobutane as the charged particles travel through the gas. The collected charge is directly proportional to the energy lost to the isobutane. The MICROMEGAS plate, located towards the back of the Oxford detector between the third and fourth wires, acts as a two-stage parallel-plate avalanche chamber separated into two regions separated by a thin electroformed micromesh. Electrons first enter a 50-300 μm amplification region and then pass through a centimeter-scale drift region [46]. The MICROMEGAS plate is segmented into four rows parallel to the beam direction and seven columns perpendicular to the beam, allowing for limited particle track

reconstruction and the ability to check the particle position against the position determined by the proportional-counting wires. Additionally, given the segmentation of the detector and its larger surface area, the MICROMEGAS plate provides an energy resolution up to a factor of 3 times better than that of the anodes [46].

In certain scenarios, the pressure of the isobutane gas can be increased such that the charged heavy particles stop in the gas and a total energy can be measured by the anodes and MICROMEGAS plate. However, the TIARA for Texas setup utilized a separate detector to measure the final energy of the particle. The particles left the Oxford detector through a 50 μm Mylar exit window where they entered a short drift region and finally were deposited in a NE102A plastic scintillator detector [9]. This scintillation detector was coupled to two photomultiplier tubes (PMTs) located at either end of the scintillator. The light generated by the scintillator detector is collected and amplified by the PMTs producing a signal that is directly proportional to the total residual energy of the particle stopped in the detector.

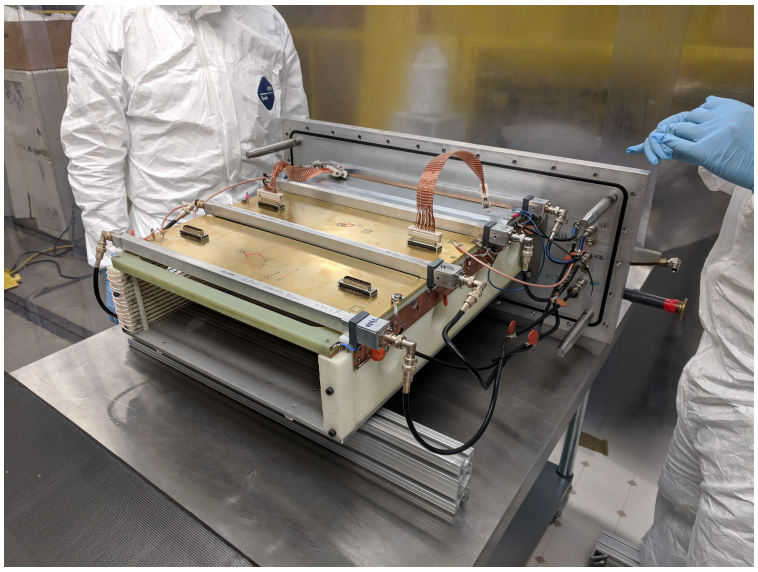

Figure 4.8: A photo of the Oxford Detector outside of its vacuum chamber. The Frisch grid, the four proportional wire counters, as well as the MICROMEGAS pad are all clearly visible.

4.1.5 Data Acquisition

TIARA makes use of a MIDAS-based data acquisition system [53] developed at the University of Surrey. This particular version of MIDAS was designed to make use of CAEN V288 controller modules. This allowed the system to be remotely programmable [44].

A set of custom-made charge-sensitive pre-amplifiers, built by Grand Accélérateur National d'Ions Lourds (GANIL) in France, read out signals from the silicon-detectors. These pre-amplifiers are mounted as close to the TIARA chamber as possible to minimize signal noise. The HPGe detectors have a set of pre-amplifiers built into their cryostat. All signals from the aforementioned pre-amplifiers are fed into CAEN N568B spectroscopy amplifiers. These amplifiers have a shaped-signal output and a fast-signal output. The fast-signal output is sent to a CAEN V895 Constant Fraction Discriminator (CFD) that generates a trigger signal for events whose pulse height surpass a set threshold value. The Oxford detector utilized a separate system, with a set of custom pre-amplifiers feeding a signal into programmable Mesytec MSCF-16 amplifiers. These amplifiers used an internal CFD to create triggers and output the associated shaped-signals.

These triggers from the fast outputs were fed into a fan-in fan-out (FIFO) module and used to define a master trigger. In the present study, triggers were formed from events on the HyBall, an event registered by either end of an Inner Barrel resistive strip, an event in the Oxford Detector, or an event in the HPGe detector. Master triggers that defined a valid event were taken only from TIARA silicon-detectors. During calibration, the master trigger was set to whichever detector was being calibrated.

Timing signals were also collected by way of Time Amplitude Converters (TACs). By taking a start and a stop trigger from different detectors, the TAC generated a pulse whose height was proportional to the start-stop time difference; this pulse was then fed into an ADC. In the present study, TACs were used to determine the time between a signal in any of TIARA's silicon-detectors and a corresponding signal in the Oxford detector. This means a start signal was defined as a valid event in the scintillator PMT and a stop signal was

defined as a master trigger from TIARA, which was delayed a predetermined period of time that ensured its arrival at the TAC module after the start signal.

Shaped outputs were sent to CAEN V875 ADCs, which would collect amplitudes in its buffer. Simultaneously, a gate generator took master triggers and created a 12 μs gate for each trigger. This gate defined a coincidence window for an event. These master triggers and coincidence window were fed into a Silena Acquistion Control (SAC) module, which would send coincident events from the ADC buffer to a VXI module. Here, all the information from the signals was compiled and time stamped, forming a complete analysis event [9].

4.1.6 TIARA for Texas

Each of these detectors worked together to form TIARA for Texas (T4T). The 10 AMeV beam of ^{23}Na impinged on a 500 μg/cm^2 deuterated-plastic target mounted in the center of the TIARA chamber. Protons from the ^{23}Na(d,p)^{24}Na reaction were deposited in the HyBall, elastic scattering was measured by the Barrel detector, and prompt gamma emission from the excited nucleus was measured by the HPGe detectors. Downstream from TIARA, the ^{24}Na daughter nuclei entered the MDM spectrometer along with the unreacted ^{23}Na primary beam. The MDM was tuned to maximize transmission of ^{24}Na particles over the unreacted ^{23}Na primary beam. As the particles exited the MDM, they were observed by the Oxford Detector, which measured the energy loss and trajectory of the particles as they traveled through the detector. Finally, a plastic scintillator on the back of the Oxford Detector stopped the particles as they exited the gas chamber and measured the total deposited energy.

This experimental setup allowed for a triple-coincidence measurement and enabled particle identification of individual elements and isotopes on an event-by-event basis. When done correctly, this technique is extremely powerful in that it allows for reconstruction of excitation spectra with very low backgrounds and also enables discrimination of individual states that would otherwise be impossible to resolve. In the present study, an alignment issue between the TIARA chamber and the entrance to the MDM significantly reduced

the transmission of ^{24}Na into these detectors. This will be discussed in more detail in the next chapter. A complete diagram of the experimental setup, without the Oxford detector, is shown in Figure 4.9. Discussion of the detailed operation of each detector is discussed below.

4.2 Charged Particle Detection

4.2.1 Light Charged Particle Interactions with Matter

Charged particle moving through matter have a much higher probability of interacting with electrons orbiting the nucleus than the the atomic nucleus itself. Therefore, the primary mechanism for energy loss of a charged particle in matter is Coulomb scattering of atomic electrons [27]. As the charged particle interacts with electrons, it will either excite the

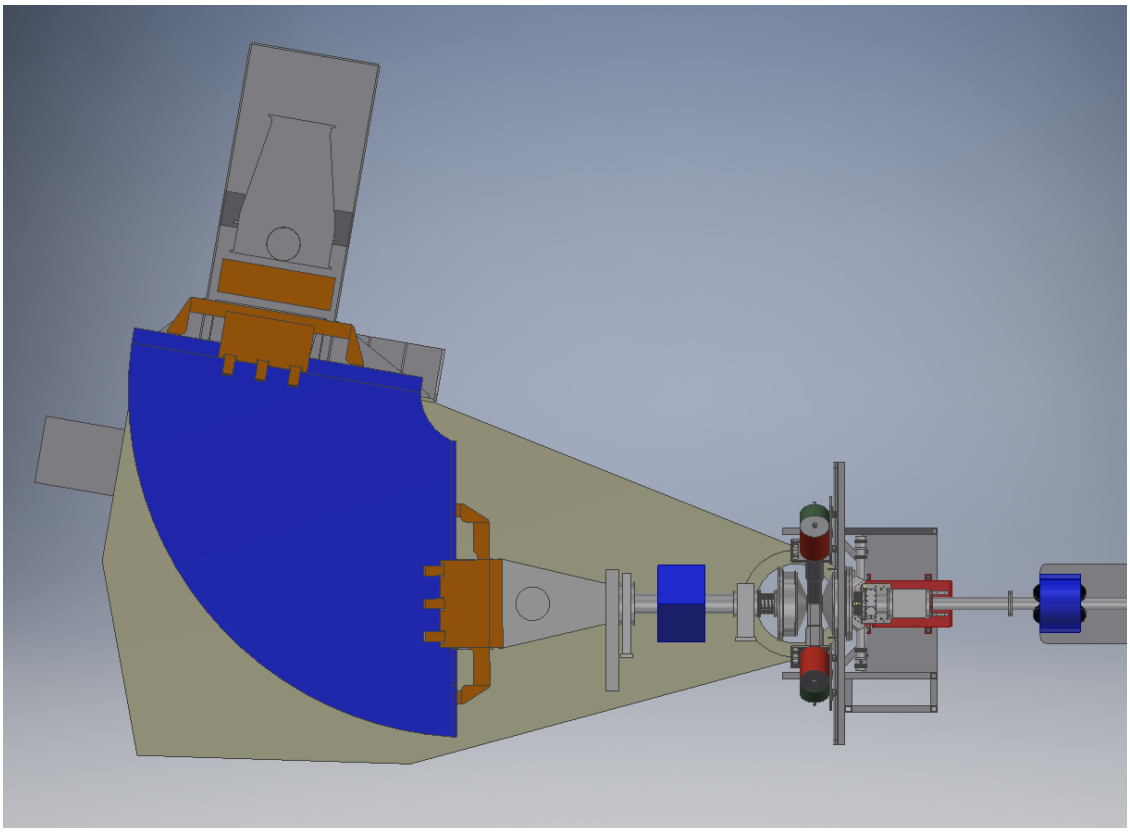

Figure 4.9: A diagram of the T4T experimental setup. Beam from the cyclotron would arrive from the right, travel through TIARA, be bent around the MDM-2 spectrometer, and then enter the Oxford detector (not pictured).

electron into a higher-energy state, referred to as excitation, or will remove the electron from the material entirely, known as ionization. These interactions happen repeatedly until the charged particle is stopped or it exits the material [54]. The stopping power of a material is given by the differential energy loss of a given particle divided by its differential path length

$$S = -\frac{dE}{dx}, \tag{4.1}$$

where S is commonly referred to as the specific energy loss. The specific energy loss is defined classically by the Bethe formula, given as

$$-\frac{dE}{dx} = \frac{4\pi e^4 z^2}{m_e v^2} NZ \left(\ln \frac{2m_e v^2}{I} \right) \tag{4.2}$$

given that $v \ll c$. Here e is the charge of the electron, v and ze are the velocity and charge of the particle being stopped, N, Z, and I are the number density, the atomic number, and the average excitation and ionization potential of the material doing the stopping, and m_e is the electron rest mass. This formula is generally true given the velocity of the charged particle remains large compared to the velocity of the orbital electrons in the stopping material [54].

Fundamentally, this means that materials with a high electron density work well to stop charged particles. Furthermore, good conductivity in the material allows for electrons excited by the charge particle to be collected and measured, as the collective energy of the excited and ionized electrons corresponds directly with the initial energy of the charged particle. While good conductivity is critical for an efficient detector, a detector that allows for low-energy electrons to flow too freely through it muddies the signal. This means an ideal detector would have good conductivity for electrons only above a certain energy. For protons of moderate energy, semiconductor detectors fit this bill and are ideal for making high efficiency measurements with good resolution. High-energy protons and heavy charged particle detectors will be discussed in further detail later.

4.2.2 General Principles of Semiconductor Detectors

In terms of resistivity, a semiconductor falls between a conductor and an insulator. Elements such as silicon or germanium form a solid periodic crystal lattice whose constituent atoms form covalent bonds with their nearest neighbors. This periodic lattice establishes a series of allowed energy bands for an electron traveling through the material. The electrons that make up the covalent bonds between atoms become part of the valence band, as they are bound to specific lattice sites within the crystal and are unable to move freely through the material. The band above the valence band is referred to as the conduction band as electrons within the conduction band are able to flow through the material. Individual bands are separated by disallowed energy regions called bandgaps.

The valence band in metals is not completely filled such that electrons only need a small amount of energy to move through the materials, making them conductors. In insulators and semiconductors the number of electrons is such that all available sites within the valence band are occupied. This means that neither material would have any electrical conductivity. The primary difference in these two materials comes from the fact that, in an insulator, the bandgap is sufficiently large so as to prevent any electron transport without significant thermal excitation. The bandgap in semiconductors is significantly smaller, meaning electrons can make the jump into the conduction band [54].

An intrinsic semiconductor is a material where the valence band is entirely filled with electrons and the conduction band is devoid of electrons. These materials are extremely difficult to create, so discussion will focus on doped semiconductors. A doped semiconductor has small amounts of dopants implanted in the lattice structure and can be broadly classified into two types: p-type and n-type. An n-type semiconductor has an excess of electrical charge (electrons) while a p-type semiconductor has an absence of electrical charge (holes). These electrons or holes are the primary carriers of electrical charge in the material.

Semiconductor detectors are formed by exploiting the behavior between adjacent n-type and p-type semiconductors. This interface between the two materials, called a p-n junction,

allows electrons from the n-type semiconductor to flow across to the p-type material and neutralizes the charge carriers. This forms a region called the depletion region pictured in Figure 4.10. This region does not have any free electrons to carry charge and therefore any signal carried out of this region must be from an electron excited into a conductive band. The area of the depletion region can be increased by applying a reverse bias voltage across the semiconductor. This has the additional effect of increasing the drift velocity of the charge carriers in this region [27].

In detector construction, an optimally-doped semiconductor with a large reverse bias voltage is employed. With a large bias across the detector, the probability of loss is mitigated and the timing response of the detector is improved due to the higher drift velocity. This also maximizes the area of the depletion region and thereby the active area of the detector.

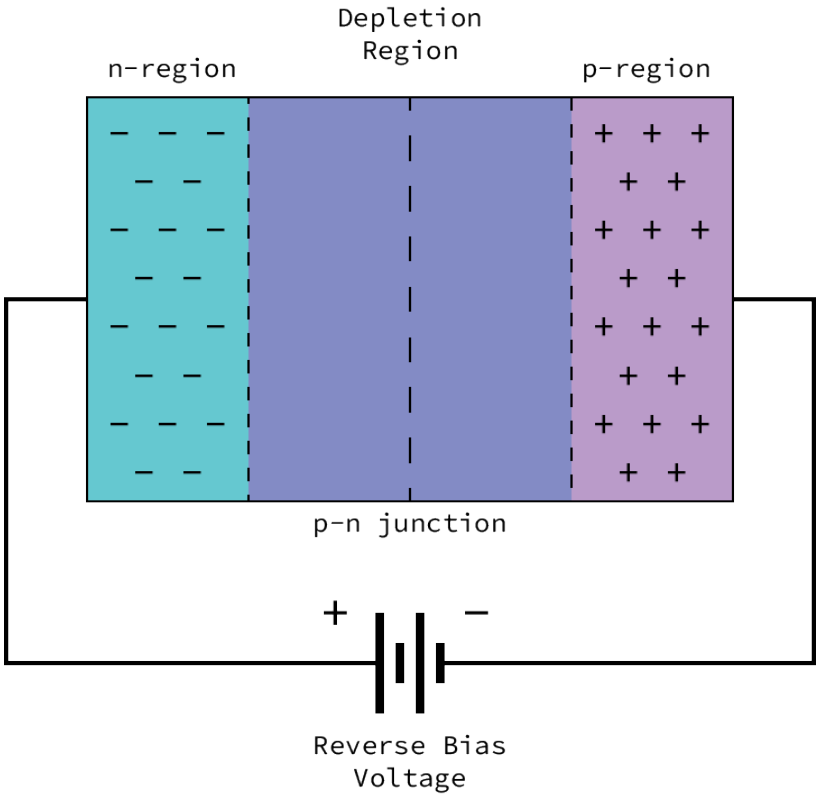

Figure 4.10: A figure of the depletion region formed at the junction of a p-type and n-type semiconductor. The area of the depletion region can be increased by increasing the reverse bias voltage.

However, applying too large of a bias risks the detector breaking down and becoming unusable [9]. Additionally, when using optimally-doped semiconductors, this bias will cause a region of the detector to become unresponsive to charged particles. Often referred to as a dead layer, this region must be accounted for when calibrating a semiconductor-based detector [54].

Charged particles incident upon a semiconductor detector will interact with and deposit energy into the material by exciting the material's electrons. These excited electrons jump out of the valence band and into the conduction band, forming electron-hole pairs along the path of the charged particle. Under the influence of the electric field generated by the reverse bias voltage, these electron-hole pairs drift across the detector creating a signal that is directly proportional to the amount of energy deposited [27].

4.2.3 General Principles of Heavy Charged Particle Detectors

Charged heavy particles interact with matter according to the same principles as their lighter siblings, described in Section 4.2.1. The challenge of heavy charged particle detection comes with the complications associated with experimental procedure. In the particular case of transfer reactions in inverse kinematics, heavy charged recoils are generally mixed with unreacted primary beam and other elements of similar A or Z. Differentiating the desired recoils from unwanted background requires supplementary techniques.

4.2.3.1 Electromagnetic Separation

Separating charged heavy recoils from unreacted primary beam is necessary in order to collect information about the recoils. To accomplish this, we utilize the fact that elements and different isotopes of those elements can be separated by their charge to mass ratio m/q using an external electromagnetic force. For high-energy charged particles, this is most easily accomplished using a magnetic dipole.

The force felt by a charged particle in a magnetic field perpendicular to its direction of

travel can be expressed as

$$F = qv \times B = qvB, \tag{4.3}$$

where q is the charge of the particle, v is the velocity of the particle, and B is the magnetic field. The radius of curvature r is related to the force it experiences by the equation

$$F = ma = \frac{mv^2}{r}, \tag{4.4}$$

where m is the mass of the particle and v is again the velocity of the particle. Combining these two equations yields

$$r = \frac{mv}{qB}. \tag{4.5}$$

This means, assuming constant velocity and magnetic field, the radius of curvature depends simply on the charge of the particle and its mass.

In the case of a magnetic spectrometer, this means that isotopes of a given element with the same energy will appear at different points in the focal plane, and different elements will also be similarly separated. Detectors capable of measuring a particle's position in the focal plane of the spectrometer can then be used to identify different isotopes, elements, or charge states of said particle. A good detector for particle identification would therefore provide reasonable position resolution in the focal plane or, ideally, provide enough information to perform track reconstruction. Energy loss detectors, such as MICROMEGAS, can also be useful in track reconstruction.

4.2.3.2 Scintillator Detectors

Heavy charged recoils carry information that can be used to identify the light ejectile when measured in coincidence. This means that knowing the total deposited energy of a charged heavy recoil is of particular use in these studies. An ideal detector is made of a material that can accurately determine the total energy of the particle across a broad energy range and produce a signal quickly enough that it can be distinguished from other

particles. Furthermore, an ideal detector can also withstand moderate beam rates and cover a large surface area. Given these necessities, a scintillation detector makes for a compelling candidate.

A scintillation detector does not directly measure the electrons excited by ionizing radiation but instead uses photons to collect a signal. As a charged particle enters a scintillating material its interactions with the material's electrons excites them into higher energy states. These electrons then rapidly de-excite to lower energy states, emitting photons in the process. The emitted photons, when measured by a photo-sensitive detector such as a photomultiplier tube, generate a signal corresponding to the energy of the deposited charged particle [27]. An ideal scintillator is transparent to the wavelength of its own emitted light, has a high conversion efficiency of kinetic energy to scintillation photons, has a relatively linear conversion, and has an index of refraction close to glass [54].

Scintillation detectors come in various forms including organic solids, organic liquids, and inorganic crystals. Each material has its own benefits and drawbacks. For this experiment, an organic solid (plastic) was chosen for the scintillation detector due to its quick response time and high conversion efficiency. However, as plastic accumulates radiation damage over time, attention had to be paid to the total beam rate the detector took. Minimizing the number of particles incident on the material helped preserve the detector's conversion efficiency.

4.3 Gamma Ray Detection

4.3.1 Interactions of Photons with Matter

Unlike with charged particles, which slow down gradually through a medium via simultaneous interactions with the material, photons interact with matter in a far less predictable way. Photons can scatter through large angles or even disappear completely as they pass through a material, making constructing a history of interactions difficult [54]. There are three primary means of interaction for photons: photo-electric absorption, Compton scattering, and pair production. The mode of interaction is determined primarily by the energy

of the photon.

Low-energy photon interactions, generally photons of a few hundred keV and lower, are dominated by photo-electric absorption. In this interaction, a photon is absorbed by an atom and completely disappears. A photo-electron is then emitted by the atom from one of its more tightly bound shells. The now-ionized atom will then usually absorb a free electron and emit one or more characteristic X-ray photons as the electron shell structure reorders itself [54]. The probability of photo-electric absorption is not exact, but generally decreases with energy (roughly as E_γ^{-3}) and increases with Z of the absorption material (roughly as Z^4) [54].

Photons with an energy of a few MeV tend to Compton scatter through a material. In this scenario, the photon loses energy by scattering off an atomic electron in the material. The energy lost by this scattering is given by

$$h\nu' = \frac{h\nu}{1 + \frac{h\nu}{m_e c^2}(1 - \cos\theta)}, \tag{4.6}$$

where θ is the scattering angle, $m_e c^2$ is the rest mass energy of the electron, and $h\nu$ and $h\nu'$ are the energy of the photon before and after the scatter [54]. A photon may Compton scatter multiple times before reaching a low enough energy to undergo photo-electric absorption and, for a finite volume, the photon may scatter out of the detector entirely [27]. In that latter case, a gamma detector would capture only a small fraction of the total initial energy of the photon. The likelihood of a Compton scattering event increases linearly with the proton number Z of the absorbing material due primarily to the increased number of electrons orbiting these larger nuclei [54].

At energies of several MeV, the primary form of energy loss comes from pair production. Pair production becomes possible when the energy of the photon becomes twice the rest mass energy of an electron. If the photon enters into the Coulomb field of a nucleus it can disappear and produce an electron-positron pair [54]. These particles will quickly slow down,

with the electron being absorbed and the positron annihilating. This annihilation generates two characteristic 511 keV annihilation photons. In reality, while pair production can occur at just over 1 MeV, it does not become the primary form of energy loss until energies increase over about 5 MeV [27]. The time scale of all these interactions is short enough such that they appear in virtual coincidence with each other. The probability of pair production scales rapidly with the total energy of the incident photon [54].

Given the general dependence of all these interaction mechanisms on the proton number of the absorption material, an ideal gamma detector is made of a high Z material that can be made in large detector volumes. Additionally, in the case of semiconductor detectors, maximizing the depletion region of the material is necessary for good energy resolution and high detector efficiency. The thickness of the depletion region in a semiconductor detector is given by

$$d = \sqrt{\frac{2\epsilon V}{eN}}, \tag{4.7}$$

where ϵ is the dielectric constant of the material, e is the charge of the electron, V is the reverse bias voltage, and N is the net impurity of the material. For semiconductor materials of similar purity as those used for charged particle detection, the maximum thickness of the depletion region can reach only 2-3 mm before the reverse bias begins to break down the material [54]. For a semiconductor-based gamma detector, the absorption medium must be of extremely high purity to optimize photon detection.

4.3.2 General Principles of High-purity Germanium Detectors

High-purity germanium detectors are extremely popular in gamma spectroscopy due to their exceptional energy resolution. In order to achieve this, the detector material must reduce impurities to less than 1 part in 10^{12} [54]. This high purity also allows for depletion region depths up to several centimeters, allowing for a larger active detector volume. However, germanium has a band gap of 0.7 eV, which means electrons within the material are easily excited into the conduction band. This is part of the reason high-purity germanium

has such good energy resolution, but it also means that thermal excitation of the material contributes to the noise in the detector signal. This issue can be solved by keeping the detector at cryogenic temperatures. By surrounding the high-purity germanium crystal with a liquid nitrogen jacket the detector can be kept at 77 Kelvin and significantly reduce detector noise. This liquid nitrogen jacket must be shielded from the surrounding air, necessitating a vacuum-sealed cryostat to house the detector [54].

Most high purity germanium detectors are designed with a coaxial configuration. In this setup, the detector volume is cylindrical with a small hole down the middle that runs the length of the material. Electrical contacts are then attached inside the hole along the central axis and along the outside of the cylinder. This creates a p-n junction with cylindrical symmetry, maximizing the depletion region and while minimizing the reverse bias voltage required to achieve it [54]. This has the additional effect of reducing electrical noise in the detector. While the crystal size of a high-purity germanium detector is relatively large for a semiconductor detector, its small size relative to other gamma ray detectors means that HPGe detectors are limited by the amount of photons that Compton scatter out of the detection volume. In some experimental setups, HPGe detectors are often used in conjunction with scintillating detectors such as bismuth germanate (BGO) due to their high photon absorption rates [9].

5. STUDY OF THE ^{23}Na(d,p)^{24}Na REACTION

5.1 Analytical Overview

This chapter describes one of the commissioning experiments for the TIARA for Texas (T4T) collaboration performed at the Texas A&M University Cyclotron Institute. As the previous chapter describes the experimental apparatus, method of beam production, and parameters of the reaction, this chapter outlines the results of the study. Previous studies of the ^{23}Na(d,p)^{24}Na reaction, methods of experimental data reduction, and data analysis are all presented. A brief discussion of the results and comparisons to previous studies follows.

5.2 Previous Studies of the ^{23}Na(d,p)^{24}Na Reaction

The ^{23}Na(d,p)^{24}Na reaction has been well-studied over the past 60 years, with numerous studies exploring its cross section, lifetimes, electromagnetic transitions, and structure. A 1963 study performed at the cyclotron laboratory at Michigan State University by Daum was among the first to probe this reaction. The experiment impinged 7.8 MeV deuterons on a ^{23}Na target in forward kinematics with a claimed energy resolution of 20 keV full width at half maximum (FWHM). After constructing a level scheme of the ^{24}Na nucleus, angular distributions and the corresponding spectroscopic factors were reported following comparison with distorted wave Born approximation (DWBA) calculations. Most importantly, this study was the first to propose the existence of two states at 2512 keV and 2563 keV instead of a single state at about 2520 keV. The 2512 keV state is the mirror state of the state populated by the $\sim$ 475 keV resonance in ^{24}Al and the 2563 keV state is the mirror state of the state populated by the $\sim$ 475 keV resonance. As the 2512 keV state was observed weakly, only a tentative spectroscopic factor was assigned [55].

The spin and parity of the ^{23}Na nucleus is $\frac{3}{2}^{+}$, which means selection rules allow population of individual levels of the ^{24}Na nucleus with multiple different spins. Comparisons with DWBA calculations may help disentangle contributions from different angular momentum

components; however, precise predictions of spin and parity are not always possible for every resonance. For the angles measured by Daum, the possibility of multiple angular momentum transfers was present for several states. The nuclear parameters for states relevant to this work are shown in Table 5.1.

A number of studies in the mid-1970s explored the decay scheme and energy levels populated by the ^{23}Na(d,p)^{24}Na reaction. Each study utilized a deuteron beam between 2-5 MeV impinged on a sodium target [56, 57, 58]. Of these experiments, two in particular stand out. A study by Ekström *et al* improved on resolution and uncertainty of the excitation energies in the ^{24}Na nucleus, providing the generally accepted energies cited in literature today. The study also eliminated an erroneously observed level at 2464 keV, significantly improved on measurements of energy levels up to about 4200 keV, and discovered two new states at 3944 keV and 4195 keV [56]. Following this, Buisman *et al* performed work to ascertain mean lifetimes and branching ratios of electromagnetic transitions in ^{24}Na. The study also made definitive spin assignments for several states, including a 3^+ assignment for the 2512 keV state, as well as discovering a new level at 3682 keV [58].

The most accurate study to date was performed in 2004 by Tomandl *et al.* The study was a joint experiment that performed a measurement of the ^{23}Na($\vec{\text{d}}$,p)^{24}Na reaction as well as the ^{23}Na(n,γ)^{24}Na reaction. The neutron capture reaction was performed at the Los Alamos Omega West reactor utilizing a neutron flux of roughly 6×10^{11} n/cm^{2}s, correspond-

E_x		$[(2J_f+1)/(2J_t+1)]S_{dp}$	
(keV)	J^π	$\ell = 2$	$\ell = 4$
2512	$0^+, 1^+, 2^+, 3^+, 4^+$	(0.08)	(0.26)
2563	$0^+, 1^+, 2^+, 3^+, 4^+$	0.068	(0.26)
3628	$0^+, 1^+, 2^+, 3^+, 4^+$	0.27	

Table 5.1: Nuclear parameters of the ^{24}Na(d,p)^{24}Na reaction from Daum after comparison with DWBA models. All values in this table are presented directly from the paper except for the excitation energy, which is given as the currently accepted value to avoid confusion. Values in parentheses are deemed tentative by the author [55].

ing to a Maxwellian temperature distribution around 350 K. An HPGe detector mounted inside a Na(Tl) annulus measured the gamma spectra. The transfer reaction was performed separately using a tandem accelerator at the Technical University of Munich and the Q3D spectrograph. A polarized beam of 17 MeV deuterons was impinged on a NaF target and proton spectra were collected with a 1.7 m long focal plane detector. Beam normalization was performed with respect to the beam current utilizing a Faraday cup, while five scattering angles between 8° and 50° and two beam polarization settings allowed for the reconstruction of angular distributions [59].

The neutron capture reaction provided the researchers with extremely precise excitation energies with uncertainties on the order of tens of eV, while the transfer reaction allowed for assignment of spectroscopic factors for every observed level. Additionally, by comparing experimentally determined angular distributions with the angular distributions generated by the CHUCK3 code, angular momentum transfers of specific states were successfully assigned for levels up to excitation energies of about 6300 keV [59]. Combined, these two experiments yielded the most comprehensive analysis of ^{24}Na to date. The nuclear parameters from this study for states relevant to this work are shown in Table 5.2.

Given this robust history of study, the ^{23}Na(d,p)^{24}Na reaction was an ideal choice for commissioning the T4T setup. With high quality level data as well as good spectroscopic factors known for states of astrophysical interest, experimental results could easily be verified.

E_x		$[(2J_f+1)/(2J_t+1)]S_{dp}$	
(keV)	J^π	$\ell = 2$	$\ell = 4$
2512	3^+	0.12	
2563	$4^+(2^+)$	0.069	
3628	3^+	0.29	

Table 5.2: Nuclear parameters of the ^{23}Na($\vec{\text{d}}$,p)^{24}Na and ^{24}Na(n,γ)^{24}Na reactions from Tomandl *et al.* Excitation energies are taken from the neutron capture reaction while spins and spectroscopic factors are taken from the transfer reaction [59]. Values in parentheses are tentative assignments.

Additionally, this would be the first triple-coincidence study of the ^{23}Na(d,p)^{24}Na reaction utilizing the TIARA silicon detectors, HPGe detectors from the Hyperion array, MDM-2 magnetic spectrograph, and Oxford detector.

5.3 Experimental Data Reduction

As this is a commissioning experiment, a significant amount of work has gone into data preparation and reduction. Machinery for streamlining future experiments has been developed, tested, modified, and prepared for other users. This section outlines the work performed to ready the raw data set for analysis and, where appropriate, discusses some of the developed techniques. Additionally, complications with the experiment and their respective solutions are discussed for the benefit of future users.

5.3.1 Detector Calibrations

In order to properly perform a triple-coincidence measurement each detector must be accurately calibrated. Each calibration process utilizing data from sealed radioactive sources was developed and automated for future users. The calibration process, described in the order it was performed, is described below.

5.3.1.1 Electronics Calibrations

In order to identify any non-linearities inherent in the electronics, a calibration of the electronics chain was performed. This process aimed to correct any biases found in the response of the electronics between the detector and the data acquisition system. Outputs from a pulser module were fed into the preamplifiers, with the resulting signals passing through the rest of the electronics chain before being digitized by the ADC. The signals generated by the pulser ranged from 0.05 to 8 Volts (V) in discrete steps, forming sharply-peaked spectra that vaguely resembled matchsticks. A sample "matchstick" spectrum can be seen in Figure 5.1. This process, repeated for each channel used in the experiment, provides a mapping that represents the response for a given channel.

To characterize and correct the response, the centroid of each peak was taken and plotted

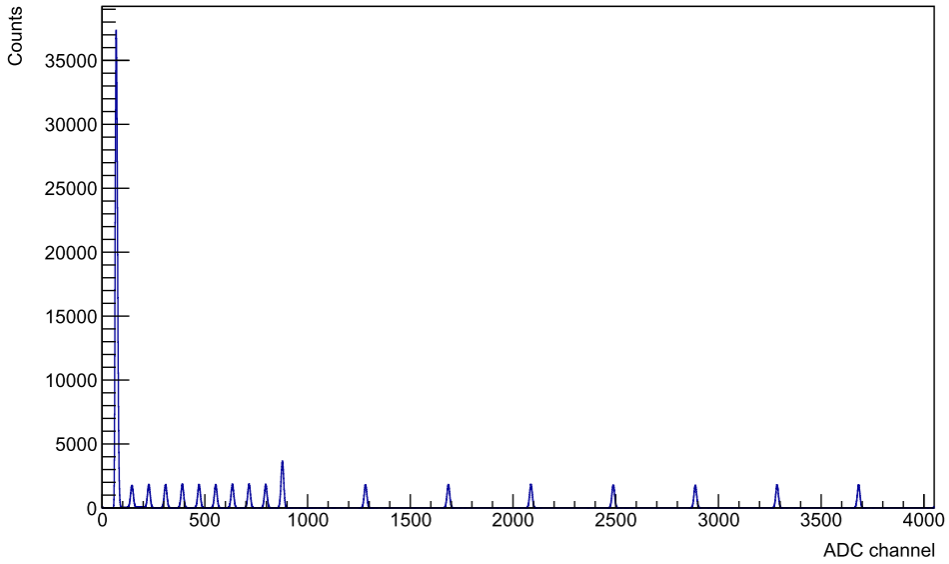

Figure 5.1: A typical "matchsticks" spectrum. The plot shows counts versus ADC channel for the pulser data from one channel. Reprinted with permission from [9].

against its respective voltage. Ideally the relationship between the centroid and the pulser voltage should be linear, with any deviation indicating a non-linear response. Correcting for non-linearities involves fitting a second-order polynomial to the detector response and applying that to the collected data before any other calibrations were performed. In this experiment, the electronics exhibited strongly linear behavior, as seen in Figure 5.2 (right), and only small second-order corrections were required.

5.3.1.2 Hyball Calibrations

The calibration of the Hyball detector, like all the silicon detectors in this work, was performed using a triple-alpha source containing ^{239}Pu, ^{241}Am, and ^{244}Cm. These radionuclides decay naturally through alpha emission, each with a characteristic primary decay branch. As the energy of each decay is well known, they can be used to calibrate the detector signals to specific energies. The energies from the triple-alpha source are shown in Table 5.3.

After first applying the corrections found during the electronics calibration, the triple-alpha source was placed at the target position and data were taken until enough counts had

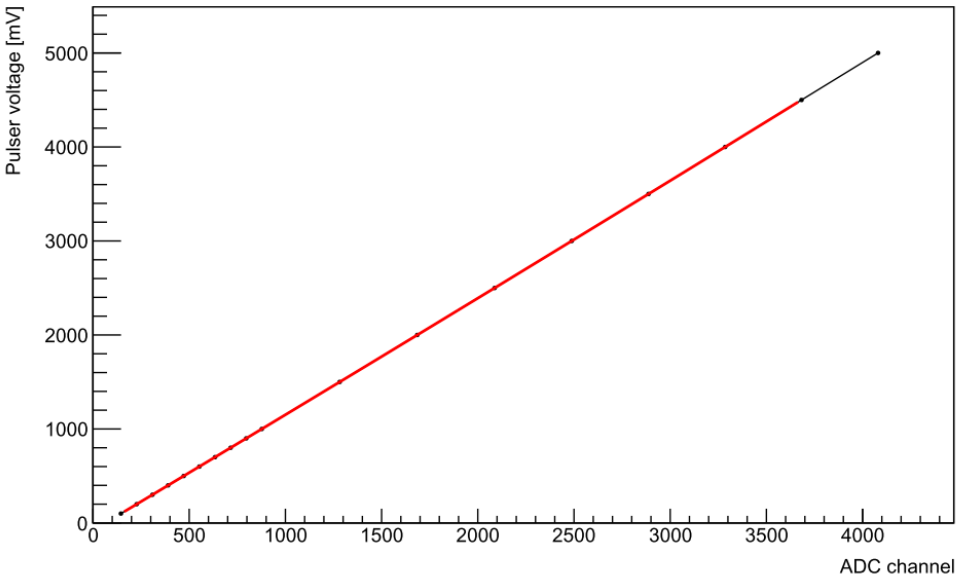

Figure 5.2: A fit of the "matchsticks" spectrum. This plot depicts the centroid of each fitted peak plotted against the pulser voltage. Fitting this data provides the corrections used to reduce non-linearities in collected data. Reprinted with permission from [9].

been collected to fit each of the three alpha peaks. The centroid of the peaks was taken and plotted against the ADC channel of its corresponding peak. The resulting plot was fit to a first-order polynomial, allowing for the extraction of the calibration coefficients for each detector channel. A sample histogram of the fitted triple-alpha source data is shown in Figure 5.3. This provided a solid preliminary calibration of the data.

During this experiment, a data acquisition failure resulted in a number of changes to the electronics chain. While attempting to diagnose the issue, several electronics channels were

Nuclide	E_α (MeV)
^{239}Pu	5.157
^{241}Am	5.486
^{244}Cm	5.805

Table 5.3: Energies of the alpha particles emitted from each nucleus in the triple-alpha source. These energies were used to calibrate the energy of the silicon detectors.

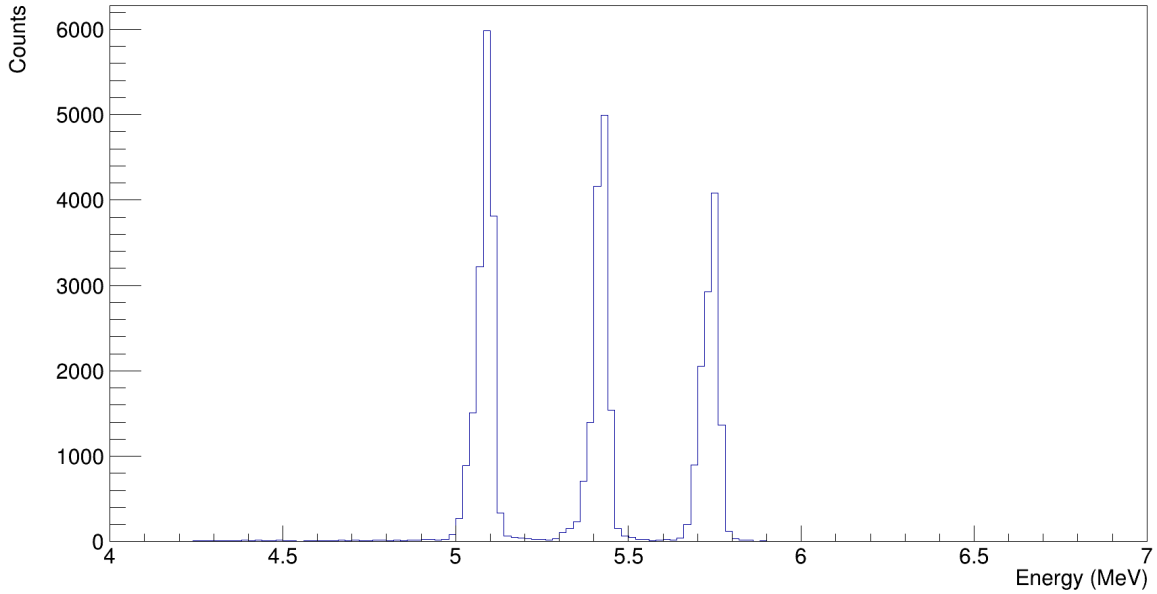

Figure 5.3: A sample Hyball calibration spectrum. This plot shows a calibrated triple-alpha spectrum for a single channel in the Hyball. The centroid of each peak corresponds to alpha energies shown in Table 5.3.

switched, gains were changed, and detector biases were adjusted without any record. Of all the detectors in the setup, the Hyball was most impacted by these changes and led to a portion of the data requiring online calibrations as well as verification of proper channel mapping. For the Hyball, channel mapping was verified by comparing pre-failure and post-failure data with recorded channel mappings and it was determined that no channels had been switched. Inspection of experimental energy spectra revealed shifts in gain or bias that effected measured lab energies. Figure 5.4 shows the aberrations in a subsection of the experimental data for a single wedge of the detector. Online calibration was performed by fitting peaks of strongly-populated, well-known states to experimental data. The predicted energy of each state for an angular range corresponding to a Hyball ring was calculated using the (d,p) reaction kinematics codes available in the NPTool library [60]. Calibration coefficients were modified to match experimental data to these values. After these corrections had been applied, a final detector resolution of 49 ± 5 keV FWHM was determined from the

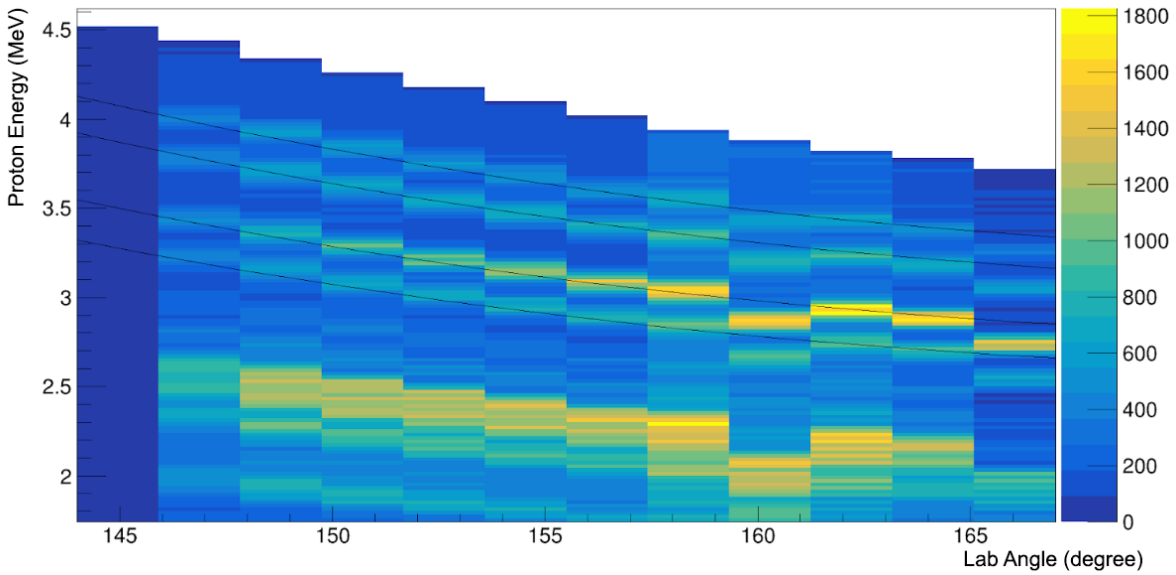

Figure 5.4: A shifted Hyball spectrum. This plot depicts the lab angle versus proton energy for wedge 2 shown before online energy calibrations were applied. Each bin on the x-axis represent the angular range of an individual ring. The black lines are the calculated kinematic curves of protons emitted from strongly-populated states in the reaction. In this particular wedge, it is clear that rings 1 and 4 required online calibration corrections.

triple-alpha source spectrum by looking at the average of the ^{239}Pu alpha peak across all Hyball rings.

5.3.1.3 Barrel Calibrations

The Barrel utilizes resistive silicon strip detectors, so the detector must be calibrated in terms of both the position and energy. As the position calibration impacts the energy calibration, the position calibration must be performed first. A resistive strip detector functions by reading energy signatures from both ends of the detector and comparing the ratio of the signals. If the strip is treated as having an upper and lower region, the position along the strip is given by

$$P = \frac{U - L}{U + L} \tag{5.1}$$

where U is the signal read from the upper portion of the detector and L is the signal read from the lower portion of the detector. This necessarily will mean that P can take values

between $P = 1$ and $P = -1$. In practice, however, the properties of silicon detectors mean that events that happen very close to a single end will read out entirely by that end. As a valid event requires signals from both ends of the detector, this effectively creates a dead zone at each end of the resistive strip. The size of this dead zone is dependent upon a number of different characteristics of the detector, but effectively limits the values of P for a valid event.

To determine the minimum and maximum values of P, the value of P is compared to the sum of the total signal $T = U + L$, creating what is basically an energy versus position relationship. From the triple-alpha source data, the T values corresponding to detected alpha particles were used to plot values of P from the alpha particles. This allowed for the extraction of the absolute highest and lowest possible values of P that corresponded to events with valid position and energy data. However, at the most extreme values of P, the event data can be unreliable. Therefore, the upper and lower edges of the P spectrum were fit using a Gauss error function, defined as

$$f(x) = \frac{a}{2}\left[\frac{2}{\sqrt{\pi}}\int_0^{(x-b)/c} e^{-t^2}dt\right] + \left|\frac{a}{2}\right|, \tag{5.2}$$

where a is the amplitude of the function, b is the inflection point of the function, and c is the slope of the curve. These parameters are fitted from data, however it is the value of b that is used for the final calibration. The position calibration parameters are then calculated as

$$j = \frac{b_U + b_L}{2} \qquad k = \frac{b_U - b_L}{2}, \tag{5.3}$$

where b_U is the parameter extracted from the upper fit of the error function and b_L is the parameter extracted from the lower fit of the error function [9].

With the position calibration complete, the energy calibration can be performed. Unfortunately, calibrating the energy from the Barrel is not as simple as fitting values of T to their respective alpha energies. This is due to ballistic deficit, a non-linear effect stemming

from the time it takes for a signal to travel the length of the resistive strip detector and the corresponding preamplifier rise time. In essence, the longer a signal has to travel along the length of the detector, the longer its rise time, and the lower the total amplitude of the signal generated by the preamplifier. For example, events that happen closer to the center of the detector have a smaller signal amplitude and a lower energy.

Given the non-linear behavior of this effect and its dependence on position, a second-order polynomial must be used that accounts for the position along the detector. This function can be ideally modeled as

$$E_{br} = T' \left[1 - e(k^2 - P^2)\right] , \tag{5.4}$$

where e is the ballistic deficit correction, k is defined in Equation 5.3, T' is the sum of the upper and lower detector signals, and P is defined in Equation 5.1. Note that T' is different than T in that it considers the bias and offset of the signals. This means T' can be expressed as

$$T' = (aU + b) + (cL + d) , \tag{5.5}$$

with a and c being the upper and lower bias and b and d being the upper and lower offset, respectively. This equation can be re-expressed entirely in terms of T by rewriting U and L in terms of T and P. The latter relationship can be expressed as

$$U = \frac{T}{2}(1 + P) \tag{5.6}$$

$$L = \frac{T}{2}(1 - P) . \tag{5.7}$$

Now Equation 5.4 can be written as

$$E_{br} = \left(\frac{T}{2}(P(a - c) + a + c) + b + d\right) \left[1 - e(k^2 - P^2)\right] , \tag{5.8}$$

which, as a function of P and E_{barrel}, can be shown to be

$$T(P, E_{br}) = \frac{2\left[(b+d)\left[1-e(k^2-P^2)\right]-E_{br}\right]}{\left[1-e(k^2-P^2)\right]\left(P(a-c)+a+c\right)}\,. \tag{5.9}$$

At first glance, Equation 5.9 may appear inelegant; however, this expression allows for calibration of the barrel as it is entirely in terms of the position, the expected energy in the barrel, and the energy calibration coefficients a through e.

Using the plot of channel sum versus P used earlier for the position calibration, one dimensional slices along the channel sum axis can be taken. These plots show the value of P for each of the three alpha peaks and, after extracting the centroid of each peak, can be used to simultaneously fit Equation 5.9 to each alpha peak and extract values of a through e. The value of E_{br} used for fitting was adjusted for the alpha particle's energy loss through a dead layer of silicon with a nominal thickness of the 0.3 μm.

5.3.1.4 High Purity Germanium Detector Calibrations

Energy calibration for the high purity germanium (HPGe) detectors was performed with a similar technique to the silicon detectors: two gamma-emitting radioactive sealed sources, ^{60}Co and ^{152}Eu, were placed sequentially on the detecting faces of each clover. Both of these

Nuclide	E_γ (keV)	Intensity (%)
^{60}Co	1173.23	99.85
	1332.49	99.98
^{152}Eu	121.78	28.53
	244.70	7.55
	344.28	26.59
	778.91	12.93
	964.06	14.51
	1112.08	13.67
	1408.01	20.87

Table 5.4: Energies of the gamma-rays emitted from each nucleus in each of the two gamma sources. These energies were used to calibrate the energy of the HPGe detectors.

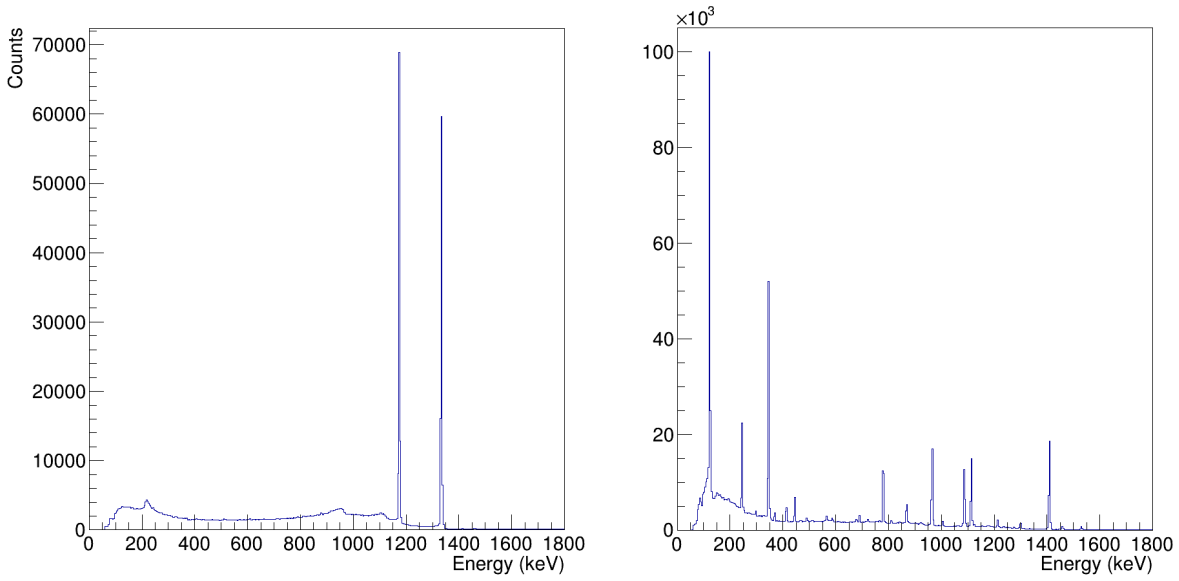

Figure 5.5: Sample HPGe calibration spectra. This plot shows a calibrated gamma-source spectrum for (*LEFT*) the ^{60}Co source and (*RIGHT*) the ^{152}Eu source for a single clover in the HPGe detectors. The centroid of each peak corresponds to gamma energies shown in Table 5.4.

sources provide high-intensity gamma-rays at a broad range of energies from 120 keV up to about 1400 keV. A chart showing specific energies and intensities is shown in Table 5.4.

The calibration was performed in two steps. An initial set of calibration parameters were generated based on a two-point linear fit to the ^{60}Co peaks. Given the exceptional energy resolution of HPGe detectors, the centroid of each peak was found by simply fitting a Gaussian function over a third-order polynomial background. After the initial parameters were generated, they were applied to the spectrum generated by the ^{152}Eu source. Both a second-order polynomial fit and a linear fit were investigated for the calibration; however, it was found that the linear fit more accurately modeled the detector response. The calibrated spectra for both the ^{60}Co and ^{152}Eu sources are shown in Figure 5.5.

The absolute detector efficiency was determined by separately considering the intrinsic efficiency and the geometric efficiency. The intrinsic efficiency of the detectors was determined using the ^{60}Co source, as the emission of the two decay gamma-rays has a distinct

angular correlation. Utilizing the ability to correlate events between clovers, the intrinsic detector efficiency could be extracted. Then, by placing the ^{152}Eu source at the target position and normalizing the shape of the collected spectra based on intrinsic efficiency, a geometric efficiency could be extracted. Both functions taken together yield the absolute efficiency of the HPGe detectors, plotted in Figure 5.6.

To reduce Compton scattering background and improve statistics for high-energy events, an add-back scheme was employed. Each clover is electronically segmented into multiple detector volumes, so readouts from different volumes could be added together to reconstruct the initial energy of the gamma-ray. The energies, taken from the cores of each detector, were summed only if the gamma-ray scattered within a single clover and the signals were measured within the logic gate of an event. While it is possible for highly energetic gamma-rays to scatter out of one clover and into another, T4T lacks the capability to correctly reconstruct these events as it would require additional, high-efficiency gamma detectors around each clover.

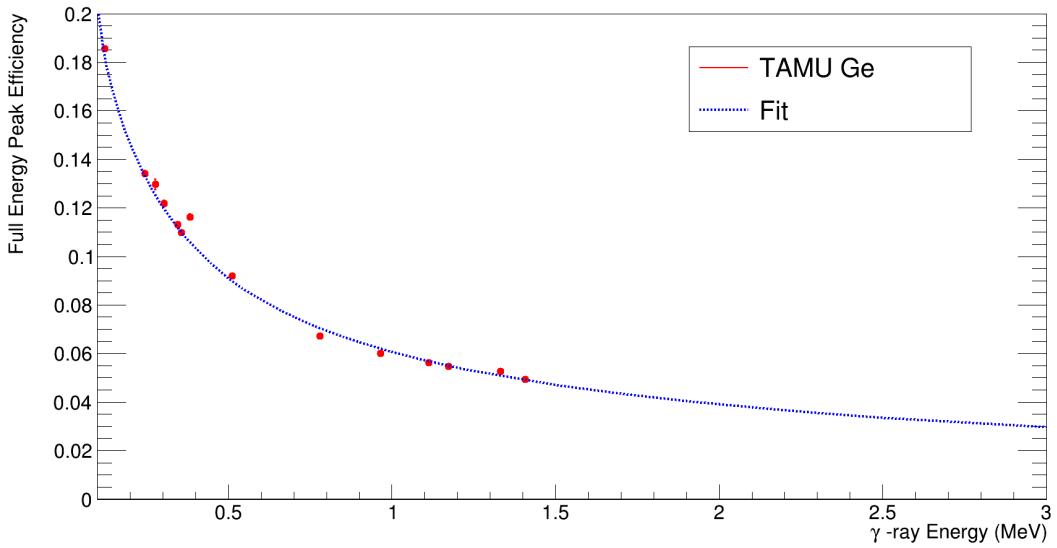

Figure 5.6: Absolute HPGe efficiency. This plot shows the absolute efficiency of the HPGe detectors as determined for the T4T stable beam experimental campaign. Reprinted with permission from [61].

Finally, a Doppler correction scheme was applied to experimental data to improve detector resolution. As this reaction was performed in inverse kinematics, the daughter nucleus continues to move after the transfer reaction and any emitted gamma-rays adopt its velocity. This means that a gamma-ray emitted at angles other than 90° relative to the particle's motion will be Doppler shifted, with gamma-rays emitted at forward angles shifting higher in energy and gamma-rays emitted at backward angles shifting lower in energy. This can be corrected for non-relativistic speeds by measuring the angle at which the gamma-ray was emitted, and applying the following equation:

$$E_{det} = \frac{E_\gamma}{\gamma(1 - \beta\cos(\theta))}\,. \tag{5.10}$$

Here E_{det} is the energy measured by the detector, θ is the angle the gamma-ray is emitted relative to the particle's motion, β is the particle's speed expressed as a fraction of the speed of light, γ is the Lorentz factor, and E_γ is the energy of the gamma-ray in the rest frame. The angle of emission was obtained from the electronic segmentation of the HPGe detectors. As discussed in Chapter 4, each clover was segmented into three slices perpendicular to the beam direction. The central angle of each of these segments was used to estimate the angle of emission, however the relatively large angular coverage of each segment meant that there was still some Doppler broadening observed after correction.

Like the Hyball, the mid-experimental changes and DAQ crash required experimental data to be adjusted on a run-by-run basis for the HPGe detectors. In particular, several of the channels for the segments and cores had been swapped during the crash. After determining the correct channel mapping, an online energy calibration was performed to well-known excited states of ^{24}Na. Plots of the corrected and uncorrected energies are shown in Figure 5.7. The energy resolution of the HPGe detectors after this correction was found to be roughly 7 ± 1 keV FWHM at gamma energies around 2 MeV.

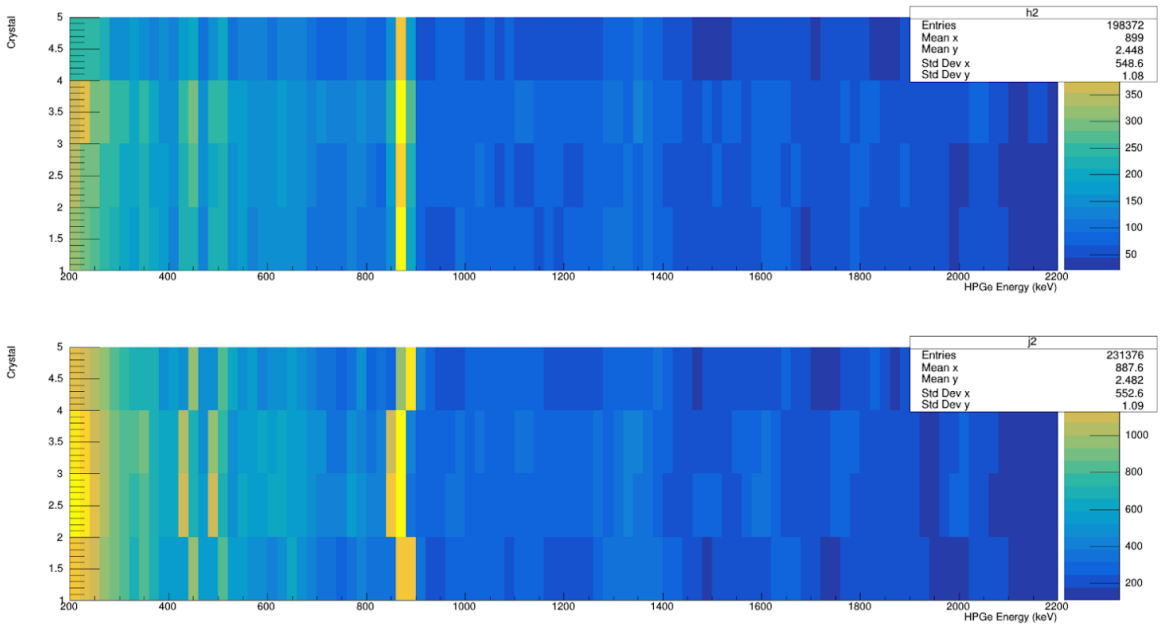

Figure 5.7: A corrected HPGe spectrum from experimental data. This plot shows the gamma energy versus crystal number for clover 2 for ($BOTTOM$) before online energy calibrations were applied and (TOP) after the online energy calibration was performed.

5.3.2 Beam Spot Minimization

An accurate estimate of the beam's position relative to the silicon detectors is necessary in order to reconstruct the physics of interest. This stems from the fact that the particles incident on the silicon detectors have a definite relationship between their energy and their angle of emission. For protons from the (d,p) reaction incident on the Hyball detector, the angle of emission has a direct correlation with the excited state from which they are decaying. Thus, the energy measured in the Hyball for a given ring and state depends on the angle of emission. Additionally, for a given beam offset, the radial angle corresponding to the angle of emission will be different. This means that the beam's center can be determined in the x-y plane by matching ring energies across radial angles.

In the Barrel, elastic scattering events follow a similar trend. The energy of elastically scattered deuterons corresponds with a position on the resistive strip detectors. Therefore, these data can be used to determine the z-position of the beam relative to the geometric

center of TIARA. Additionally, by comparing the z-position attained in each segment of the Barrel, the beam's angle can also be deduced.

The beam spot minimization utilized the Barrel and Hyball data to simultaneously constrain the beam's position in x, y, and z, as well as the beam's angle relative to TIARA's primary axis of symmetry[1]. A chi-squared minimization routine utilized experimental data to accomplish this. In the Barrel, the deuterons from elastic scattering were used to establish a z-position on each Barrel strip. The minimization routine then assumed the beam angle and a z-position for the target, calculated the expected position of scattered deuterons on the resistive strip detector, and compared these results with the experimental data. For the Hyball, protons from specific excited states of the (d,p) reaction were isolated in the experimental data. Then, the minimization routine assumed x-, y-, and z-positions for the target, calculated the expected position a proton would hit the Hyball detector, and compared that to experimental data. The chi-squared values were then combined into a single value and this process was iterated with new target positions until the chi-squared value of both fits had been minimized.

The result was a target position and beam angle that closely approximated the experimental conditions. In the present data set, the minimized beam position was given as

$$(x, y, z) = (0.68, 5.69, 6.30) \text{ mm}$$

relative to the geometric center of TIARA. Additionally, the beam angle was shown to be relatively close to parallel to the primary axis of symmetry. However, during the minimization process, two issues with the data set were discovered that required modifications to data analysis procedures. These issues are discussed in the sections below.

[1]For clarity, the beam axis is synonymous with the z-axis, the y-axis runs perpendicular to the z-axis in the up and down direction, and the x-axis is perpendicular to both. As TIARA can be best approximated as cylindrically symmetric, its primary axis of symmetry is along the z-axis.

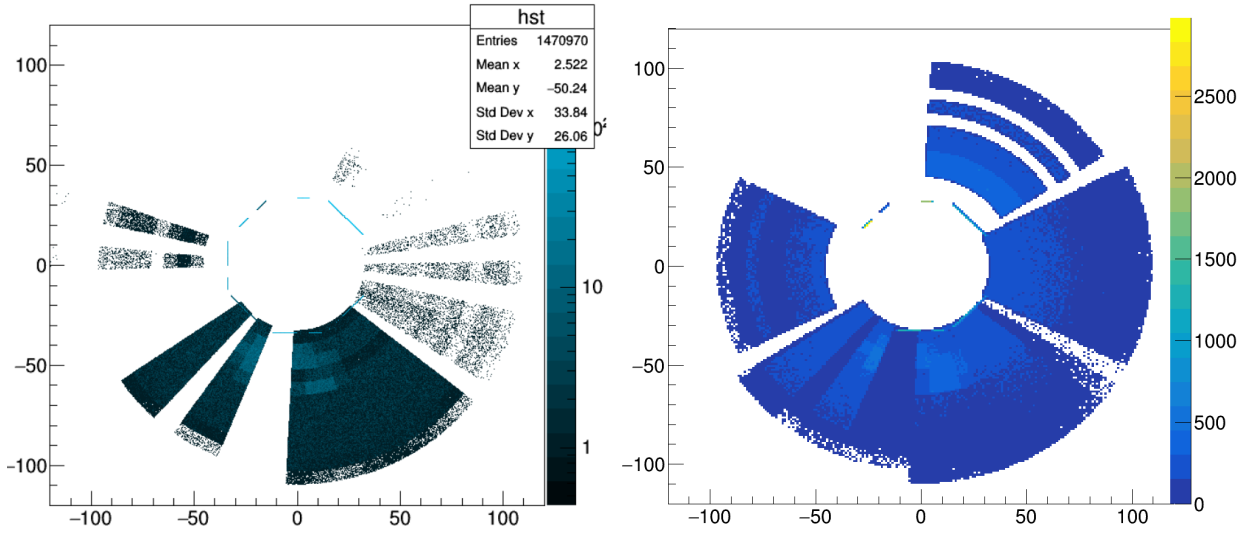

Figure 5.8: Decoupling of rings and sectors in the Hyball. (*LEFT*) A plot of the impact matrix for the Hyball showing the events from data analyzed with ring and sector coupling enabled. (*RIGHT*) The impact matrix for the Hyball showing the events from data analyzed with ring and sector matching disabled. The units of the x- and y-axes are in arbitrary units, and it should be noted that wedge 5 was not active during this experiment. Its absence manifests as the large gap in the upper left-hand corner of both plots.

5.3.2.1 Ring and Sector Decoupling

As the Hyball is a double-sided silicon strip detector (DSSD), it has segmentation both along radial angles and lab angles (θ_{lab}). As discussed in Chapter 4, the segmented detector volumes along radial angles are referred to as sectors and the segmented detector volumes along θ_{lab} are referred to as rings. A valid event in the Hyball is considered to have energy deposited in both the ring and the sector, allowing for more precise position reconstruction on an event-by-event basis.

After the experiment concluded, it was discovered that the gains on most of the Hyball sectors had been increased so high that most of the sector data was irrecoverable. This had the effect of reducing the number of valid Hyball events by an order of magnitude. By eliminating the ring and sector matching requirement for a valid event, the bulk of the Hyball data could be recovered. The impact of decoupling the ring and sector data can be seen in Figure 5.8. However, this had the unintended consequence of dampening

the Hyball's sensitivity to the radial angle of events and, by extension, the efficacy of the position minimization. A solution was devised wherein the radial angle was inherited from the detector wedge, creating six distinct radial angles for events rather than the typical forty-eight possible angles. The impact this change had on beam spot minimization and event reconstruction appears negligible.

5.3.2.2 Focal Plane Detector

The position minimization also indicated that the beam was abnormally high relative to the geometric center of TIARA. This was confirmed by inspecting the data from the focal plane detector. While it was clear from signals generated by the plastic scintillator detector that some recoils from the reaction did make it through the MDM and into the Oxford detector (see Figure 5.9), the beam appears to have been just on the edge of the focal plane acceptance window. When data from the silicon detectors were investigated in coincidence

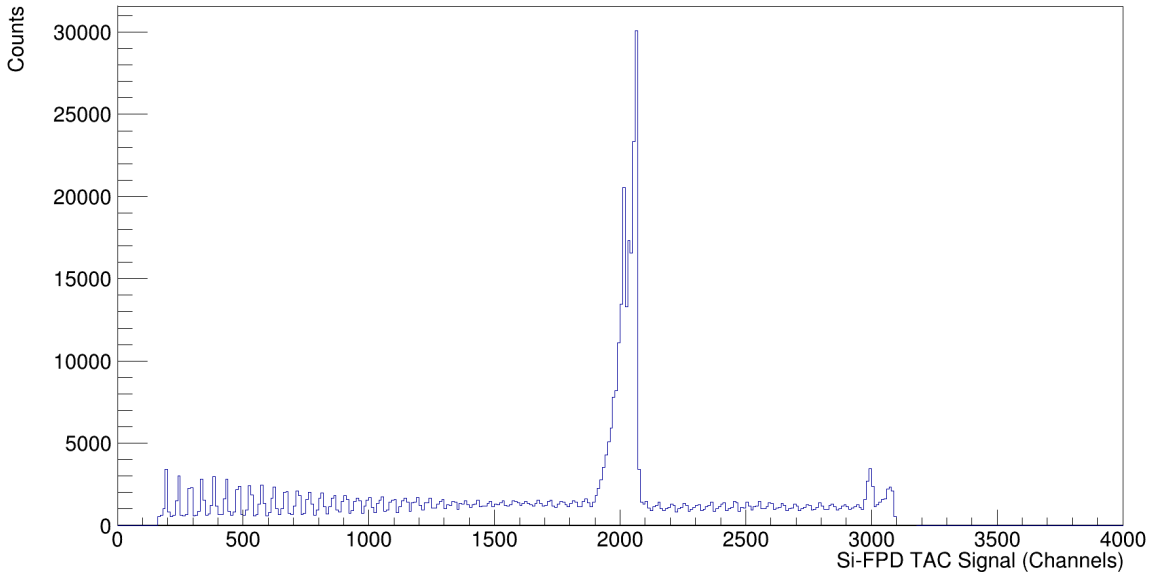

Figure 5.9: TAC peak from the plastic scintillator. This plot shows the time to amplitude converter (TAC) peak generated by events impacting the plastic scintillator detector at the end of the Oxford detector. The large peak around channel 2000 are events that arrive in coincidence with events in the silicon detector, which, for this work, can be assumed to be primarily events from ^{24}Na recoils.

with suspected ^{24}Na events in the focal plane detector, the number of Hyball events dropped by over an order of magnitude. This was a significantly larger drop in statistics than other experiments run during the same campaign had seen when performing a triple-coincidence measurement [9, 62]. However, requiring events in the silicon detectors to be in coincidence with events in the focal plane detector significantly reduced the background, as can be seen in Figure 5.10.

As the states of astrophysical interest in this study are already weakly populated, the decision was made to disregard the focal plane detector data in order to preserve statistics. This decision significantly reduced the ability to clean up background in the HPGe and silicon data, and made this study more reliant on previously published reaction data. However, alternative techniques to isolate individual states were implemented using the available experimental data, coincident gamma-rays in particular. Subsequent experiments using the T4T array have been successful in avoiding similar problems with beam alignment.

5.4 Experimental Data Analysis

Following the data reduction stage, reaction parameters could be extracted from the experimental data. This section outlines the process for constructing the ^{24}Na excitation energy spectrum, creating angular distributions for individual states, and extracting spectroscopic factors.

5.4.1 Excitation Energy Spectrum

The excitation energy spectrum effectively shows the excited states of the daughter nucleus populated by the transfer reaction. The spectrum, shown in Figure 5.11, can be constructed directly from the recorded lab energy of the proton and the lab angle at which it was measured. This calculation is derived from conservation of four-momentum before and after the reaction. Knowing the energy and direction of the incoming beam as well as the

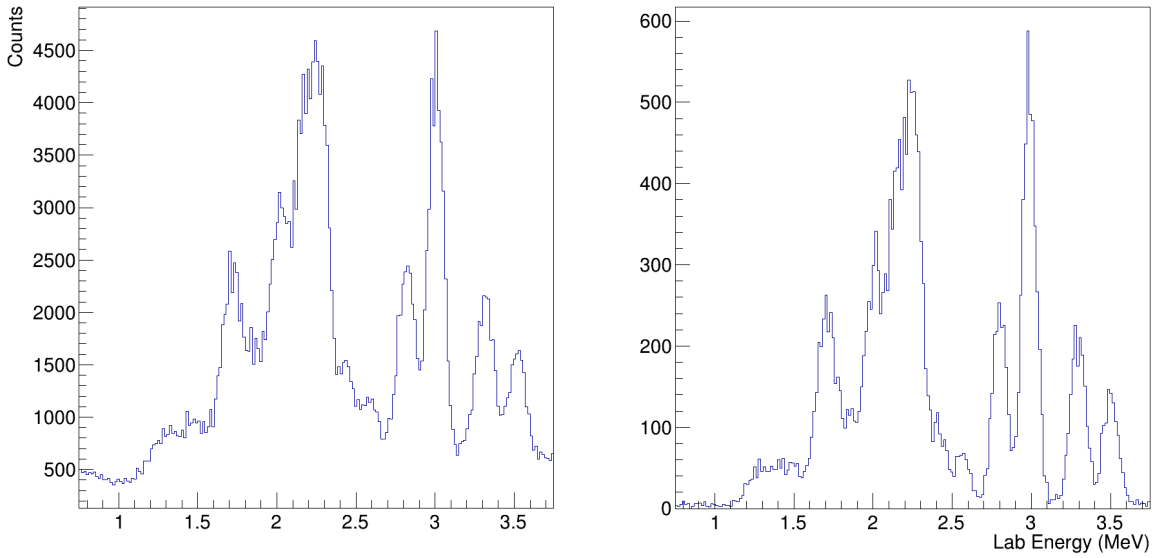

Figure 5.10: Lab energy of particles incident on the Hyball relative to the TAC peak. (*LEFT*) A plot of the lab energy for particles incident on the Hyball without a TAC coincidence gate. (*RIGHT*) The lab energy for particles incident on the Hyball showing events that arrive in coincidence with a TAC gate. While the raw number of events drops significantly when requiring coincidence with the TAC gate, it is also notable that the background drops to nearly zero.

rest masses of nuclei involved, the excitation energy of the recoil nucleus can be given as

$$E_x = m_1 + m_2 - m_3 - 2m_4 + T_1 + T_3 - \sqrt{p_3^2 + p_1^2 - 2p_3p_1cos\theta_3 - m_4^2}\,. \tag{5.11}$$

Here, the subscripts refer to each particle involved in the reaction. Index 1 is the beam-like particle, index 2 is the target, index 3 is the ejectile, and index 4 is the recoil. The kinetic energy is represented by T, the momentum is given as p, and the reaction angle is given by θ. The masses, represented by m, are taken to be the rest mass of the particle (so $c \equiv 1$). It should be noted that the momentum of the beam-like particle is only taken along the z-axis.

The excitation energy spectrum in this work considers only events from the Hyball detector, as events in the Barrel detector could not be resolved with sufficient energy resolution to be meaningfully reconstructed. This limitation stems primarily from the inability to gate on events in the focal plane detector to reduce background from the Barrel, as well as the

intrinsically poor energy resolution of the Barrel. Additionally, Hyball events are required to have a multiplicity of one, ensuring only single-particle events are considered.

Figure 5.11 reveals a number of features of the reaction, chiefly strong single-particle states in ^{24}Na populated by the ^{23}Na(d,p)^{24}Na reaction. Comparing this spectrum with previous studies done by Daum [55] and Tomandl *et al* [59] reveals good agreement with previous studies done in forward kinematics. However, this also reveals the inherent trade-off between experiments performed in forward kinematics and inverse kinematics: while inverse kinematics can simultaneously measure a much broader range of laboratory angles, it does so at the expense of energy resolution. This means that excited states that may be individually discernible in forward kinematics appear in doublets or triplets in inverse kinematics. These unresolved states can be isolated by investigating particle-gamma coincidence.

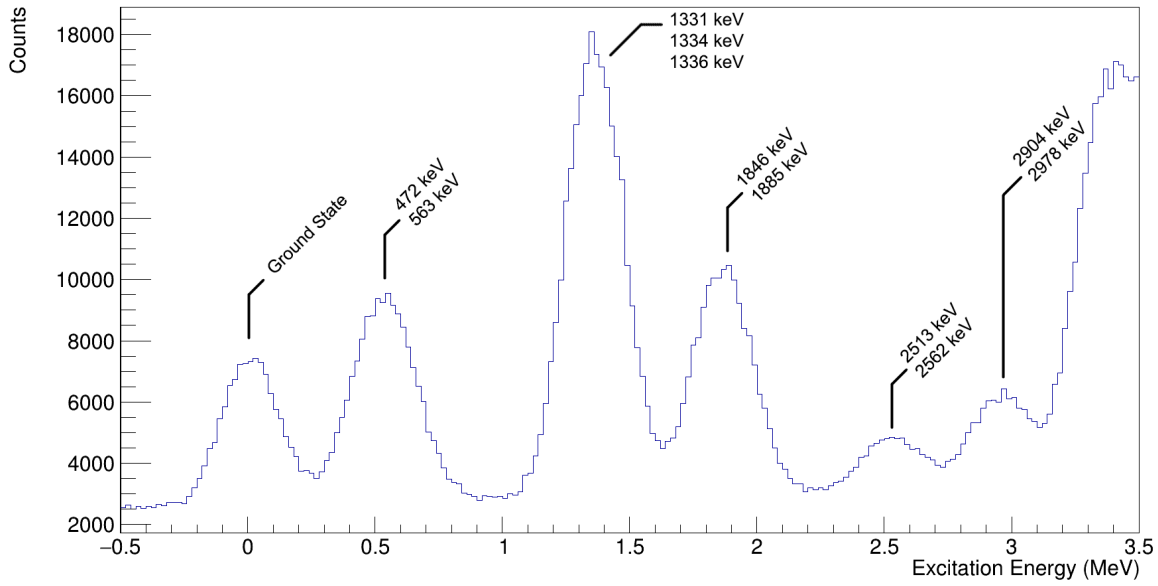

Figure 5.11: Excitation energy spectrum for the ^{23}Na(d,p)^{24}Na reaction. The spectrum was reconstructed from the excitation energy, which was calculated from the lab energy of protons in the Hyball. This plot shows several well-populated excited states from the ^{24}Na nucleus.

5.4.1.1 Particle-Gamma Coincidence

Each low-lying state in ^{24}Na has its own unique gamma-decay scheme. Knowledge of this decay scheme can be leveraged to disentangle excited states. Figure 5.12 depicts the excitation energy spectrum versus measured gamma energy. Each horizontal band has an internal structure that reflects the gamma-decays that occur for a given excitation energy. For a clearly resolved state, this structure would indicate the different gamma-decay branches available to the state. Bands with multiple unresolved states will contain the decay structure of each state in the band. States with unique gamma-ray energies within a band can be cleanly separated from other states from those unique gamma-rays.

An application of this technique can be seen in Figure 5.13, where coincidence with two characteristic gamma-rays from the 1846 keV excited state is required in the Hyball data. Because the gamma-rays are unique to the 1846 keV state, the remaining counts in the

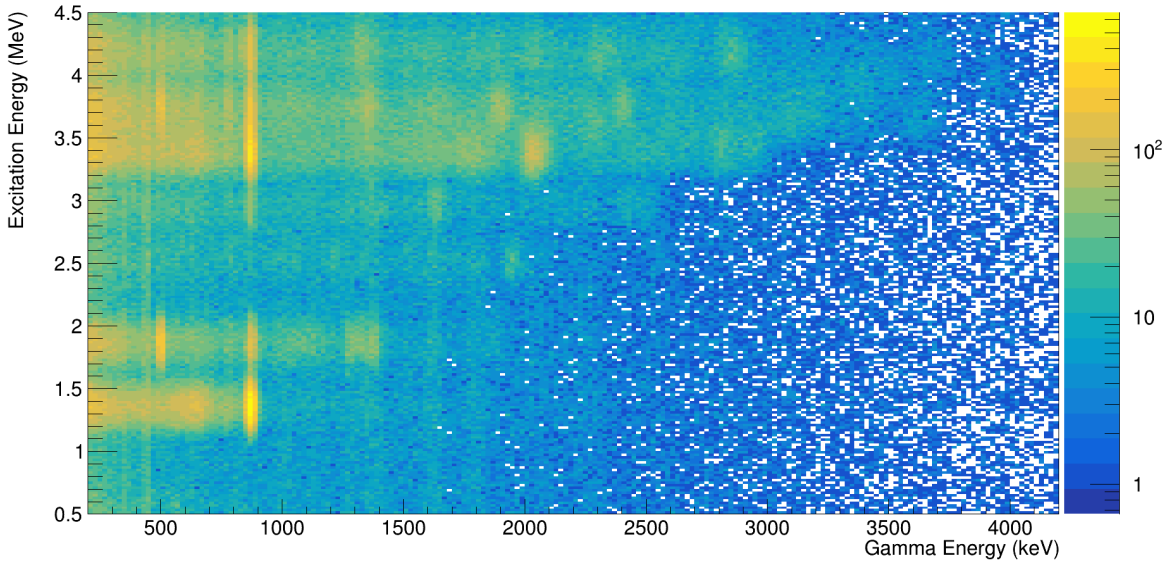

Figure 5.12: Excitation energy as a function of gamma-ray energy. This plot shows the excitation energy spectrum as function of coincident gamma-ray energy. Horizontal bands correspond to the peaks seen in Figure 5.11 while the internal structure of the bands corresponds to gamma-decays for specific states. Normally, this information can be used to construct a decay scheme; however, the large background inherent in this data set makes it difficult to exploit this capability of the experimental setup.

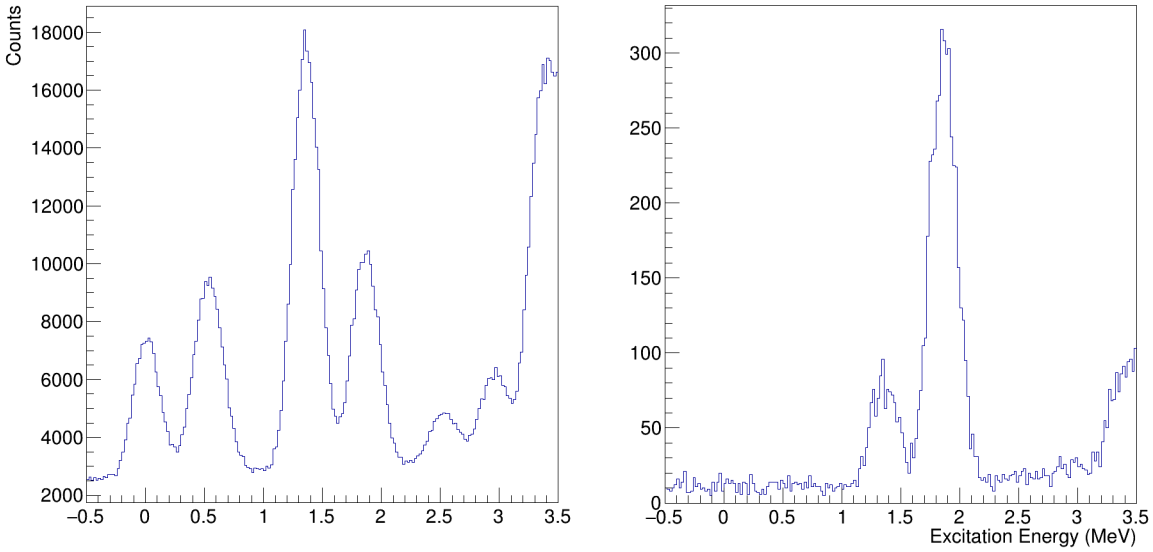

Figure 5.13: Particle-gamma coincidence utilized to isolate a single state. (*LEFT*) A plot of the excitation energy spectrum showing low-lying excited states in the ^{24}Na nucleus. Of note here is the 1846 keV and 1885 keV doublet. (*RIGHT*) The same excitation spectrum with a coincidence gate on the 500 keV and 502 keV gamma-ray emitted from the 1846 keV state. This now restricts the excitation energy spectrum to events in the Hyball directly populated by the 1846 keV excited state.

Hyball must only be from that state. The opposite technique can also be employed, where excitation energy peaks can be used to isolate individual gamma-ray transitions for specific states. Given the overall better energy resolution of the HPGe detector, this work utilized the latter technique to isolate states of astrophysical interest.

5.4.2 Angular Distributions from DWBA Calculations

Angular distributions are simply functions describing the variation of the derivative of the cross section with respect to the solid angle, plotted vs. the reaction polar angle. As discussed in Chapter 3, these functions can be determined theoretically via DWBA calculations, which assume the transfer of a neutron into a shell model orbital. The shape of these distributions is governed primarily by the the orbital angular momentum transfer quantum number (ℓ). The reaction code TWOFNR [41] was used to generate angular distributions for three separate states: the 2512 keV state, the 2563 keV state, and the 3628 keV state.

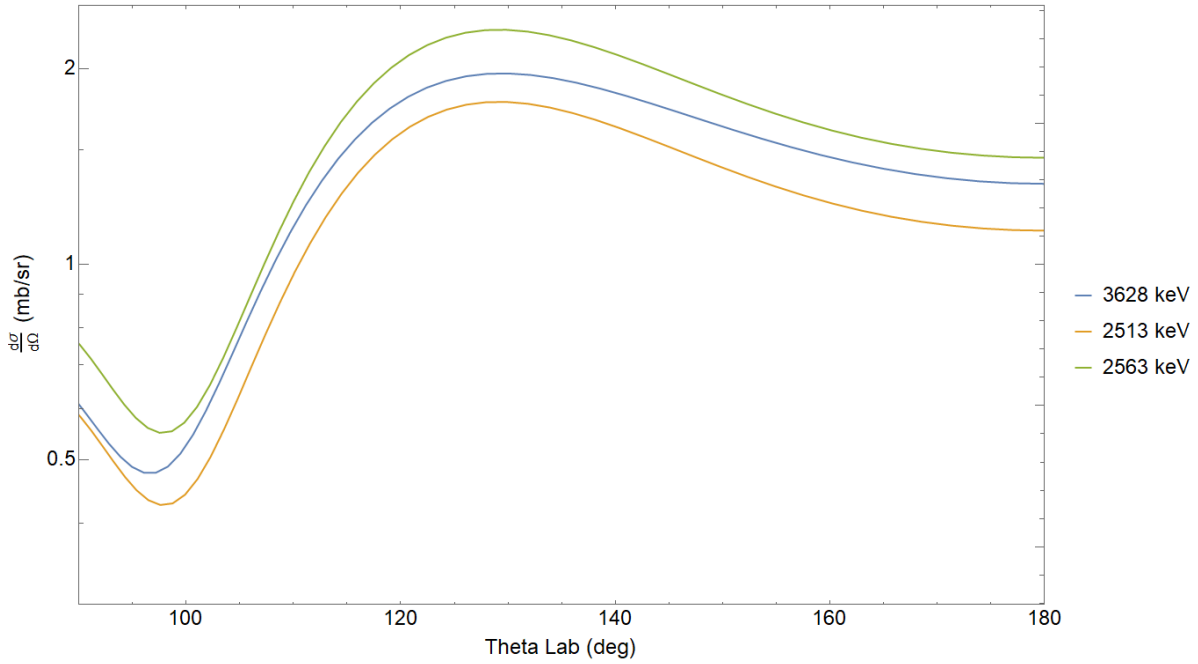

Figure 5.14: Theoretical angular distributions generated by TWOFNR.

The angular momentum transfer of each of these states has been established in previous studies [55, 59], so the DWBA calculations assumed the ℓ values presented in Table 5.2 for the calculation of each state. The optical model parameters used for the calculations were taken from Tomandl *et al* and are listed in Table 5.5 [59]. The resulting angular distributions are shown in Figure 5.14 and will be compared to the experimentally determined angular distributions in Section 5.4.4.

V (MeV)	r (fm)	a (fm)	W_d (MeV)	r_d (fm)	a_d (fm)	V_so (MeV)	r_so (MeV)	a_so (fm)	r_c (fm)
Input Channel: ^{23}Na + d									
87.5	1.17	0.738	12.28	1.325	0.728	7.82	1.07	0.66	1.3
Output Channel: ^{24}Na + p									
53.0	1.25	0.65	11.5	1.25	0.47	8	1.25	0.65	1.25

Table 5.5: Input parameters for DWBA calculations. This table shows optical potential input parameters for DWBA calculations of the ^{23}Na(d,p)^{24}Na reaction [59].

5.4.3 Angular Distributions from Experimental Data

Angular distributions can be extracted from experimental data by evaluating the number of events for a given excited state over a well-defined angular range. Within the T4T experimental setup, TIARA is the only detector that allows for well-defined position measurements of ejectiles. As such, the angular distributions for this experiment are determined from the silicon detectors surrounding the target position. The Barrel detector, while capable of providing both energy and position information, was not used to identify ejectiles from the transfer reaction. Therefore, only data from the Hyball were used to construct angular distributions and it is the only detector considered from this point forward.

An angular distribution is given by the equation

$$\frac{d\sigma}{d\Omega} = \frac{N_{det}}{\epsilon \cdot I \cdot t \cdot d\Omega}\,, \tag{5.12}$$

where N_{det} is the number of events detected, $I \cdot t$ is the experimental luminosity, $d\Omega$ is the solid angle, and ϵ is the absolute efficiency of the detector. The absolute efficiency can defined as a product of the intrinsic efficiency of the detector ϵ_d, the experimental live time ϵ_{lt}, and the geometric efficiency ϵ_g. The solid angle is given as

$$d\Omega = 2\pi(\cos\theta_{min} - \cos\theta_{max}) \tag{5.13}$$

for a given angular range θ_{min} to θ_{max}, which, when visualized, assumes the shape of an annulus. By convolving terms such that

$$d\Omega' = \epsilon_g \cdot \epsilon_d \cdot d\Omega \tag{5.14}$$

$$C = \epsilon_{lt} \cdot I \cdot t\,, \tag{5.15}$$

Equation 5.12 can be further simplified to

$$\frac{d\sigma}{d\Omega} = \frac{N_{det}}{C \cdot d\Omega'} \,. \tag{5.16}$$

For the purposes of this work, C will be referred to as the normalization constant and $d\Omega'$ will be referred to as the effective solid angle. Determining angular distributions therefore requires the evaluation of each of these terms, and the process for determining each is outlined below.

5.4.3.1 Effective Solid Angle

The effective solid angle, as shown above, is comprised of three separate components: the geometric efficiency, the intrinsic detector efficiency, and the solid angle coverage. For the silicon detectors, the intrinsic detection efficiency is approximated to unity. Therefore, only the solid angle coverage of the detector and the geometric efficiency need to be defined.

Determining the solid angle coverage of the detector volume required defining an angular binning based on the detector's segmentation. Each Hyball wedge is segmented into 16 separate rings and each individual wedge covers lab angles between 137° and 170° (with each ring covering roughly 2°). By design, several of the rings are shadowed by the Barrel detector and therefore do not detect any of the ejectiles from the transfer reaction. Several more rings on the boundary region between the shadowed section of the Hyball and the unobstructed section and are subject to hard-to-quantify edge-effects. This meant that, as viewed from the target position, only 10 of the 16 rings were considered in this study. To optimize the number of counts in each angular bin, the rings were separated into five angular ranges each comprised of two rings.

The geometric efficiency and solid angle associated with each angular range was determined via Monte Carlo simulation. This was accomplished by using GEANT4 to perform high-statistics simulations of the ^{23}Na(d,p)^{24}Na reaction that populated excited states of the recoil and recorded the ejectiles captured in each angular bin. The simulation emitted

θ_{lab} (degree)	$d\Omega'$	Uncertainty
165.75	0.115636	0.001
161.25	0.129528	0.002
157.25	0.131394	0.005
152.25	0.13884	0.001
149.5	0.0935629	0.003

Table 5.6: Effective solid angles and their associated uncertainties for each angular range used to calculate experimental angular distributions. The reported θ_{lab} is given as the center of the angular range.

protons isotropically in the center of mass frame and channels that were not functional in the experiment were disabled in the simulation. The results from the transfer reaction simulation were compared to simulations performed with an alpha source at rest placed at the target position. Finally, to estimate the uncertainty of the solid angle, the beam position was varied to reflect the uncertainties in the position minimization. The resulting effective solid angle is shown in Table 5.6.

5.4.3.2 Detected Events

Calculating the number of events in a given detector is slightly more complex when dealing with states that are unresolved in the deuteron singles spectrum. Requiring particle-gamma coincidence isolates individual excited states; however, this introduces biases from the HPGe detectors. To correct for these effects, the number of events captured by the silicon detector as a function of the number of events captured by the HPGe detectors can be written as

$$N_{det} = \frac{N_{Ge}}{\epsilon_{Ge} \cdot b}\,, \tag{5.17}$$

where N_{Ge} is the number of events captured by the HPGe detectors, ϵ_{Ge} is the absolute efficiency of the HPGe detectors, and b is the branching ratio. More specifically, the branching ratio is the fraction of gamma-rays that decay via an individual decay mode relative to other deexcitations from a given excited state. Selecting a unique, well-resolved gamma-ray with

a known branching ratio is necessary to effectively implement particle-gamma coincidence measurements.

With a coincident gamma-decay selected, the energy spectrum from the HPGe detectors was gated on the desired angular range and plotted over a narrow range in the vicinity of the chosen gamma-ray energy. The peak was then fitted with a Gaussian function with a freely varying amplitude on top of a polynomial background. The order of the polynomial background depended on the behavior of the background in close proximity to the peak of interest; however, for this work most backgrounds were modeled with a third-order polynomial. The background was initially determined by inspecting the HPGe energy spectrum in coincidence with events other than those associated with the transfer reaction. Once fit parameters for the background were determined, the background was fixed (save for a scaling factor) and fit to the HPGe energy spectrum of interest. A canvas of sample fits from the 2512 keV state are shown in Figure 5.15. The integral of the Gaussian function allowed the number of events within the peak to be ascertained.

Having extracted N_{Ge}, the value ϵ_{Ge} was determined from the absolute efficiency function constructed during calibration. At higher energies, the value of ϵ_{Ge} could be on the order of 2% to 3%, so this technique required the selection of states that were strongly populated by the transfer reaction. Weakly populated states or states without one or two preferential gamma-decays are difficult to reconstruct without a significant amount of statistics.

5.4.3.3 Normalization Constant

Part of the function of the Barrel detector is to collect data to perform beam normalization. Typically, this process is performed by constructing the angular distribution of a well-known reaction present in the experimental data and comparing it to the calculated cross section. If the values of N_{det} and $d\Omega'$ are known for this reaction, a value for the normalization constant C can be ascertained. The normalization constant is generally considered to be invariant through the experimental run time.

For transfer reactions in inverse kinematics, it is often convenient to normalize experimen-

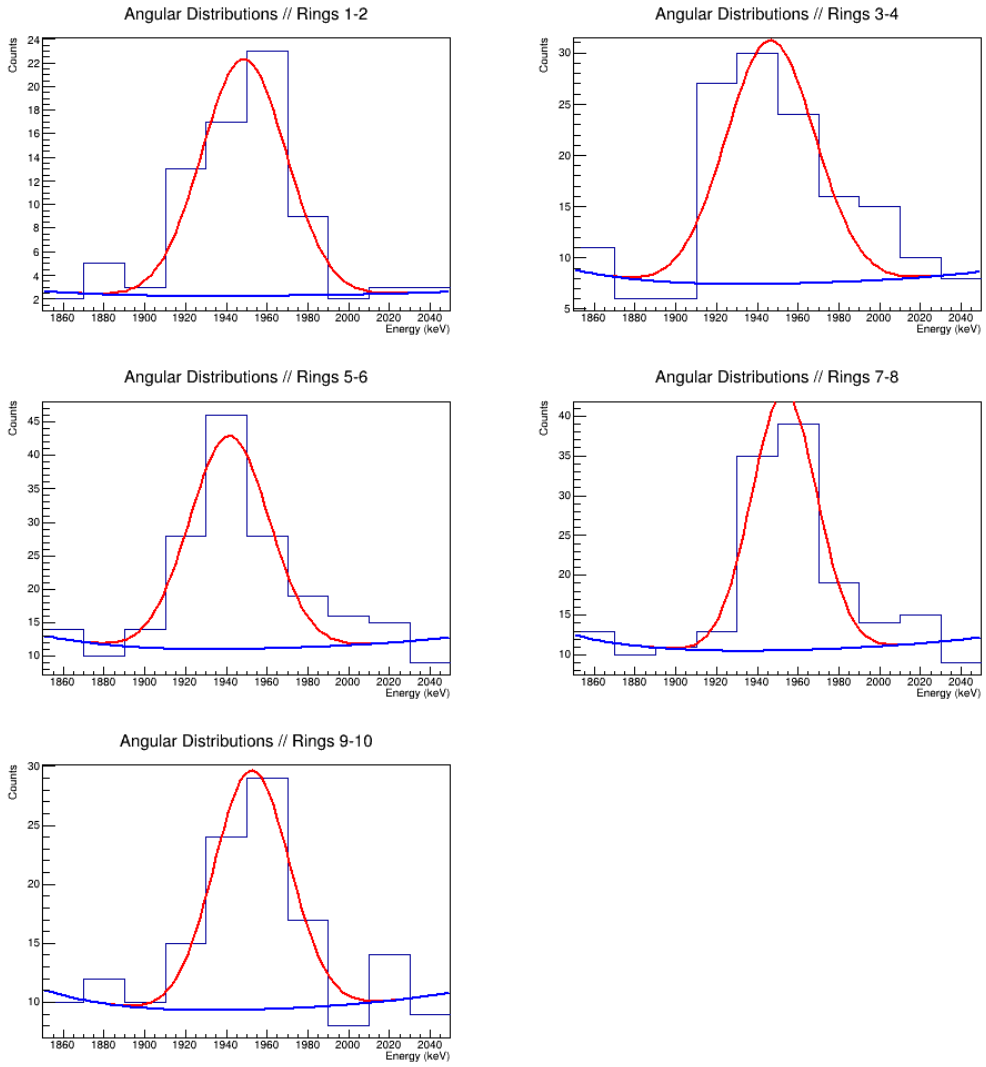

Figure 5.15: Sample fits to determine N_{Ge}. This canvas displays fits for the 2512 keV excited state in ^{24}Na. The background was fit to a third-order polynomial while the gamma-ray peak at 1950 keV was fit to a normalized Gaussian function.

tal data to elastic deuteron scattering. Cross sections for elastic scattering are dominated by the well-known Rutherford scattering process, and corrections to the Rutherford scattering can be calculated using DWBA codes. Evidence of elastic scattering readily appears in a narrow energy range in the Barrel. An experiment run during the same experimental campaign successfully employed this technique to determine the normalization constant with uncertainties around $\pm 20\%$ [9]. However, the spectroscopic factors determined by this experiment

disagreed with literature by over a factor of two and the data were eventually normalized to literature values. These issues were attributed to problems with beam tuning and the size and shape of the beam profile on target. That study also had a longer experimental run time than the present work, as well as fewer technical issues with data acquisition. As such, the decision was made to perform a normalization relative to previously published spectroscopic factors.

Since the ^{23}Na(d,p)^{24}Na reaction is a well-documented reaction, the normalization was made to the spectroscopic factor of a strongly-populated excited state at 3628 keV. This state has the same spin and angular momentum transfer as the primary state of astrophysical interest (at 2512 keV) and has a strong gamma-ray transition directly to the ground state. From Equation 3.59, a formula for the normalization constant can be given generally as

$$C = \frac{N_{det}}{d\Omega' \cdot S_{dp} \cdot \left(\frac{d\sigma}{d\Omega}\right)_{th}}, \tag{5.18}$$

where $S_{dp} \equiv C^2S$ and $\left(\frac{d\sigma}{d\Omega}\right)_{th}$ is the angular distribution predicted by DWBA calculations. Using a N_{det} determined from the 3628 keV state and the spectroscopic value for the state as given by Tomandl *et al*, the normalization constant for this experiment was found to be $C = 120700 \pm 10900$, or roughly $\pm 9\%$ uncertainty.

5.4.4 Spectroscopic Factors

As discussed in Chapter 3, the spectroscopic factor is a dimensionless quantity that describes how strongly a given state exhibits single-particle behavior. In the present study, spectroscopic factors have been obtained by fitting angular distributions generated by DWBA calculations to angular distributions constructed from experimental data. The details for each state investigated in the present work are described below.

5.4.4.1 $E_x = 2512\ keV$

The 2512 keV state is the primary state of astrophysical interest in this study. The state has an adopted J^π of 3^+ and is moderately populated in ^{23}Na(d,p)^{24}Na reaction via the

θ_{lab} (degree)	N_{Ge}	Uncertainty
165.75	52	9
161.25	65	14
157.25	78	15
152.25	65	12
149.5	47	12

Table 5.7: Events detected by the HPGe detectors for the 2512 keV state. This table shows the number of events counted in the HPGe detectors and their associated uncertainties for each angular range used to calculate experimental angular distributions. The reported θ_{lab} is given as the center of the angular range.

$\ell = 2$ transfer of a neutron into the $1d_{3/2}$ and $1d_{5/2}$ shells. The excitation energy has been determined with high precision in previous studies to be 2512.33±0.33 keV [59]; however, it appears at 2508±9 keV in this study. In order to extract a value for N_{det}, a gamma-decay branch with a gamma-ray energy of 1950 keV and a branching ratio of 0.939 was selected to isolate the state from the nearby 2563 keV state. An absolute efficiency of the HPGe detectors at this energy was found to be $\epsilon_{Ge} = 0.0397$, and values of N_{Ge} for each angular bin are shown in Table 5.7.

Figure 5.16 shows the experimentally determined angular distribution plotted with the theoretical angular distribution obtained from DWBA calculations for an $\ell = 2$ transfer. The spectroscopic factor used to scale the theoretical angular distribution was obtained by a least-squares fit of the calculated angular distribution to the experimental data. A spectroscopic factor of $S_{dp} = 0.0852 \pm 0.0085$ was obtained. The implications of this result will be discussed further in Section 5.5.

5.4.4.2 $E_x = 2563\ keV$

The 2563 keV state is also a state of astrophysical interest in this study, as it corresponds with the state populated by the ~ 663 keV resonance in ^{24}Al. The state has an adopted J^π of 4^+ and is weakly populated in ^{23}Na(d,p)^{24}Na reaction via the $\ell = 2$ transfer of a neutron into the $1d_{5/2}$ shell. The excitation energy has been determined with high precision in previous

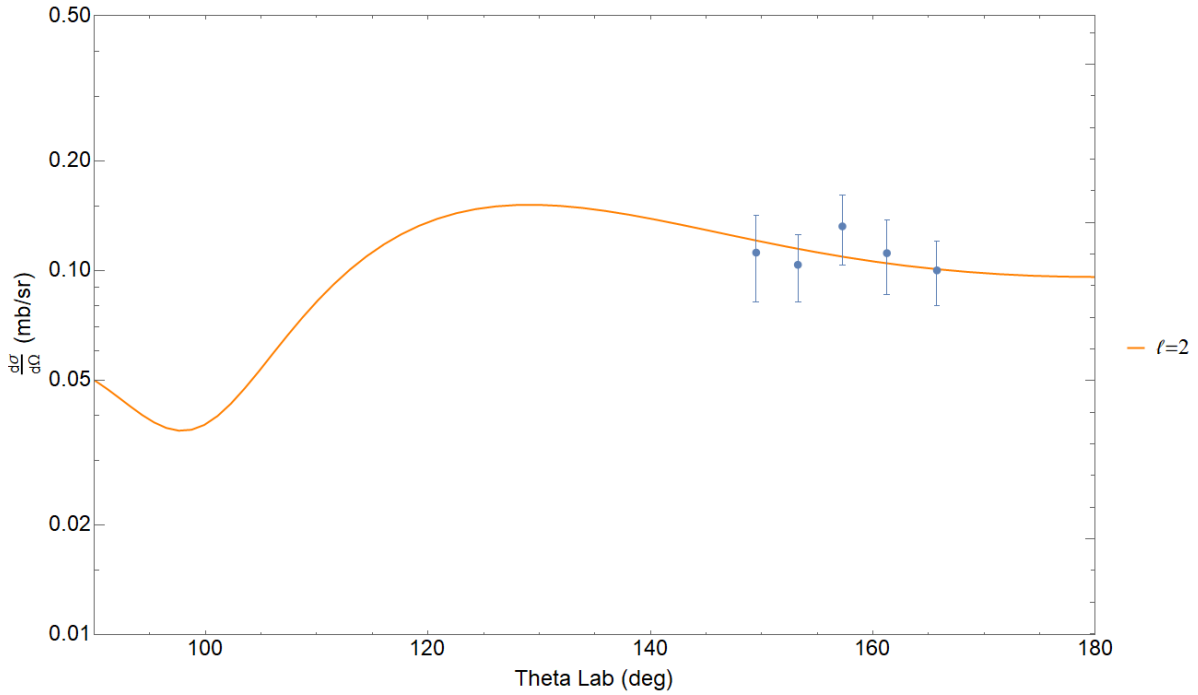

Figure 5.16: Experimental angular distribution of the 2512 keV state. The angular distribution is normalized to the 3628 keV state. Experimental data are shown with its uncertainties by the points in blue. The calculated angular distribution is shown in orange and is scaled by a spectroscopic factor of $S_{dp} = 0.0852$.

studies to be 2563.16±0.35 keV [59], but was not able to be determined in this study.

As this state decays through one of three gamma-decays, several attempts were made to locate these gamma-rays in coincidence with protons arriving in the Hyball. Despite exploring a variety of wider angular ranges, there simply were not enough events in the HPGe detectors to isolate this state and construct an angular distribution. Section 5.5 will discuss this issue in further detail.

5.5 Discussion

To adequately address the results of this experiment, three main topics will be addressed: the experimental results with regard to previous studies, the astrophysical implications of the measurement, and potential improvements for future experiments utilizing the T4T experimental setup.

5.5.1 Experimental Results

A chi-squared fit was performed between the experimental data and the calculated angular distributions for the 2512 keV state. This fit included the uncertainties on the experimental values in determining the spectroscopic factor. The bulk of the uncertainty reported with this fit arises from corresponding uncertainty on the experimental data. This is influenced primarily by the low statistics associated with the particle-gamma coincidence measurement.

While a lack of data made it impossible to isolate the 2563 keV state and determine a spectroscopic factor, the spectroscopic factor extracted for the 2512 keV state is relatively close to values from previous studies. The value reported by Daum, which is furthest from agreement with the present study, was reported as tentative. The Tomandl *et al* measurement, the most recent study on this reaction, is in relatively close agreement with both values proposed by this work. All referenced values can be seen in Table 5.8.

5.5.2 Astrophysical Implications

As laid out in Chapter 2, the 2512 keV state in ^{24}Na is a mirror state of the 2349 keV state in ^{24}Al, which is the state populated by the dominant resonance in the ^{23}Mg(p,γ)^{24}Al reaction at classical novae temperatures [15]. For light nuclei, the spectroscopic factor of mirror states in mirror nuclei can be assumed to be the same [63]. This means that the spectroscopic factor determined in this work can be used for the mirror state in ^{24}Al.

The single-particle partial width is given by Equation 3.54 and is governed primarily by the penetration factor P_C and the single-particle reduced width θ_{sp}. The penetration factor can be easily calculated numerically; however, it depends strongly on the resonance energy

E_x		$[(2J_f+1)/(2J_t+1)]S_{dp}$			
(keV)	J^π	Daum	Tomandl	Present	ΔPresent
2512	2^+	(0.08)	0.12	0.149	0.0149
2563	$4^+(2^+)$	0.068	0.069	N/A	N/A

Table 5.8: Spectroscopic factors from Daum, Tomandl *et al*, and the present work.

of the state of interest. The current accepted resonance energy for the state of interest is $E_r = 480.8$ keV from the revised Gammasphere measurement [16]. Using this resonance energy, a penetration factor of $P_C = 2.93905 \times 10^{-6}$ was determined using a numerical code developed at the University of Edinburgh. The single-particle reduced width was taken to be $\theta_{sp} = 0.6$, a value that generally concurs with previously published literature [15, 63]. From this, a single-particle partial width of $\Gamma_{sp} = 2360$ meV was obtained.

From Equation 3.53, the proton partial width is given as

$$\Gamma_p = C^2S\,\Gamma_{sp}\,, \tag{5.19}$$

where $C^2S \equiv S_{dp}$ and Γ_{sp} is the single-particle partial width calculated above. Taking the value of $S_{dp} = 0.085 \pm 0.0085$ determined in this work, a proton partial width of $\Gamma_p = 201 \pm 20$ meV was determined. While slightly higher than previous values reported by other studies, this value is broadly in line with previous literature. Assuming a gamma partial width of $\Gamma_\gamma = 33$ meV, determined from shell model calculations of unbound states in ^{24}Al [15], this yields a resonance strength of $\omega\gamma = 25 \pm 3$ meV from Equation 3.48. A secondary method of obtaining the resonance strength comes from adopting the gamma partial width of the state in the mirror ^{24}Na nucleus, scaling it based on the gamma energy and multipolarity of the deexcitation, and using that as the gamma partial width for the ^{24}Al nucleus. The partial width is related to the decay constant of the state by the relation

$$\Gamma_\gamma = \frac{1}{\lambda_\gamma}\,, \tag{5.20}$$

where λ_γ is the decay constant given by the equation

$$\lambda(\bar{\omega}L) = \frac{8\pi}{\hbar L[(2L+1)!!]^2}\left(\frac{E_\gamma}{\hbar c}\right)^{(2L+1)} B(\bar{\omega}L)\,. \tag{5.21}$$

The scaling factor for the partial widths can therefore be determined by taking the ratio of

Γ_p (meV)	Γ_γ (meV)	$\omega\gamma$ (meV)	Source
489	47	27	Kubono *et al* [19]
185	33	25	Herndl *et al* [15]
170 ± 70	33 ± 17	24 ± 18	Iliadis *et al* [63]
		38^{+21}_{-15}	Erikson *et al* [18]
201 ± 20	33	25 ± 3	Present Work (th)
201 ± 20	39 ± 12	29 ± 10	Present Work (exp)

Table 5.9: Comparison of reaction parameters from previous literature and this work. This table is a comparison of the proton partial width, gamma partial width, and resonance strength from previous literature and this work. The value from Herndl *et al* comes primarily from shell model calculations, while at least one of the values from this work and Kubono *et al* are determined experimentally. The values from Iliadis *et al* are collected from previous literature and used for simulations of reaction rates in classical novae. The value from Erikson *et al* obtains the resonance strength from a direct measurement of the ^{23}Mg(p,γ)^{24}Al reaction. For the values presented from present work, the first (th) uses the gamma partial width calculated from theory while the second (exp) uses the experimentally determined gamma partial width adopted from the ^{24}Na mirror and scaled to the ^{24}Al transition.

the gamma decay energies. For this treatment, the value B can be treated as a constant and the multipolarity of the transition can be assumed to be the same for both states. Information about electromagnetic deexcitation from the unbound state in ^{24}Al has been taken from Lotay *et al* [17] and the method yields a resonance strength of $\omega\gamma = 29 \pm 10$ meV.

Table 5.9 shows relevant resonance parameters from this work and previous literature. In general, the resonance strength found by this work agrees well with previous theory calculations and other indirect measurements. It also agrees with the value determined by a direct measurement of the reaction with the caveat that the present measurement depends on the theoretical calculation of the gamma partial width or a value assumed from the mirror nucleus. As Γ_γ dominates the resonance strength, the discrepancy likely stems from the outsize influence of the theoretical value in calculating the resonance strength. Further constraints on the gamma partial width or a repeat of the direct measurement may help resolve the differences between these values.

5.5.3 Potential Improvements

The primary complication in this study stems from a lack of statistics to confidently perform particle-gamma coincidence measurements. This problem manifests primarily in the inability to isolate weakly-populated states via particle-gamma coincidence (such as the 2563 keV state. In the context of this work, while it is difficult to say precisely how much more data would be required to isolate the 2563 keV state, a factor of two to three more data may allow for its isolation.

Improvements could come from one of several places: increased solid angle coverage, increases in geometric efficiency, or simply planning a longer experimental run for experiments that will require particle-gamma coincidences. The two detector-based solutions, improving the geometric efficiency and increasing the solid angle, are generally difficult to implement. In this work, both the geometric efficiency and the solid angle are most limited by the disabled sections of the Hyball and non-functional portions of the Barrel. However, in other studies when coincidence with the focal plane detector is required, the geometric efficiency becomes further restricted by the acceptance window of recoils into the MDM-2 spectrometer [9]. For future experiments, this may require performing longer experimental runs when states of interest will require particle-gamma coincidence measurements.

Furthermore, some experimental uncertainty with respect to the solid angle can be addressed by better characterizing the profile of the beam from the cyclotron. In the present study, the uncertainty on the position and profile of the beam was the primary contribution to solid angle uncertainty. Subsequent experiments performed with T4T have improved geometric alignment between TIARA and the MDM-2 spectrometer. Additionally, extra time was allotted during setup to properly tune the beam at the target position.

6. PHOTON STRENGTH FUNCTION STUDIES IN ^{58}Fe

6.1 Heavy Element Nucleosynthesis

The production of heavy elements in the Universe depends keenly on stellar nucleosynthesis. The stellar environment acts as a furnace, fusing lighter nuclei formed during Big Bang nucleosynthesis to form larger elements. Stellar evolution, the process that drives stellar nucleosynthesis, stems from a star enabling nuclear reactions as a means of supporting itself against gravity and is thought to primarily generate elements lighter than iron. Elements heavier than iron are generated in one of two neutron-capture processes: the slow-capture process (s-process) and the rapid-capture process (r-process). The r-process primarily occurs during explosive nucleosynthesis, including supernovae nucleosynthesis and neutron star mergers, while the s-process occurs in more stable stellar environments. Together these processes generate about half of the overall abundance of heavier elements and directly determine the abundance of heavy elements observed in the Universe.

Elemental abundances can be determined by measuring the electromagnetic spectrum across a wide range of frequencies. However, focusing on gamma-ray spectroscopy can yield information specifically about nucleosynthesis of elements ejected into the interstellar medium. Measuring photons emitted from the decay of certain elements provides insight into not only the abundance of a particular element, but also its isotopes [64]. Long-lived radioactive elements ejected into the interstellar medium can be particularly useful spectroscopy candidates as the Universe is nearly transparent to photons at gamma-ray energies and thus they are not obscured by dust clouds or other features.

Certain long-lived radioactive isotopes ejected into the interstellar medium also appear in galactic cosmic rays. By directly measuring the abundance of these elements, inferences can be made about the evolution of nearby clusters of stars [65]. With recent advances in detector technology, the ability to measure extremely rare radioactive isotopes has opened

the door to new methods of probing stellar evolution.

Two radioactive isotopes, ^{26}Al and ^{60}Fe, provide a window into the inner-workings of massive stars and core collapse supernovae. With half-lives on the order of millions of years, they propagate into the interstellar medium, and even end up deposited on Earth and the lunar surface [66]. In particular, the gamma-ray spectrum for ^{60}Fe has only recently been observed [67], making it an ideal check and compliment to current studies of ^{26}Al.

6.2 Production of ^{60}Fe

With a half-life of about 2.62 million years [65], ^{60}Fe is thought to be produced via successive neutron captures from stable forms of iron as seen in Figure 6.1. ^{60}Fe is therefore synthesized in neutron-rich environments such as those reached during core He and C shell burning [68]. It appears as if ^{60}Fe is created in massive stars ($M_{\odot} > 12$ solar masses) just before or during their transition into core collapse supernovae [69]. In addition, it is also possible that ^{60}Fe is synthesized in large amounts in rare sub-types of Type Ia supernovae [70].

In massive stars, stellar nucleosynthesis requires a neutron-rich environment and temperatures at or below about 2 gigakelvin (GK). Above this temperature, the cross-sections of both the ^{59,60}Fe(γ,n) and ^{59,60}Fe(γ,p) reactions increase dramatically [71]. Different models

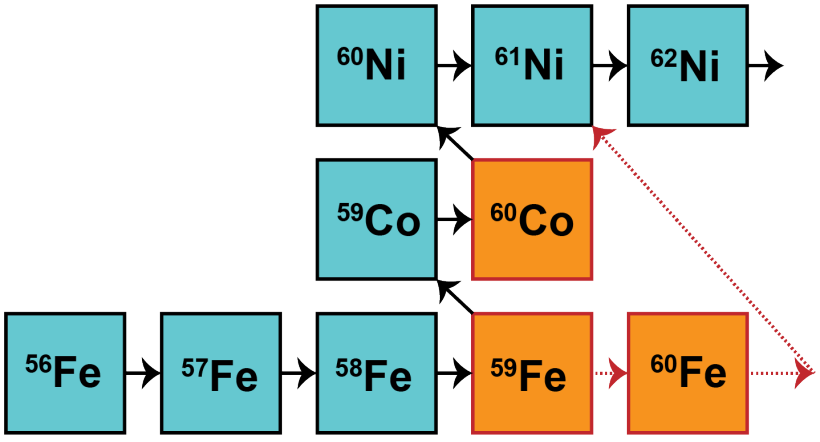

Figure 6.1: Stellar production of ^{60}Fe. This plots shows production of ^{60}Fe from stable forms of iron. Also, the branching point for the s-process at ^{59}Fe is clearly seen here.

disagree on the specifics of production methods of ^{60}Fe. For example, one model propose that burning is limited primarily to the He and C shell phases. For smaller stars ($M_{\odot} < 40$ solar masses), the higher temperatures in C shell burning allow for production of α-particles. These α-particles are the catalyst for the ^{22}Ne(α,n)^{25}Mg reaction, resulting in a higher free neutron flux and a decent yield of ^{60}Fe. In larger stars, the production of ^{60}Fe occurs in the He shell burning phase [64]. However, another model suggests relatively little production of the isotope in larger stars ($M_{\odot} > 25$ solar masses).

Core collapse supernovae present one final opportunity for the production of ^{60}Fe as the blast wave crosses the mantle of the star during the explosion. According to models, supernovae with peak temperatures around 2.2 GK can foster production of ^{60}Fe from local abundances of ^{20}Ne, ^{12}C, ^{23}Na, and ^{22}Ne left by the last C shell burning phase [71]. Some models suggest that, in most forms of core collapse supernovae, the yield from explosive nucleosynthesis is roughly in the 1×10^{-5} to 4×10^{-5} $M_{\odot}$ range. Type II and some rarer Type Ia supernovae, however, could produce yields of ^{60}Fe at almost 100 times that rate [70, 72].

6.3 Astrophysical Relevance

Given the unique stages of star's life cycle in which ^{60}Fe is produced, this isotope provides insight into a number of different facets of stellar evolution and even the dynamics of large star clusters. As noted previously, the gamma-ray emission of ^{60}Fe serves as a powerful astrophysical tool. The gamma-ray lines emerge from the decay of ^{60}Fe's short-lived daughter nucleus ^{60}Co, a cascade of two gamma rays at 1172.9 and 1332.5 keV as seen in Figure 6.2. These two gammas occur with nearly equal intensities, making them prime targets for observation [73]. Gamma rays are obscured while the ^{60}Fe nucleus is buried deep in the core of a star during stellar nucleosynthesis. Gamma-ray photons can only be observed after a supernova or once the ^{60}Fe has been ejected into the interstellar medium. In the case of observation directly after a supernova, these lines are seen as relatively strong characteristic gamma-rays and can be used to estimate the number of supernovae occurring in a particular

region [64] as well as verify our stellar-mass averaged predicted yields from models of massive star evolution and nucleosynthesis [73].

Given its long half-life, detecting gamma rays from diffuse ^{60}Fe in the Galaxy shows that stellar nucleosynthesis is ongoing in the Universe and invites comparison to diffuse ^{26}Al emission. The commensurate half-life of ^{26}Al as well as its similar production sites, namely massive stars and supernovae, allows the ratio of gamma-ray emissions from the two radioactive isotopes to be compared directly. Observing this ratio allows us to glean new information about the stellar environments that produce ^{60}Fe and act as a significant constraint on massive-star models as a whole, including their stellar structure, nucleosynthesis, and their transition towards supernovae [73].

Sampling the amount of ^{60}Fe deposited by galactic cosmic rays provides additional insight into stellar and explosive nucleosynthesis. Since any deposited ^{60}Fe would most likely come from the core of the star, its ratios to commonly-produced stable iron isotopes reveal details about the time between ^{60}Fe's synthesis and ejection [65]. This feature makes ^{60}Fe a nucleosynthesis-clock isotope for timing the difference between synthesis and expulsion.

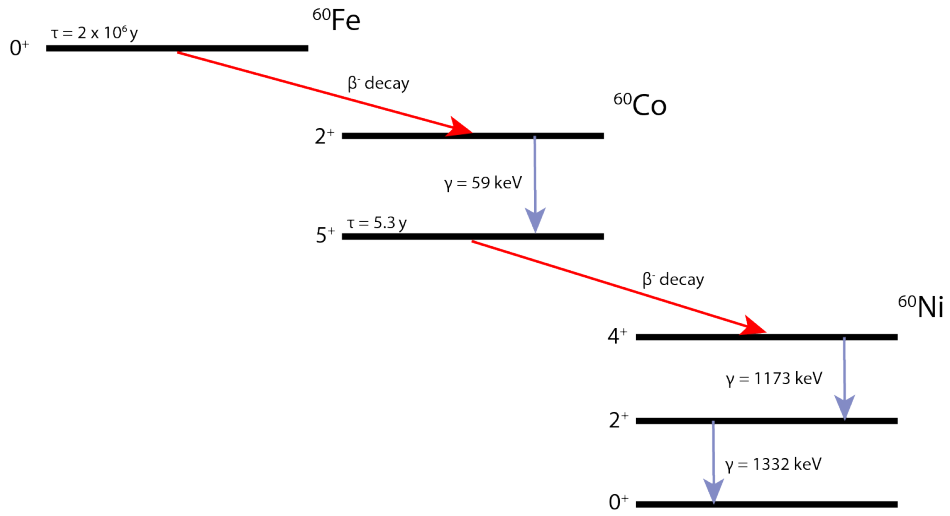

Figure 6.2: Decay of ^{60}Fe, specifically highlighting the gamma-ray cascade during the transition to ^{60}Ni. The 59 keV transition only occurs at about 2% the rate of the 1173 keV and 1332 keV transitions.

Additionally, by looking at this ratio in deep sea ferromanganese crusts and lunar samples, information about specific supernova activity in our local Galactic neighborhood can be inferred [66]. These data are complementary to other methods of determining supernovae rates and acts as a check on rates determined by other astrophysical measurements. Specific results from recent experiments utilizing these techniques are described in further detail in the following subsections.

6.3.1 Gamma-Ray Spectroscopy

It is only recently that detectors with the appropriate sensitivity have been capable of making precise measurements of gamma rays emitted by ^{60}Fe in the interstellar medium. While these photons have been seen in experiments from as early as 1982, their sensitivity has been so low as to only place rough upper limits on the ratio of ^{60}Fe/^{26}Al based on relatively small statistics. A current study was performed on the SPI spectrometer aboard the ESA's INTEGRAL spacecraft. Consisting of 19 germanium detectors with active BGO shielding, the SPI spectrometer is currently in a high-eccentricity orbit around Earth in order to avoid local radiation belts and minimize background for the spectrometer. The detector itself is sensitive to photons between 15 keV and 8 MeV with about 3 degrees of angular resolution. Analyzing 2.5 years worth of data has allowed for confirmation of a ^{60}Fe signal at 4.9σ [74].

In order to make any conclusions about the significance of these signals, the researchers made the simplifying assumption that the distribution of ^{60}Fe in the Galaxy is similar to the distribution of ^{26}Al. Given their similar production sites and commensurate half-life, this assumption is a relatively reasonable one to make. That considered, a flux ratio of ^{60}Fe/^{26}Al was found to be $(14.8 \pm 6.0)\%$ [74]. This agrees with recent theoretical limits on this ratio that, using a standard stellar-mass distribution function, placed the ratio at $(18.5 \pm 6.25)\%$ [71]. Furthermore, the study focused specifically on observations of the Cygnus and Vela regions in an attempt to better understand variations in the distribution of ^{60}Fe throughout the Galaxy. While the study did not identify significant signals of ^{60}Fe

in these regions, further studies continue to search for signals using newer datasets collected by SPI/INTEGRAL [74].

Further improvements can be made to the detectors themselves. The germanium detectors in SPI have experienced damage over their years in space as they are continually bombarded by cosmic rays. Thermal annealing of the germanium detectors allows temporary restoration of the detector's sensitivity, but the next generation of gamma-ray telescopes should improve sensitivities and spatial resolution such that a better understanding of the distribution of ^{60}Fe can be developed [64].

6.3.2 Galactic Cosmic Rays

Galactic cosmic rays present a unique opportunity to measure the local distribution of ^{60}Fe close to earth. Consisting of nuclei accelerated to nearly the speed of light by supernovae and solar winds, galactic cosmic rays generally originate from within our Galaxy. Their elemental makeup and intrinsic energy depend upon their origin and the manner of their acceleration. Several methods have been leveraged to derive properties of local supernovae and massive stars utilizing ^{60}Fe galactic cosmic rays.

6.3.2.1 Satellite Observatories

The Cosmic Ray Isotope Spectrometer (CRIS) was launched aboard NASA's ACE spacecraft in 1997. CRIS consists of a scintillating fiber hodoscope to gather particle trajectory information as well as four stacks of silicon solid state detectors to measure the energy loss of the cosmic rays and total energy deposited into the detector. This allows for the measurement of a given particle's mass, charge, and energy per nucleon. In this way, the detector can effectively perform particle identification on individual cosmic rays. This can be seen in Figure 6.3 as a classic cross plot of the energy loss versus the energy deposition.

The data, collected over the course of 17 years, allows for calculation of the ratio between ^{60}Fe to other iron isotopes. This ratio, namely ^{60}Fe/^{56}Fe, allows for estimates of the time between nucleosynthesis and acceleration out of the star. Given a number of uncertainties,

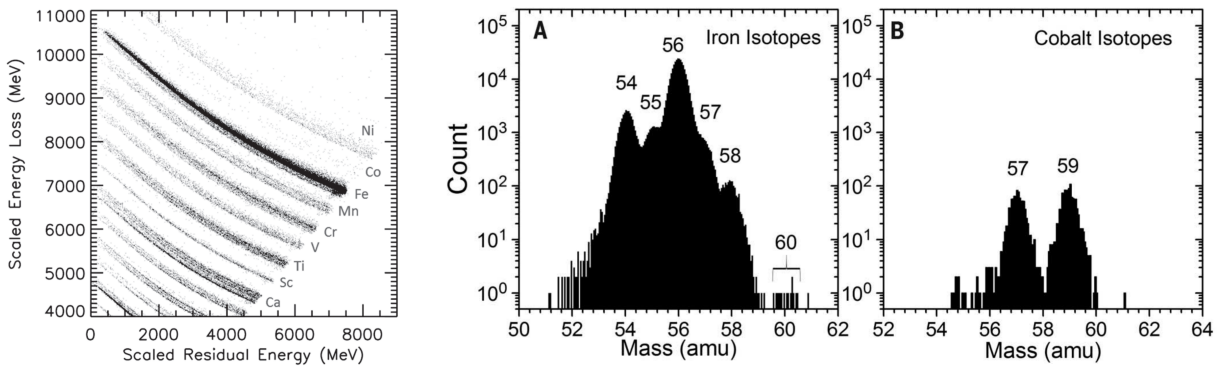

Figure 6.3: Satellite observations of ^{60}Fe. (*LEFT*) A cross plot of the energy loss versus the total energy deposited in the detector. These bands correspond to individual elements between and including Calcium and Nickel, and some separation between different isotopes can even be seen. (*CENTER and RIGHT*) Iron and Cobalt mass histograms from the data collected by CRIS. This data is then used to calculate isotopic ratios. Reprinted with permission from [65].

this is a difficult metric to accurately calculate, but recent work finds a mean time between nucleosynthesis and acceleration to be 10^5 years. Additionally, this work places an upper limit on the distance between Earth and the production sites of ^{60}Fe to within a spherical volume with a radius of 620 parsecs. There are more than 20 localized groups of stars within this range that could contribute to the ^{60}Fe observed by CRIS [65].

6.3.2.2 Terrestrial and Extraterrestrial Deposition

^{60}Fe deposited in deep sea sediment and ferromanganese crusts provides a time line for near-Earth supernova activity spanning millions of years. A global survey of these sediments and crusts reveals that an appreciable accumulation of the radioactive isotope. Using the samples' ^{10}Be and ^{26}Al content, researchers determined their age using accelerator mass spectrometry. Collectively the samples span a time period dating back over 10 million years with time resolutions varying from 30,000 years to 2 million years depending on the individual sample [66].

The samples yield significant amounts of ^{60}Fe with their influx localized to between 1.5-3.2 and 6.5-8.7 million years ago. These localized influxes imply a series of supernovae

fronts hitting the Earth in quick succession. The current rate of supernovae in our local Galactic neighborhood within about 100 parsecs, currently estimated at one event per every 2-4 million years, stands at odds with these observations. The data collected from these samples would suggest a rate of two to three supernova per million years, assuming a diffuse distribution of ^{60}Fe. However, the possibility also exists that higher concentrations of ^{60}Fe came to rest in the interstellar medium only to be accelerated by a common driver, such as an expanding superbubble shell driven by supernovae and solar winds from massive stars [66]. Regardless, this data indicates ongoing nucleosynthesis and widespread massive-star ejections in our local Galaxy.

These results are supported by another study performed on samples of lunar material taken during the Apollo missions. The samples, collected during the Apollo 12, 15, and 16 missions, vary from surface samples to core samples from up to 15 cm below the surface. Using a similar accelerator mass spectrometry analysis method to the Wallner *et al* study, concentrations of ^{60}Fe were detected at levels an order of magnitude higher than predicted by calculations [75]. These enhanced levels appear to confirm the time localized, elevated levels observed in the Wallner *et al* study and generally support the time line put forward by that work.

6.4 Experimental Determination of ^{59}Fe(n,γ)^{60}Fe

As the previous sections outline, ^{60}Fe plays an important role in a number of astrophysical processes; however, a number of uncertainties exist that limit our ability to precisely determine some of these processes. A paper by Jones *et al* reviews the bulk of these existing uncertainties in exhaustive detail, however they find that reaction rates have some of the most profound effects on the final yield of ^{60}Fe. Based on simulations, the yields scale monotonically with the reaction rates. This means if the uncertainty on the reaction rate of ^{59}Fe(n,γ)^{60}Fe spans two orders of magnitude, the expected yields of ^{60}Fe share that same uncertainty [69]. This can be seen in Figure 6.4.

The reason this reaction rate creates so much uncertainty stems from the fact that ^{60}Fe is

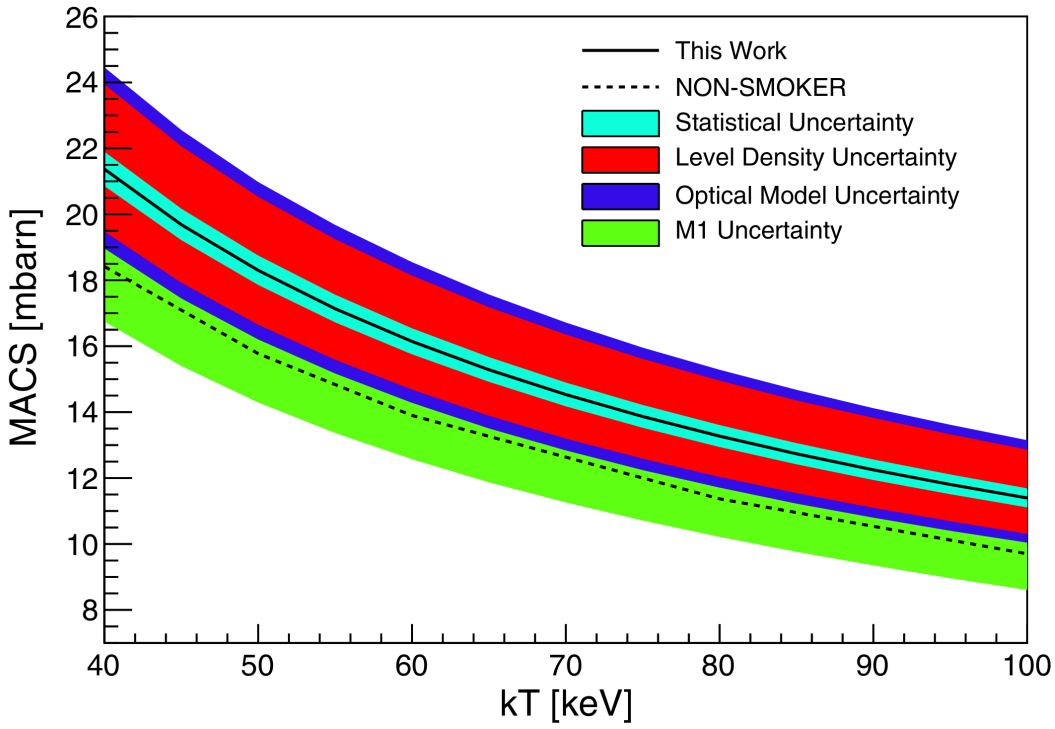

Figure 6.4: The Maxwellian averaged cross-section and its uncertainties determined from the Coulomb dissociation of ^{60}Fe. Reprinted with permission from [76].

the product of a branching point in the s-process (see Figure 6.1). The s-process begins during core He burning and then occurs again during C shell burning, the same burning phases important to nucleosynthesis of ^{60}Fe. The s-process path to ^{60}Fe depends on a branch point at the relatively short-lived ^{59}Fe nucleus. At lower neutron densities in He shell burning, the β-decay of ^{59}Fe dominates the transition and limits the amount of ^{60}Fe produced. Stepping to the higher temperatures and neutron densities of C shell burning allows the ^{59}Fe(n,γ)^{60}Fe reaction to become effective [68]. ^{60}Fe can also be destroyed via the ^{60}Fe(n,γ)^{61}Fe reaction, making this an important rate for predicting the overall abundance of ^{60}Fe during nucleosynthesis.

Two experiments probing the ^{59}Fe(n,γ)^{60}Fe and the ^{60}Fe(n,γ)^{61}Fe reaction rates have been performed in the past decade. Utilizing the Karlsruhe Van de Graaff accelerator to generate a quasistellar neutron spectrum, a measurement of the ^{60}Fe(n,γ)^{61}Fe reaction at relevant core

He-burning stellar temperatures was made. This resulted in an increase of the Maxwellian-averaged cross-section (MACS) by roughly a factor of two ($\sigma = 9.9 \pm^{2.8\ (\mathrm{syst})}_{1.4\ (\mathrm{stat})}$ for $kT = 25$ keV) [68]. A second study indirectly measured the ^{59}Fe(n,γ)^{60}Fe via the Coulomb dissociation of ^{60}Fe. The experiment, performed at the GSI Helmholtzzentrum für Schwerionenforschung in Darmstadt, Germany, created ^{60}Fe fragments and measured the time-reversed photodissociation reaction ^{60}Fe(γ,n)^{59}Fe. A Maxwellian averaged cross-section determined for the reaction and the results, shown in Figure 6.4, indicate that current theoretical estimates of the reaction rate are reasonable but serves to highlight the inherent uncertainties in these estimates. The researchers specifically indicate the need for further constraints on the photon strength function of the ^{59}Fe(n,γ)^{60}Fe reaction rate to reduce a major component of uncertainty [76].

6.4.1 Photon Strength Function of ^{58}Fe

A direct measurement of the ^{59}Fe(n,γ)^{60}Fe reaction cannot be easily made due to the difficulty of producing a ^{59}Fe target for a spallation neutron source. Additionally, even though rare isotope beams of ^{59}Fe can be produced with sufficient intensity, no facility is currently capable of creating a neutron target, and measurements using a neutron time-of-flight technique are impractical [77]. However, the reaction rate can be probed indirectly using a surrogate reaction. Using this technique and the ^{59}Fe(d,p)^{60}Fe reaction, the photon strength function can be constrained. The photon strength function, also described Chapter 7, governs the theoretical reaction rate and therefore will also constrain theoretical estimates of the ^{59}Fe(n,γ)^{60}Fe reaction rate.

Work is currently ongoing to benchmark this technique using the ^{57}Fe(n,γ)^{58}Fe and ^{57}Fe(d,p)^{58}Fe reactions. The ^{57}Fe(n,γ)^{58}Fe reaction has already been measured at the Los Alamos Neutron Science Center and the analysis of that data is the subject of Chapter 9. The ^{57}Fe(d,p)^{58}Fe reaction will be measured in late 2020 using a new detector array designed and built at the Cyclotron Institute as part of its collaboration with Los Alamos National Laboratory under the Center for Excellence in Nuclear Training and University Research

(CENTAUR) grant.

6.4.1.1 Nuclear Structure Considerations

A significant enhancement in the low-energy region of the photon strength function was observed in ^{56,57}Fe in 2004 [78]. This low-energy enhancement, or upbend, has been confirmed in iron by other methods [79], and also observed in other nuclei including some rare-earth elements [80, 81]. If the upbend is present in nuclei approaching the neutron drip line, it could have a significant effect on the neutron-capture cross section, increasing (n,γ) reaction rates by up to two orders of magnitude [82]. While ^{58}Fe is still a stable isotope, constraining its photon strength function and determining if this low-energy enhancement is present will have the added benefit of indicating how this enhancement evolves with changing nuclear structure. In addition, different techniques for determining the photon strength function have yielded different results. Ensuring that neutron transfer and neutron capture obtain similar results is an important step in affirming the assumptions made for compound nuclei. These observations, when incorporated with other nuclear data, this information can help inform our understanding of the behavior of the photon strength function in neutron-rich nuclei.

7. THEORY OF THE PHOTON STRENGTH FUNCTION

7.1 Theoretical Overview

This chapter discusses the general principles of the statistical nucleus, and how capture reactions in the statistical regime differ from reactions that capture into discrete, resolved states. The photon strength function is discussed in some detail, as well as nuclear level densities. Various models of both of these quantities are presented to lend context to the simulation work presented in Chatper 9.

7.2 The Statistical Model of the Nucleus

Chapter 3 laid out the principles of reaction cross sections in the region of well-separated resonances. However, as the resonance energy in a nucleus increases, individual energy levels tend to get closer together. This trend continues with increasing energy until many resonances start to completely overlap and the average cross section begins to vary smoothly with energy. In this energy regime, the narrow-resonance treatment begins to break down and a statistical model of the nucleus becomes necessary.

It was Bohr who first proposed the concept of a compound nucleus, treating reactions as many-body processes involving an intermediate stage [31]. In addition, Bohr hypothesized that the decay of the compound nucleus was independent of the method of formation. While this property was intended to only apply to isolated resonances in the compound nucleus, it was expected that the behavior would extend to compound states in the continuum. This expectation came from the idea that the compound nucleus did not decay very quickly after its formation, giving enough time for the excitation energy to be distributed over many degrees of freedom. In other words, the compound nucleus had time to reach a sort of thermodynamic equilibrium before decaying. These assumptions were important in developing Hauser-Feshbach theory, described in detail below.

7.2.1 Hauser Feshbach Theory

From Bohr's independence hypothesis, a compound reaction cross section consisting of a formation channel α and a decay channel α' can be written as

$$\sigma_{re}(\alpha, \alpha') = \sigma_{\alpha} P_{\alpha'} \,, \tag{7.1}$$

where σ_{α} is the cross section of the entrance channel, $P_{\alpha'}$ is the probability for the decay of the compound nucleus to proceed via channel α', and the spins of the particles are momentarily ignored. Each formation and decay channel is composed of a particle pair. In the case of the entrance channel, this would be the incident particle and the compound nucleus. For the decay channel, the particle pair would be composed of the compound nucleus and the decay particle. The reciprocity theorem dictates that the reaction width of the (α, α') reaction is related to its inverse such that

$$k_{\alpha}^2 \sigma_{re}(\alpha, \alpha') = k_{\alpha'}^2 \sigma_{re}(\alpha', \alpha) \,, \tag{7.2}$$

where, for a selected channel i, k_i is the wave number of the particle pair. Applying the independence hypothesis to Equation 7.2 and rearranging the result yields the relation

$$\frac{k_{\alpha}^2 \sigma_{\alpha}}{P_{\alpha}} = \frac{k_{\alpha'}^2 \sigma_{\alpha'}}{P_{\alpha'}} \,. \tag{7.3}$$

Clearly the two sides of this equation are independent from one-another; however, this considers only one entrance channel and one decay channel.

Extension into the continuum region requires averaging over all the resonance structure such that

$$\langle \sigma_{re}(\alpha, \alpha') \rangle = \sum_{J\pi} \langle \sigma_{re}(\alpha, \alpha') \rangle^{J\pi} \,, \tag{7.4}$$

where J is the total angular momentum and π is the parity of each resonance over which

the cross section is averaged. From this, each individual resonance can be separated into the cross section for formation of a compound nucleus C from entrance channel α multiplied by the branching ratio for the decay of the compound nucleus through channel α', given as

$$\langle \sigma_{re}(\alpha, \alpha') \rangle^{J\pi} = \sigma_{\alpha C}^{J\pi} \frac{P_{\alpha'}^{J\pi}}{\sum\limits_{\alpha''} P_{\alpha''}^{J\pi}} \,. \tag{7.5}$$

Here, the $\sum\limits_{\alpha''} P_{\alpha''}^{J\pi}$ represents the summation over all possible decay channels of the compound nucleus and therefore is equal to unity. Using the reciprocity theorem once more and rearranging similar to Equation 7.3 yields

$$\frac{(2I_1+1)(2I_2+1)k_\alpha^2 \sigma_{\alpha C}^{J\pi}}{P_\alpha^{J\pi}} = \frac{(2I_1'+1)(2I_2'+1)k_{\alpha'}^2 \sigma_{\alpha' C}^{J\pi}}{P_{\alpha'}^{J\pi}} \,, \tag{7.6}$$

where I_1 and I_2 are the spins of the particles in a given channel. From this, summing over all the available decay channels provides the relationship

$$P_{\alpha'}^{J\pi} = \frac{(2I_1'+1)(2I_2'+1)k_{\alpha'}^2 \sigma_{\alpha' C}^{J\pi}}{(2I_1''+1)(2I_2''+1)k_{\alpha''}^2 \sigma_{\alpha'' C}^{J\pi}} \,. \tag{7.7}$$

For the cross section of the formation of the compound nucleus, a generalized transmission coefficient from continuum theory can be used and the cross section can be written as

$$\sigma_{\alpha C} = \sum_{J\pi} \sigma_{\alpha C}^{J\pi} \tag{7.8}$$

$$= \frac{\pi}{k_\alpha^2} \sum_\ell (2\ell+1) \hat{T}_\ell(\alpha) \,, \tag{7.9}$$

where ℓ is the orbital angular momentum, and $\hat{T}_\ell(\alpha)$ is the transmission coefficient for channel α and orbital angular momentum ℓ. Averaged over many resonances, the transmission coefficient will not have a dependence on J. This means Equation 7.9 can be rewritten for

a specific spin and parity as

$$\sigma_{\alpha C}^{J\pi} = \frac{\pi}{k_\alpha^2} \frac{2J+1}{(2I_1+1)(2I_2+1)} \sum_{s=|I_1-I_2|}^{I_1+I_2} \sum_{\ell=|J-s|}^{J+s} \hat{T}_\ell(\alpha)\,. \tag{7.10}$$

Now, from Equations 7.4, 7.5, 7.7, and 7.10, a final expression for the average cross section can be written as

$$\langle \sigma_{re}(\alpha,\alpha') \rangle = \frac{\pi}{k_\alpha^2} \sum_{J\pi} \frac{2J+1}{(2I_1+1)(2I_2+1)} \frac{\left[\sum_{s\ell} \hat{T}_\ell(\alpha)\right]\left[\sum_{s'\ell'} \hat{T}_{\ell'}(\alpha')\right]}{\sum_{\alpha''}\sum_{s''\ell''} \hat{T}_{\ell''}(\alpha'')}\,. \tag{7.11}$$

This equation is the Hauser-Feshbach formula for an energy-averaged cross section in the continuum region [29]. The sums for J, π, ℓ, and s are assumed to run over all values allowed by selection rules. For the specific case of neutron capture, the transmission coefficient $T_\ell(\alpha)$ can be calculated using the optical model. The gamma-decay channel $T_{\ell'}(\alpha')$, however, is given by the transmission function

$$T(E_\gamma) = 2\pi E_\gamma^{2L+1} f^{XL}(E_\gamma)\,. \tag{7.12}$$

Here, E_γ is the gamma energy, XL is the multipolarity type, and f_{XL} is the photon strength function, which will be discussed in the next section.

7.3 The Photon Strength Function

Functionally, the photon strength function is a statistical quantity that describes the γ-decay properties of excited nuclei [83]. While it is known that the electromagnetic transmission probability generally goes as E_γ^{2L+1}, it can be experimentally probed by considering it as a component of the photon strength function

$$f^{XL}(E_\gamma) = \frac{\langle \Gamma^{XL}(E_\gamma) \rangle}{E_\gamma^{2L+1}} \rho(E_\gamma, J)\,, \tag{7.13}$$

where Γ^{XL} is the transmission probability of a given multipole transition, ρ is the nuclear level density. Broadly speaking, the photon strength function can be viewed as the probability a gamma-ray with energy E_γ will be emitted from the nucleus.

The average widths for different multipolarities were first estimated by Blatt and Weisskopf using a single-particle model [84]. To accomplish this, a uniform distribution of gamma-ray strength was assumed across resonances, resulting in the relation

$$\langle \Gamma^{XL} \rangle = \Gamma^{XL}_{sp} \frac{D}{D_0}\,, \tag{7.14}$$

where D is the average level spacing for resonances with similar spins and parities, D_0 is the average spacing of s-wave resonances, and Γ^{XL}_{sp} is the single-particle estimate of the gamma partial width for a given transition. Omitting the spin statistical factors, estimates for the first three multipolarities can therefore be given by

$$\langle \Gamma^{E1}_{sp} \rangle = 8.9 \times 10^{-2} A^{2/3} E_\gamma^3 \frac{D(E)}{D_0} \tag{7.15}$$

$$\langle \Gamma^{M1}_{sp} \rangle = 2.1 \times 10^{-2} E_\gamma^3 \frac{D(E)}{D_0} \tag{7.16}$$

$$\langle \Gamma^{E2}_{sp} \rangle = 7.9 \times 10^{-8} A^{4/3} E_\gamma^5 \frac{D(E)}{D_0}\,, \tag{7.17}$$

where the numerical constants are based on a nuclear radius of $R = 1.35A^{1/3}$, a neutron effective charge of $\bar{e} = -e\frac{Z}{A}$, and a radial overlap integral approximated by $I_L \approx \frac{3R^L}{L+3}$ where L is the multipolarity of the gamma-ray [85]. From these estimates, reduced photon strength functions for the E1 and M1 transition can be given as

$$\langle k_{E1} \rangle = \frac{\langle \Gamma^{E1}_{sp} \rangle}{E_\gamma^3 A^{2/3} D} \tag{7.18}$$

$$\langle k_{M1} \rangle = \frac{\langle \Gamma^{M1}_{sp} \rangle}{E_\gamma^3 D}\,. \tag{7.19}$$

These reduced photon strength functions only begin to agree with experimental data when

$D_0 \approx 15$ MeV [85]. This value for D_0 is over an order of magnitude larger than the actual single-particle spacing of $0.5 - 1$ MeV. Generally, this is accepted to be a reflection of the fact that the Weisskopf estimates overestimate the transition strengths due to some of their fundamental assumptions. In practice, D_0 is used as an adjustable parameter to fit to experimental values [85].

A number of different phenomenological models have been developed for different multipolarities. Generally, transitions within the compound nucleus of multipolarities higher than E2 are fairly rare, as the E^{2L+1} term from Equation 7.13 significantly suppresses the strength. As such, only E1, M1, and E2 transitions are considered and the following subsections consider a few of the models utilized by this work.

7.3.1 E1 Strength Function

One model of the E1 strength approaches the electric dipole as analogous to the giant dipole resonance (GDR) found in photonuclear reaction data. Comparisons with experimental data from photonuclear reactions show that the GDR is well-approximated by a Lorentzian function, such that the cross section is given as

$$\sigma(E) = \frac{\sigma_G E^2 \Gamma_G^2}{(E^2 - E_G^2)^2 + E^2 \Gamma_G^2}\,, \tag{7.20}$$

where σ_G, E_G, and Γ_G are the cross section, peak position, and FWHM of the GDR, respectively.

In his 1955 dissertation, Brink hypothesized that the GDR is independent of the initial excitation of the nucleus [86]. This implied that the gamma absorption cross section depended only on the energy of the photon, which allowed Axel to derive the photon strength function for the electric dipole by invoking the detailed balance principle [87]. The strength is given by the equation

$$f_{SLO}^{E1}(E_\gamma) = \frac{1}{3(\pi c\hbar)^2} \frac{\sigma_G E^2 \Gamma_G^2}{(E^2 - E_G^2)^2 + E^2 \Gamma_G^2}\,, \tag{7.21}$$

where σ_G, E_G, and Γ_G are the same as above. This model is often referred to as the Standard Lorentzian (SLO). While this model successfully reproduces behaviors observed in medium and heavy nuclei, it begins to fall apart at energies below 2 MeV or energies close to the neutron separation energy.

In an attempt to better model the electric dipole strength function at low energies, Kadmenskii, Markushev, and Furman developed a photon strength function based on the Fermi liquid model [88]. This model is notable for the fact that it produces a non-zero value as the gamma energy approaches zero. Assuming a spherical nucleus, the strength function is given as

$$f^{E1}_{KMF}(E_\gamma, T) = \frac{F_K}{3(\pi c\hbar)^2} \frac{\sigma_G E_G \Gamma_G \Gamma^T_G(E_\gamma, T)}{(E^2 - E^2_G)^2}\,, \tag{7.22}$$

where F_K is approximated as $F_K = 0.7$ and $\Gamma^T_G(E_\gamma, T)$ is the giant electric dipole resonance damping width given by

$$\Gamma^T_G(E_\gamma, T) = \Gamma_G \frac{E^2_\gamma + 4\pi^2 T^2}{E^2_G}\,. \tag{7.23}$$

In both of these equations the temperature T is taken to be

$$T(E_x) = \sqrt{(E_x - E_P)/a}\,, \tag{7.24}$$

where E_x is the difference in energy between the initial and final state and E_P is the pairing energy. This model more accurately reproduces experimentally observed E1 transitions at low energies; however, like the standard Lorentzian, it fails to accurately describe transitions near the neutron separation energy [89].

The Phenomenological Generalized Lorentzian (GLO) model combines a Lorentzian with the non-zero limit at low gamma energies of the KMF model. The functional form of this model is given by

$$f^{E1}_{GLO}(E_\gamma, T) = \frac{\sigma_G \Gamma_G}{3(\pi c\hbar)^2} \left[\frac{E_\gamma \Gamma_G \Gamma^T_G(E_\gamma, T)}{(E^2 - E^2_G)^2 + E^2_\gamma (\Gamma^T_G(E_\gamma, T))^2} + F_K \frac{4\pi^2 T^2 \Gamma^T_G(E_\gamma = 0, T)}{E^5_G} \right], \tag{7.25}$$

where $\Gamma_G^T(E_\gamma, T)$ and T are as given above. This model performs well for some spherical nuclei [90].

7.3.2 M1 Strength Function

The M1 transition is roughly 1/7 the intensity of the E1 strength and therefore has a smaller contribution to the electromagnetic transition. The simplest model of the M1 strength function is given by its single-particle strength, given by

$$f^{M1} = k_{M1} \tag{7.26}$$

where the constant k_{M1} is chosen for the nucleus of interest. Most M1 strength functions include a magnetic dipole at about 9 MeV.

Over the past two decades, evidence has arisen that the M1 strength plays a role in a low energy enhancement of the photon strength function for certain nuclei. Studies in iron have shown that adding a small M1 scissors mode to the strength function improves the prediction of neutron capture cross section for deformed nuclei [91]. To model this, the M1 strength is taken to be a standard Lorentzian shape such that the strength function is given as

$$f_{SLO}^{M1}(E_\gamma) = \frac{1}{3(\pi\hbar c)^2} \frac{\sigma_M E_\gamma \Gamma_M^2}{(E_\gamma^2 - E_M^2)^2 + E_\gamma^2 \Gamma_M^2}\,, \tag{7.27}$$

where the parameters E_M, Γ_M, and σ_M are the maximum values of the energy, partial width, and cross section of a chosen resonance. Typical E_M values are roughly 2-3 MeV. This model is also used for spin-flip nuclei and conforms to the Brink hypothesis.

7.3.3 E2 Strength Function

This work assumes all E2 transitions are given by their single-particle strength. This means that E2 transitions are taken to be energy-independent constant. The strength function is given by

$$f^{E2} = k_{E2} \tag{7.28}$$

where the constant k_{E2} is chosen for the nucleus of interest.

7.4 Nuclear Level Density

As discussed earlier in the chapter, as the resonance energy in a nucleus increases, individual resonances get closer together until they begin to overlap completely. Modeling the change in the density of states as a function of energy can be fairly difficult. Nuclear models can accurately reproduce low-lying energy levels and densities; however, at higher excitation energies a statistical treatment becomes more appropriate. Early attempts to model this behavior in heavy nuclei treated the nucleus as a Fermi gas, which approximated the nuclear level density to be

$$\rho(E) = \frac{e^{\sqrt{4aE}}}{12a^{1/4}E^{5/4}}\,. \tag{7.29}$$

Here, a is the nuclear level density parameter. However, this model fails to account for the fact that the nucleus is composed of two different nucleons, each of which form pairs with themselves.

To compensate for this pairing effect, the Back-Shifted Fermi Gas (BSFG) was developed. This model addressed odd-even effects by including the energy required to separate pairs of nucleons. The BSFG model is given by

$$\rho(E,J) = f(J)\frac{e^{\sqrt{4a(E-E_1)}}}{12\sqrt{2}a^{1/4}(E-E_1)^{5/4}}\,, \tag{7.30}$$

where a is again the level density parameter and E_1 is a back-shift representative of the energy between pairs of nucleons. The function $f(J)$ is has the form

$$f(J) = \frac{2J+1}{2\sigma^2}e^{-(J+\frac{1}{2})^2/2\sigma^2}\,, \tag{7.31}$$

where σ is the spin cut-off parameter. In this model, σ is given by the relationship

$$\sigma^2 = 0.0888A^{2/3}a^{1/2}(E-E_1)^{1/2}\,, \tag{7.32}$$

where A is the nuclear mass.

In 1965, Gilbert and Cameron introduced a phenomenological model of the nuclear level density that provided a constant nuclear temperature model at low energies and a normal Fermi gas at higher energies [92]. The Constant Temperature (CT) model used by this work is approximated by the exponential function

$$\rho(E, J) = \frac{f(J)}{T} e^{(E-E_0)/T}\,, \tag{7.33}$$

where T is the nuclear temperature and E_0 is the back-shift. Both of these parameters are meant to be adjusted to fit experimental data. The function $f(J)$ is as given above, and the value of the spin cut-off parameter for this model is typically taken to be

$$\sigma = 0.98 A^{0.29}\,. \tag{7.34}$$

8. THE DETECTOR FOR ADVANCED NEUTRON CAPTURE EXPERIMENTS

8.1 Experimental Overview

The data used in this analysis were originally taken in September 2017 using the Detector for Advanced Neutron Capture Experiments (DANCE) at the Los Alamos Neutron Science Center (LANSCE). Utilizing a linear accelerator to drive a pulsed proton beam up to 800 MeV, this high intensity beam impinges on the Lujan Center's tungsten spallation source. The water-cooled and moderated target emits a white source of spallation neutrons that can be simultaneously sent to each flight path in the Lujan Center [93]. DANCE, located on flight path 14, is a 3.6π array of 160 BaF_2 detectors arranged around a spherical ^{6}LiH shell. The ^{6}LiH shell significantly reduces background from scattered neutrons in the 10-100 keV energy regime [94]. The high solid angle coverage allows DANCE to reconstruct events with multi-step cascades of gamma rays.

For a given experimental run, a production target is placed at the center of DANCE and exposed to the neutron beam generated by the spallation source. During the 2017 experiment, the target was a roughly 130 mg sample made up of ^{57}Fe at over 95% purity. As accurate determinations of the ^{57}Fe(n,γ)^{58}Fe cross section currently exist, this experiment was optimized to measure the gamma-cascades resulting from neutron capture. The ^{6}Li and ^{235}U beam monitors will not be considered in the analysis.

8.1.1 Primary Beam Production

Primary beam production is accomplished with a three-stage linear accelerator that was formerly part of the Los Alamos Meson Physics Facility (LAMPF). Hydrogen ions are accelerated to 750 keV in one of three Cockroft-Walton generators with each generator accelerating a source of H^+, H^-, or polarized H^- respectively. Ions are then combined, pulsed, and bunched into the proper time structure for acceleration. The second acceleration stage begins when ions are injected into a drift-tube linear accelerator that accelerates both H^-

and H^+ ions to 100 MeV. This is accomplished by exploiting the opposite phases of the radio-frequency driver such that the two ions are accelerated simultaneously. The third and final stage utilizes a 48-sector side coupled cavity linear accelerator to bring the ions to a maximum energy of up to 800 MeV. This final stage delivers beam in 120 Hz macropulses 800 μs in duration, each consisting of micropulses 60 ps in duration separated by 5 ns. Each macropulse can be delivered at up to three different energies [95].

8.1.2 Neutron Production

After acceleration, the hydrogen ions intended for neutron production at the Lujan Center are then delivered to the Proton Storage Ring (PSR). The PSR bunches the 800 μs macropulses into 125 ns pulses at a rate of 20 Hz [93]. This results in approximately 1250 revolutions of the first bunch in the PSR before extraction [95]. The extracted proton beam, reaching average currents up to 135 μA, is directed towards the Manuel Lujan Jr. Neutron Scattering Center (Lujan Center) and impinged upon a water-cooled split-tungsten target with a flux trap and backscattering moderator. This allows the tungsten target to produce spallation neutrons at an extremely high peak flux. The backscattering moderator creates a white source of neutrons ranging from thermal energies up to MeV range. These neutrons are then collimated and can be delivered simultaneously to all of the 16 flight paths in the Lujan Center [93]. The Lujan Center and several of the flight paths are illustrated in Figure 8.1; however discussion will focus on flight path 14 from this point onward.

Flight path 14, seen in Figure 8.2, has a direct view of the neutron moderator below the tungsten spallation target. A shutter opens and closes to allow the beam from the moderator onto the flight path. Neutrons from the moderator are then collimated and a beam of neutrons is then delivered to the target position inside DANCE. Unreacted neutrons continue through DANCE and impinge on a beam dump at the end of the flight path.

The neutron energy is calculated from a time of flight technique. A start pulse is generated when a beam bunch is released from the PSR and a stop pulse is generated by a selected detector event. Since the time between release from the PSR and the beam's arrival at the

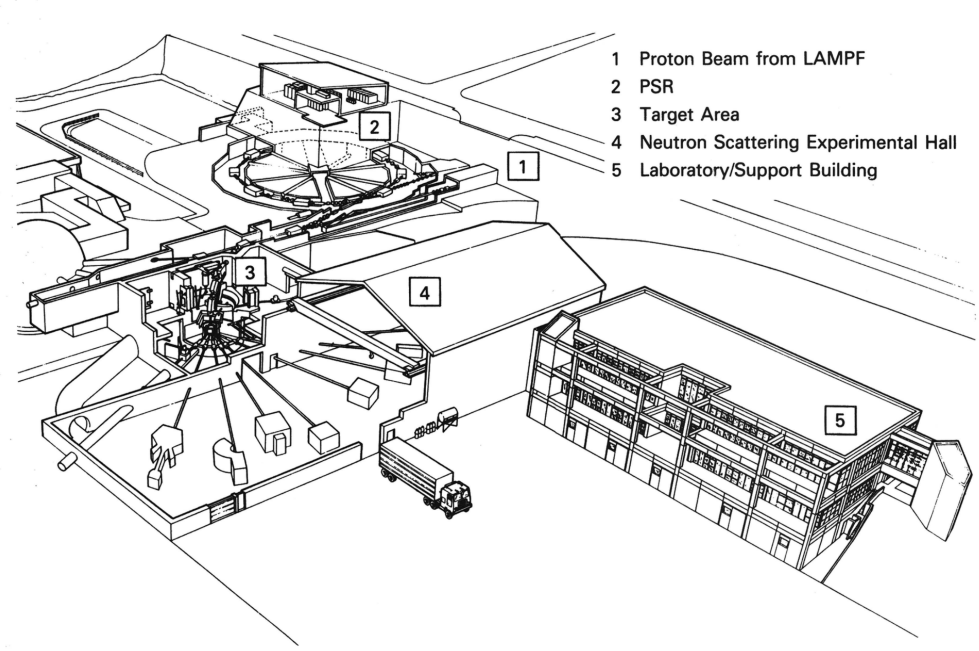

Figure 8.1: A diagram of the PSR and the LANSCE facility. Beam from LAMPF enters from the right (1), is bunched by the PSR (2), released towards the tungsten spallation target (3), and finally is collimated and delivered to the experimental flight paths (4) in the Lujan Center. Reprinted with permission from [95].

tungsten spallation target is well known, a time of flight for the neutron can be measured by taking the time between the beam release from the PSR and the detected event less the

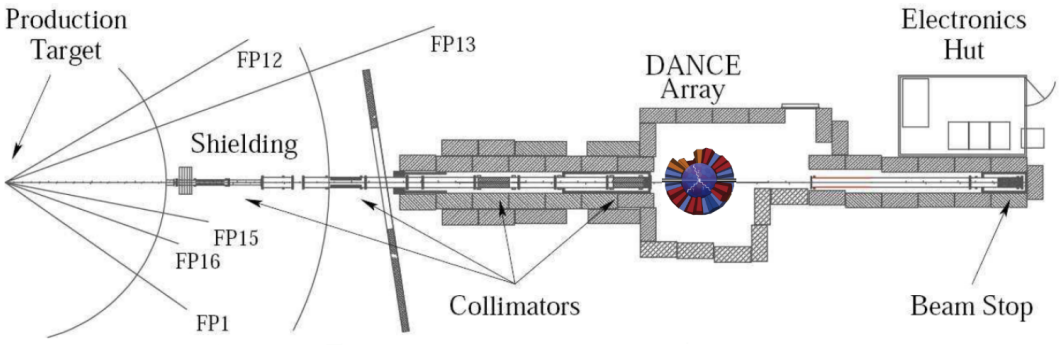

Figure 8.2: A diagram of DANCE in the Lujan Center including the shielding, shutter, and beam collimators. Reprinted with permission from [96].

time of flight between the PSR and the spallation target. For neutrons with an energy of less than about an MeV, the time of flight correlates precisely with the energy of the neutron as represented by the non-relativistic equation

$$E_n = \frac{1}{2} m_n \frac{l_{\mathrm{FP}}^2}{t_{\mathrm{TOF}}^2} \tag{8.1}$$

where E_n is the neutron energy, m_n is the neutron mass, l_{FP} is the length of the flight path, and t_{TOF} is the time of flight. The uncertainty in the neutron energy can then be obtained by propagating the error of the two measurable values, resulting in

$$\Delta E_n = 2E_n \sqrt{\left(\frac{\Delta l_{\mathrm{FP}}}{l_{\mathrm{FP}}}\right)^2 + \left(\frac{\Delta t_{\mathrm{TOF}}}{t_{\mathrm{TOF}}}\right)^2}. \tag{8.2}$$

For most neutrons, the uncertainty in the time of flight is governed primarily by the pulse width from the PSR. For thermal and epithermal neutrons, the time spread is determined by the time spent in the moderator and is given roughly by

$$\Delta t_{\mathrm{TOF}} = \frac{7.1}{\sqrt{(E_n)^{1/2}}} \quad \mu\mathrm{s}, \tag{8.3}$$

where Δt_{TOF} is the time spread for thermal neutrons [95]. A typical neutron flux is roughly proportional to $1/E_n$ for neutron energies between 1 eV and 1 MeV. This means there are approximately 3×10^5 s^{-1} neutrons per energy decade [97].

8.1.3 The Detector for Advanced Neutron Capture Experiments

The Detector for Advanced Neutron Capture Experiments (DANCE) is a 3.6π BaF_2 scintillating-crystal gamma-detector situated on flight path 14 in the Lujan Center. Pictured in Figure 8.3, DANCE is designed to perform neutron capture and fission studies on stable and radioactive targets by capturing the prompt gammas from the reactions of interest. A ^{6}LiH shell is fitted just around inner radius of the BaF_2 detectors in order to reduce the scattered neutron background. The large solid angle coverage and relatively high efficiency

of the BaF_2 detector allows DANCE to capture multi-step gamma-cascades on an event-by-event basis [94].

8.1.3.1 Barium Fluoride Detectors

DANCE is segmented into 162 separate elements with vacant positions at the beam entrance and exit, allowing up to 160 detectors to be mounted in the array. Each crystal comes in one of four different shapes such that they all pack closely together and cover the same solid angle. When assembled, the BaF_2 form a shell with an inner radius of approximately 17 cm and a thickness of 15 cm. Glued to the back of each crystal is a photomultiplier tube (PMT) that converts the scintillated photons into signals that can be measured by the data acquisition system [97].

The high level segmentation and roughly 87% detector efficiency allows for recovery of

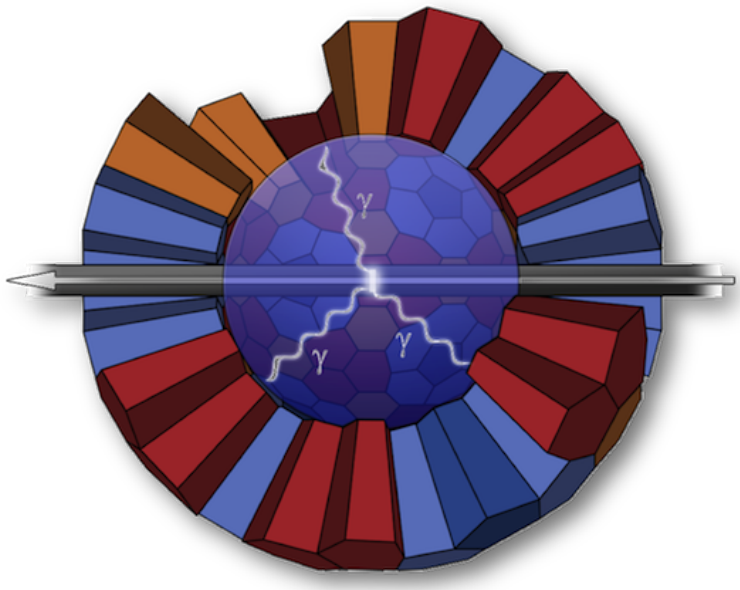

Figure 8.3: A diagram of DANCE exhibiting its closely packed BaF_2 crystals and the position of the target. The different colors represent the four different crystal shapes and the shaded sphere depicts the location of the ^{6}LiH shell. Reprinted with permission from [96].

multiple-scatter events through clusterization of the detectors as well as total energy reconstruction [97]. As a photon can Compton scatter through multiple crystals, a cluster is formed by considering all the nearest-neighbor crystals that fire and summing the captured energy in each crystal into a single cluster energy. The timing resolution of the BaF_2 detectors also allows for reconstruction of multi-step gamma-cascades, or the number of photons emitted after a given neutron capture event. The number of gammas generated by a particular event is referred to as the multiplicity. By knowing the multiplicity of the event and the clusterized energy of each emitted gamma allows for the total energy of an event to be calculated. Particular reactions can be isolated for analysis by only considering events where the total energy is equal to the Q-value of the reaction [98].

8.1.4 Beam Monitors

A neutron flux measurement is taken downstream of DANCE by one of three neutron detectors. Thermal neutrons can be detected using a ^{3}He proportional counter, while higher-energy neutrons are registered by two complementary detectors. The first is a ^{6}LiF conversion foil mounted at a 45°angle to the beam, backed by two silicon detectors placed 2 inches offset to the left and right of the beam [99]. The second, coming shortly after the silicon detector, is a ^{235}U fission chamber. As this analysis did not attempt to determine a cross-section, no neutron beam monitors were used and they will not be discussed further in this work.

8.1.5 Targets

The design of DANCE allows target cans to be inserted from the downstream of the array where they are pushed upstream in the beam pipe until they reach the center of the detector. For this experiment, two targets were used: a ^{208}Pb target and a ^{57}Fe target. The lead target was used to estimate the background scattered neutron spectrum. Since ^{208}Pb is a doubly magic nucleus, the neutron capture cross section is extremely small and no neutron resonances exist below 100 keV. This means taking data with this target inserted allows for an accurate neutron scatter background to be determined.

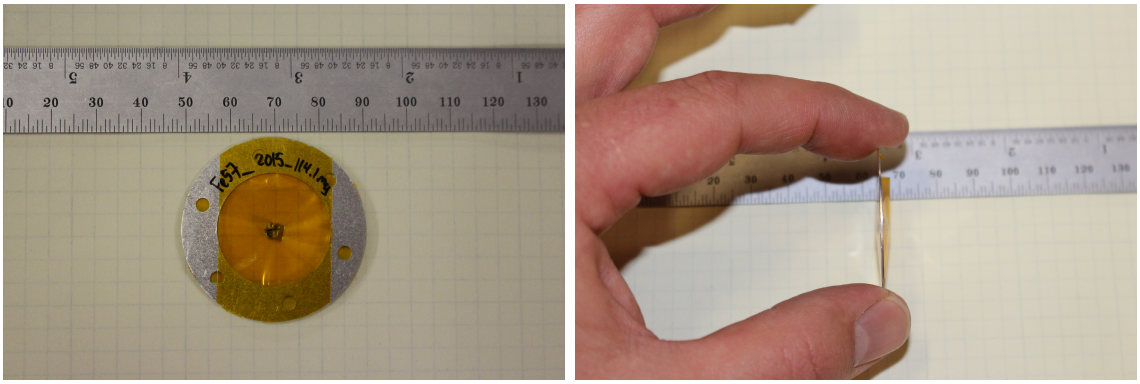

Figure 8.4: Several images of the ^{57}Fe target used during the September 2017 experimental run.

The ^{57}Fe production target was obtained from Trace Sciences in October of 2015. Its isotopic composition, outlined in detail in Table 8.1, was primarily the desired ^{57}Fe with two other isotopes of iron appearing in small relative abundance. All other contaminants were present in concentrations less than 700 ppm. About 114 mg of the material was suspended within a circular target ring by a piece of Kapton tape before it was mounted inside of DANCE. The target was never intended to be used for a cross section measurement and as such is non-uniform in nature. Pictures of the production target can be seen in Figure 8.4.

Isotope	^{54}Fe	^{56}Fe	^{57}Fe	^{58}Fe
Enrichment (%)	-	0.57	95.93	3.50

Table 8.1: Isotopic abundances of the ^{57}Fe target used during the September 2017 experimental run.

8.1.6 Data Acquisition

DANCE employs an array of CAEN VX1730 14-bit waveform digitizers to capture signals off the PMTs attached to the BaF_2 crystals. Capable of up to 500 MS/s, these digitizers are flashed with DPP-PSD firmware that allow for on-board pulse shape discrimination

and individual channel self-triggering. Captured signals are typically digitized into 40 to 48 sample waveforms that can then be accessed for later analysis, though this parameter can be modified depending on the experiment. These digitizers also read in signals from the downstream beam monitors as well as the start time from the PSR (T0), allowing for the event-by-event time of flight measurement required to determine the neutron energy [100]. Event reconstruction utilizes information from a 47-bit time stamp generated by the digitizers during data collection [99].

The acquisition system was built using the MIDAS framework, enabling online experimental control through a web-based or command line interface. The CAEN digitizers were connected to the DAQ computer using optical cables routed through a proprietary CAEN optical link PCI card. This allows for a theoretical maximum data capture of up to 3 GB/s [100]. As DANCE often sees high event rates, this allows for shorter dead times DAQ dead times.

8.2 Gamma Ray Detection

Since the basic principles of photon interactions with matter are covered in Chapter 4, this section will focus primarily on the properties and use of scintillating materials. Recapping briefly from Section 4.2.3.2, a scintillating detector utilizes a detector material that converts ionizing radiation into fluorescent photons. These photons are then measured by a PMT or other light-sensitive detector. The ideal scintillator is transparent to the wavelength of its own emitted light, has a high conversion efficiency of kinetic energy to scintillation photons, has a relatively linear conversion, and has an index of refraction close to glass [54]. Scintillating materials can be broadly broken into two categories: organic scintillators and inorganic scintillators. Organic scintillators generally have a lower conversion efficiency but are relatively fast. Inorganic scintillators typically have superior light output and energy linearity but are usually slower than organics (with some notable exceptions). Specifically for gamma detection, choosing a higher-Z material increases the likelihood of the incident gamma ray interacting with the detector material, making inorganic scintillators the preferred material

for gamma spectroscopy.

8.2.1 General Principles of Inorganic Scintillators

Inorganic scintillators are, primarily, a crystalline lattice structure similar to the materials used in the semiconductor detectors described in Chapter 4 Section 4.2.2. However, unlike in semiconductor detectors, impurities called activators are added to the crystal structure. These activators allow electrons excited into the conduction band to de-excite through the otherwise energetically-forbidden bandgap region and produce visible photons. The structure of these activators within the crystal determines the wavelength of the emitted light and the general properties of the scintillator [54].

Inorganic scintillators without activators also exist, however these materials often have a lower light output and smaller capture cross-sections than activated inorganic scintillators. Additionally, due to the larger bandgap in these materials, the wavelength of the florescence is smaller in most unactivated inorganic scintillators than it is in activated inorganic scintillators [54]. This makes certain unactivated scintillators well-suited for specialized applications.

8.2.1.1 Barium Fluoride Detectors

Barium fluoride is an unactivated inorganic scintillator with a unique decay structure that can be split into two components. The first component of the decay, the fast component, takes place in under 1 ns and results in fluorescence in the ultraviolet region of light. This fast component comes from ionizing radiation creating a hole in the outer core band of the ionic crystal and an electron from the valence band jumping up to fill the hole. The second component, the slow component, averages closer to 600 ns with generally longer wavelengths of emitted light [54]. Typically detectors consist primarily of neutron-magic ^{138}Ba due in part to its abundance relative to other barium isotopes. The total light yield for a barium fluoride detector is about 1800 photons per MeV, or roughly 20% less emitted light than that of a sodium iodide detector. However, the crystal's dense structure, fast timing, and relative insensitivity to scattered neutrons make it an ideal candidate for a gamma calorimeter in a

neutron-rich environment like the Lujan Center [94].

9. STUDY OF THE ^{57}Fe(n,γ)^{58}Fe REACTION

9.1 Analytical Overview

The following chapter describes the analysis of the ^{57}Fe(n,γ)^{58}Fe reaction data taken using the Detector for Advanced Neutron Experiments (DANCE) at the Los Alamos Neutron Science Center. As the previous chapter outlines the experimental apparatus and the origin of the data set, this chapter outlines the results of the study. Previous studies of the ^{57}Fe(n,γ)^{58}Fe reaction, methods of experimental data reduction, simulation of electromagnetic deexcitation in the ^{58}Fe nucleus, and the resulting analysis are all presented. A brief discussion of the results with recommendations for further work concludes the chapter.

9.2 Previous Studies of the ^{57}Fe(n,γ)^{58}Fe Reaction

The ^{57}Fe(n,γ)^{58}Fe reaction has been the focus of a number of studies over the past several decades. Most of these studies have focused on determining the neutron capture cross section and other reaction parameters, such as the thermal cross section, the gamma-ray cross section, and resonance-by-resonance reduced partial widths for gamma-rays and neutrons. As the neutron capture cross section has been well determined, with the most recent measurement in 2014 [101], the present work did not attempt to measure the cross section.

Several studies have focused on measuring neutron capture resonances in the ^{57}Fe nucleus. Knowledge of these resonances is useful in constraining the photon strength function. The most comprehensive studies were led by Rohr *et al* at the Central Bureau for Nuclear Measurements (CBNM) in Geel on GELINA, a 150 MeV electron linear accelerator, and at Oak Ridge National Laboratory on ORELA, another electron accelerator [102, 103]. Both of these studies were instrumental in first identifying the strongest neutron capture resonances across a broad energy range. The results from these and other studies were compiled in a 2006 review by Mughabghab [85], which is the primary source for the resonance parameters

used in this work.

At the time of writing, there is no published work on the photon strength function of the ^{58}Fe nucleus, however other iron nuclei have recently been the subject of several studies on the topic. An initial study led by Voinov *et al* identified a low-energy enhancement (LEE) to the photon strength function using Oslo-type experiments. The initial 2004 study that first identified the LEE in the ^{56,57}Fe nuclei noted a factor of 10 enhancement over traditional models [78]. Subsequent studies on these iron nuclei further confirmed and detailed the nature of the LEE [104, 79]. This LEE has also been observed in some rare-earth elements [80, 81], suggesting it may be present in other neutron-rich nuclei.

9.3 Experimental Data Reduction

The experimental data have been analyzed using a recent version of the DANCE Analyzer [105], a comprehensive analysis framework developed and maintained by the DANCE group at Los Alamos National Laboratory. The analyzer processes data in two main stages: the first stage reads and processes data from MIDAS files, extracting waveforms from detectors, and converting them into individual raw events that are then saved into binary files. The second stage reads events from the binary files and uses the information to construct physics events. Each physics event is assigned a plethora of calculated values, including a neutron energy determined from time of flight, a cluster energy derived from the sum of crystal energies in a clusterized[1] event, a multiplicity based on the number of clusterized photons detected within a fixed time of flight window, and an energy sum calculated from the sum of cluster energies. The second analysis stage also applied calibrations to the aforementioned values and created histograms for further analysis of the data. The analyzer requires a number of procedures to prepare the experimental data for analysis, all of which are detailed in this section.

[1] The concept of clusters will be discussed in more detail in Section 9.4.

9.3.1 Alpha Background Removal

As discussed in Chapter 8, BaF_2 detectors have a unique decay structure with two distinct components in the form of a fast component and a slow component. The presence of a fast signal is important for a fast timing detector; however, it is also useful for discriminating among different types of particles. The two decay components are excited differently by charged and neutral particles, therefore using pulse shape discrimination allows for rudimentary particle identification.

The DANCE DAQ captures two signals from the BaF_2 crystals: a fast integral that corresponds to the energy of the fast component of the decay, and a total integral that corresponds to the energy of the fast component and the slow component. By plotting the total integral against the fast integral, signals from charged particles in the detector can be cleanly separated from signals from neutral particles. Figure 9.1 shows a plot of the fast signal versus the total signal for the $^{57}Fe(n,\gamma)^{58}Fe$ reaction. Here, the signals from charged alpha particles and neutral gamma-rays are clearly separated. This method allows the background from internal alpha decays that are characteristic of BaF_2 detectors to be removed from gamma-ray spectra.

9.3.2 Detector Calibrations

Given that this work did not attempt to derive a neutron capture cross section, only two main calibrations were required. The first was a calibration of the neutron time of flight, which was used to calculate neutron energy on an event-by-event basis, and the second was the calibration of each BaF_2 crystal. The techniques used to perform both calibrations follow.

9.3.2.1 Time Deviation Calibration

The time of flight measurement for neutrons is dependent upon a start signal, triggered from the release of a protons from the PSR, and a stop signal, taken to be an event in the BaF_2 detectors. However, any signal generated by the detectors must travel through the

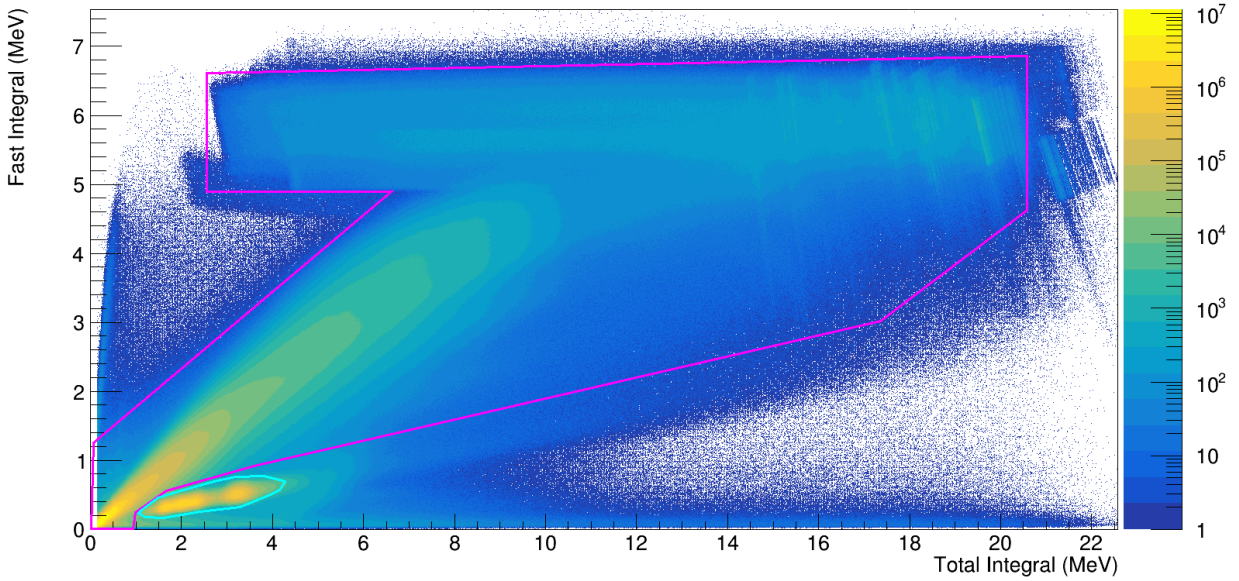

Figure 9.1: A plot of the total integral versus the fast integral in the barium fluoride detectors for the ^{57}Fe(n,γ)^{58}Fe reaction. The plot shows two two-dimensional gates: a light blue gate encircles the alpha decays while the magenta gate shows the gamma-rays.

electronics chain before being registered by the DAQ, and this can introduce deviations in detector timing. To reduce these variations, one detector is selected as a reference and time deviations are calculated relative to it. These corrections are generated on a run-by-run basis, ensuring consistency within the experimental data.

9.3.2.2 Barium Fluoride Detector Calibration

A ^{88}Y calibration source was used as a first step in the BaF_2 detector calibration. The source's two distinct gamma-rays, shown in Table 9.1, were used to acquire initial calibration parameters. However, BaF_2 detectors are very sensitive to temperature changes and even relatively small shifts in ambient temperature can effect light output from the detectors. This behavior can be offset by using the internal alpha activity intrinsic to BaF_2 crystals to provide run-by-run calibration values to account for temperature fluctuations. To accomplish this, the five alpha peaks were fit to a template based on the known response of each crystal, and calibration parameters were extracted from the fit of this spectrum to the observed data.

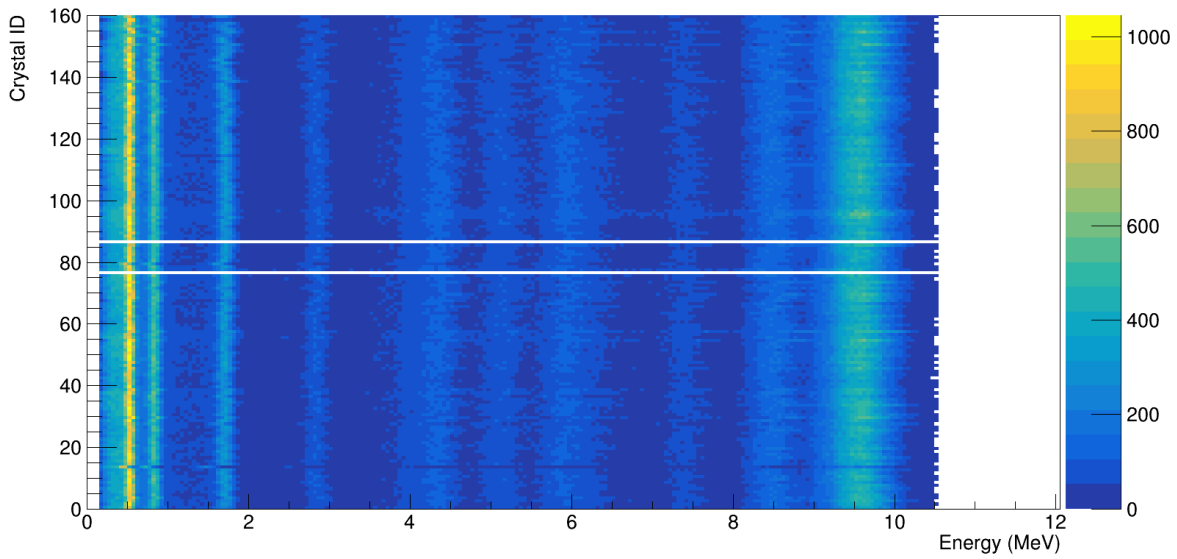

Figure 9.2: Plot of gamma energy versus crystal number. This plot shows the calibrated gamma energy versus the crystal number with gates on both the energy sum and a crystal multiplicity of two. Note the general agreement of the gamma energy between individual crystals.

Inspecting the experimental data after applying parameters from the alpha calibration revealed non-linear behavior at high gamma energies (> 4 MeV), impacting the gamma-ray energy resolution across the entire detector. As no well-resolved high energy peaks were visible in the experimental data, a re-calibration was applied utilizing a second-order polynomial fit and parameters from a previous experiment. This previous experiment had been run shortly after the ^{57}Fe experiment, so there were minimal differences in the experimental setup, and had been successfully calibrated to gamma-rays up to 7 MeV. After implementing these changes, final corrections were made by hand on a crystal-by-crystal basis utilizing online data. The final calibration is shown in Figure 9.2 for a sample multi-step gamma cascade from experimental data.

9.3.3 Contaminant Background Subtraction

After calibrations had been completed, the experimental data was inspected for possible backgrounds in the gamma energy spectra. The primary culprit for potential backgrounds

often comes from impurities in the production target. This can be accounted for by placing an energy sum gate on the experimental data. Essentially, the gamma-rays emitted from a neutron capture event will have an energy sum equal to the neutron separation energy of the nucleus plus the energy of the resonance into which the neutron is captured. By requiring the sum of the energies of gamma-rays captured by the BaF_2 detectors in a single event to be equal to the neutron separation energy, capture reactions on particular isotopes can be effectively isolated.

The neutron separation energy of ^{58}Fe is 10.044 MeV, while the neutron separation energy of ^{59}Fe, the product of neutron-capture on the next-nearest target contaminant, is at roughly 6.5 MeV [85]. These energy sum peaks are well resolved in the experimental data, indicating that no background from the target was expected within the energy sum gate used to investigate the ^{57}Fe(n,γ)^{58}Fe reaction data. A ^{208}Pb background run was also examined to determine the effect of elastic scattering of neutrons and their absorption in the BaF_2 crystals. A sample energy sum spectrum comparing elastic scattering on ^{208}Pb and neutron capture on the iron target is shown in Figure 9.3. From this figure, it is clear that the neutron-capture energy sum peak at just over 10 MeV is well separated from the background runs. As a precautionary measure, a background subtraction based on the elastic scattering scattering data was performed on a subset of the experimental data. The background subtraction exhibited negligible change to the multi-step gamma-cascades, and thus was not implemented fully for this data set.

Nuclide	E_γ (keV)
^{88}Y	898.0
	1836.1

Table 9.1: Energies of the gamma-rays emitted from the ^{88}Y source. These energies were used to perform initial calibrations of the BaF_2 detectors.

9.3.3.1 Waveform Analysis and Pile-up Removal

This data set was one of the first to implement a new pile-up removal technique developed by Chris Prokop. Pile-up occurs when multiple events are captured in a single crystal within a single coincidence window, leading to recorded crystal energies significantly higher than the two separate physics events alone. This new technique utilized the waveform from the BaF_2 detectors to identify pile-up events by looking at the integral's change from baseline. Effectively, two integrals were taken from the waveform: a baseline integral taken before the fast signal's appearance, and a trailing edge integral taken at the very end of the event. These two integrals were then compared to calculate the waveform ratio. In a good event,

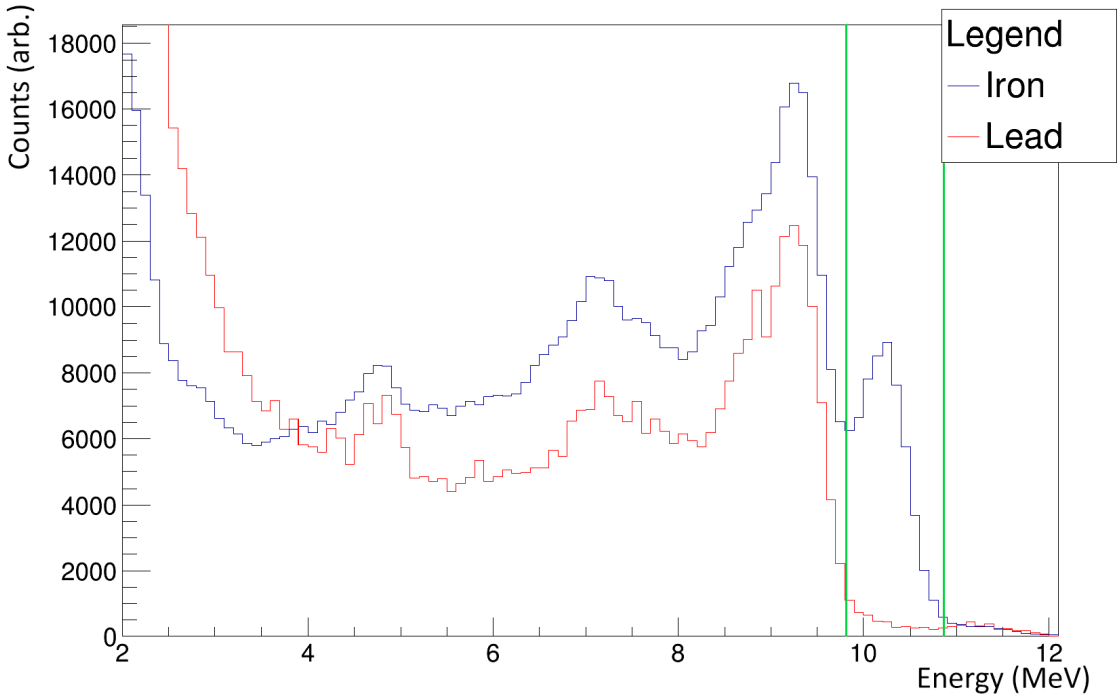

Figure 9.3: Energy sum plot of ^{57}Fe and ^{208}Pb. The energy sum of the iron cascades and the energy sum of the lead cascades clearly show the neutron capture peak in iron at just above 10 MeV separated from the lead background. The iron data are gated on the 3.955 keV neutron resonance ($J^\pi = 0^-$) and both data sets are gated on multiplicity 2 cascades. The lead data are roughly scaled to fit based on a normalization of the high energy gamma-rays between 11-12 MeV. The green vertical bars indicate the energy sum gate used to construct multi-step gamma-cascades.

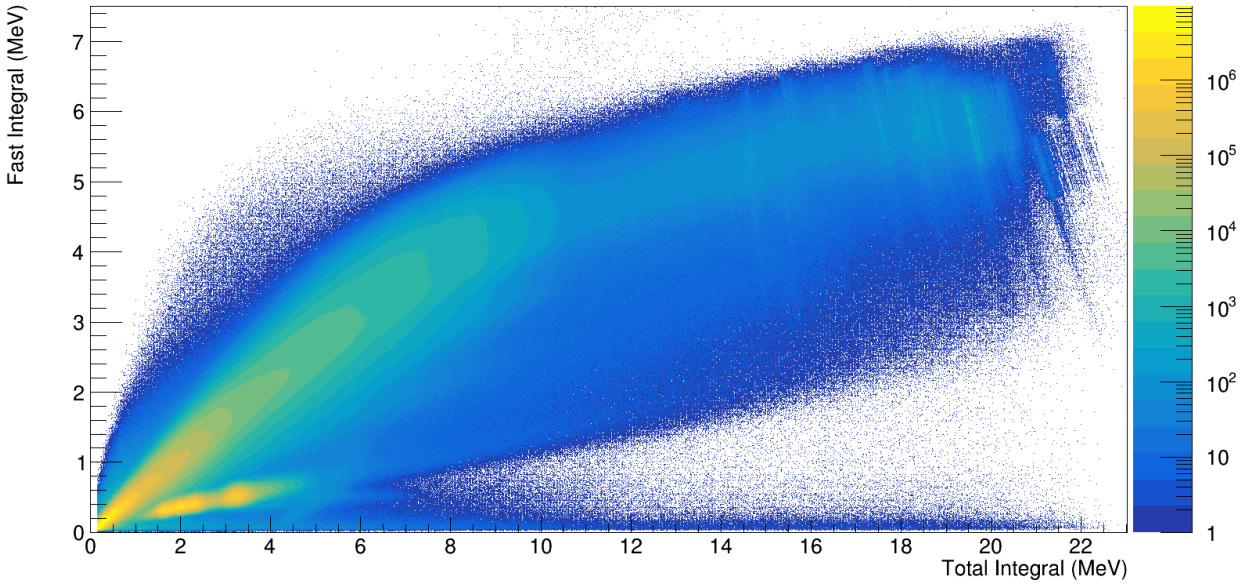

Figure 9.4: A plot of the total integral versus the fast integral for the ^{57}Fe(n,γ)^{58}Fe reaction with pile-up removed.

the wave form ratio should fall in a narrow band corresponding to a set percent change between baseline and the trailing edge. Events falling outside this waveform ratio band are rejected. Figure 9.4 shows the same total integral versus fast integral plot from Figure 9.1 but with the pile-up removal gate applied.

9.4 Characterizing Behavior of Gamma-Decay after Neutron Capture

Following the data reduction stage, characteristic behaviors of the ^{57}Fe(n,γ)^{58}Fe reaction were extracted from the experimental data and compared to simulations. The comparisons allow for changes in the photon strength function and other qualities of nuclear structure to be tuned to match experimental data.

9.4.1 Gamma-Decays in Experimental Data

As mentioned in the previous section, an energy sum gate was applied to the experimental data to isolate the neutron capture reaction of interest. Following this, the relevant neutron resonances were isolated, and multi-step gamma-cascades as well as multiplicity distributions were constructed for the resonances of interest. The process of extracting cascade-related

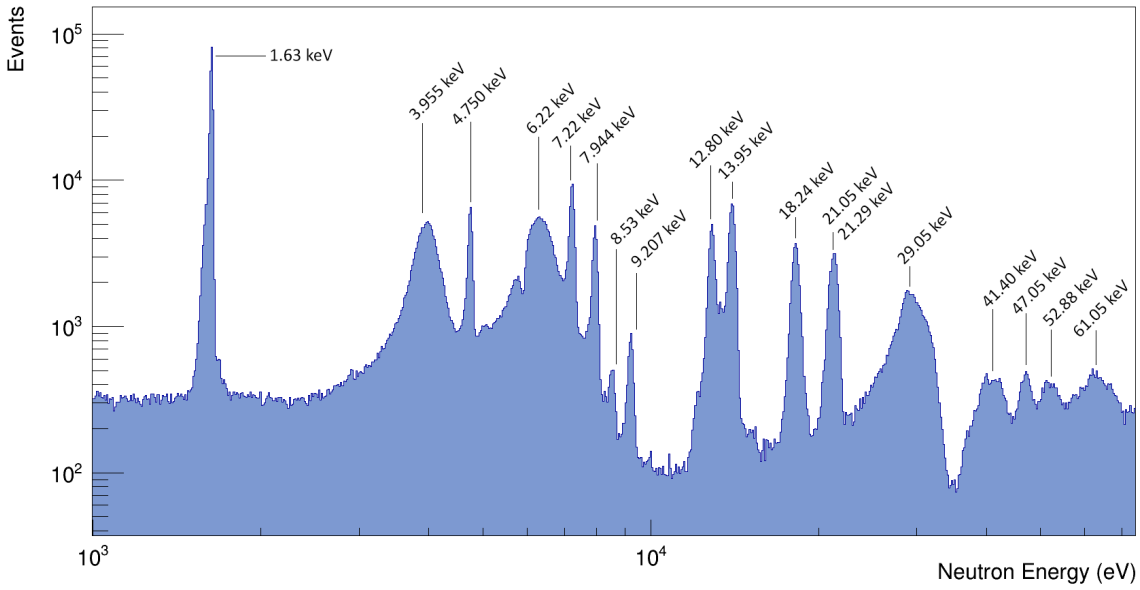

Figure 9.5: Plot of events as a function of neutron energy. This plot shows events as a function of calibrated neutron energy gated on energy sum and a crystal multiplicity of three. Strongly populated states from the neutron capture reaction are identified with their energies.

quantities and brief examples of how it can help to characterize the behavior of statistical nuclei follows.

9.4.1.1 Neutron Resonances in ^{57}Fe

As discussed at the beginning of this Chapter, the neutron capture resonances in ^{57}Fe have been determined by multiple studies and cataloged by Mughabghab [85]. Constraining the photon strength function required identification of strong neutron resonances with well-known spins and parities in the experimental data. To accomplish this, physics events were plotted as a function of neutron energy and well-populated resonances could easily be identified matched to literature values. Figure 9.5 shows the neutron energy spectrum for the ^{57}Fe(n,γ)^{58}Fe reaction with strongly populated resonances labeled. While a significant number of resonances were populated in the neutron capture reaction, only those with known spins and parities were used in this work. Those resonances are listed in Table 9.2.

E_r (keV)	J	ℓ
1.63	2	1
3.955	0	0
6.22	1	0
13.95	1	0
29.05	1	0
41.40	1	0
47.05	1	0
61.05	1	0

Table 9.2: Neutron resonances in ^{57}Fe used for this study. A number of p-wave resonances have been observed between 4 keV and 14 keV; however, most of these states lack spin assignments. This makes them of limited use in this analysis and they are therefore omitted from this table. All values were sourced from Mughaghab [85].

9.4.1.2 Crystal and Cluster Multiplicity

The DANCE Analyzer defines two types of multiplicity for a given physics event: crystal multiplicity and cluster multiplicity. Crystal multiplicity is simply the number of crystals that fire in a physics event. Cluster multiplicity is slightly more complicated, however it's quite similar to the add-back technique described in Chapter 5. Gamma-rays have a tendency to scatter through a detector volume, depositing energy across multiple crystals. Therefore, when neighboring crystals detect signals within the same event, the crystal multiplicities and energies are clustered. Figure 9.6 shows a diagram and describes an example of this process. This provides a more accurate estimate of the multiplicity of an event and helps to reduce background, as neutrons scattered into the detector volume tend to have a lower cluster multiplicity than gamma-rays.

9.4.1.3 Multi-Step Gamma-Cascades

After a neutron capture event, the compound nucleus formed by the capture will decay to its ground state after successive gamma-ray emissions. Each gamma-ray carries with it a fraction of the initial excitation energy and some component of the total angular momentum. In other words, if an excited nucleus decays from to ground state through the emission of

three gamma-rays, the sum of the energy of those three gamma-rays would be equal to the excitation energy of the nucleus and the vector sum of the angular momentum would be equal to the difference in angular momentum between the excited state and the ground state. The reconstruction of a complete decay chain from a single deexcitation is referred to as a multi-step gamma-cascade (MSC).

MSCs are the primary metric used to constrain the photon strength function in this work.

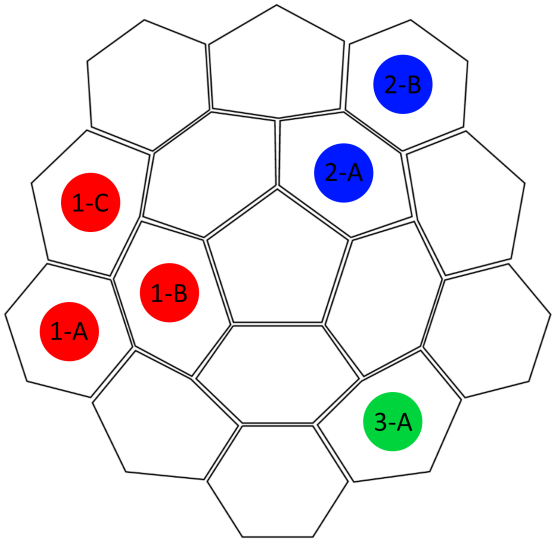

Figure 9.6: An explanation of cluster multiplicity. This diagram shows a number of BaF_2 crystals within the DANCE detector. Assume three different gamma-rays are scattered into this detector volume during a hypothetical event. The first gamma-ray (gamma-ray 1) enters into the crystal marked 1-A, then scatters into 1-B, and finally into 1-C before fully depositing its energy. A similar process occurs with gamma-ray 2, where it enters into the crystal marked 2-A and is scattered into 2-B before fully depositing its energy. The third gamma-ray fully deposits its energy into the crystal marked 3-A. Here, the crystal multiplicity three event for gamma-ray 1 is transformed into a cluster multiplicity one event. Similarly, gamma-ray 2 is also clustered together. For this hypothetical event, the crystal multiplicity would be six while the cluster multiplicity would be three.

As DANCE is a calorimeter, it can accurately reconstruct entire gamma-decay chains from a nucleus decaying from an excited state after a neutron capture. These reconstructed spectra effectively serve as event-by-event decay schemes. As the emitted gamma-rays carry some information about the spin and parity of their initial state, with enough captured events, patterns and structure in the gamma-cascades can be identified. These features often have direct relation to nuclear structure. For example, features appearing towards the center of a gamma-cascade may indicate a preference for the nucleus to deexcite through the quasi-continuum before populating discrete low-lying states. This behavior may indicate useful information about the photon strength function that would help to constrain it.

9.4.1.4 Multiplicity Distribution

Each physics event captured by DANCE is assigned an event multiplicity, a measure of how many gamma-rays were detected by the calorimeter for a single gamma-cascade. Multiplicity distributions show the number of events within a resonance for each multiplicity. As the relative intensities of different multiplicities are dependent on fundamental nuclear structure, multiplicity distributions can indicate important properties of electromagnetic de-excitation. For example, a multiplicity distribution that shows preferences towards lower multiplicities may indicate high-energy transitions that feed lower-lying states. These distributions can also provide insight about the nuclear level density (NLD) of the nucleus.

9.4.2 Determining Nuclear Structure from Gamma-Decay

Having extracted observable quantities from experimental data, the problem becomes how to use them to determine nuclear structure information. This is accomplished by comparing the experimental data with simulated data using nuclear structure as inputs for the simulation. In the case of this work, this means simulating gamma-cascades. As described in Chapter 7, the photon strength function is determined primarily by the transmission probability of a given electromagnetic transition and the nuclear level density. Therefore, a reasonable estimate of both of these values is made, and simulations are run using those esti-

mates as inputs. The generated gamma-cascades are compared to experimental data to see if the simulations reproduce observed features of that data. If the simulations do not reproduce observed features, the inputs are adjusted, more simulations are run, and the comparison begins again. When the nuclear structure inputs have been sufficiently constrained by this iterative process, they can then be used to calculate other useful information about the nucleus, such as its neutron capture cross section. The method of simulating gamma-cascades is described in more detail in the next section.

9.4.3 Simulation of Gamma-Decays

Once experimentally accessible quantities of gamma-decay have been isolated in the data, models to replicate these behaviors can be constructed. A number of different methods to simulate the behavior of gamma-ray emission in statistical nuclei have been developed. Recently, Monte Carlo-based methods have shown particular promise in helping constrain photon strength functions in heavy nuclei [106, 107]. Most simulation work was performed using DICEBOX, described in detail below.

9.4.3.1 DICEBOX

DICEBOX, a purpose-built Monte Carlo cascade generator for high excitation decays, was used to generate gamma-decay from excited states in ^{58}Fe. A detailed description of DICEBOX and its associated algorithms has been published by Bečvàř [108], but functionally the code assumes the extreme statistical model of the nucleus. Under a certain critical energy E_{cr}, DICEBOX assumes that all states are discrete and well-known, while above that energy it constructs states as a random discretization of the nuclear level density. Gamma-decays between states above E_{cr} are characterized by randomized partial radiation widths and each partial radiation width is considered statistically independent from every other width. The randomization of these partial widths is performed such that they fit a normal distribution with zero mean and variance, obeying the Porter-Thomas distribution. Additionally, each decay is initiated from a single resonance with well-defined spin, parity, and energy.

Simulations are generated in terms of nuclear supra-realizations (NSR) and nuclear realizations (NR), which take into account fluctuations in the construction of the simulated nucleus. Each simulation of a given NSR and NR has a fixed number of cascades that DICEBOX simulates. A cascade begins by populating the initial resonance, then allowing the gamma-decay to decay through the constructed nucleus. For decays between states above E_{cr}, transitions are determined through Monte Carlo methods that consider the partial radiation widths of the discretized states. Below E_{cr}, the code selects allowed states based on the input conditions and then selects a state at random. Transitions are allowed until the ground state is reached and the cascade is terminated.

The inputs to DICEBOX allow for fine tuning of the nuclear level density (NLD), the coupling and transition strengths of electric and magnetic transitions, as well as numerous other variables. For this work, four possible variations on the photon strength functions have been considered: a generalized Lorentzian (GLO), a Standard Lorentzian (SLO), a model featuring low-energy enhancement based on the observed behavior of the ^{56,57}Fe nuclei (upbend), and a global photon strength function model proposed by Stephane Goriely (gor) [110]. Each strength function can be seen in Figure 9.7. The generalized details of each strength function are as follows:

- **GLO**: The shape of the E1 transition strength of this model is given by the Phenomenological Generalized Lorentzian, while the M1 and E2 transitions strengths are assumed to be single-particle. The nuclear level density is taken to be a Back-Shifted Fermi Gas.

- **SLO**: This model utilizes a Standard Lorentzian shape for the E1 component of the photon strength function. This model also assumes single-particle models for the M1 and E2 transition strengths and a Constant Temperature nuclear level density model.

- **upbend**: This model is a close approximation of the photon strength function observed in ^{56,57}Fe nuclei by Voinov *et al* [78]. The shape of the E1 transition strength is given

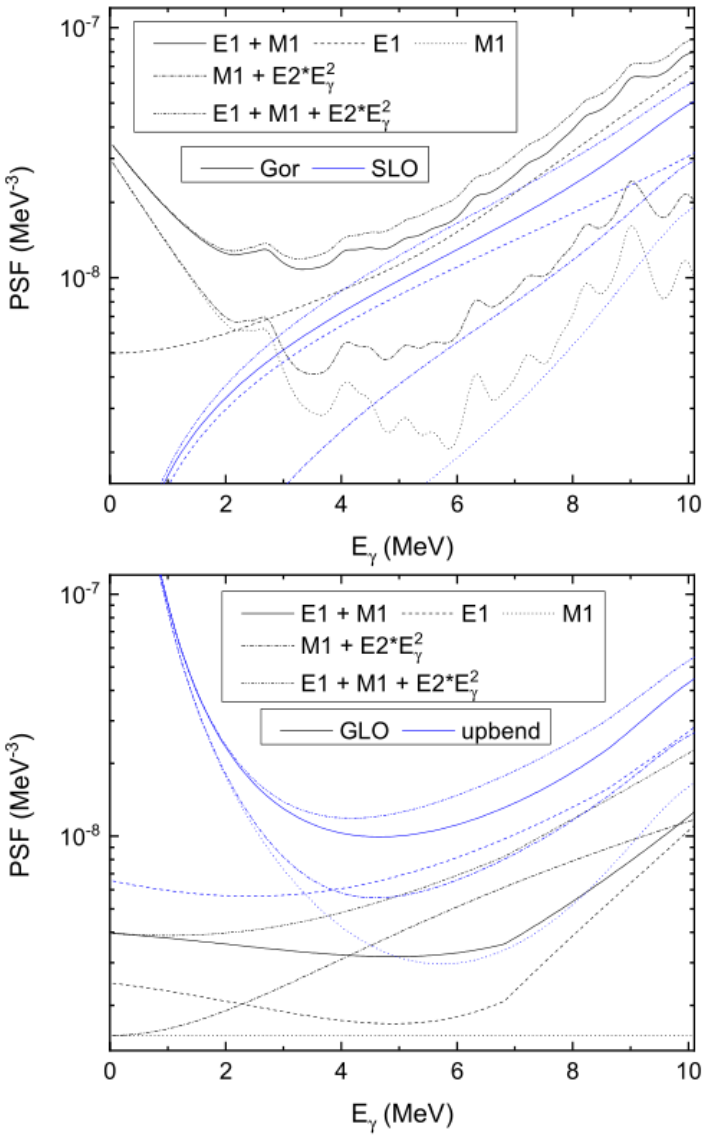

Figure 9.7: A figure of the photon strength functions generated by the different DICEBOX input files plotted as a function of gamma energy. This figure shows specifically how each model varies the electric and magnetic transitions. Reprinted with permission from [109].

by a model proposed by Kadmenskij, Markushev and Furman, often called the KMF model. The M1 transition strength is given by a Lorentzian scaled for an exponential low-energy enhancement corresponding to the behavior observed by Brown and Larsen [111]. The E2 transition strength is taken to be singe-particle in nature, and a Constant Temperature nuclear level density is assumed.

- **gor**: This model is almost entirely theoretically constructed, meaning there are very few parameters to be adjusted. The details of this model are given in detail by Goriely [110].

Using these models, simulations of gamma-cascades were generated by DICEBOX. Each photon strength function model was run with 20 NSR and 3 NR, making for a total of 60 individual simulations per model. The simulations each contained 200,000 gamma-cascades, or 1.2×10^7 total cascades per photon strength function model. However, in order to compare the outputs from DICEBOX simulations to the experimental data, the detector response of the DANCE array had to be incorporated into each simulation.

9.4.3.2 Detector Response

In order to fold in the detector response to simulated gamma-cascades, an extremely accurate model of DANCE is simulated in GEANT4. The fundamentals of the simulation have been detailed by Jandel *et al* [98]; however, this study uses a slightly updated version called DICEBOX-DANCE (DBD). DBD uses the cascades generated by DICEBOX as events that it then propagates through the GEANT4 model of DANCE using Monte Carlo-methods. For a given cascade, the simulation will generate gamma-rays equal to the energy and multiplicity given by the source data. These gamma-rays will then be scattered through the detector volume, simulating compounding effects such as Compton scattering and energy loss through materials surrounding the target and detectors. The events registered in the simulated detector volume then have an energy correction applied to simulate the resolution of the BaF_2 crystals before being written out to binary files. The outputs of DBD are designed to be processed by the DANCE Analyzer, allowing direct comparison of simulated multiplicity distributions, energy sums, and MSCs to experimental data.

9.5 Discussion

This section provides an overview of the conclusions established from comparisons of simulated and experimental gamma-cascades. Figures are provided in this section to help

establish important relationships; however, Appendix A contains a complete compendium of all plots used in this analysis.

9.5.1 Experimental Data Analysis

As established earlier in the Chapter, a number of resonances were found in the experimental data. However, due to uncertainties in the spins and parities, only the resonances in Table 9.2 were considered. This meant that primarily $J^\pi = 1^-$ states were considered in this work. To establish that the ^{58}Fe nucleus was behaving in a statistical manner, different 1^- states were normalized and compared for consistency. Figure 9.8 shows the six s-wave states for different multiplicities. The consistent behavior of the multi-step gamma-cascades among these different resonances of the same spin and parity indicates that a statistical treatment of this nucleus is likely appropriate.

At this point it is relevant to note that each multi-step cascade has been normalized such that the integral of the area under the cascade is unity. This normalization allows for direct comparisons between cascades from various resonances without concern for how well-populated the resonance is by neutron capture. The same approach was taken with simulated data. As such, all plots are shown as relative intensity as a function of gamma-ray energy.

9.5.2 Comparison to Simulations

As discussed previously, comparisons with simulations generated with DICEBOX are delineated by the spin and parity of the initial resonance. The multi-step gamma-cascades are shown with a central line representing the median intensity for a given gamma energy and a likelihood band representing the twentieth and eightieth percentiles around that intensity. This effectively serves as a likelihood band, indicating the phase space the relative intensity is most likely fall within for a given gamma energy. It should be noted that the phase space of a given gamma energy is independent of the phase space of any other gamma energy. For example, if in one simulation a state around 9 MeV is strongly populated, it is unlikely that

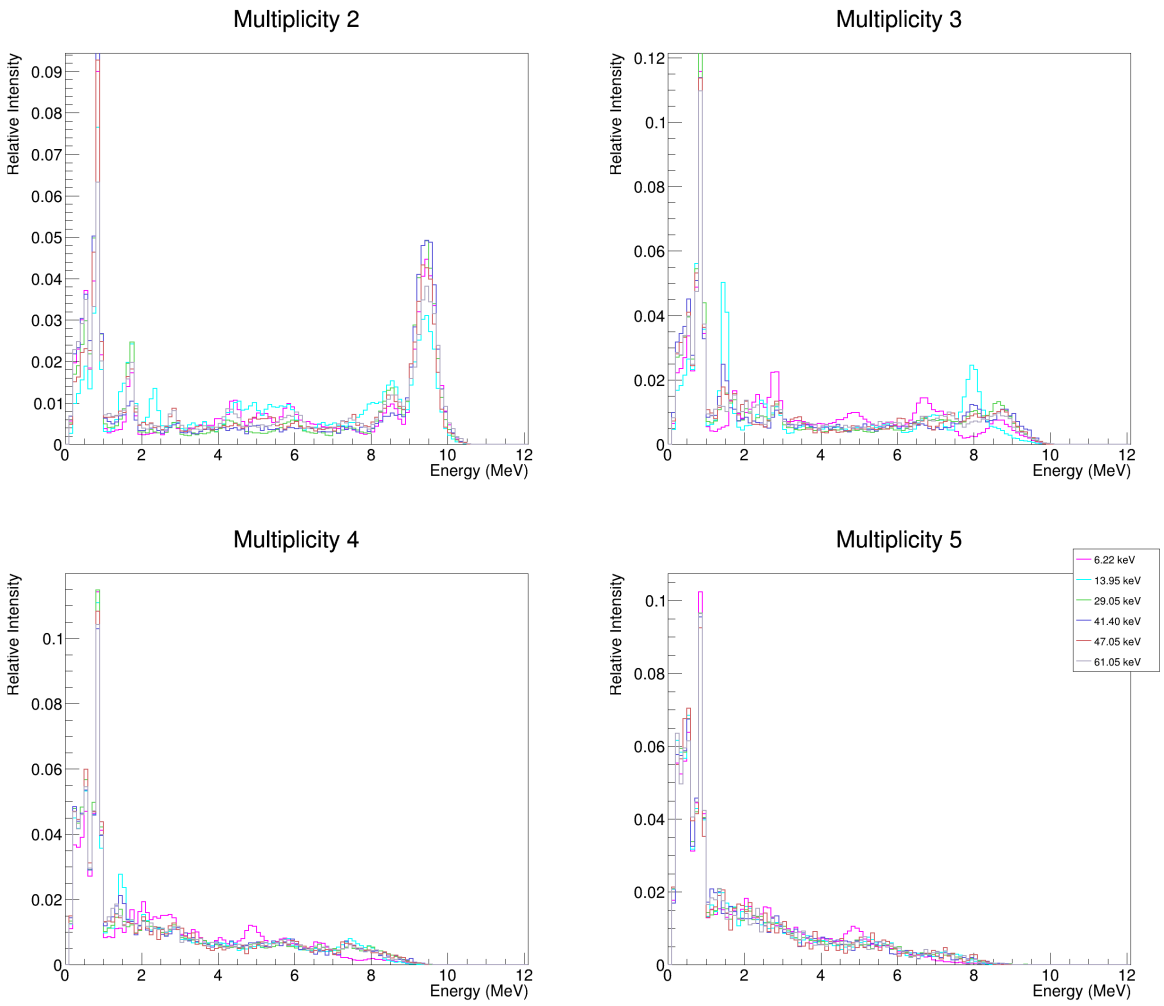

Figure 9.8: Comparison of the multi-step gamma-cascades of 1^- states between multiplicities two and five. The relative consistency of these cascades between various resonances indicates that a statistical treatment is likely appropriate.

states in the 4-6 MeV region will be strongly populated in that same simulation, even though the likelihood band may indicate a large variation among simulations in that energy range.

Each of the four models described in the previous sections were compared with the experimental data and evaluated for agreement. For the 1^- resonances the three highly populated resonances (6.22 keV, 29.05 keV, and 13.95 keV) were chosen for comparison. These three states also represented the widest variations in MSCs from 1^- resonances. The simulations of the 2^+ and 0^- resonances were compared to their respective experimentally

determined analogues (1.63 keV and 3.955 keV, respectively). Most comparisons are made with multiplicity three or greater, as E_{cr} in the DICEBOX simulations was set at 4.34 MeV and multiplicity two cascades preferentially decayed to one of only a few low-lying states.

The GLO model does by far the worst job of reproducing the observed data. As can be seen in Figure 9.9, the model over-predicts the relative intensity of observed gamma-ray transitions at energies between 4-6 MeV. The simulations also predict structure in the multiplicity three and four gamma-cascades that simply does not appear, seen in Figure 9.11 and Figure 9.12. As this is the only model that uses the Back-Shifted Fermi-Gas model for nuclear level density, it may indicate that this is the incorrect NLD for this nucleus. Otherwise, these simulations does not provide any other useful information.

The Goriely model (gor) tends to over-predict transition strengths around 4-6 MeV as well, as seen in Figure 9.9 and Figure 9.10. While this model does a good job of reproducing multiplicity distributions of 1^- resonances, it does a poor job of reproducing structure in MSCs, as can be seen in Figure 9.11. The discrepancies most likely stem from a poor fit

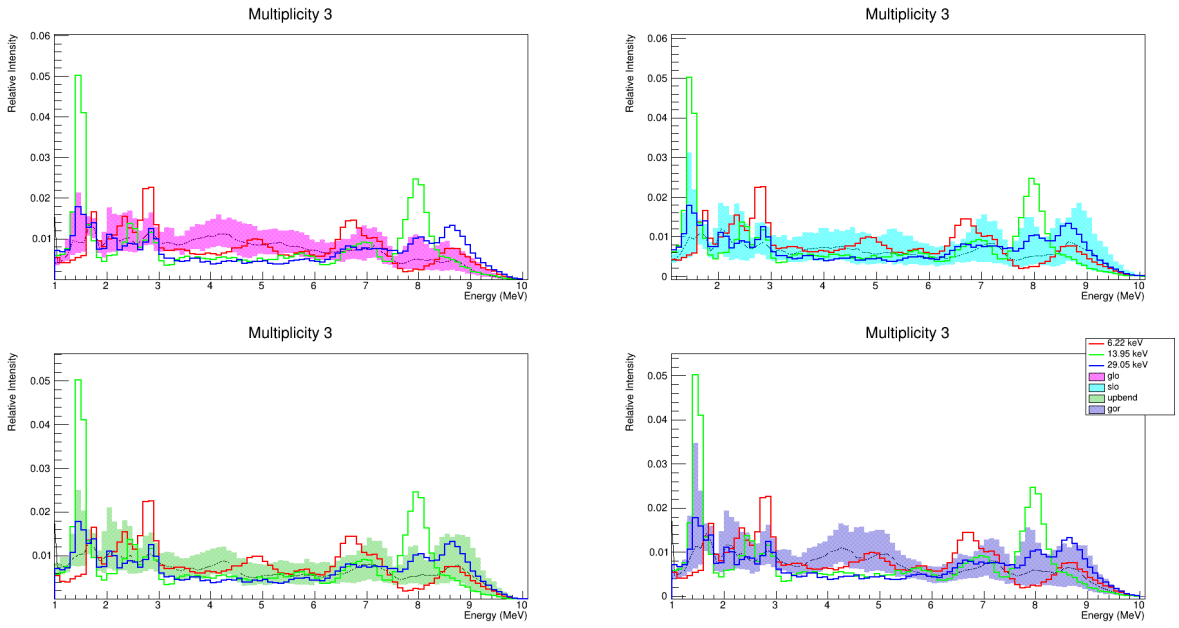

Figure 9.9: Comparison of the multi-step gamma-cascades from 1^- resonances with simulated cascades for multiplicity three cascades.

of the NLD used in this model; however, as this is a primarily phenomenological model, it is difficult to say precisely. Generally, this model does not appear to be in good agreement with the experimental data.

The upbend model appears to damp transitions in the 4-6 MeV range and over-emphasize transitions at low energies, as can be seen in Figure 9.11. This likely stems from this model's preference towards low-energy transitions due to its large low-energy enhancement. However, the upbend model does seem to correctly predict the relative intensity for several resonances outside that 4-6 MeV range. The low-energy structure of this model also seems to agree well with experimental data, as can be seen in Figure 9.10. Additionally, the multiplicity distributions of the experimental results generally fall within the ranges suggested by the upbend model.

Finally, the SLO model appears to agree most broadly with the experimental data. Multiplicity distributions are reproduced relatively well compared to the other models and generally it succeeds where others fail at reproducing MSC features. This can be seen most

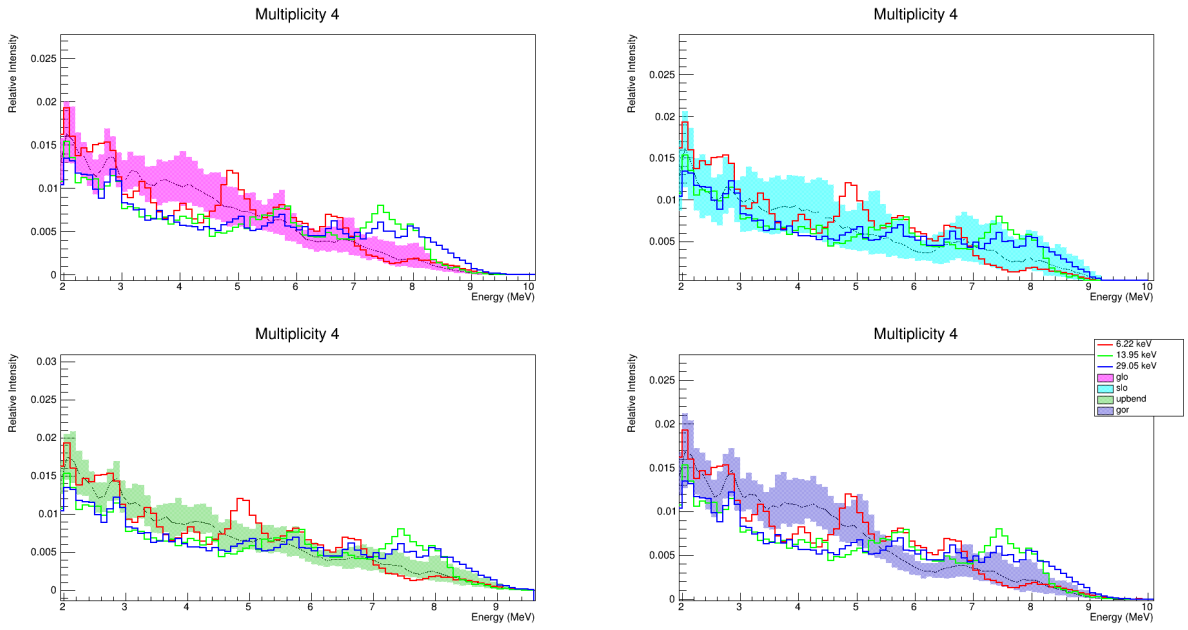

Figure 9.10: Comparison of the multi-step gamma-cascades from 1^- resonances with simulated cascades for multiplicity four cascades.

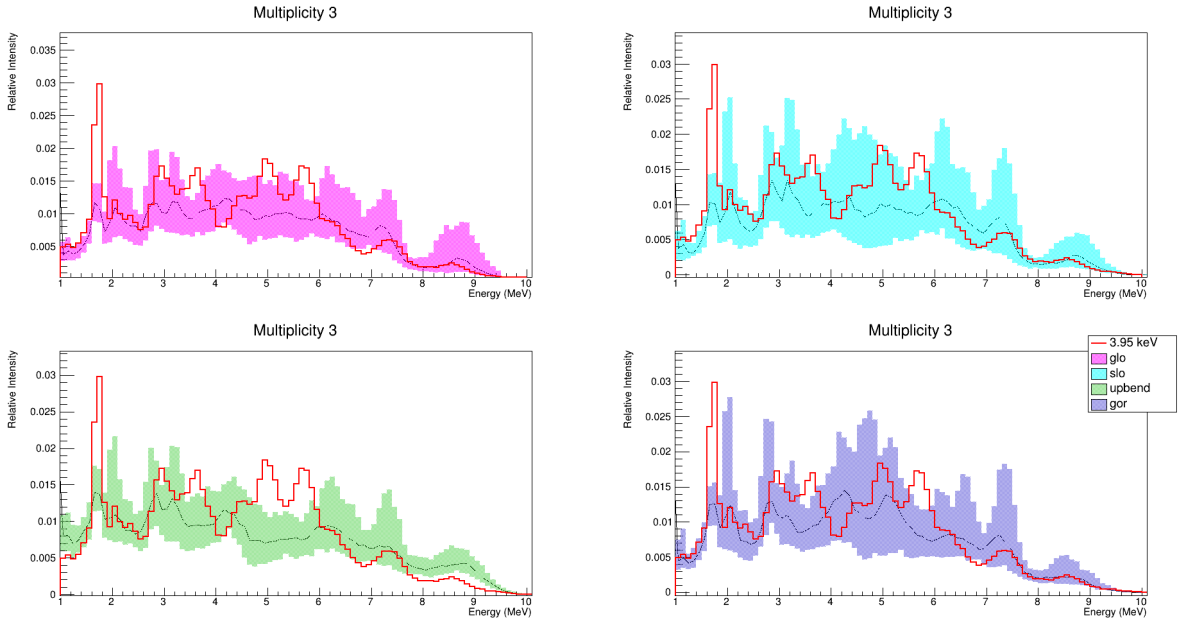

Figure 9.11: Comparison of the multi-step gamma-cascades from 0^- resonances with simulated cascades for multiplicity three cascades.

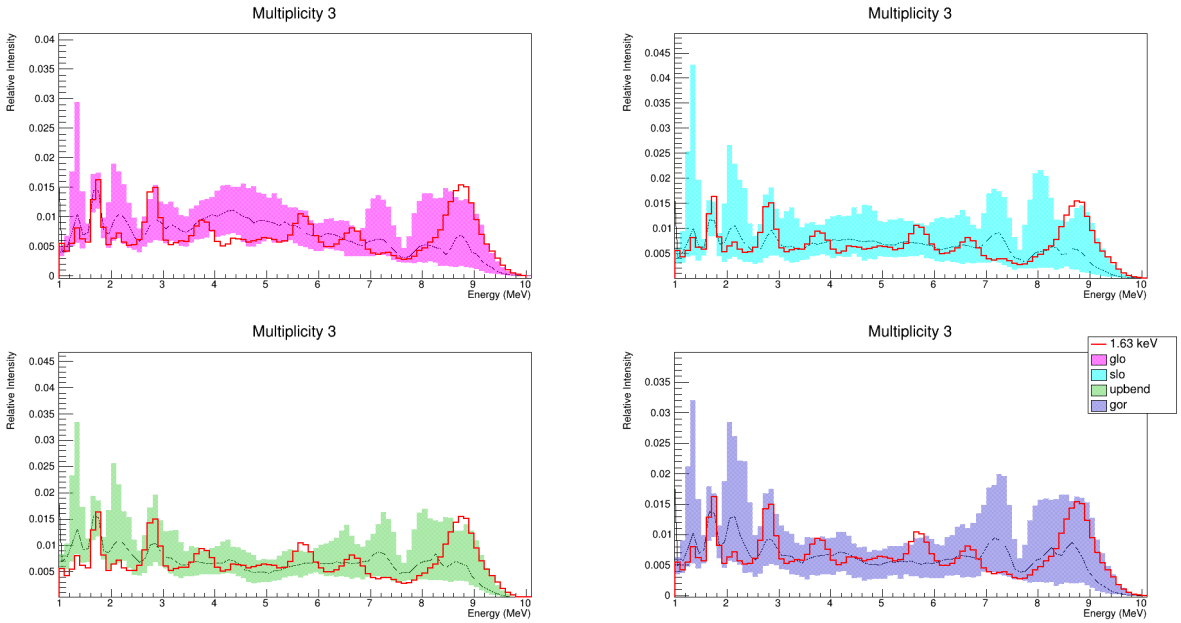

Figure 9.12: Comparison of the multi-step gamma-cascades from 2^+ resonances with simulated cascades for multiplicity three cascades.

prominently in Figure 9.12, where an increase in relative intensity between 6-7 MeV is reproduced well by the SLO model but none of the other models. It is worth noting, however, that this model also has the widest likelihood band of all four models for most resonances.

Comparisons were also made between experimental data and batched simulations. Batched simulations are an approach where NRs are summed across NSRs to reduce extreme variations within NSRs. This technique was used in a study on ^{96}Zr to investigate gamma-decays in the limit of low nuclear level density [112]. In the present work, the simulations were batched in groups of three following the work of Winkelbauer *et al.* Generally, this had the effect of reducing the size of the likelihood band and damping some of the structure in the MSCs. The conclusions in comparing the batched simulations were broadly the same as those above.

9.5.3 Conclusions

Of the four photon strength function models simulated, the SLO model performed the best in reproducing the experimental data. Goriely's model in its current form does not appear to be the correct treatment for this nucleus. However, the two photon strength function models that used a Constant Temperature model of the nuclear density (SLO and upbend) more closely reproduced MSC features and relative intensity, providing an initial constraint on choices of the photon strength function. It seems unlikely that the ^{58}Fe nucleus exhibits as strong a LEE as the ^{56,57}Fe nuclei; however, that does not rule out its presence generally. The experimental data seem to suggest that a weaker LEE may be an appropriate treatment for this nucleus. However, with regard to the primary motivation of this work, a recommendation of the SLO model to describe this nucleus will yield reasonable agreement with experimental data.

9.5.4 Proposed Future Work

The photon strength function of this nucleus can be further constrained by refining the models presented in this work. The most promising avenue would be creating a version

of the SLO model that exhibits a weak LEE or reducing the intensity of the LEE in the upbend model. Additionally, a version of the Goriely model with a weak LEE may help to bring that model closer to the observed data. Additionally, it may be appropriate to introduce a Gilbert-Cameron nuclear level density model to some of the simulations. The Gilbert-Cameron model is effectively a hybrid between a Constant Temperature model and a Back-Shifted Fermi Gas, and may improve agreement between simulated and observed cascades.

After constraining the photon strength function, further work could be performed by implementing the new photon strength function in CGM, a Monte Carlo Hauser-Feshbach reaction model [113], and evaluating how that changes the calculated neutron capture cross section on ^{57}Fe. Additionally, these data could be examined for a direct component of capture in ^{58}Fe [114]. This exercise would be a significant departure from the current analysis framework, but may reveal valuable information about the behavior of the nucleus and therefore bears consideration.

10. SUMMARY

This work has successfully completed two studies, both either utilizing or providing data for indirect experimental methods to extract astrophysically relevant information.

The first study probed the dominant resonance of the ^{23}Mg(p,γ)^{24}Al reaction at classical novae temperatures by investigating the mirror state in ^{24}Na. To accomplish this, the ^{23}Na(d,p)^{24}Na reaction was studied in inverse kinematics using TIARA for Texas. This study was one of a series of commissioning experiments for the detector setup, which successfully utilized TIARA, the MDM-2 magnetic spectrometer, the Oxford detector, and four HPGe detectors from the Hyperion array to perform multiple-coincidence measurements.

A ^{23}Na beam at 10 AMeV was delivered by the Texas A&M Cyclotron Institute's K150 cyclotron and impinged upon a 500 μg/cm^2 deuterated polyethelene target. Ejectiles from the reaction were detected in the Hyball, and characteristic gamma-rays were identified in the HPGe detectors. Beam alignment issues prevented the use of the Oxford detector; however, data from the Hyball and the HPGe detectors were used in coincidence to successfully isolate gamma-rays from the mirror state of interest.

The collected data were successfully normalized to the 3628 keV state in ^{24}Na utilizing the spectroscopic factor determined by Tomandl *et al.* DWBA calculations utilizing optical parameters from studies by Tomandl *et al* and Daum of the ^{23}Na(d,p)^{24}Na reaction were performed, and a spectroscopic factor of $S_{dp} = 0.0852 \pm 0.0085$ was determined. This value was used to estimate the proton partial width of the ^{24}Al state of interest at $\Gamma_p = 201 \pm 20$ meV. Using a theoretical value for the gamma partial width, a resonance strength of $\omega\gamma = 25 \pm 3$ meV was calculated. Both of these values agree with previous literature. Finally, improvements to reduce statistical uncertainty in future experiments were discussed.

The second study examined the photon strength function of ^{58}Fe. Data collected at the Los Alamos Neutron Science Center on the Detector for Advanced Neutron Capture Experiments in 2017 were analyzed using a forward analysis method. A new pile-up removal

technique was implemented and numerous neutron resonances were identified. Multi-step gamma-cascades, energy sum spectra, and multiplicity distributions were extracted from the experimental data.

The Monte Carlo cascade generator DICEBOX was employed to test four theoretical models of the photon strength function. Comparisons with models that simulated an Oslo-type upbend indicated that a strong low energy enhancement is unlikely in this nucleus. A theoretical model proposed by Goriely also failed to reproduce features observed in the experimental data. A model employing single-particle E1 and M1 strengths best approximated the experimental results. Proposals for future simulation work were also presented, as further study will be required to better constrain the photon strength function of this nucleus.

REFERENCES

[1] A. G. Lemaître, "A Homogeneous Universe of Constant Mass and Increasing Radius accounting for the Radial Velocity of Extra-galactic Nebulae," *Monthly Notices of the Royal Astronomical Society*, vol. 91, no. 5, pp. 483–490, 1931.

[2] R. A. Alpher, H. Bethe, and G. Gamow, "The Origin of Chemical Elements," *Phys. Rev.*, vol. 73, pp. 803–804, 1948.

[3] H. A. Bethe, "Energy Production in Stars," *Phys. Rev.*, vol. 55, pp. 103–103, 1939.

[4] E. M. Burbidge, G. R. Burbidge, W. A. Fowler, and F. Hoyle, "Synthesis of the Elements in Stars," *Rev. Mod. Phys.*, vol. 29, pp. 547–650, 1957.

[5] F. LeBlanc, *An Introduction to Stellar Astrophysics*. Chichester, West Sussex, U.K: Wiley, 2010.

[6] A. E. Champagne and M. Wiescher, "Explosive Hydrogen Burning," *Annual Review of Nuclear and Particle Science*, vol. 42, no. 1, pp. 39–76, 1992.

[7] R. Hounsell, M. F. Bode, P. P. Hick, A. Buffington, B. V. Jackson, J. M. Clover, A. W. Shafter, M. J. Darnley, N. R. Mawson, I. A. Steele, A. Evans, S. P. S. Eyres, and T. J. O'Brien, "EXQUISITE NOVA LIGHT CURVES FROM THE SOLAR MASS EJECTION IMAGER SMEI," *The Astrophysical Journal*, vol. 724, no. 1, pp. 480–486, 2010.

[8] NASA/CXC/M.Weiss, "Nova Aquilae: Chandra Discovers Eruption and Pulsation in Nova Outburst," 2001.

[9] R. Wilkinson, *Measurement of $^{19}Ne(p,\gamma)^{20}Na$ in Relation to Explosive Stellar Phenomena*. PhD thesis, University of Surrey, 2019.

[10] H. Schatz, A. Aprahamian, V. Barnard, L. Bildsten, A. Cumming, M. Ouellette, T. Rauscher, F.-K. Thielemann, and M. Wiescher, "End Point of the *rp* Process on Accreting Neutron Stars," *Phys. Rev. Lett.*, vol. 86, pp. 3471–3474, 2001.

[11] J. A. Hoffman, H. L. Marshall, and W. H. G. Lewin, "Dual character of the rapid burster and a classification of X-ray bursts," *Nature*, vol. 271, no. 5646, pp. 630–633, 1978.

[12] R. H. Cyburt, A. M. Amthor, A. Heger, E. Johnson, L. Keek, Z. Meisel, H. Schatz, and K. Smith, "DEPENDENCE OF X-RAY BURST MODELS ON NUCLEAR REACTION RATES," *The Astrophysical Journal*, vol. 830, no. 2, p. 55, 2016.

[13] R. Longland, C. Iliadis, A. E. Champagne, J. R. Newton, C. Ugalde, A. Coc, and R. Fitzgerald, "Charged-particle thermonuclear reaction rates: I. Monte Carlo method and statistical distributions," *Nuclear Physics A*, vol. 841, pp. 1–30, 2010.

[14] C. Iliadis, A. Champagne, J. Jose, S. Starrfield, and P. Tupper, "The Effects of Thermonuclear Reaction-Rate Variations on Nova Nucleosynthesis: A Sensitivity Study," *The Astrophysical Journal Supplement Series*, vol. 142, no. 1, pp. 105–137, 2002.

[15] H. Herndl, M. Fantini, C. Iliadis, P. M. Endt, and H. Oberhummer, "Thermonuclear reaction rate of ^{23}Mg(p,γ)^{24}Al," *Physical Review C*, vol. 58, no. 3, pp. 1798–1803, 1998.

[16] U. Chowdhury, K. G. Leach, C. Andreoiu, A. Bader, M. Brodeur, A. Chaudhuri, A. T. Gallant, A. Grossheim, Gwinner, R. Klawitter, A. A. Kwiatkowski, A. Lennarz, T. D. Macdonald, J. Pearkes, B. E. Schultz, and J. Dilling, "First direct mass measurement of the neutron-deficient nucleus ^{24}Al," *Physical Review C*, vol. 92, no. 045803, 2015.

[17] G. Lotay, P. J. Woods, D. Seweryniak, M. P. Carpenter, N. Hoteling, R. V. F. Janssens, D. G. Jenkins, T. Lauritsen, C. J. Lister, A. Robinson, and S. Zhu, "First in-beam γ-ray spectroscopy study of ^{24}Al and its implications for the astrophysical ^{23}Mg(p,γ)^{24}Al reaction rate in ONe novae," *Physical Review C*, vol. 77, no. 042802(R), 2008.

[18] L. Erikson, C. Ruiz, F. Ames, P. Bricault, L. Buchmann, A. A. Chen, J. Chen, H. Dare, B. Davids, C. Davis, C. M. Deibel, M. Dombsky, S. Foubister, N. Galinski, U. Greife, U. Hager, A. Hussein, D. A. Hutcheon, J. Lassen, L. Martin, D. F. Ottewell, C. V. Ouellet, G. Ruprecht, K. Setoodehnia, A. C. Shotter, A. Teigelhöfer, C. Vockenhuber, C. Wrede, and A. Wallner, "First direct measurement of the ^{23}Mg(p,γ)^{24}Al reaction," *Physical Review C*, vol. 81, no. 045808, 2010.

[19] S. Kubono, T. Kajino, and S. Kato, "Structure of ^{24}Al for the stellar reaction rate of ^{23}Mg(p,γ)^{24}Al," *Nuclear Physics A*, vol. 588, no. 2, pp. 521 – 536, 1995.

[20] D. W. Visser, C. Wrede, J. A. Caggiano, J. A. Clark, C. Deibel, R. Lewis, A. Parikh, and P. D. Parker, "Measurement of ^{23}Mg$(p,\gamma)^{24}$Al resonance energies," *Phys. Rev. C*, vol. 76, p. 065803, 2007.

[21] M. Greenfield, S. Brandenburg, A. Drentje, P. Grasdizk, H. Riezebos, S. Van Der Werf, A. Van Der Woude, M. Harakeh, W. Sterrenburg, and B. Brown, "The ^{24}Mg(^{3}He, t)^{24}Al reaction and L=1 giant resonance systematics using an effective ^{3}He-n interaction at 27 MeV/nucleon," *Nuclear Physics A*, vol. 524, no. 2, pp. 228 – 250, 1991.

[22] R. G. T. Zegers, R. Meharchand, T. Adachi, S. M. Austin, B. A. Brown, Y. Fujita, M. Fujiwara, C. J. Guess, H. Hashimoto, K. Hatanaka, M. E. Howard, H. Matsubara, K. Nakanishi, T. Ohta, H. Okamura, Y. Sakemi, Y. Shimbara, Y. Shimizu, C. Scholl, A. Signoracci, Y. Tameshige, A. Tamii, and M. Yosoi, "Spectroscopy of ^{24}Al and extraction of Gamow-Teller strengths with the ^{24}Mg(^{3}He,t) reaction at 420 MeV," *Phys. Rev. C*, vol. 78, p. 014314, 2008.

[23] C. Wrede, J. A. Clark, C. M. Deibel, T. Faestermann, R. Hertenberger, A. Parikh, H. Wirth, S. Bishop, A. A. Chen, K. Eppinger, B. M. Freeman, R. Krucken, O. Lepyoshkina, G. Rugel, , and K. Setoodehnia, "Properties of ^{20}Na, ^{24}Al, ^{28}P, ^{32}Cl, and ^{36}K for studies of explosive hydrogen burning," *Phys. Rev. C*, vol. 82, p. 035805, 2010.

[24] D. Hutcheon, C. Ruiz, J. Fallis, J. D'Auria, B. Davids, U. Hager, L. Martin, D. Ottewell, S. Reeve, and A. Rojas, "Measurement of radiative capture resonance energies with an extended gas target," *Nuclear Instruments and Methods in Physics Research Section A: Accelerators, Spectrometers, Detectors and Associated Equipment*, vol. 689, pp. 70 – 74, 2012.

[25] V. Margerin, G. Lotay, P. J. Woods, M. Aliotta, G. Christian, B. Davids, T. Davinson, D. T. Doherty, J. Fallis, D. Howell, O. S. Kirsebom, D. J. Mountford, A. Rojas, C. Ruiz, and J. A. Tostevin, "Inverse Kinematic Study of the ^{26g}Al$(d,p)^{27}$Al Reaction and Implications for Destruction of ^{26}Al in Wolf-Rayet and Asymptotic Giant Branch Stars," *Phys. Rev. Lett.*, vol. 115, p. 062701, 2015.

[26] N. K. Timofeyuk, R. C. Johnson, and A. M. Mukhamedzhanov, "Relation between Proton and Neutron Asymptotic Normalization Coefficients for Light Mirror Nuclei and its Relevance to Nuclear Astrophysics," *Phys. Rev. Lett.*, vol. 91, p. 232501, 2003.

[27] K. S. Krane, *Introductory Nuclear Physics*. Wiley, 1987.

[28] C. R. Brune and B. Davids, "Radiative Capture Reactions in Astrophysics," *Annual Review of Nuclear and Particle Science*, vol. 65, no. 1, pp. 87–112, 2015.

[29] C. Iliadis, *Nuclear Physics of Stars*. Weinheim: Wiley-VCH, 2007.

[30] H. Beer, F. Voss, and R. R. Winters, "On the calculation of Maxwellian-averaged capture cross sections," *The Astrophysical Journal Supplement Series*, vol. 80, pp. 403–424, 1992.

[31] N. Bohr, "Neutron capture and nuclear constitution," *Nature*, vol. 137, no. 3461, pp. 344–348, 1936.

[32] D. A. Hutcheon, S. Bishop, L. Buchmann, M. L. Chatterjee, A. A. Chen, J. M. D'Auria, S. Engel, D. Gigliotti, U. Greife, D. Hunter, A. Hussein, C. C. Jewett, N. Khan, M. Lamey, A. M. Laird, W. Liu, A. Olin, D. Ottewell, J. G. Rogers, G. Roy, H. Sprenger, and C. Wrede, "The DRAGON facility for nuclear astrophysics at

TRIUMF-ISAC: Design, construction and operation," *Nuclear Instruments and Methods in Physics Research, Section A: Accelerators, Spectrometers, Detectors and Associated Equipment*, vol. 498, no. 1-3, pp. 190–210, 2003.

[33] R. Wilkinson, G. Lotay, A. Lennarz, C. Ruiz, G. Christian, C. Akers, W. N. Catford, A. A. Chen, D. Connolly, B. Davids, D. A. Hutcheon, D. Jedrejcic, A. M. Laird, L. Martin, E. McNeice, J. Riley, and M. Williams, "Direct Measurement of the Key $E_{\mathrm{c.m.}} = 456$ keV Resonance in the Astrophysical $^{19}\mathrm{Ne}(p,\gamma)^{20}\mathrm{Na}$ Reaction and Its Relevance for Explosive Binary Systems," *Phys. Rev. Lett.*, vol. 119, p. 242701, 2017.

[34] G. Baur, C. Bertulani, and H. Rebel, "Coulomb dissociation as a source of information on radiative capture processes of astrophysical interest," *Nuclear Physics A*, vol. 458, no. 1, pp. 188 – 204, 1986.

[35] G. Baur, "Breakup reactions as an indirect method to investigate low-energy charged-particle reactions relevant for nuclear astrophysics," *Physics Letters B*, vol. 178, no. 2, pp. 135 – 138, 1986.

[36] H. M. Xu, C. A. Gagliardi, R. E. Tribble, A. M. Mukhamedzhanov, and N. K. Timofeyuk, "Overall Normalization of the Astrophysical S Factor and the Nuclear Vertex Constant for $^{7}\mathrm{Be}(p,\gamma)^{8}\mathrm{B}$ Reactions," *Phys. Rev. Lett.*, vol. 73, pp. 2027–2030, 1994.

[37] M. G. Mayer, "On Closed Shells in Nuclei. II," *Phys. Rev.*, vol. 75, pp. 1969–1970, 1949.

[38] O. Haxel, J. H. D. Jensen, and H. E. Suess, "On the "Magic Numbers" in Nuclear Structure," *Phys. Rev.*, vol. 75, pp. 1766–1766, 1949.

[39] G. R. Satchler, *Introduction to Nuclear Reactions.* Houndmills, Basingstoke, Hampshire: Macmillan, 1990.

[40] W. N. Catford, *What Can We Learn from Transfer, and How Is Best to Do It?*, pp. 67–122. Berlin, Heidelberg: Springer Berlin Heidelberg, 2014.

[41] M. Igarashi, "Two-step finite-range DWBA code, TWOFNR," 2020.

[42] I. J. Thompson, "Coupled reaction channels calculations in nuclear physics," *Computer Physics Reports*, vol. 7, no. 4, pp. 167 – 212, 1988.

[43] R. C. Johnson and P. J. R. Soper, "Contribution of Deuteron Breakup Channels to Deuteron Stripping and Elastic Scattering," *Phys. Rev. C*, vol. 1, pp. 976–990, 1970.

[44] M. Labiche, W. Catford, R. Lemmon, C. Timis, R. Chapman, N. Orr, B. Fernández-Domínguez, G. Moores, N. Achouri, N. Amzal, S. Appleton, N. Ashwood, T. Baldwin, M. Burns, L. Caballero, J. Cacitti, J. Casadjian, M. Chartier, N. Curtis, K. Faiz, G. de France, M. Freer, J. Gautier, W. Gelletly, G. Iltis, B. Lecornu, X. Liang, C. Marry, Y. Merrer, L. Olivier, S. Pain, V. Pucknell, B. Raine, M. Rejmund, B. Rubio, F. Saillant, H. Savajols, O. Sorlin, K. Spohr, C. Theisen, G. Voltolini, and D. Warner, "TIARA: A large solid angle silicon array for direct reaction studies with radioactive beams," *Nuclear Instruments and Methods in Physics Research Section A: Accelerators, Spectrometers, Detectors and Associated Equipment*, vol. 614, no. 3, pp. 439 – 448, 2010.

[45] D. Pringle, W. Catford, J. Winfield, D. Lewis, N. Jelley, K. Allen, and J. Coupland, "The Oxford MDM-2 magnetic spectrometer," *Nuclear Instruments and Methods in Physics Research Section A: Accelerators, Spectrometers, Detectors and Associated Equipment*, vol. 245, no. 2, pp. 230 – 247, 1986.

[46] A. Spiridon, E. Pollacco, B. Roeder, A. Saastamoinen, R. Chyzh, M. Dag, R. Tribble, L. Trache, G. Pascovici, and R. D. Oliveira, "Upgrade of the TAMU MDM-focal plane detector with MicroMegas technology," *Nuclear Instruments and Methods in Physics Research Section B: Beam Interactions with Materials and Atoms*, vol. 376, pp. 364 – 368, 2016. Proceedings of the XVIIth International Conference on Electromagnetic Isotope Separators and Related Topics (EMIS2015), Grand Rapids, MI, U.S.A., 11-15 May 2015.

[47] D. P. May, "The operational parameters for the Texas A&M high B mode electron cy-

clotron resonance ion source," *Review of Scientific Instruments*, vol. 69, no. 2, pp. 688–690, 1998.

[48] E. Kelly, "General description and operating characteristics of the Berkeley 88-inch cyclotron," *Nuclear Instruments and Methods*, vol. 18-19, pp. 33 – 40, 1962.

[49] W. N. Catford, R. C. Lemmon, C. N. Timis, M. Labiche, L. Caballero, and R. Chapman, "Transfer Reaction Studies with Exotic Nuclei," *AIP Conference Proceedings*, vol. 704, no. 1, pp. 185–194, 2004.

[50] R. Hughes, J. Burke, R. Casperson, S. Ota, S. Fisher, J. Parker, C. Beausang, M. Dag, P. Humby, J. Koglin, E. McCleskey, A. McIntosh, A. Saastamoinen, A. Tamashiro, E. Wilson, and T. Wu, "The hyperion particle-γ detector array," *Nuclear Instruments and Methods in Physics Research Section A: Accelerators, Spectrometers, Detectors and Associated Equipment*, vol. 856, pp. 47 – 52, 2017.

[51] D. Youngblood, Y.-W. Lui, H. Clark, P. Oliver, and G. Simler, "Response of a resistive wire detector to 240 MeV alpha particles," *Nuclear Instruments and Methods in Physics Research Section A: Accelerators, Spectrometers, Detectors and Associated Equipment*, vol. 361, no. 3, pp. 539 – 542, 1995.

[52] Y. Giomataris, P. Rebourgeard, J. Robert, and G. Charpak, "MICROMEGAS: a high-granularity position-sensitive gaseous detector for high particle-flux environments," *Nuclear Instruments and Methods in Physics Research Section A: Accelerators, Spectrometers, Detectors and Associated Equipment*, vol. 376, no. 1, pp. 29 – 35, 1996.

[53] S. Ritt and et. al., "MIDAS - Maximum Integrated Data Acquisition System," 2020.

[54] G. F. Knoll, *Radiation Detection and Measurement*. Wiley, 2010.

[55] C. Daum, "The ^{23}Na(d, p)^{24}Na reaction and the nuclear structure of ^{24}Na," *Nuclear Physics*, vol. 45, pp. 273 – 295, 1963.

[56] P. Ekström, J. Tillman, and L. Carlén, "Energy levels of ^{24}Na from the ^{23}Na(d, pγ)^{24}Na reaction," *Nuclear Physics A*, vol. 210, no. 3, pp. 458 – 464, 1973.

[57] P. Smulders, "Lifetimes and Branching Ratios of Excited States of ^{24}Na," *Nuclear Physics A*, vol. 210, pp. 579–589, 1973.

[58] A. Buisman and P. Smulders, "Electromagnetic transition strengths in ^{24}Na," *Nuclear Physics A*, vol. 228, no. 2, pp. 205 – 215, 1974.

[59] I. Tomandl, J. Novák, V. Burjan, S. Raman, T. von Egidy, H.-F. Wirth, U. Köster, W. Schauer, J. W. Starner, E. T. Jurney, G. Graw, R. Hertenberger, A. Gollwitzer, B. Valnion, and A. Metz, "Nuclear spectroscopy of ^{24}Na via ($\vec{\text{d}}$,p) and (n,γ) reactions," *Phys. Rev. C*, vol. 69, p. 014312, 2004.

[60] A. Matta, P. Morfouace, N. De Séréville, F. Flavigny, M. Labiche, and R. Shearman, "NPTool: a simulation and analysis framework for low-energy nuclear physics experiments," *Journal of Physics G: Nuclear and Particle Physics*, vol. 43, p. 15, 2016.

[61] S. Ota and *et al Phys. Rev. C (In Preparation)*, 2020.

[62] S. Ota, G. Christian, G. Lotay, W. Catford, E. Bennett, S. Dede, D. Doherty, S. Hallam, J. Hooker, C. Hunt, H. Jayatissa, A. Matta, M. Moukaddam, G. Rogachev, A. Saastamoinen, J. Tostevin, S. Upadhyayula, and R. Wilkinson, "Decay properties of ^{22}Ne+α resonances and their impact on s-process nucleosynthesis," *Physics Letters B*, vol. 802, p. 135256, 2020.

[63] C. Iliadis, R. Longland, A. E. Champagne, and A. Coc, "Charged-particle thermonuclear reaction rates: III. Nuclear physics input," *Nuclear Physics A*, vol. 841, pp. 251–322, 2010.

[64] W. Wang, "Diffuse Emission of ^{26}Al and ^{60}Fe in the Galaxy," in *Astrophysics*, ch. 5, pp. 89–122, InTech, 2012.

[65] W. R. Binns, M. H. Israel, E. R. Christian, A. C. Cummings, G. A. De Nolfo, K. A. Lave, R. A. Leske, R. A. Mewaldt, E. C. Stone, T. T. Von Rosenvinge, and M. E. Wiedenbeck, "Observation of the ^{60}Fe nucleosynthesis-clock isotope in galactic cosmic rays," *Science*, vol. 352, no. 6286, pp. 677–680, 2016.

[66] A. Wallner, J. Feige, N. Kinoshita, M. Paul, L. K. Fifield, R. Golser, M. Honda, U. Linnemann, H. Matsuzaki, S. Merchel, G. Rugel, S. G. Tims, P. Steier, T. Yamagata, and S. R. Winkler, "Recent near-Earth supernovae probed by global deposition of interstellar radioactive ^{60}Fe," *Nature*, vol. 532, no. 7597, pp. 69–72, 2016.

[67] R. Diehl, "Measuring ^{26}Al and ^{60}Fe in the Galaxy," *New Astronomy Reviews*, vol. 50, no. 7-8, pp. 534–539, 2006.

[68] E. Uberseder, R. Reifarth, D. Schumann, I. Dillmann, C. D. Pardo, J. Görres, M. Heil, F. Käppeler, J. Marganiec, J. Neuhausen, M. Pignatari, F. Voss, S. Walter, and M. Wiescher, "Measurement of the ^{60}Fe(n,γ)^{61}Fe cross section at stellar temperatures," *Physical Review Letters*, vol. 102, no. 15, pp. 1–4, 2009.

[69] S. W. Jones, H. Möller, C. L. Fryer, C. J. Fontes, R. Trappitsch, W. P. Even, A. Couture, M. R. Mumpower, and S. Safi-Harb, "^{60}Fe in core-collapse supernovae and prospects for X-ray and gamma-ray detection in supernova remnants," *Monthly Notices of the Royal Astronomical Society*, vol. 485, no. 3, pp. 4287–4310, 2019.

[70] S. E. Woosley, "Neutron-rich Nucleosynthesis in Carbon Deflagration Supernovae," *The Astrophysical Journal*, vol. 476, no. 2, pp. 801–810, 1997.

[71] M. Limongi and A. Chieffi, "The Nucleosynthesis of ^{26}Al and ^{60}Fe in Solar Metallicity Stars Extending in Mass from 11 to 120 $M_{\odot}$: The Hydrostatic and Explosive Contributions," *The Astrophysical Journal*, vol. 647, no. 1, pp. 483–500, 2006.

[72] F. X. Timmes, S. E. Woosley, and D. H. Hartmann, "Galactic Chemical Evolution: Hydrogen through Zinc," *Astrophysics Journal*, vol. 449, no. 204, pp. 1–22, 1995.

[73] R. Diehl, "Cosmic Gamma-Ray Spectroscopy," *Astronomical Review*, vol. 9, no. 3, pp. 1–54, 2014.

[74] W. Wang, M. J. Harris, R. Diehl, H. Halloin, B. Cordier, A. W. Strong, K. Kretschmer, J. Knödlseder, P. Jean, G. G. Lichti, J. P. Roques, S. Schanne, A. Von Kienlin, G. Wei-

denspointner, and C. Wunderer, "SPI observations of the diffuse ^{60}Fe emission in the Galaxy," *Astronomy and Astrophysics*, vol. 469, no. 3, pp. 1005–1012, 2007.

[75] L. Fimiani, D. L. Cook, T. Faestermann, J. M. Gómez-Guzmán, K. Hain, G. Herzog, K. Knie, G. Korschinek, P. Ludwig, J. Park, R. C. Reedy, and G. Rugel, "Interstellar ^{60}Fe on the surface of the moon," *Physical Review Letters*, vol. 116, no. 15, 2016.

[76] E. Uberseder, T. Adachi, T. Aumann, S. Beceiro-Novo, K. Boretzky, C. Caesar, I. Dillmann, O. Ershova, A. Estrade, F. Farinon, J. Hagdahl, T. Heftrich, M. Heil, M. Heine, M. Holl, A. Ignatov, H. T. Johansson, N. Kalantar, C. Langer, T. Le Bleis, Y. A. Litvinov, J. Marganiec, A. Movsesyan, M. A. Najafi, T. Nilsson, C. Nociforo, V. Panin, S. Pietri, R. Plag, A. Prochazka, G. Rastrepina, R. Reifarth, V. Ricciardi, C. Rigollet, D. M. Rossi, D. Savran, H. Simon, K. Sonnabend, B. Streicher, S. Terashima, R. Thies, Y. Togano, V. Volkov, F. Wamers, H. Weick, M. Weigand, M. Wiescher, C. Wimmer, N. Winckler, and P. J. Woods, "First experimental constraint on the ^{59}Fe(n,γ)^{60}Fe reaction cross section at astrophysical energies via the coulomb dissociation of ^{60}Fe," *Physical Review Letters*, vol. 112, no. 21, 2014.

[77] A. Couture and R. Reifarth, "Direct measurements of neutron capture on radioactive isotopes," *Atomic Data and Nuclear Data Tables*, vol. 93, no. 5, pp. 807–830, 2007.

[78] A. Voinov, E. Algin, U. Agvaanluvsan, T. Belgya, R. Chankova, M. Guttormsen, G. E. Mitchell, J. Rekstad, A. Schiller, and S. Siem, "Large Enhancement of Radiative Strength for Soft Transitions in the Quasicontinuum," *Physical Review Letters*, vol. 93, no. 14, 2004.

[79] M. D. Jones, A. O. Macchiavelli, M. Wiedeking, L. A. Bernstein, H. L. Crawford, C. M. Campbell, R. M. Clark, M. Cromaz, P. Fallon, I. Y. Lee, M. Salathe, A. Wiens, A. D. Ayangeakaa, D. L. Bleuel, S. Bottoni, M. P. Carpenter, H. M. Davids, J. Elson, A. Görgen, M. Guttormsen, R. V. F. Janssens, J. E. Kinnison, L. Kirsch, A. C. Larsen, T. Lauritsen, W. Reviol, D. G. Sarantites, S. Siem, A. V. Voinov, and S. Zhu,

"Examination of the low-energy enhancement of the γ-ray strength function of ^{56}Fe," *Phys. Rev. C*, vol. 97, p. 024327, 2018.

[80] M. Wiedeking, L. A. Bernstein, M. Krtička, D. L. Bleuel, J. M. Allmond, M. S. Basunia, J. T. Burke, P. Fallon, R. B. Firestone, B. L. Goldblum, R. Hatarik, P. T. Lake, I.-Y. Lee, S. R. Lesher, S. Paschalis, M. Petri, L. Phair, and N. D. Scielzo, "Low-Energy Enhancement in the Photon Strength of ^{95}Mo," *Phys. Rev. Lett.*, vol. 108, p. 162503, 2012.

[81] A. Simon, M. Guttormsen, A. C. Larsen, C. W. Beausang, P. Humby, J. T. Burke, R. J. Casperson, R. O. Hughes, T. J. Ross, J. M. Allmond, R. Chyzh, M. Dag, J. Koglin, E. McCleskey, M. McCleskey, S. Ota, and A. Saastamoinen, "First observation of low-energy γ-ray enhancement in the rare-earth region," *Phys. Rev. C*, vol. 93, p. 034303, 2016.

[82] A. C. Larsen and S. Goriely, "Impact of a low-energy enhancement in the γ-ray strength function on the neutron-capture cross section," *Phys. Rev. C*, vol. 82, p. 014318, 2010.

[83] G. A. Bartholomew, E. D. Earle, A. J. Ferguson, J. W. Knowles, and M. A. Lone, *Gamma-Ray Strength Functions*, pp. 229–324. Boston, MA: Springer US, 1973.

[84] J. M. Blatt and V. F. Weisskopf, "Theoretical Nuclear Physics," *New York*, 1952.

[85] S. F. Mughabghab, *Atlas of Neutron Resonances: Resonance Parameters and Thermal Cross Sections. Z=1-100.* Elsevier, 2006.

[86] D. M. Brink, *Some Aspects of the Interaction of Fields with Matter.* PhD thesis, University of Oxford, 1955.

[87] P. Axel, "Electric Dipole Ground-State Transition Width Strength Function and 7-Mev Photon Interactions," *Phys. Rev.*, vol. 126, pp. 671–683, 1962.

[88] S. Kadmenskii, V. Markushev, and V. Furman, "Dynamical enhancement of parity violation effects for compound states and giant 0^- resonances," *Sov. J. Nucl. Phys.*, vol. 37:3, 1983.

[89] S. A. Sheets, *Photon Strength Function and Resonance Spin Assignments in 95,96Mo.* PhD thesis, North Carolina State University, 2007.

[90] B. Bayarbadrakh, *Neutron Capture Reactions on Gadolinium Isotopes.* PhD thesis, North Carolina State University, 2010.

[91] M. R. Mumpower, T. Kawano, J. L. Ullmann, M. Krtička, and T. M. Sprouse, "Estimation of M1 scissors mode strength for deformed nuclei in the medium- to heavy-mass region by statistical Hauser-Feshbach model calculations," *Physical Review C*, vol. 96, no. 2, pp. 1–10, 2017.

[92] A. Gilbert and A. G. W. Cameron, "A COMPOSITE NUCLEAR-LEVEL DENSITY FORMULA WITH SHELL CORRECTIONS," *Canadian Journal of Physics*, vol. 43, no. 8, pp. 1446–1496, 1965.

[93] P. W. Lisowski and K. F. Schoenberg, "The Los Alamos Neutron Science Center," *Nuclear Instruments and Methods in Physics Research Section A: Accelerators, Spectrometers, Detectors and Associated Equipment*, vol. 562, no. 2, pp. 910 – 914, 2006. Proceedings of the 7th International Conference on Accelerator Applications.

[94] M. Heil, R. Reifarth, M. Fowler, R. Haight, F. Kappeler, R. Rundberg, E. Seabury, J. Ullmann, J. Wilhelmy, and K. Wisshak, "A $4\pi BaF_2$ detector for (n,γ) cross-section measurements at a spallation neutron source," *Nuclear Instruments and Methods in Physics Research Section A: Accelerators, Spectrometers, Detectors and Associated Equipment*, vol. 459, no. 1, pp. 229 – 246, 2001.

[95] P. W. Lisowski, C. D. Bowman, G. J. Russell, and S. A. Wender, "The Los Alamos National Laboratory Spallation Neutron Sources," *Nuclear Science and Engineering*, vol. 106, no. 2, pp. 208–218, 1990.

[96] K. Macon, *Direct Measurements of Nuclear Reactions in Hot Stellar Environments.* PhD thesis, Louisiana State University, 2016.

[97] R. Reifarth, T. Bredeweg, A. Alpizar-Vicente, J. Browne, E.-I. Esch, U. Greife, R. Haight, R. Hatarik, A. Kronenberg, J. O'Donnell, R. Rundberg, J. Ullmann, D. Vieira, J. Wilhelmy, and J. Wouters, "Background identification and suppression for the measurement of (n,γ) reactions with the DANCE array at LANSCE," *Nuclear Instruments and Methods in Physics Research Section A: Accelerators, Spectrometers, Detectors and Associated Equipment*, vol. 531, no. 3, pp. 530 – 543, 2004.

[98] M. Jandel, T. Bredeweg, A. Couture, M. Fowler, E. Bond, M. Chadwick, R. Clement, E.-I. Esch, J. O'Donnell, R. Reifarth, R. Rundberg, J. Ullmann, D. Vieira, J. Wilhelmy, J. Wouters, R. Macri, C. Wu, and J. Becker, "GEANT4 simulations of the DANCE array," *Nuclear Instruments and Methods in Physics Research Section B: Beam Interactions with Materials and Atoms*, vol. 261, no. 1, pp. 1117 – 1121, 2007. The Application of Accelerators in Research and Industry.

[99] A. Couture. Personal communication, 2020.

[100] S. Mosby, F. Tovesson, A. Couture, D. Duke, V. Kleinrath, R. Meharchand, K. Meierbachtol, J. OD́onnell, B. Perdue, D. Richman, and D. Shields, "A fission fragment detector for correlated fission output studies," *Nuclear Instruments and Methods in Physics Research Section A: Accelerators, Spectrometers, Detectors and Associated Equipment*, vol. 757, pp. 75 – 81, 2014.

[101] T. Wang, M. Lee, G. Kim, Y. Oh, W. Namkung, T.-I. Ro, Y.-R. Kang, M. Igashira, and T. Katabuchi, "Measurement of keV-neutron capture cross-sections and capture γ-ray spectra of ^{56}Fe and ^{57}Fe," *Nuclear Instruments and Methods in Physics Research Section B: Beam Interactions with Materials and Atoms*, vol. 268, no. 5, pp. 440 – 449, 2010.

[102] G. Rohr, A. Brusegan, F. Corvi, R. Shelley, T. V. D. Veen, and E. Procedure, "Resonance Parameters of ^{57}Fe," in *Nuclear Data for Science and Technology*, pp. 139–142, Dordrecht: Springer, 1983.

[103] G. Rohr, "The Status of Structural Material Data in the Resolved Resonance Region," in *Proceedings of the NEANDC/NEACRP Specialist's Meeting on Fast-Neutron Capture Cross Sections* (A. B. Smith and W. P. Poenitz, eds.), pp. 394–416, Argonne National Laboratory, Office of Scientific and Technical Information, 1982.

[104] A. V. Voinov, S. M. Grimes, U. Agvaanluvsan, E. Algin, T. Belgya, C. R. Brune, M. Guttormsen, M. J. Hornish, T. Massey, G. E. Mitchell, J. Rekstad, A. Schiller, and S. Siem, "Level density of ^{56}Fe and low-energy enhancement of γ-strength function," *Physical Review C - Nuclear Physics*, vol. 74, no. 1, pp. 1–6, 2006.

[105] C. Prokop, C. Fry, and A. Couture, "DANCE Analzyer GitHub," 2020.

[106] J. Kroll, B. Baramsai, G. E. Mitchell, U. Agvaanluvsan, F. Bečvář, T. A. Bredeweg, A. Chyzh, A. Couture, D. Dashdorj, R. C. Haight, M. Jandel, A. L. Keksis, M. Krtička, J. M. O'Donnell, W. Parker, R. S. Rundberg, J. L. Ullmann, S. Valenta, D. J. Vieira, C. Walker, and C. Y. Wu, "Strength of the scissors mode in odd-mass Gd isotopes from the radiative capture of resonance neutrons," *Physical Review C - Nuclear Physics*, vol. 88, no. 3, pp. 1–15, 2013.

[107] J. L. Ullmann, T. Kawano, T. A. Bredeweg, A. Couture, R. C. Haight, M. Jandel, J. M. O'Donnell, R. S. Rundberg, D. J. Vieira, J. B. Wilhelmy, J. A. Becker, A. Chyzh, C. Y. Wu, B. Baramsai, G. E. Mitchell, and M. Krtika, "Cross section and γ -ray spectra for ^{238}U (n, γ) measured with the DANCE detector array at the Los Alamos Neutron Science Center," *Physical Review C - Nuclear Physics*, vol. 89, no. 3, pp. 1–8, 2014.

[108] F. Bečvář, "Simulation of γ cascades in complex nuclei with emphasis on assessment of uncertainties of cascade-related quantities," *Nuclear Instruments and Methods in Physics Research Section A: Accelerators, Spectrometers, Detectors and Associated Equipment*, vol. 417, no. 2, pp. 434 – 449, 1998.

[109] M. Krtička. Personal communication, 2020.

[110] M. Krtička, S. Goriely, S. Hilaire, S. Péru, and S. Valenta, "Constraints on the dipole photon strength functions from experimental multistep cascade spectra," *Phys. Rev. C*, vol. 99, p. 044308, 2019.

[111] B. A. Brown and A. A. Larsen, "Large low-energy M1 strength for ^{56,57}Fe within the nuclear shell model," *Physical Review Letters*, vol. 113, no. 25, pp. 1–5, 2014.

[112] J. R. Winkelbauer, S. M. Mosby, A. Couture, H. Y. Lee, J. L. Ullmann, T. Kawano, G. Rusev, and M. Jandel, "Statistical neutron capture in the limit of low nuclear level density," *Physical Review C*, vol. 99, no. 024318, 2019.

[113] B. Becker, P. Talou, T. Kawano, Y. Danon, and I. Stetcu, "Monte Carlo Hauser-Feshbach predictions of prompt fission γ rays: Application to $n_{\mathrm{th}} + ^{235}$U, $n_{\mathrm{th}} + ^{239}$Pu, and ^{252}Cf (sf)," *Phys. Rev. C*, vol. 87, p. 014617, 2013.

[114] A. Ratkiewicz, J. A. Cizewski, J. E. Escher, G. Potel, J. T. Burke, R. J. Casperson, M. McCleskey, R. A. E. Austin, S. Burcher, R. O. Hughes, B. Manning, S. D. Pain, W. A. Peters, S. Rice, T. J. Ross, N. D. Scielzo, C. Shand, and K. Smith, "Towards Neutron Capture on Exotic Nuclei: Demonstrating $(d, p\gamma)$ as a Surrogate Reaction for (n, γ)," *Phys. Rev. Lett.*, vol. 122, p. 052502, 2019.

APPENDIX A

COMPARISON OF SIMULATIONS TO EXPERIMENTAL DATA

The following section contains figures produced during the comparison of experimental data to results from DICEBOX simulations. Each figure includes in its caption relevant information about the different states and models depicted. Unless otherwise noted, the axes should be assumed to be in units of energy (MeV) versus normalized intensity (arbitrary).

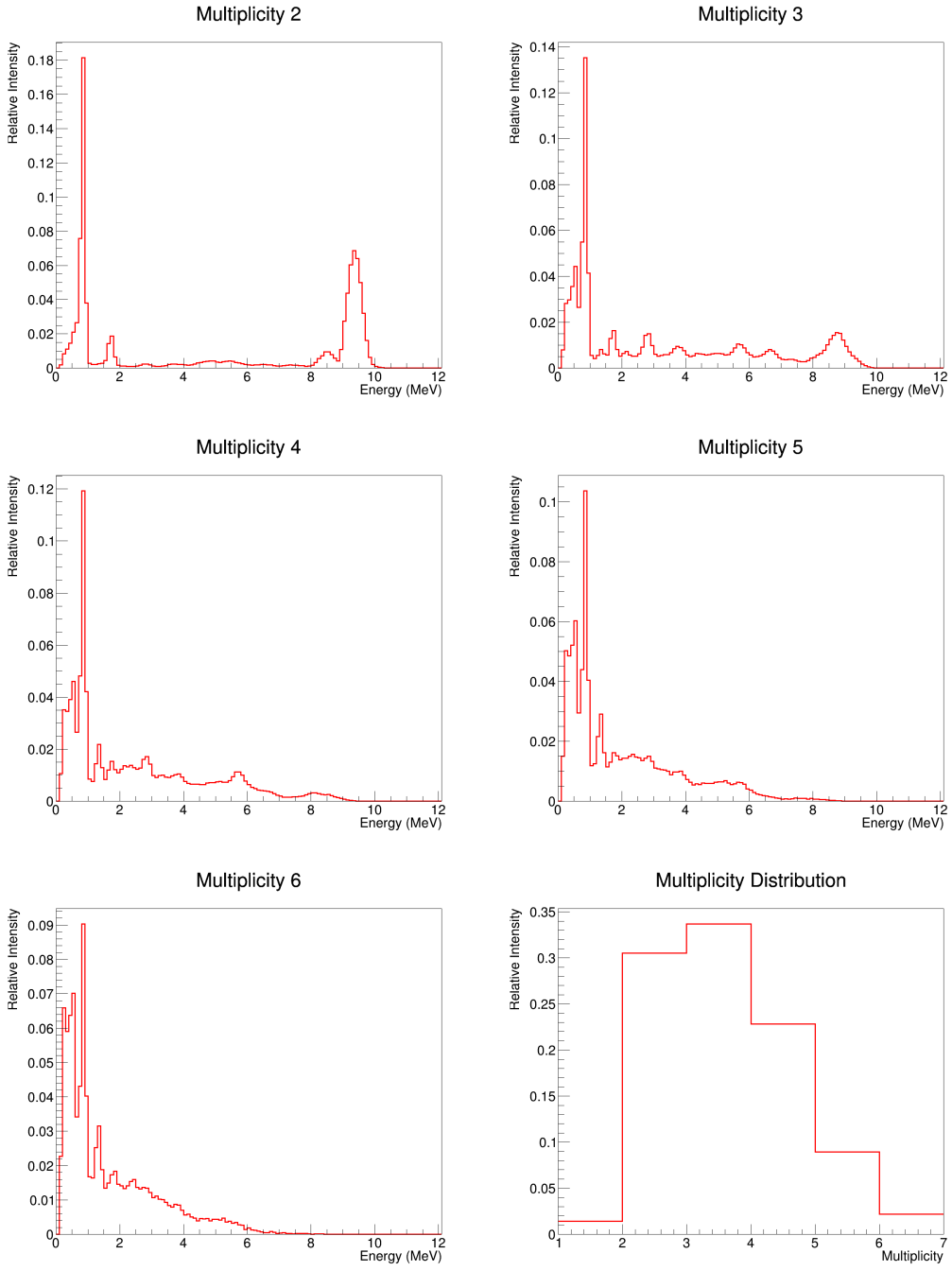

Figure A.1: Multi-step gamma-cascades and multiplicity distribution of the 1.62 keV resonance in ^{57}Fe. This is a p-wave resonance with $J^{\pi} = 2^{+}$.

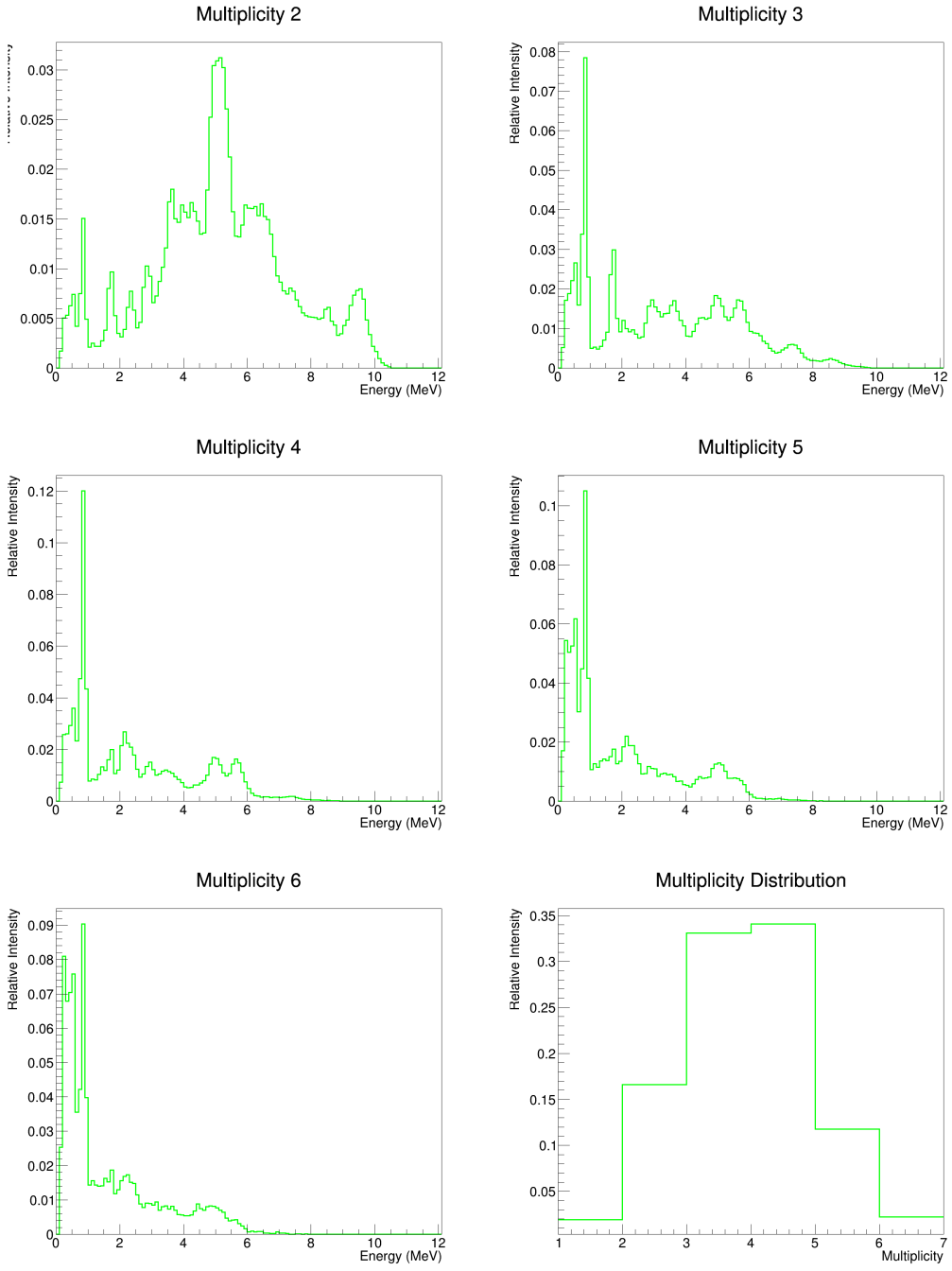

Figure A.2: Multi-step gamma-cascades and multiplicity distribution of the 3.955 keV resonance in ^{57}Fe. This is a s-wave resonance with $J^{\pi} = 0^{-}$.

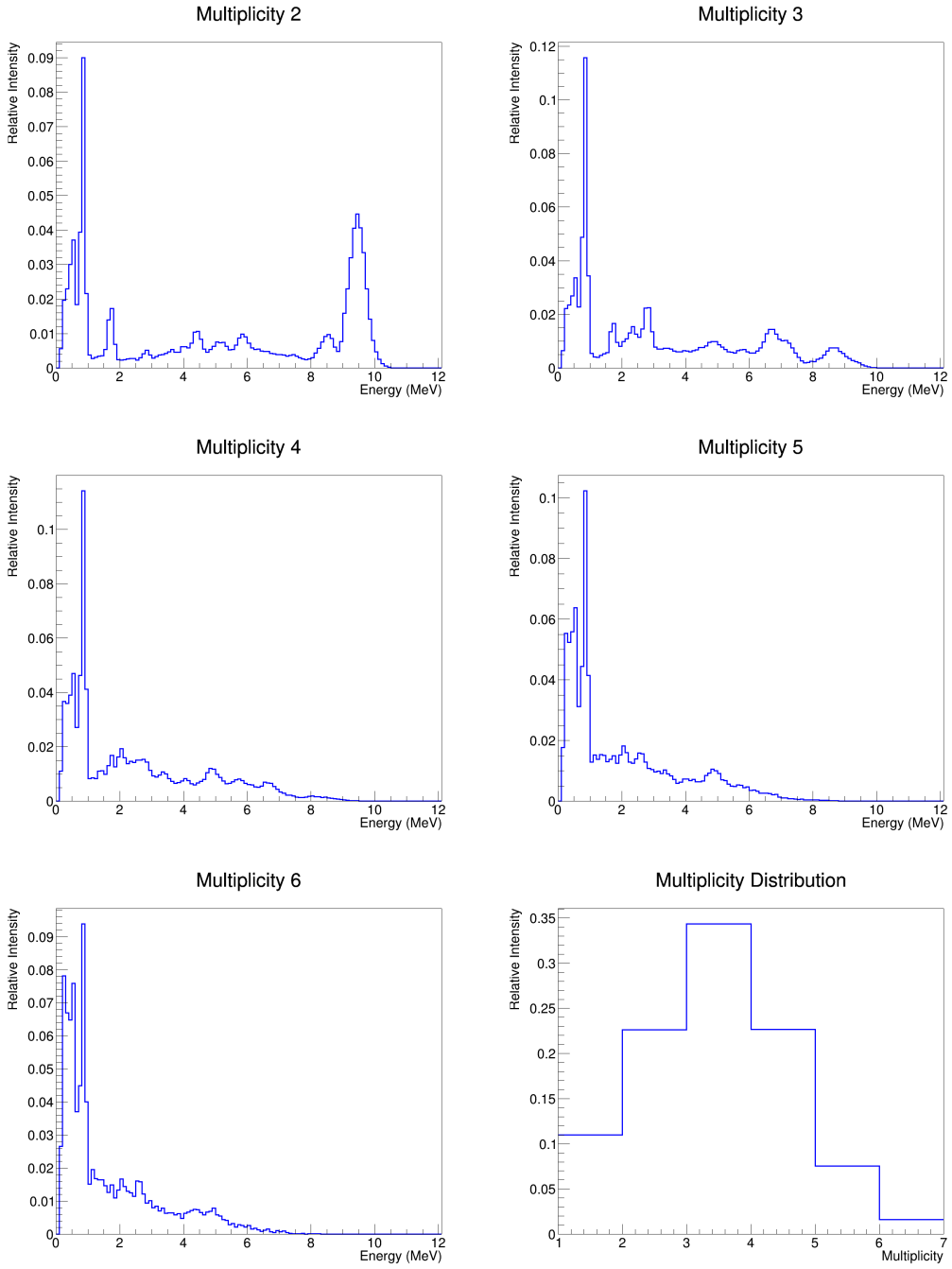

Figure A.3: Multi-step gamma-cascades and multiplicity distribution of the 6.22 keV resonance in ^{57}Fe. This is a s-wave resonance with $J^{\pi} = 1^{-}$.

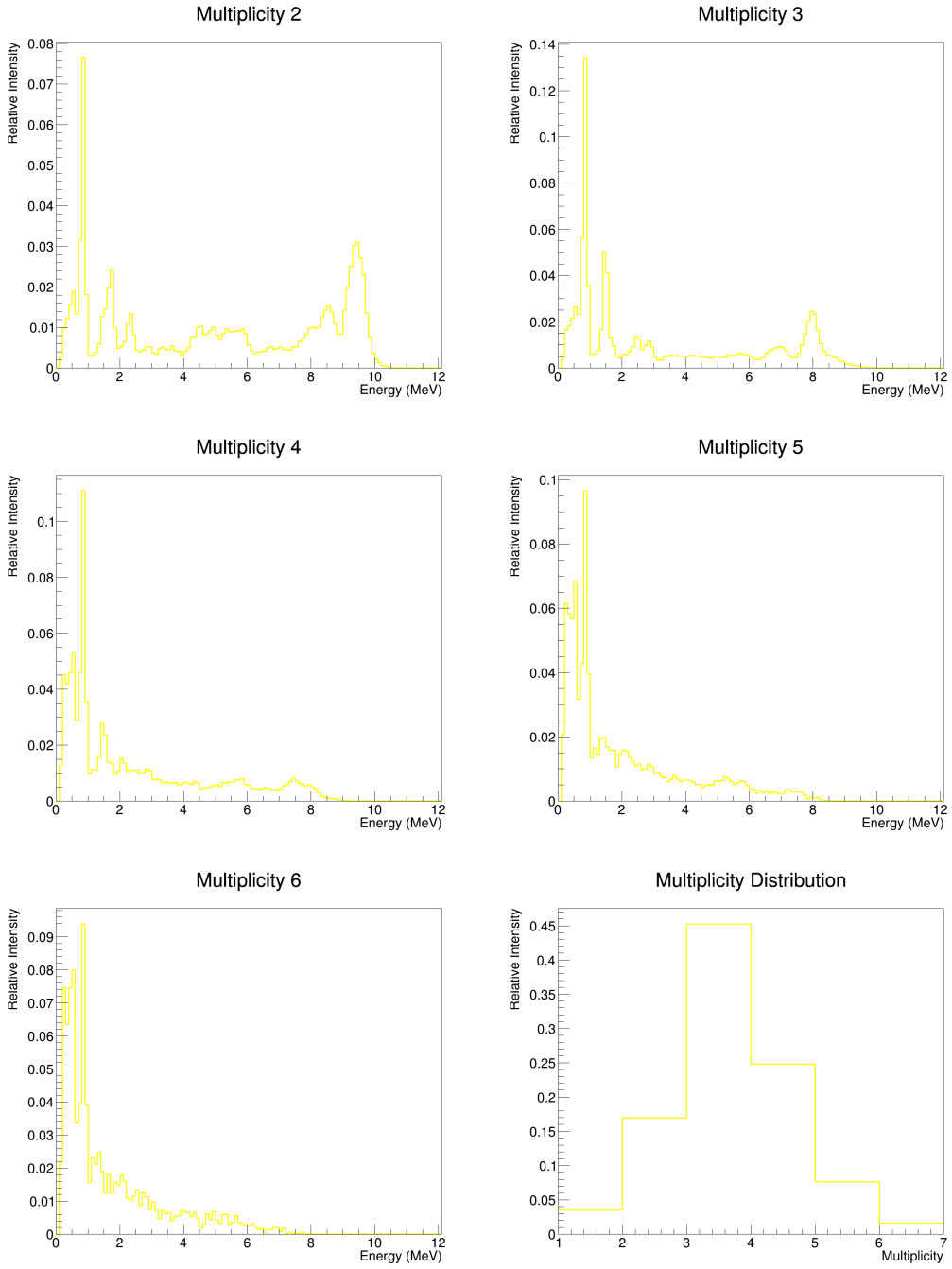

Figure A.4: Multi-step gamma-cascades and multiplicity distribution of the 13.95 keV resonance in ^{57}Fe. This is a s-wave resonance with $J^{\pi} = 1^{-}$.

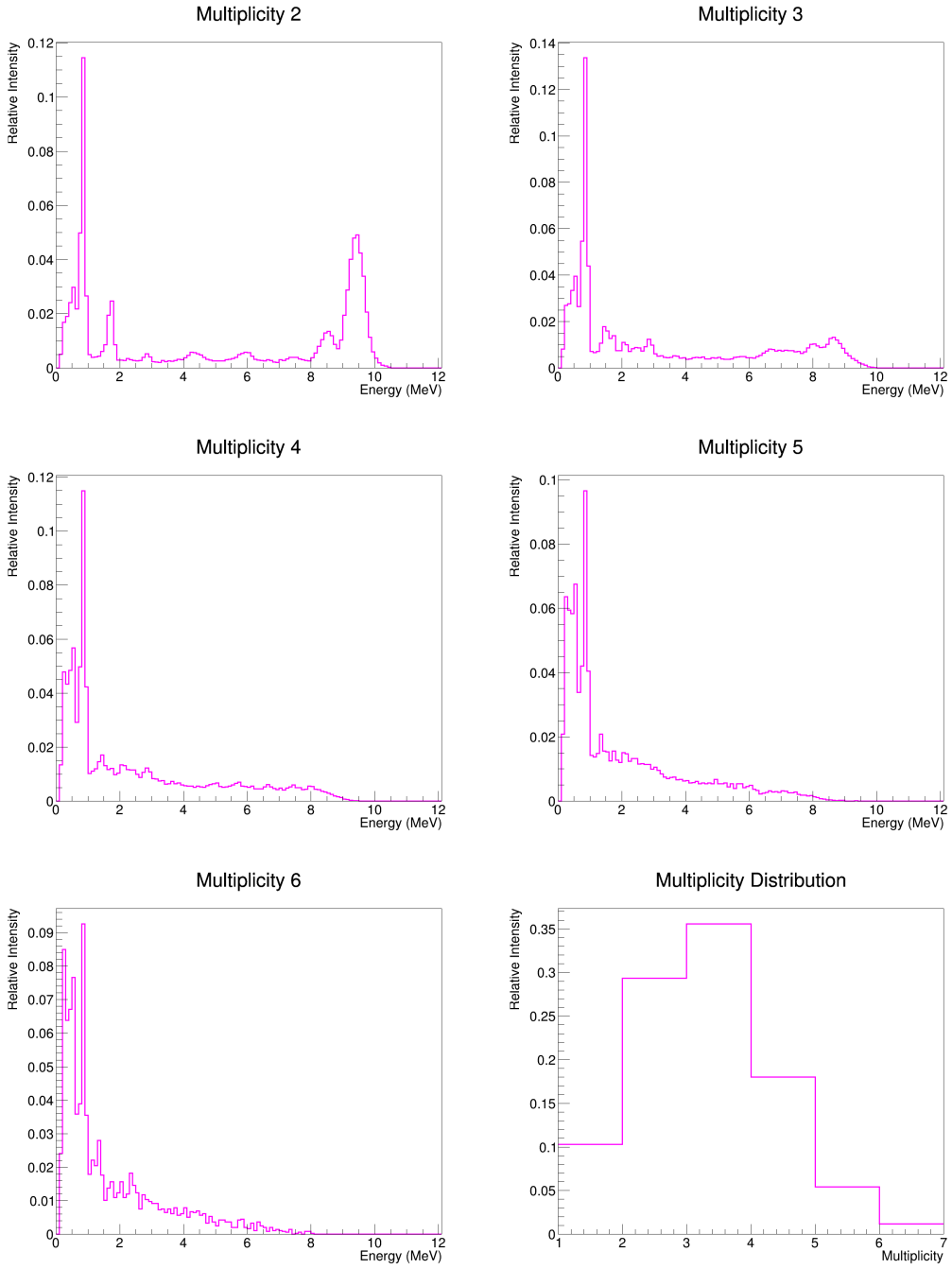

Figure A.5: Multi-step gamma-cascades and multiplicity distribution of the 29.05 keV resonance in ^{57}Fe. This is a s-wave resonance with $J^{\pi} = 1^{-}$.

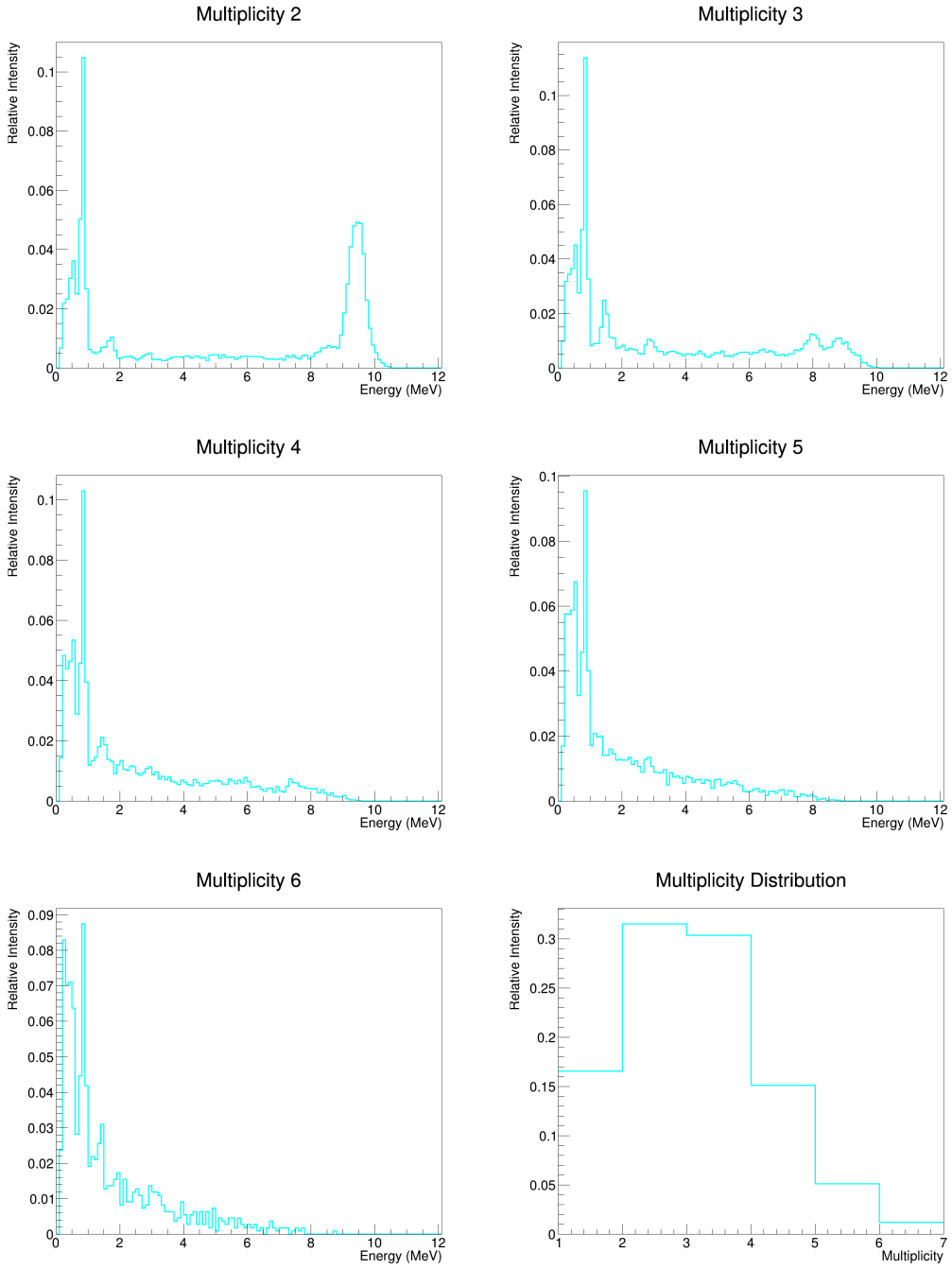

Figure A.6: Multi-step gamma-cascades and multiplicity distribution of the 41.40 keV resonance in ^{57}Fe. This is a s-wave resonance with $J^{\pi} = 1^{-}$.

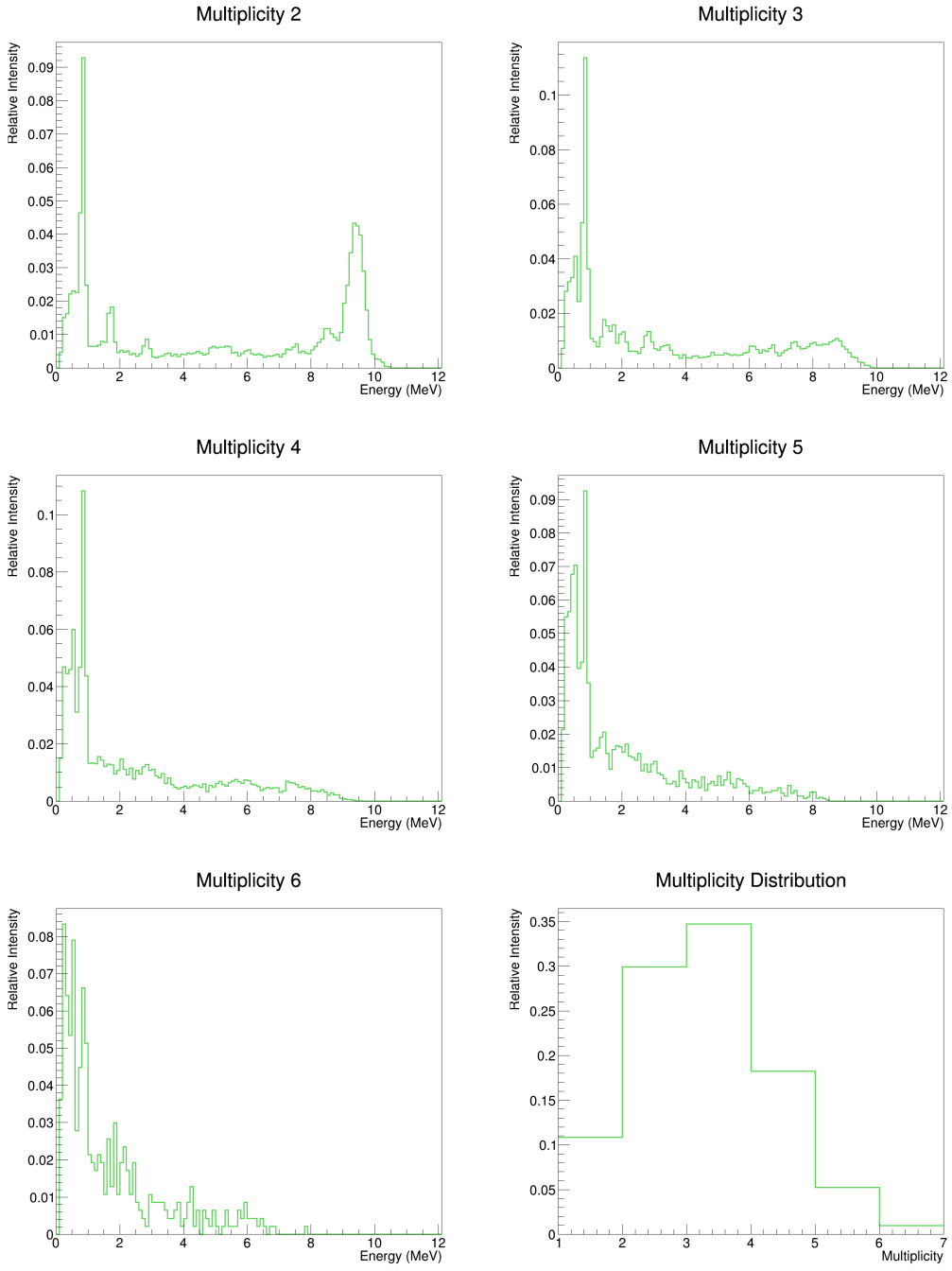

Figure A.7: Multi-step gamma-cascades and multiplicity distribution of the 47.05 keV resonance in ^{57}Fe. This is a s-wave resonance with $J^{\pi} = 1^{-}$.

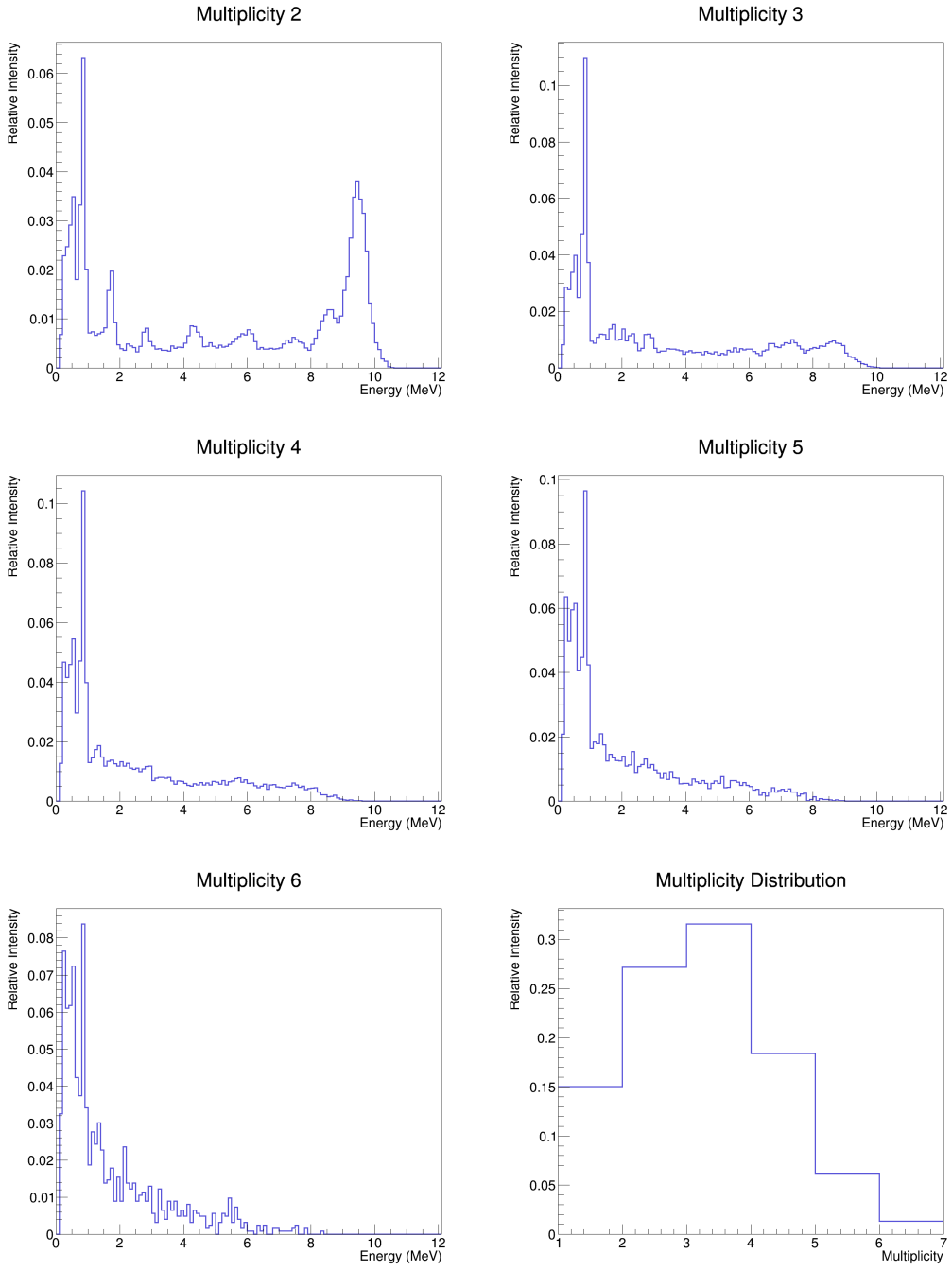

Figure A.8: Multi-step gamma-cascades and multiplicity distribution of the 61.05 keV resonance in ^{57}Fe. This is a s-wave resonance with $J^{\pi} = 1^{-}$.

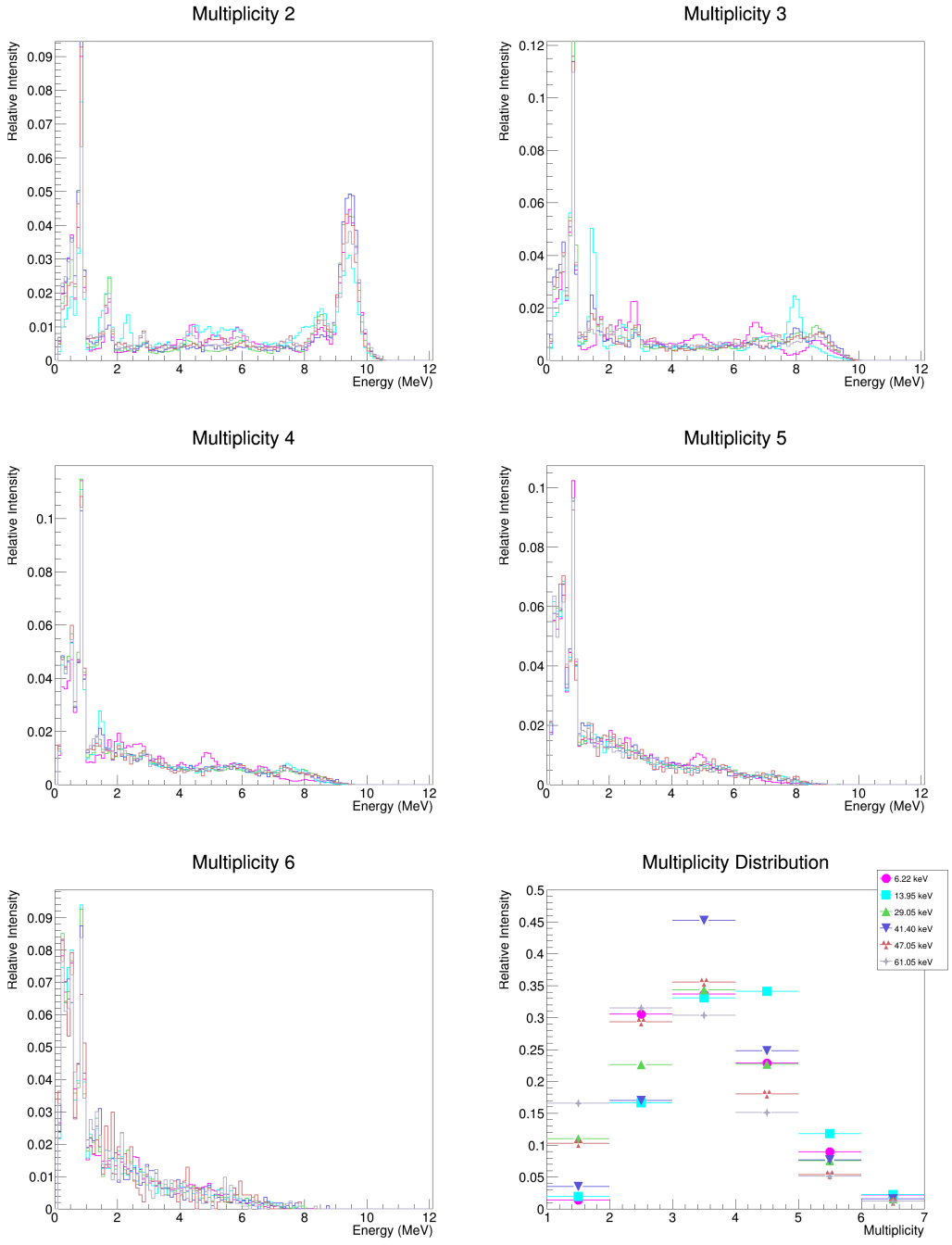

Figure A.9: Comparison of multi-step gamma-cascades and multiplicity distributions of 1^- resonances.

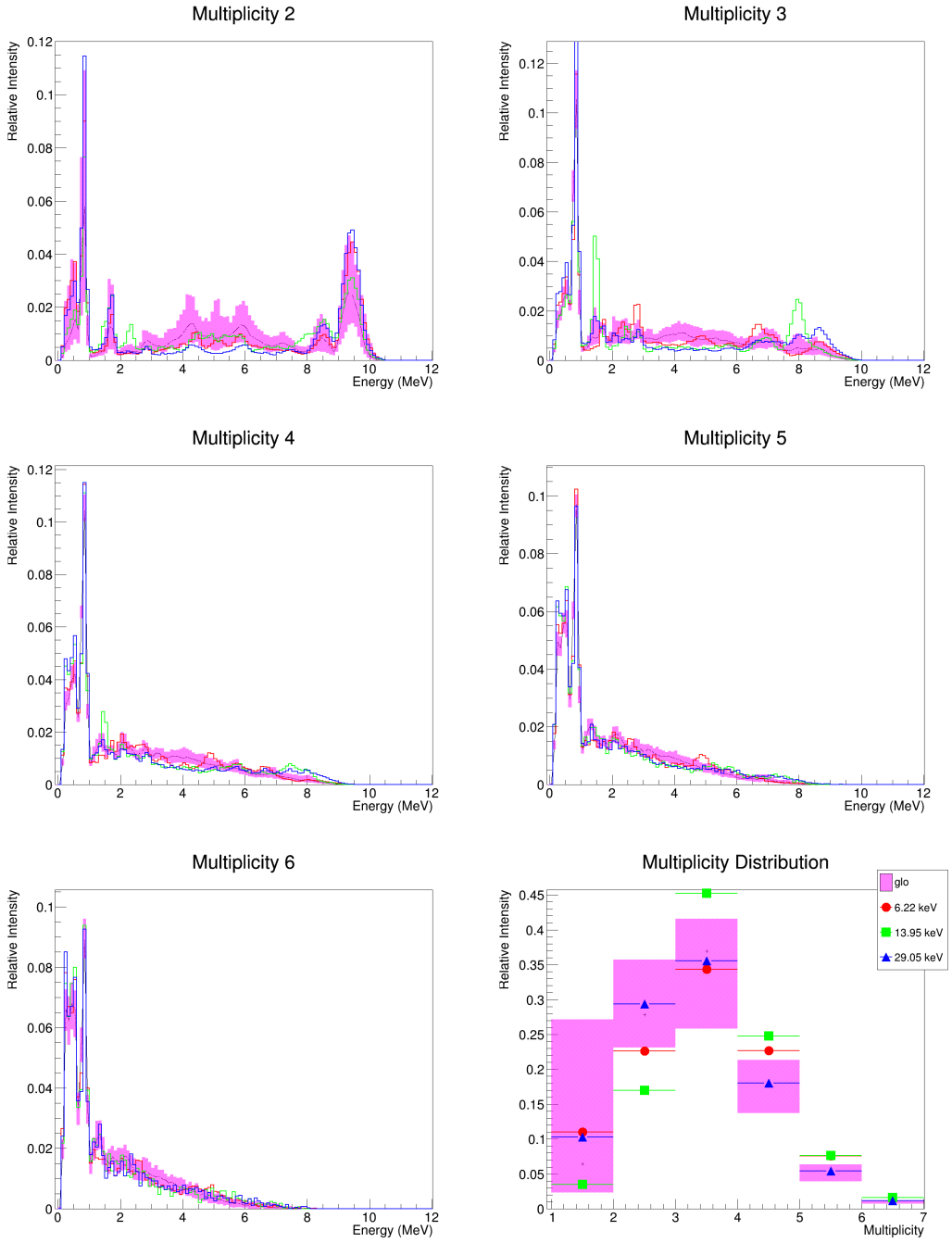

Figure A.10: Comparison of GLO simulations and 1^- resonances. This plot shows multi-step gamma-cascades and multiplicity distributions of experimental and simulated 1^- resonances. The simulations in this figure were produced using the GLO model of the photon strength function.

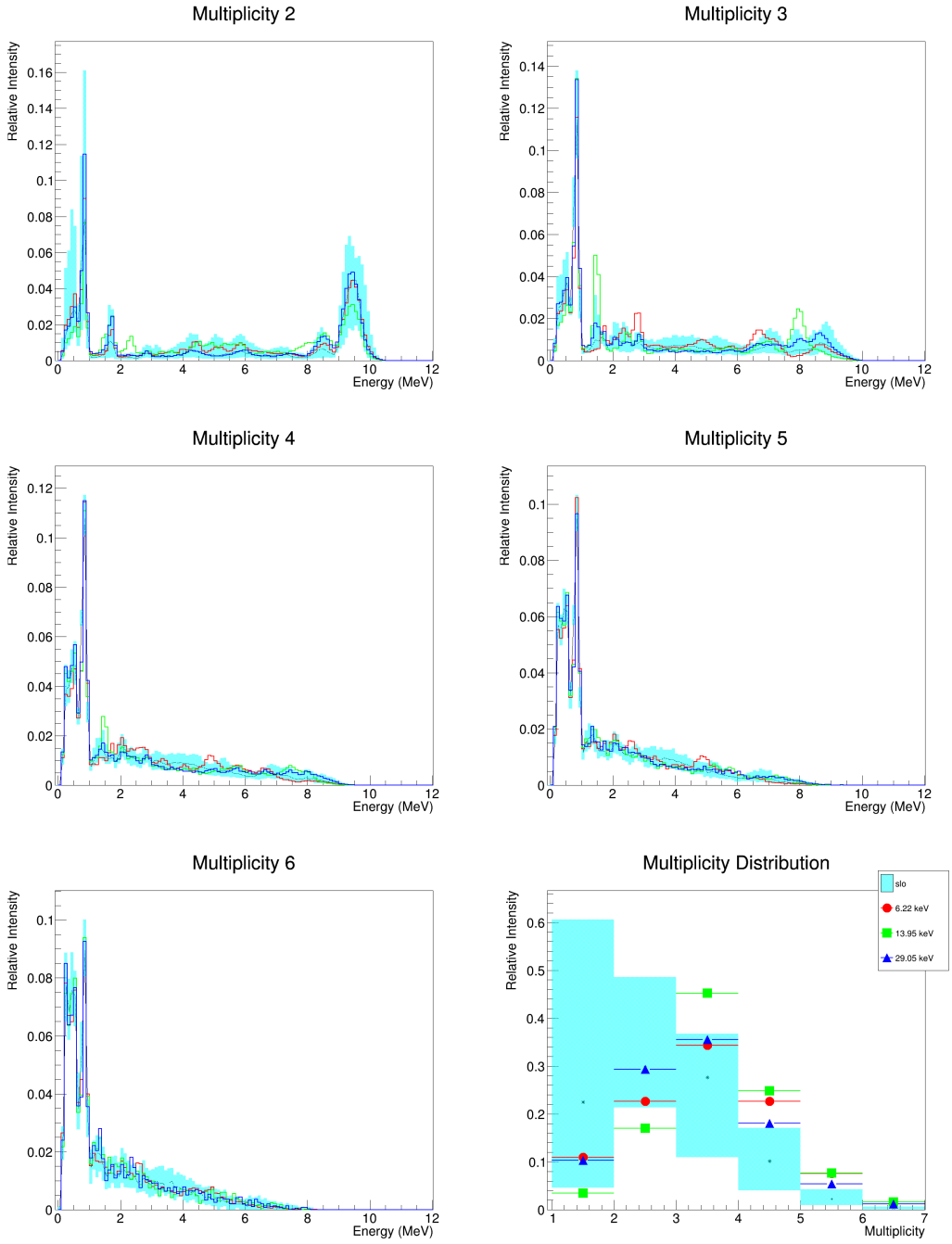

Figure A.11: Comparison of SLO simulations and 1^- resonances. This plot shows multi-step gamma-cascades and multiplicity distributions of experimental and simulated 1^- resonances. The simulations in this figure were produced using the SLO model of the photon strength function.

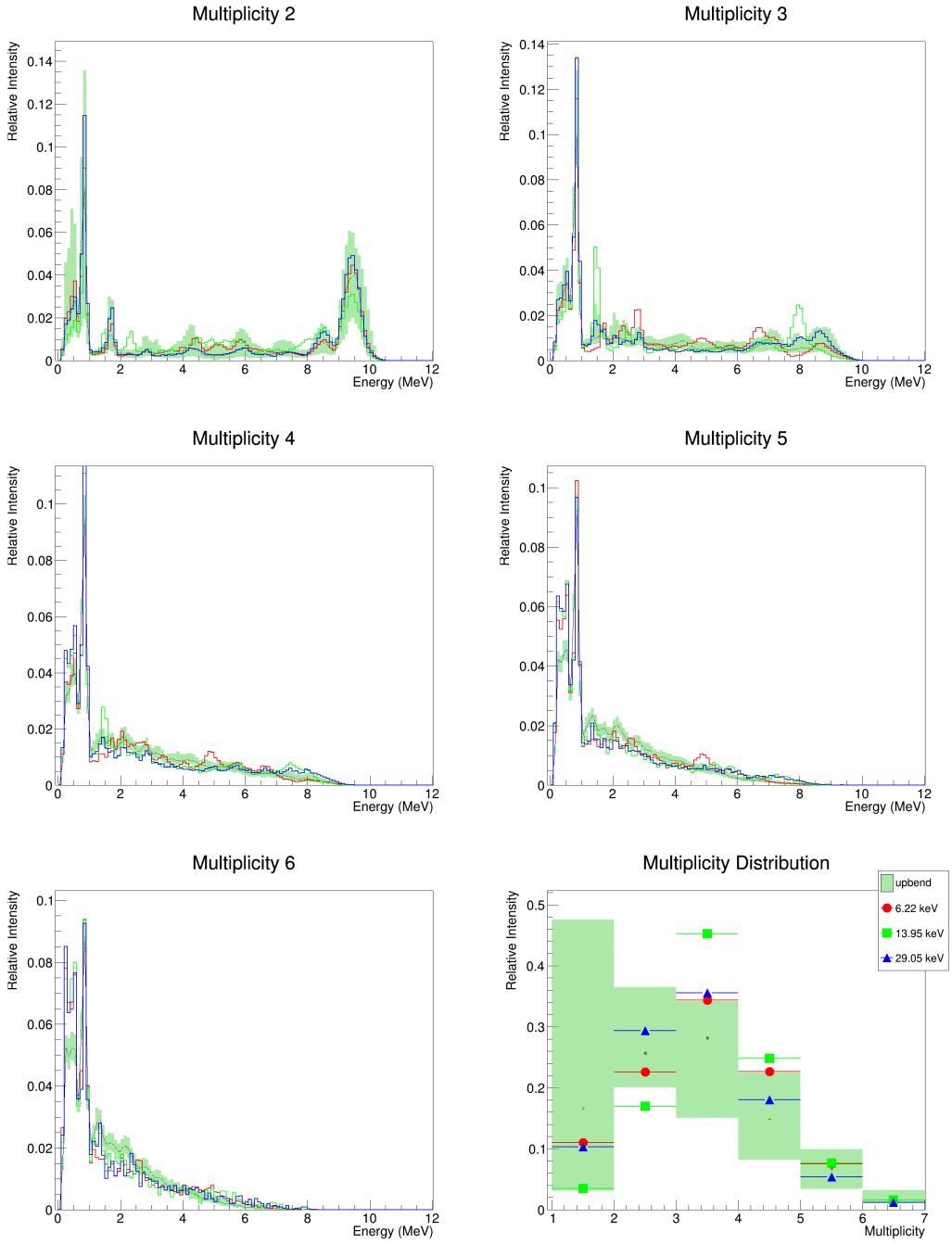

Figure A.12: Comparison of upbend simulations and 1^- resonances. This plot shows multi-step gamma-cascades and multiplicity distributions of experimental and simulated 1^- resonances. The simulations in this figure were produced using the upbend model of the photon strength function.

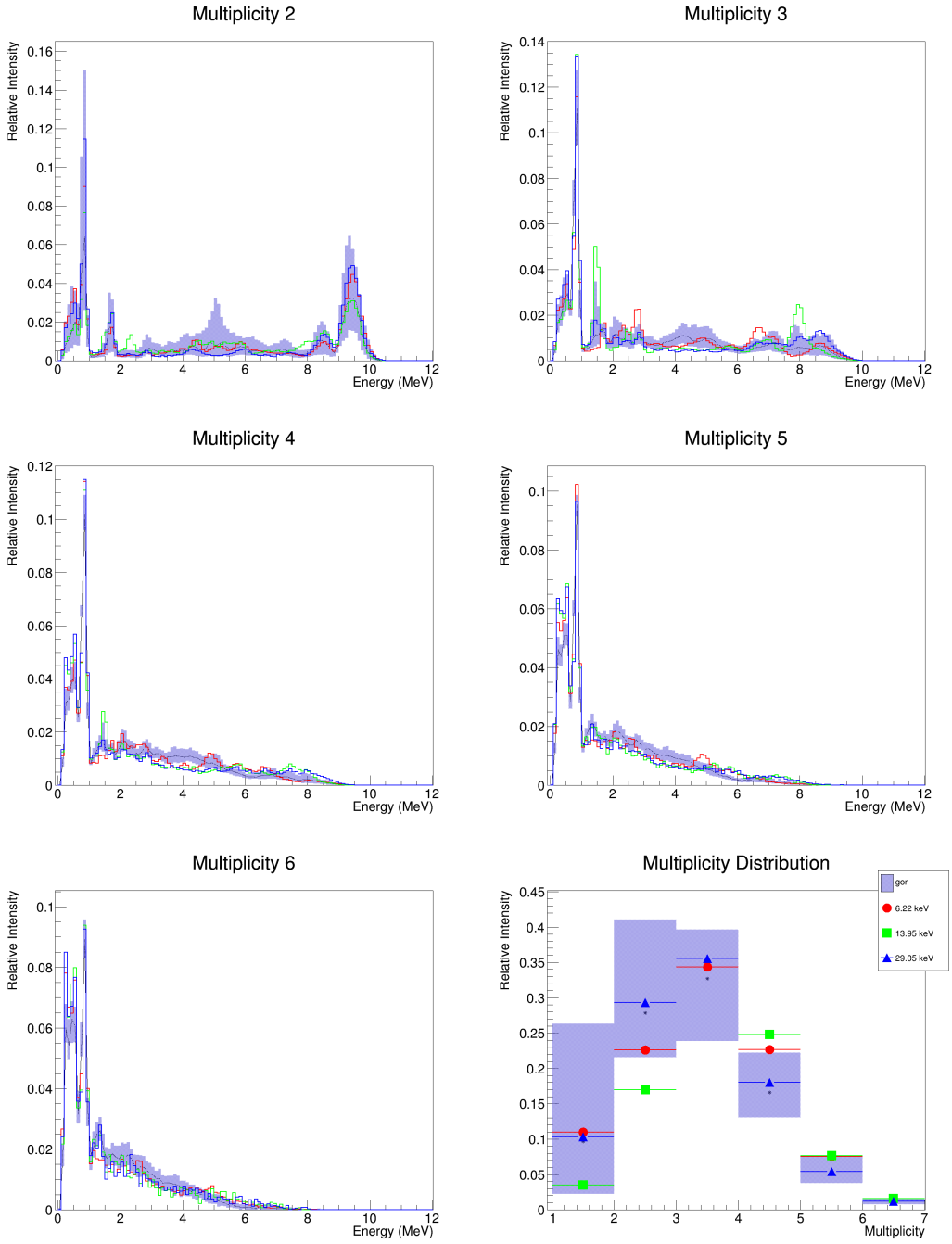

Figure A.13: Comparison of gor simulations and 1^- resonances. This plot shows multi-step gamma-cascades and multiplicity distributions of experimental and simulated 1^- resonances. The simulations in this figure were produced using the Goriely model of the photon strength function.

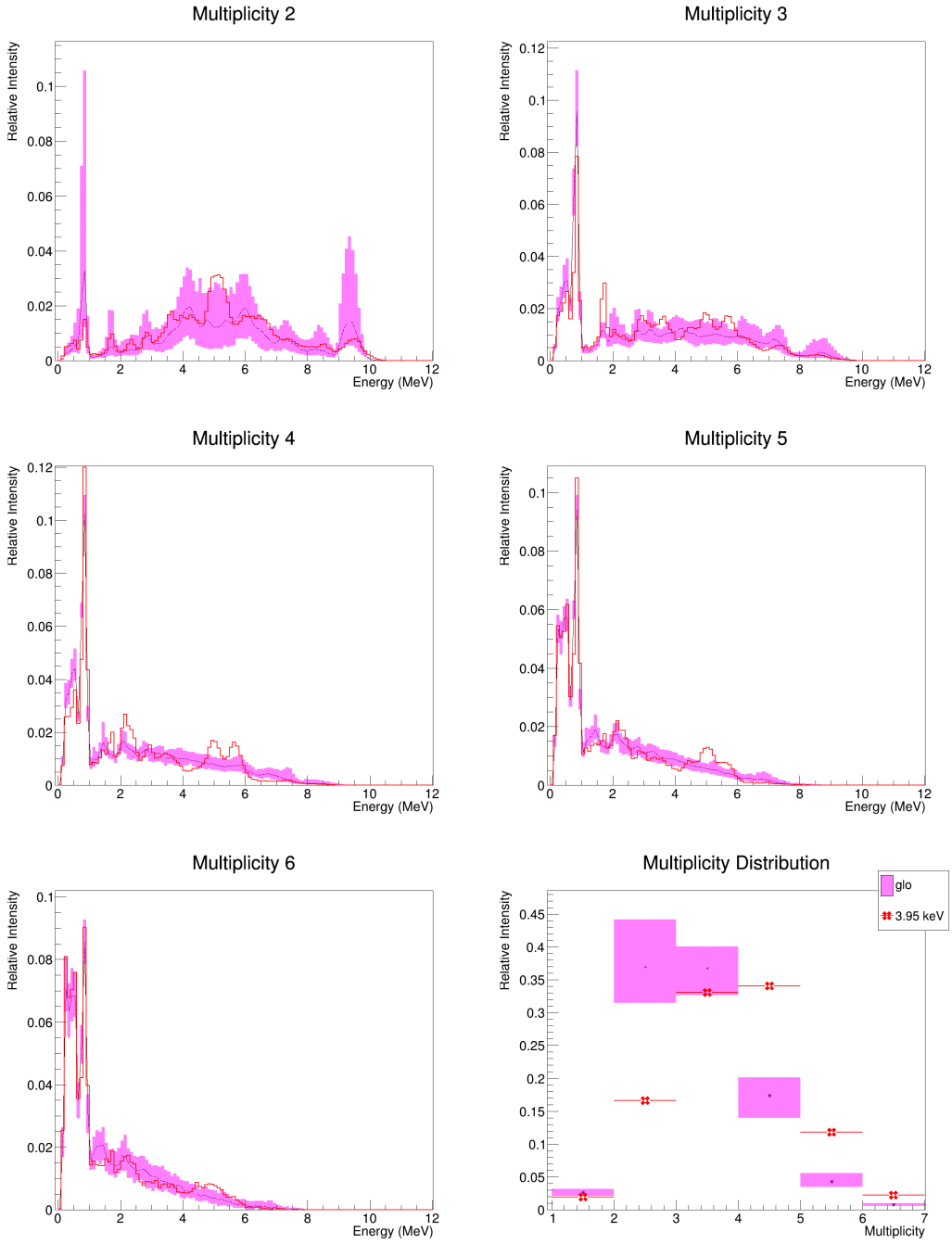

Figure A.14: Comparison of GLO simulations and 0^- resonances. This plot shows multi-step gamma-cascades and multiplicity distributions of experimental and simulated 0^- resonances. The simulations in this figure were produced using the GLO model of the photon strength function.

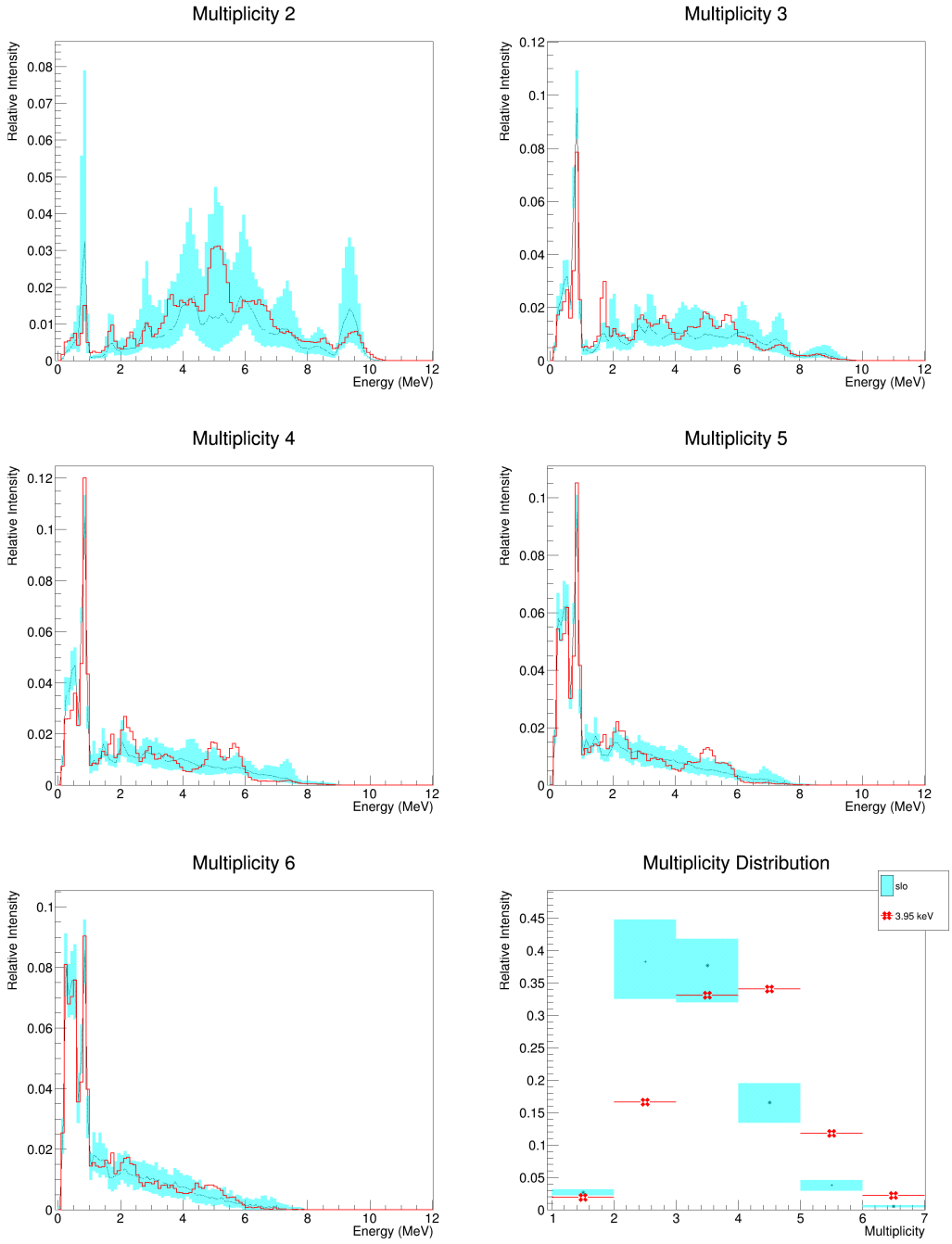

Figure A.15: Comparison of SLO simulations and 0^- resonances. This plot shows multi-step gamma-cascades and multiplicity distributions of experimental and simulated 0^- resonances. The simulations in this figure were produced using the SLO model of the photon strength function.

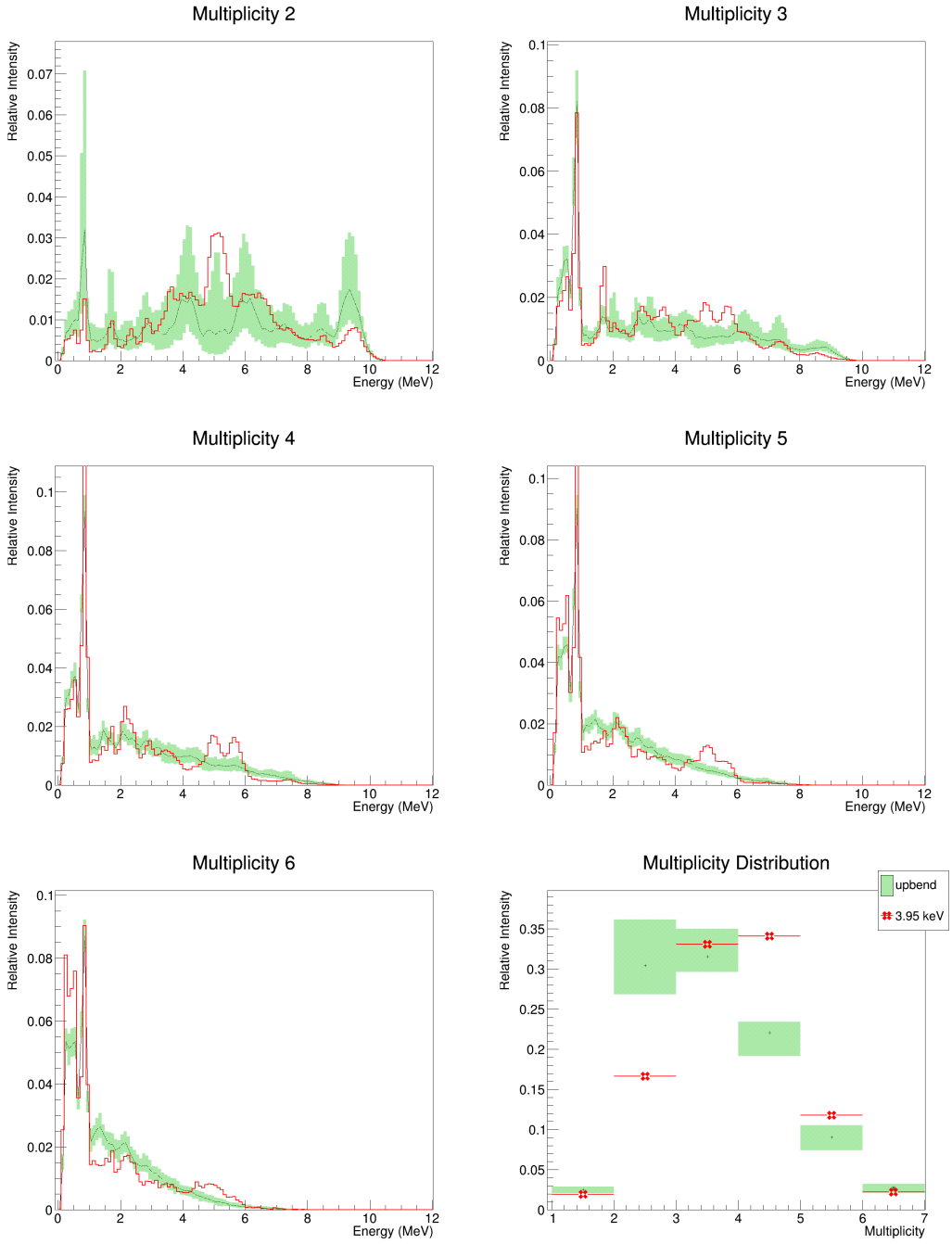

Figure A.16: Comparison of upbend simulations and 0^- resonances. This plot shows multi-step gamma-cascades and multiplicity distributions of experimental and simulated 0^- resonances. The simulations in this figure were produced using the upbend model of the photon strength function.

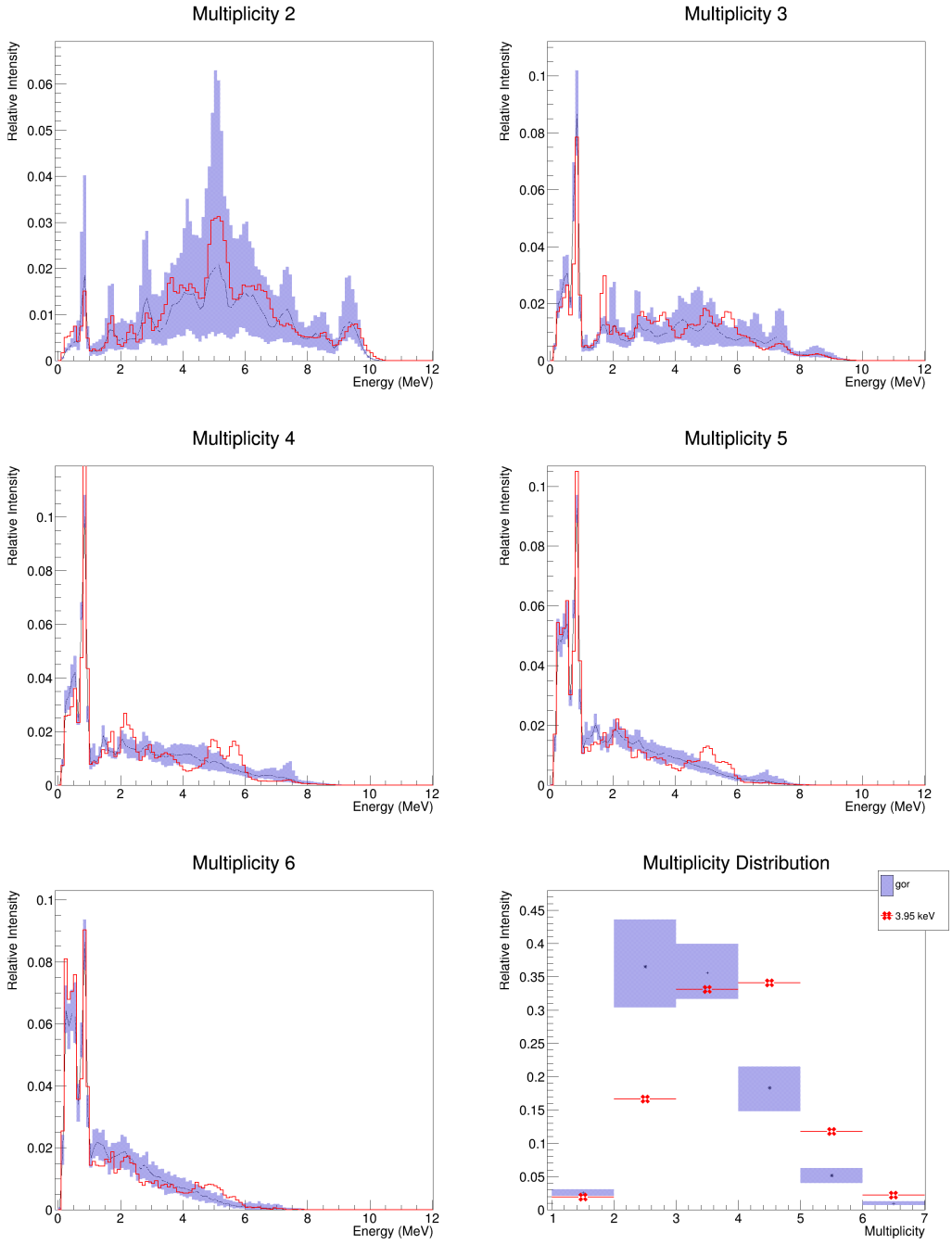

Figure A.17: Comparison of gor simulations and 0^- resonances. This plot shows multi-step gamma-cascades and multiplicity distributions of experimental and simulated 0^- resonances. The simulations in this figure were produced using the Goriely model of the photon strength function.

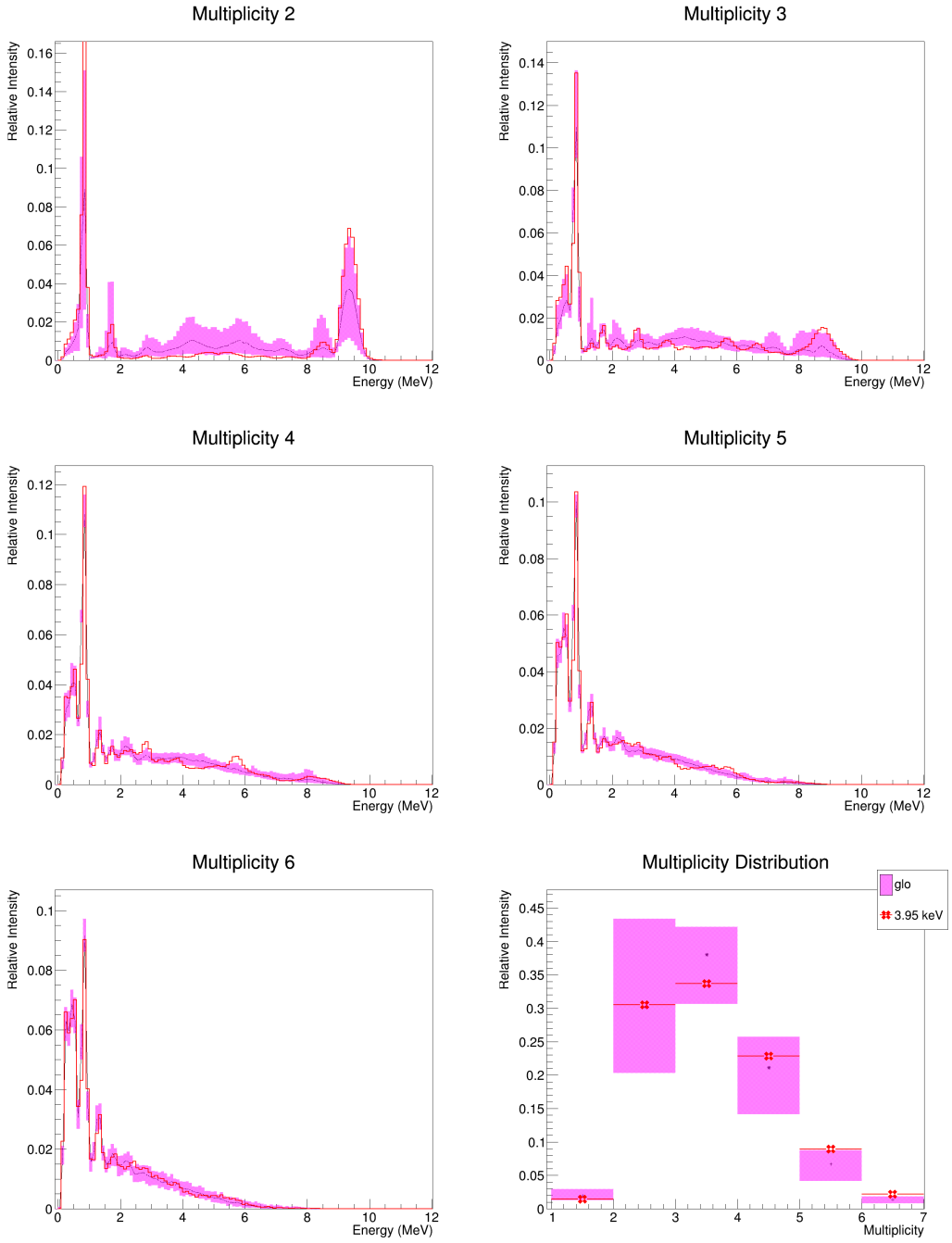

Figure A.18: Comparison of GLO simulations and 2^+ resonances. This plot shows multi-step gamma-cascades and multiplicity distributions of experimental and simulated 2^+ resonances. The simulations in this figure were produced using the GLO model of the photon strength function.

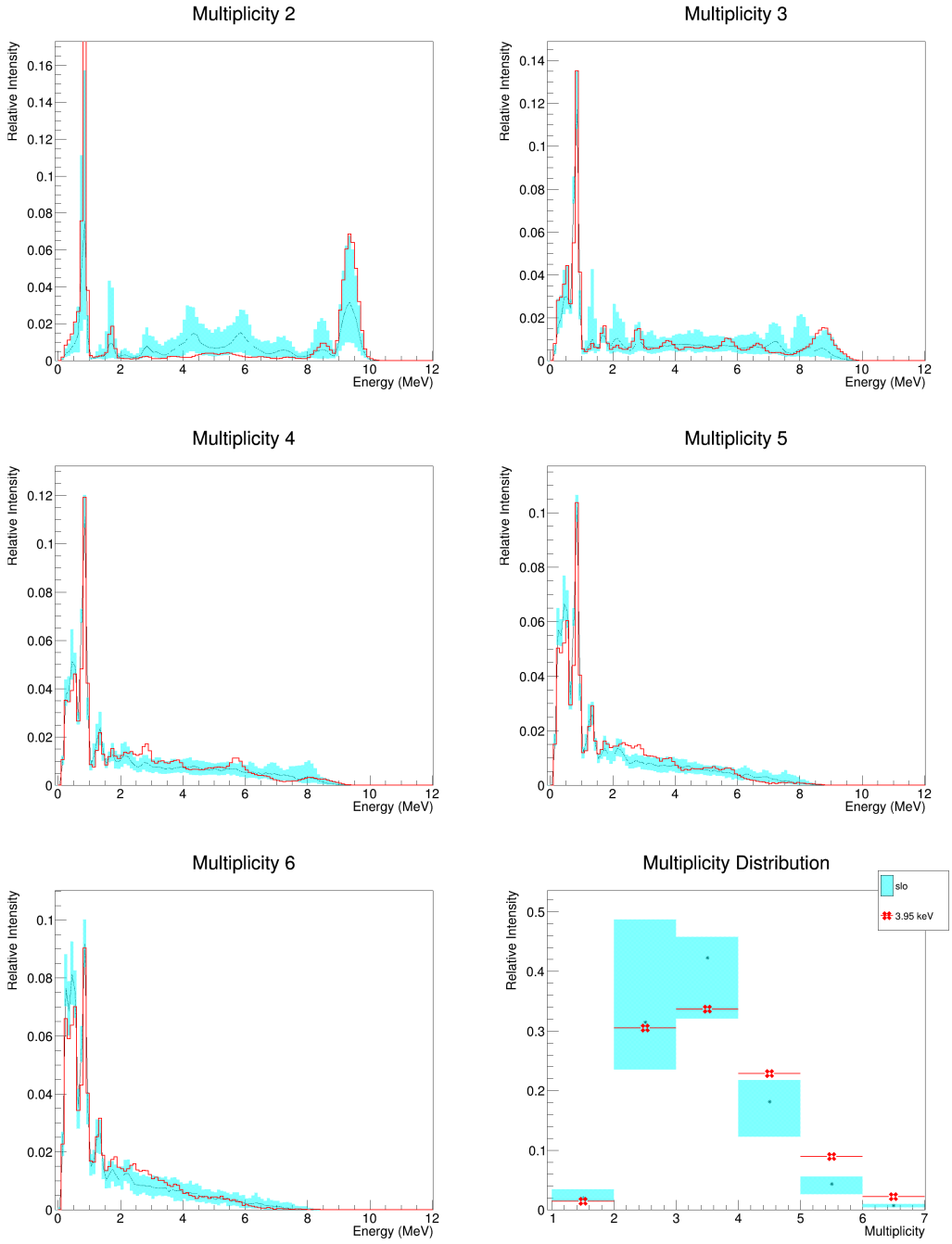

Figure A.19: Comparison of SLO simulations and 2^+ resonances. This plot shows multi-step gamma-cascades and multiplicity distributions of experimental and simulated 2^+ resonances. The simulations in this figure were produced using the SLO model of the photon strength function.

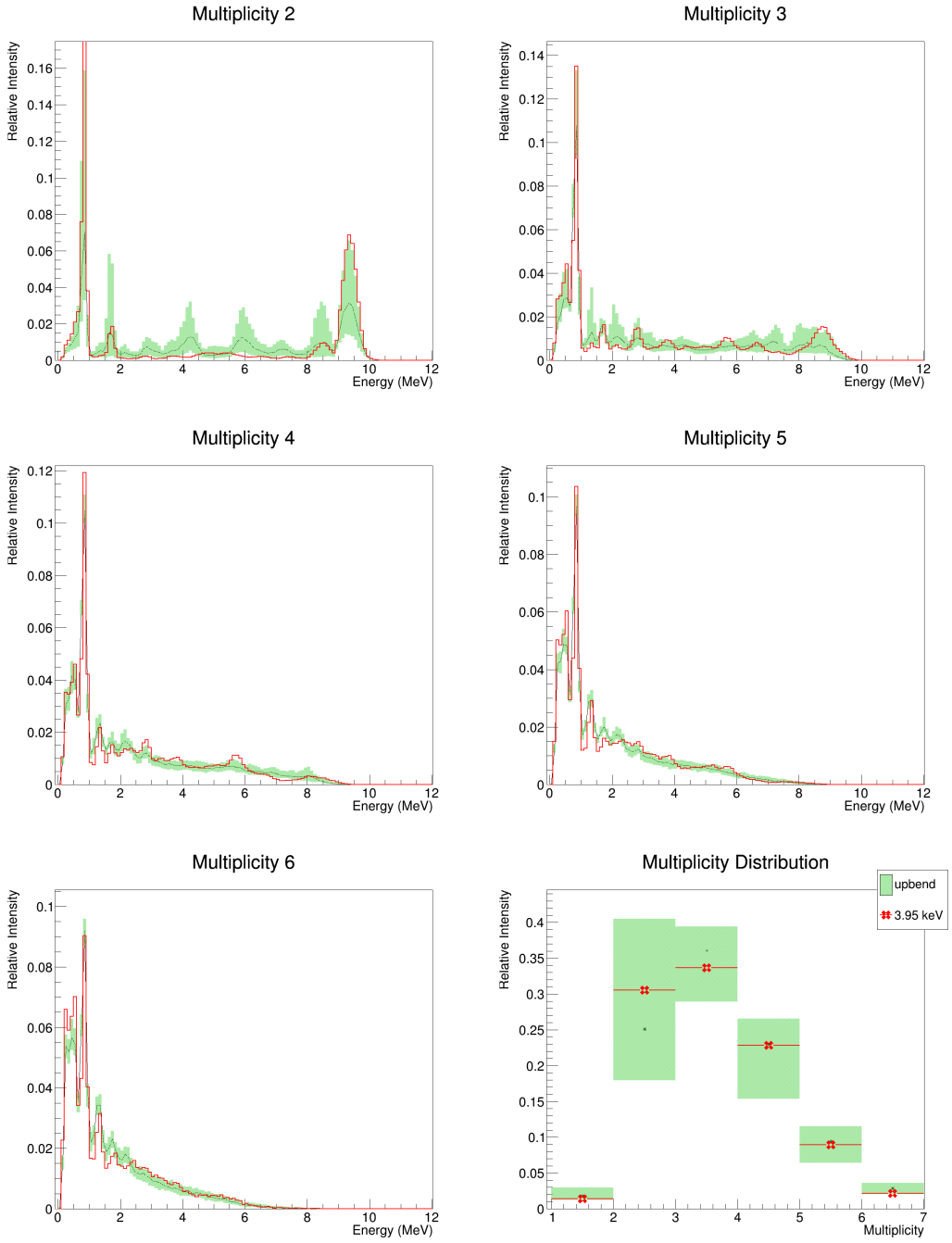

Figure A.20: Comparison of upbend simulations and 2^+ resonances. This plot shows multi-step gamma-cascades and multiplicity distributions of experimental and simulated 2^+ resonances. The simulations in this figure were produced using the upbend model of the photon strength function.

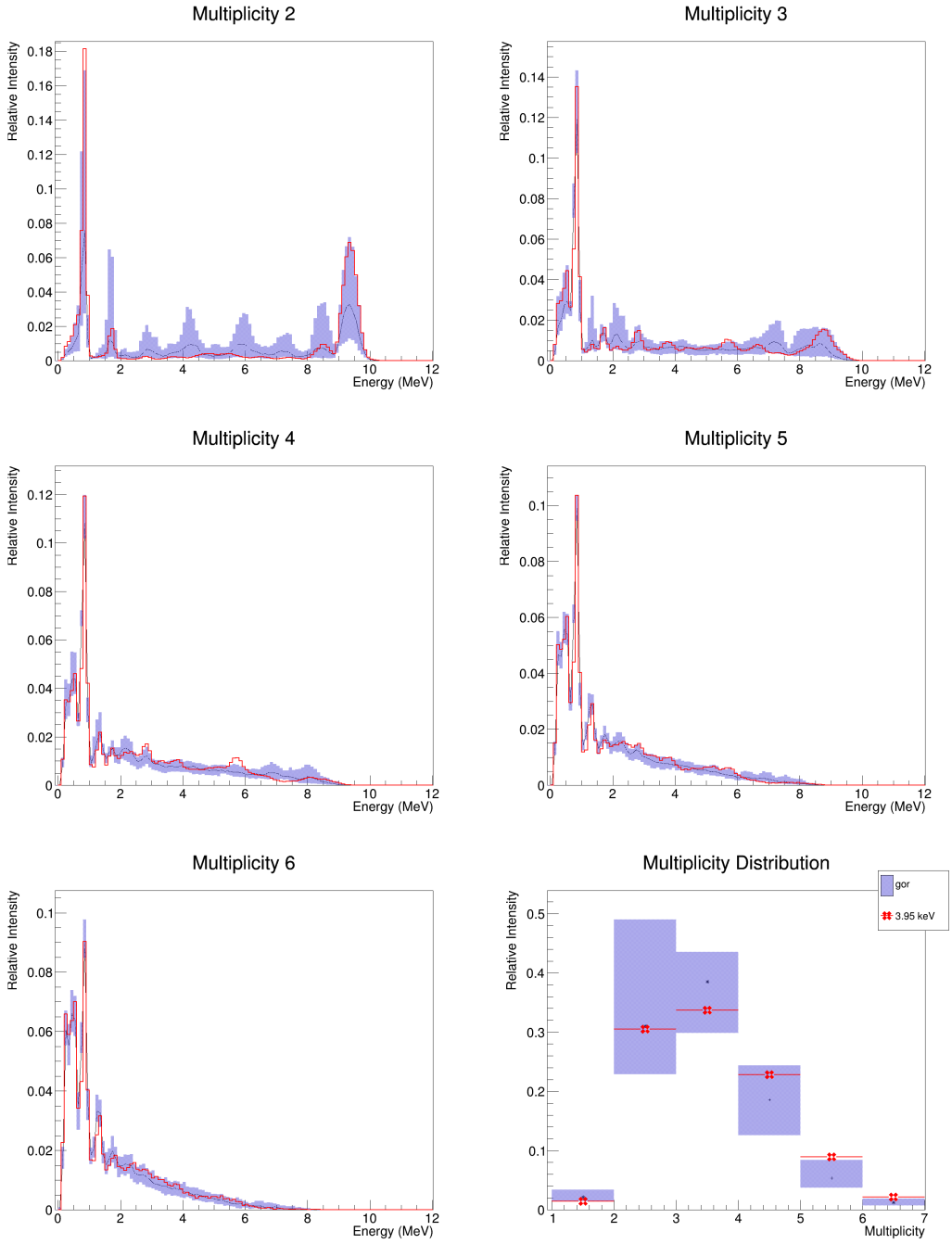

Figure A.21: Comparison of gor simulations and 2^+ resonances. This plot shows multi-step gamma-cascades and multiplicity distributions of experimental and simulated 2^+ resonances. The simulations in this figure were produced using the Goriely model of the photon strength function.

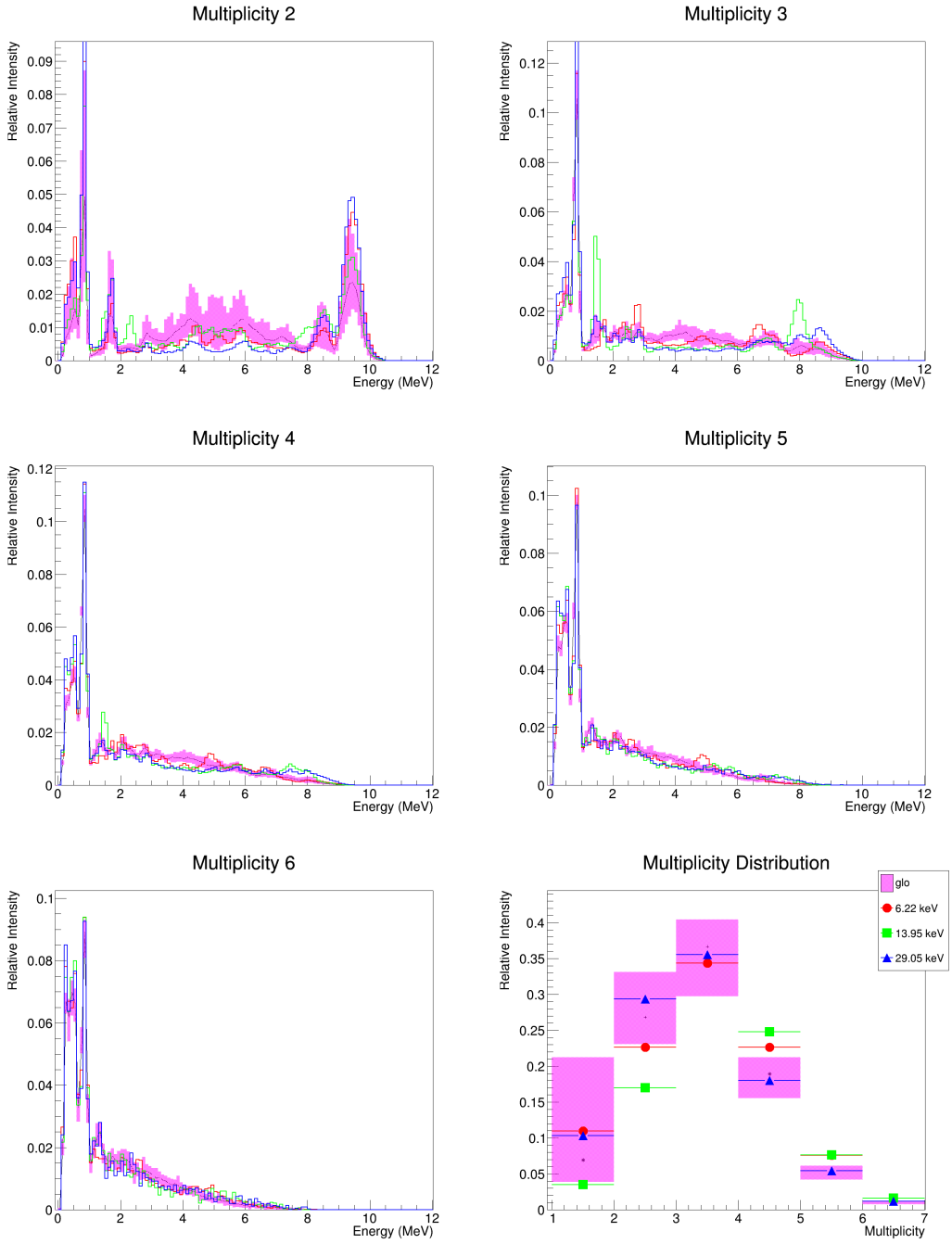

Figure A.22: Comparison of batched GLO simulations and 1^- resonances. This plot shows batched multi-step gamma-cascades and multiplicity distributions of experimental and simulated 1^- resonances. The simulations in this figure were produced using the GLO model of the photon strength function.

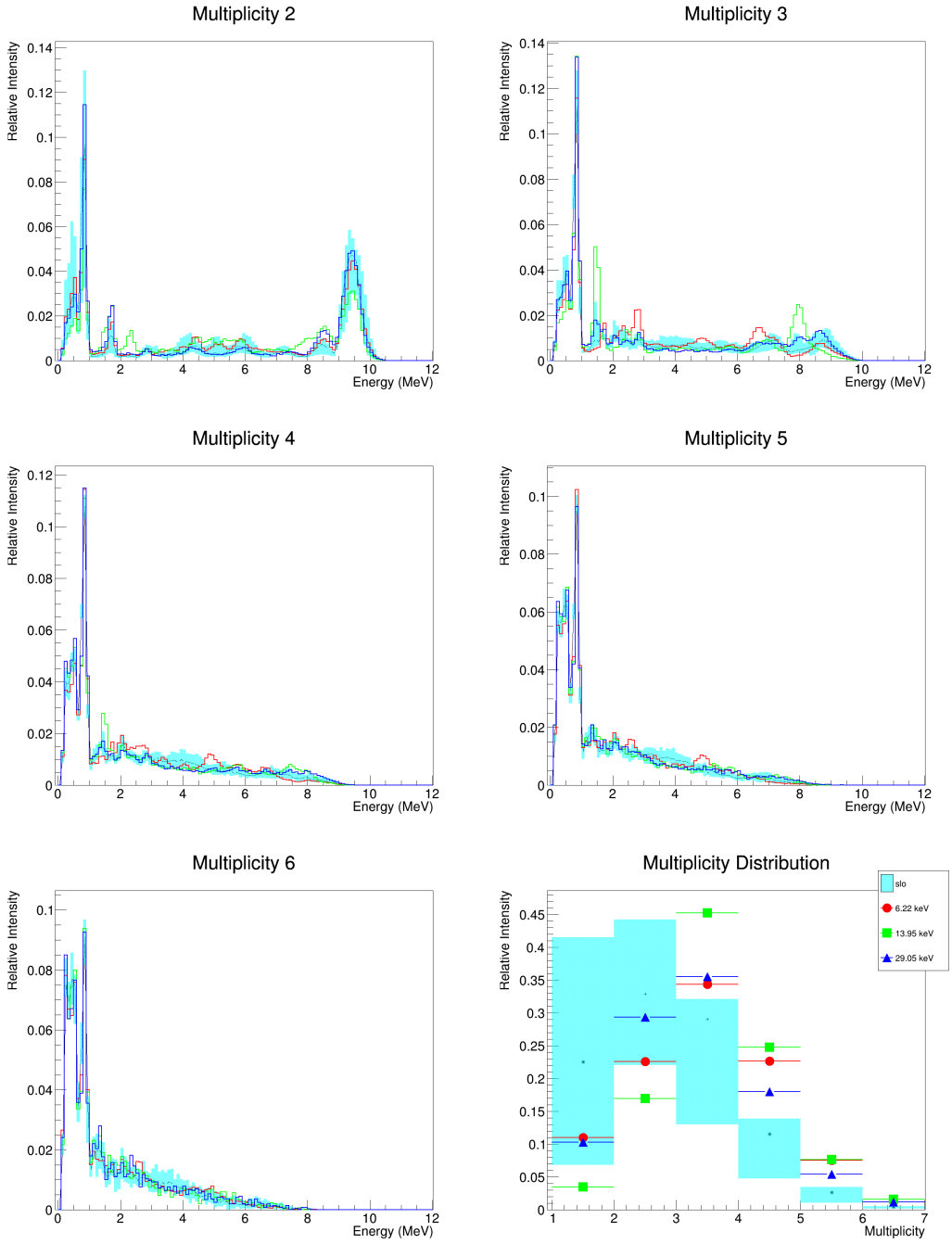

Figure A.23: Comparison of batched SLO simulations and 1^- resonances. This plot shows batched multi-step gamma-cascades and multiplicity distributions of experimental and simulated 1^- resonances. The simulations in this figure were produced using the SLO model of the photon strength function.

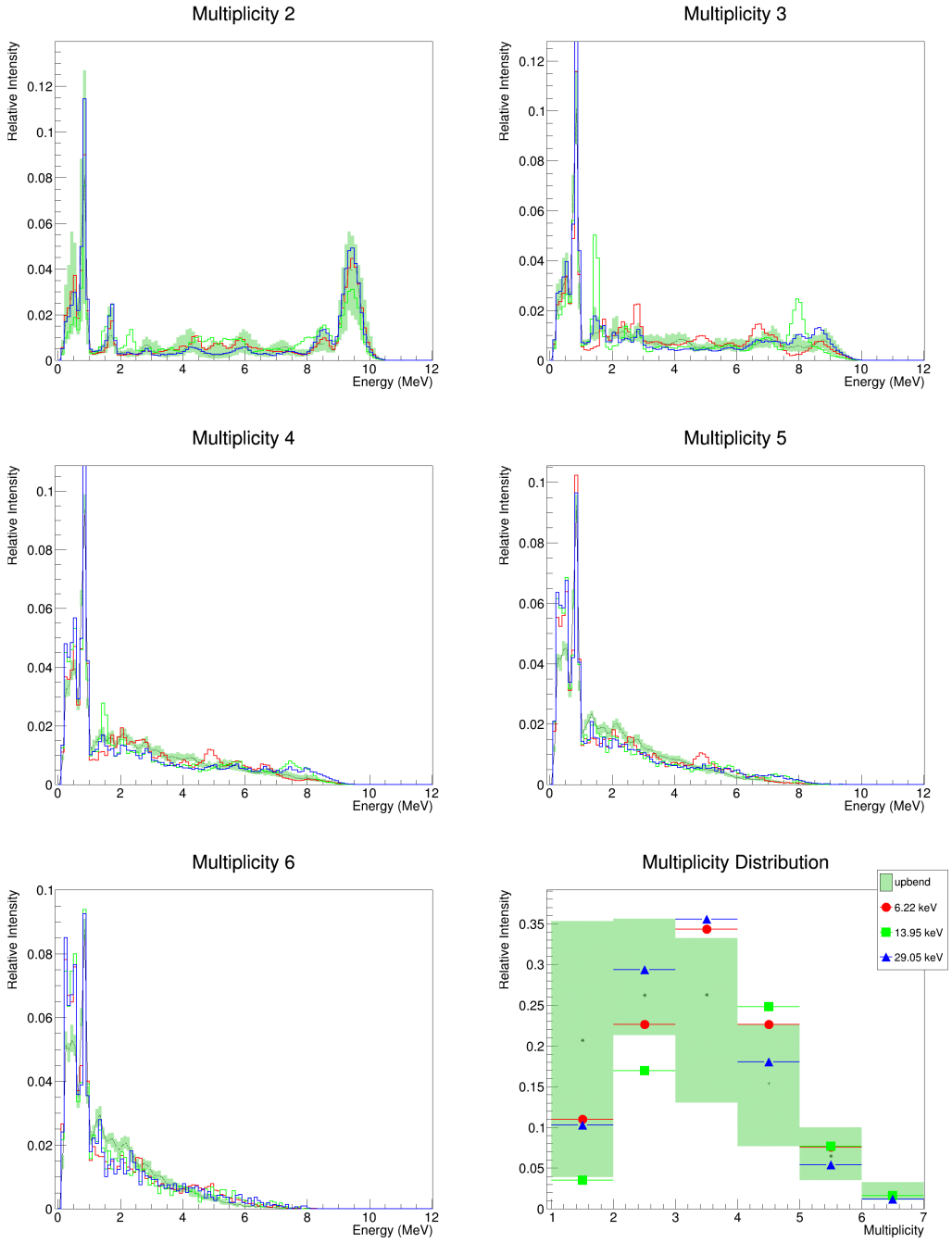

Figure A.24: Comparison of batched upbend simulations and 1^- resonances. This plot shows batched multi-step gamma-cascades and multiplicity distributions of experimental and simulated 1^- resonances. The simulations in this figure were produced using the upbend model of the photon strength function.

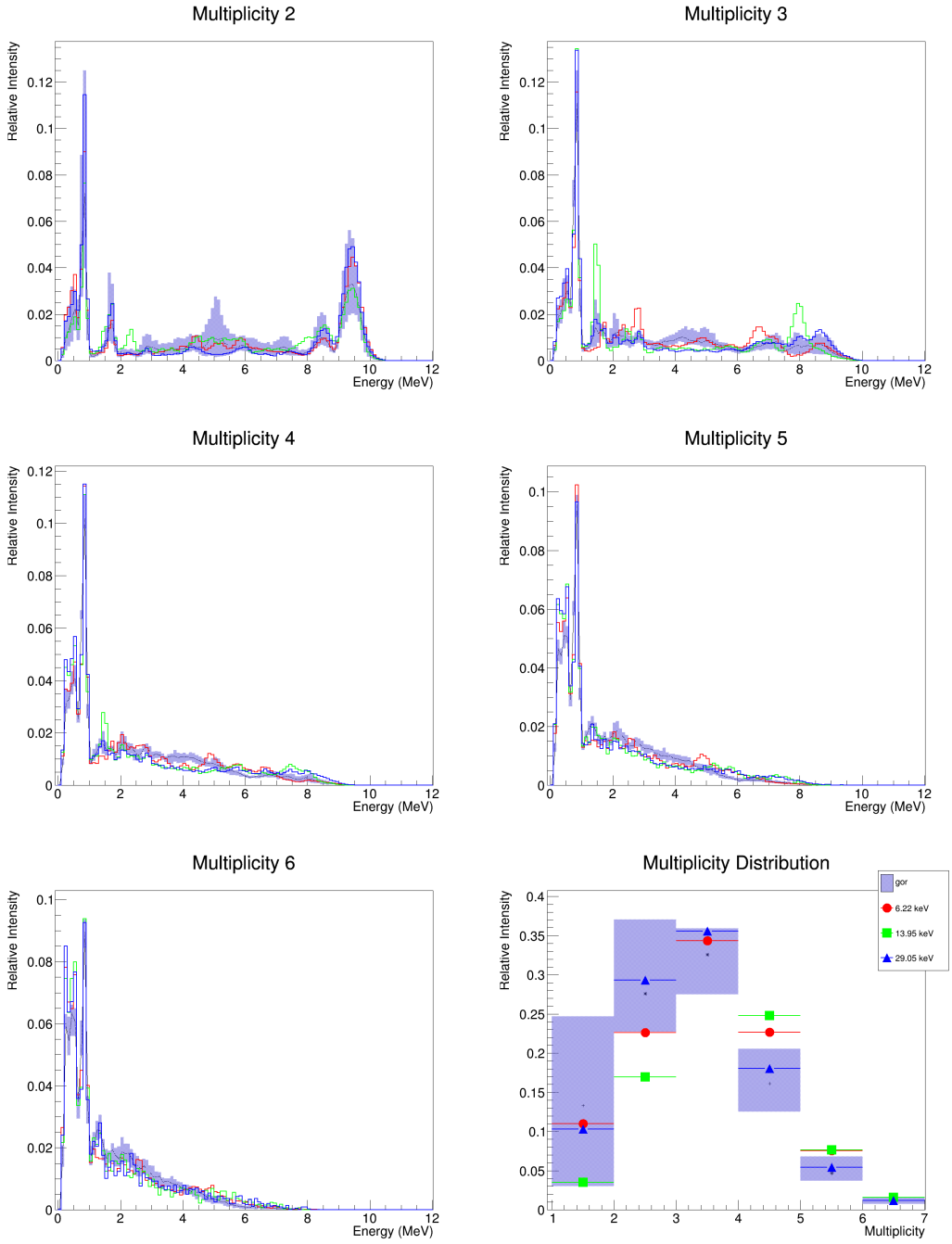

Figure A.25: Comparison of batched gor simulations and 1^- resonances. This plot shows batched multi-step gamma-cascades and multiplicity distributions of experimental and simulated 1^- resonances. The simulations in this figure were produced using the Goriely model of the photon strength function.

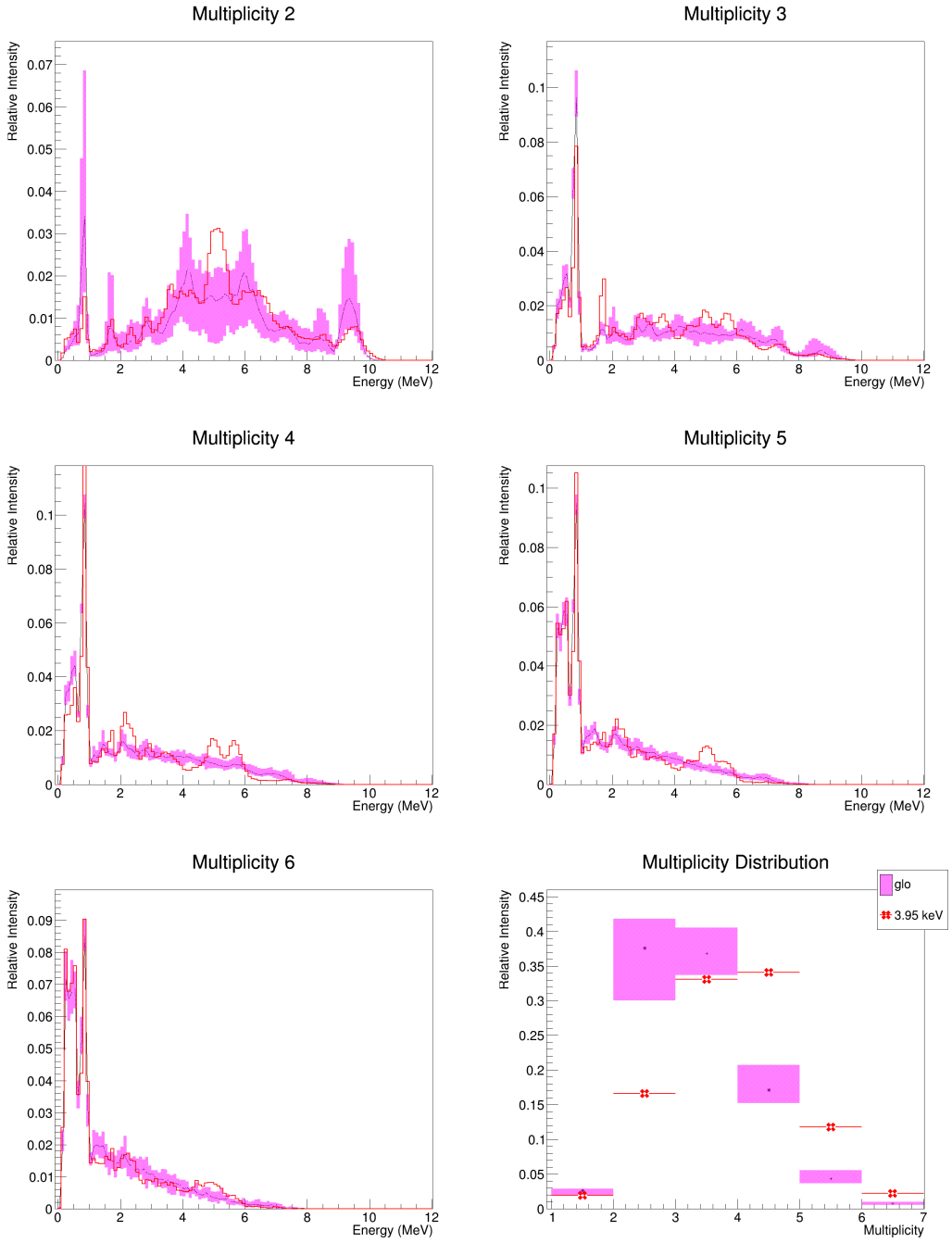

Figure A.26: Comparison of batched GLO simulations and 0^- resonances. This plot shows batched multi-step gamma-cascades and multiplicity distributions of experimental and simulated 0^- resonances. The simulations in this figure were produced using the GLO model of the photon strength function.

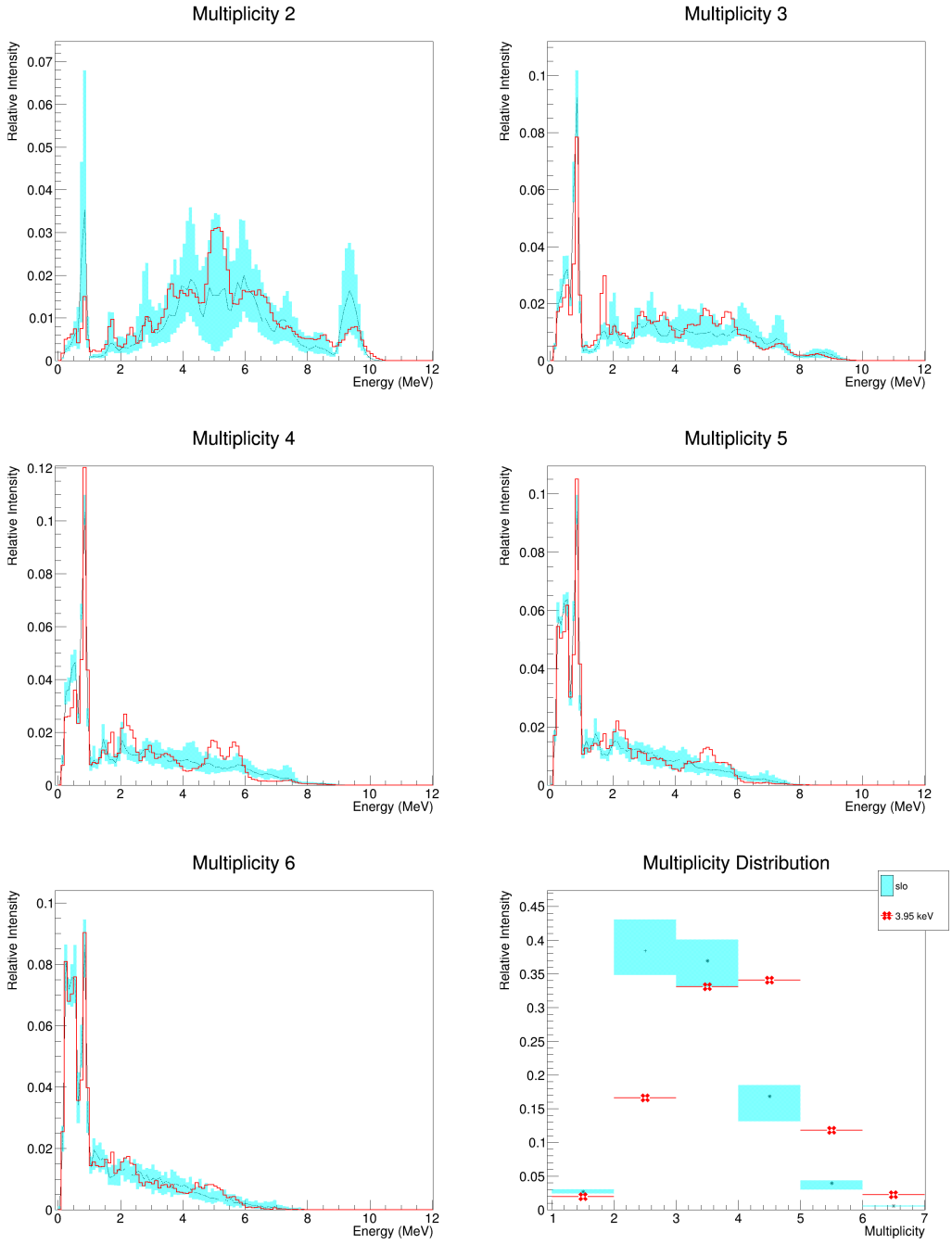

Figure A.27: Comparison of batched SLO simulations and 0^- resonances. This plot shows batched multi-step gamma-cascades and multiplicity distributions of experimental and simulated 0^- resonances. The simulations in this figure were produced using the SLO model of the photon strength function.

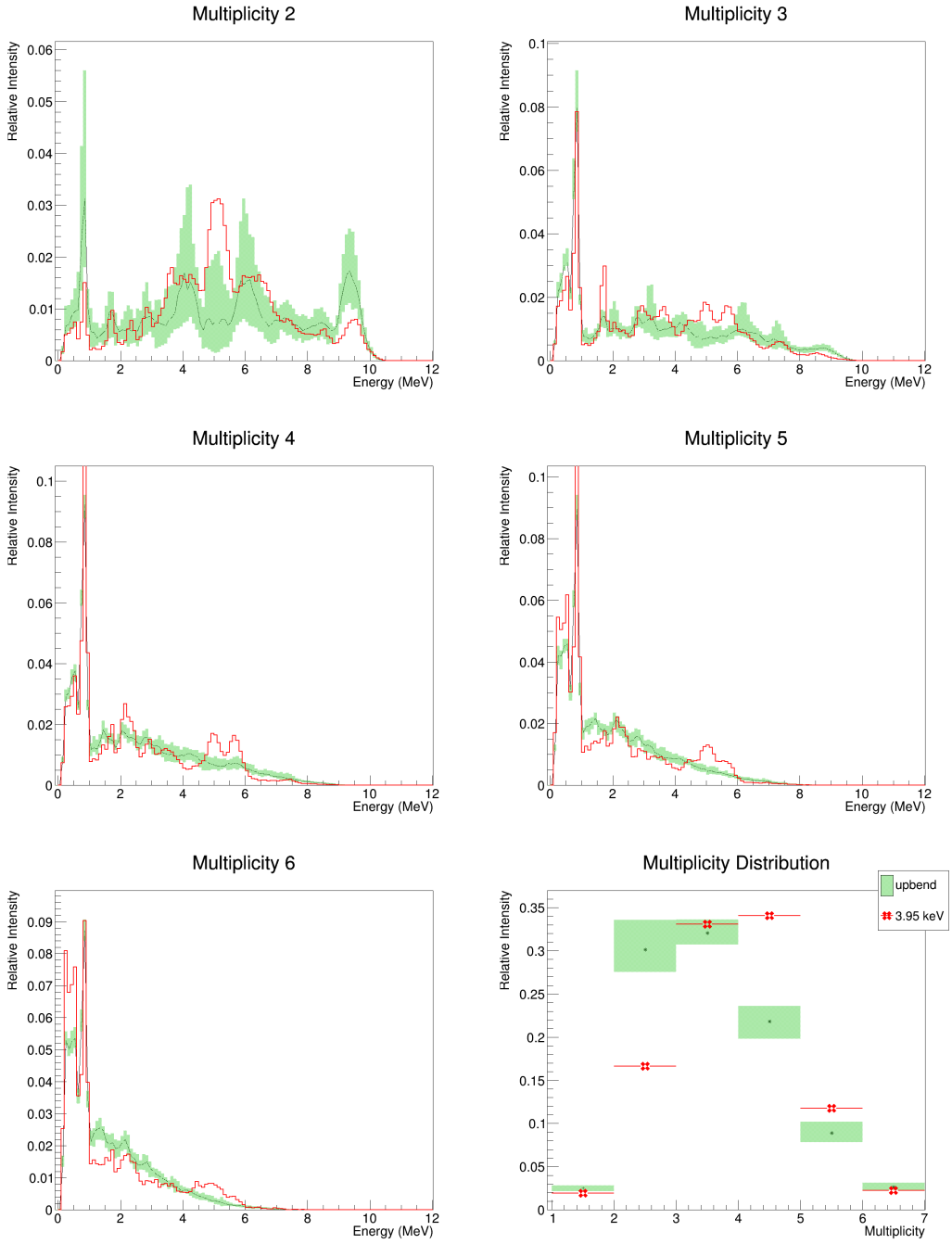

Figure A.28: Comparison of batched upbend simulations and 0^- resonances. This plot shows batched multi-step gamma-cascades and multiplicity distributions of experimental and simulated 0^- resonances. The simulations in this figure were produced using the upbend model of the photon strength function.

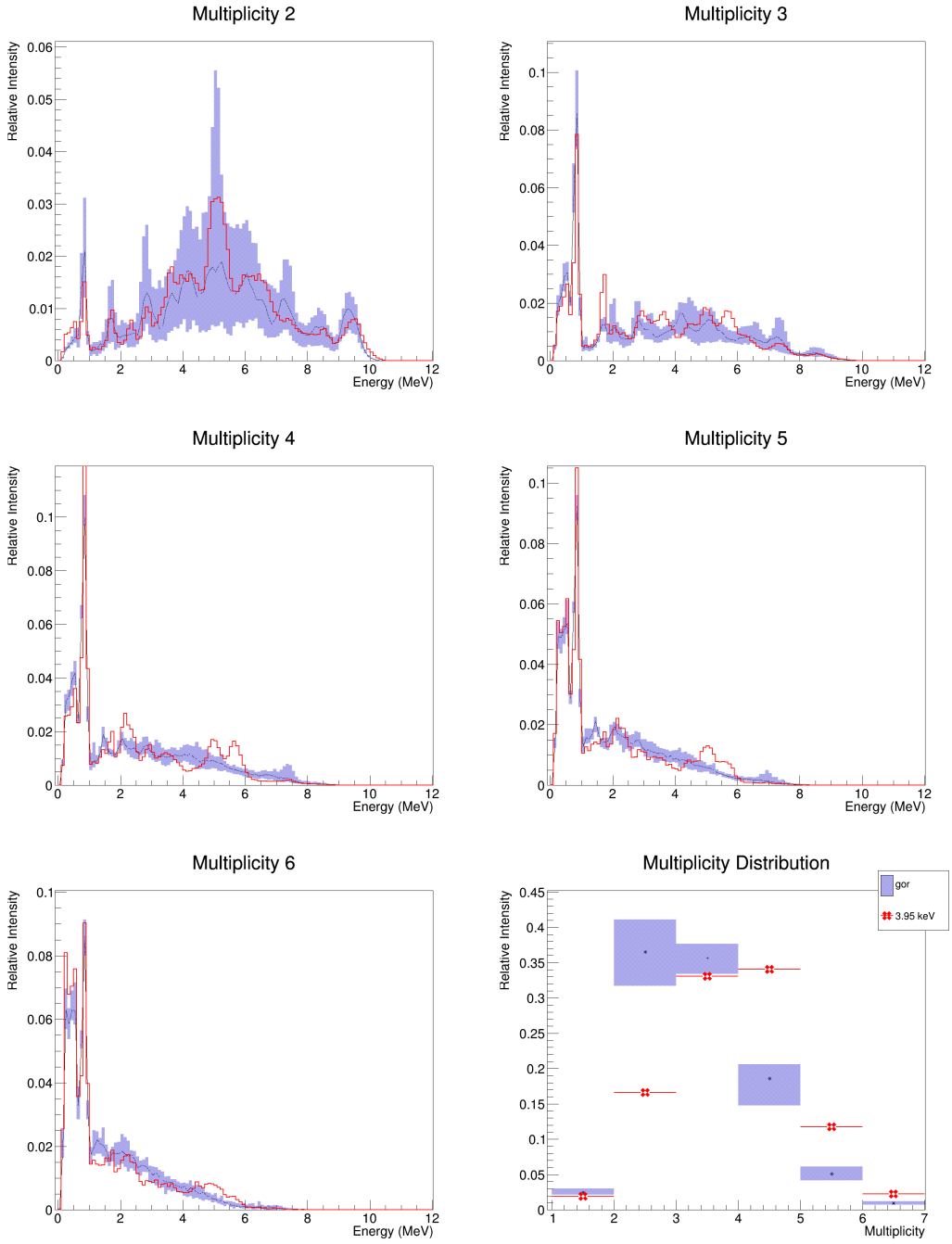

Figure A.29: Comparison of batched gor simulations and 0^- resonances. This plot shows batched multi-step gamma-cascades and multiplicity distributions of experimental and simulated 0^- resonances. The simulations in this figure were produced using the Goriely model of the photon strength function.

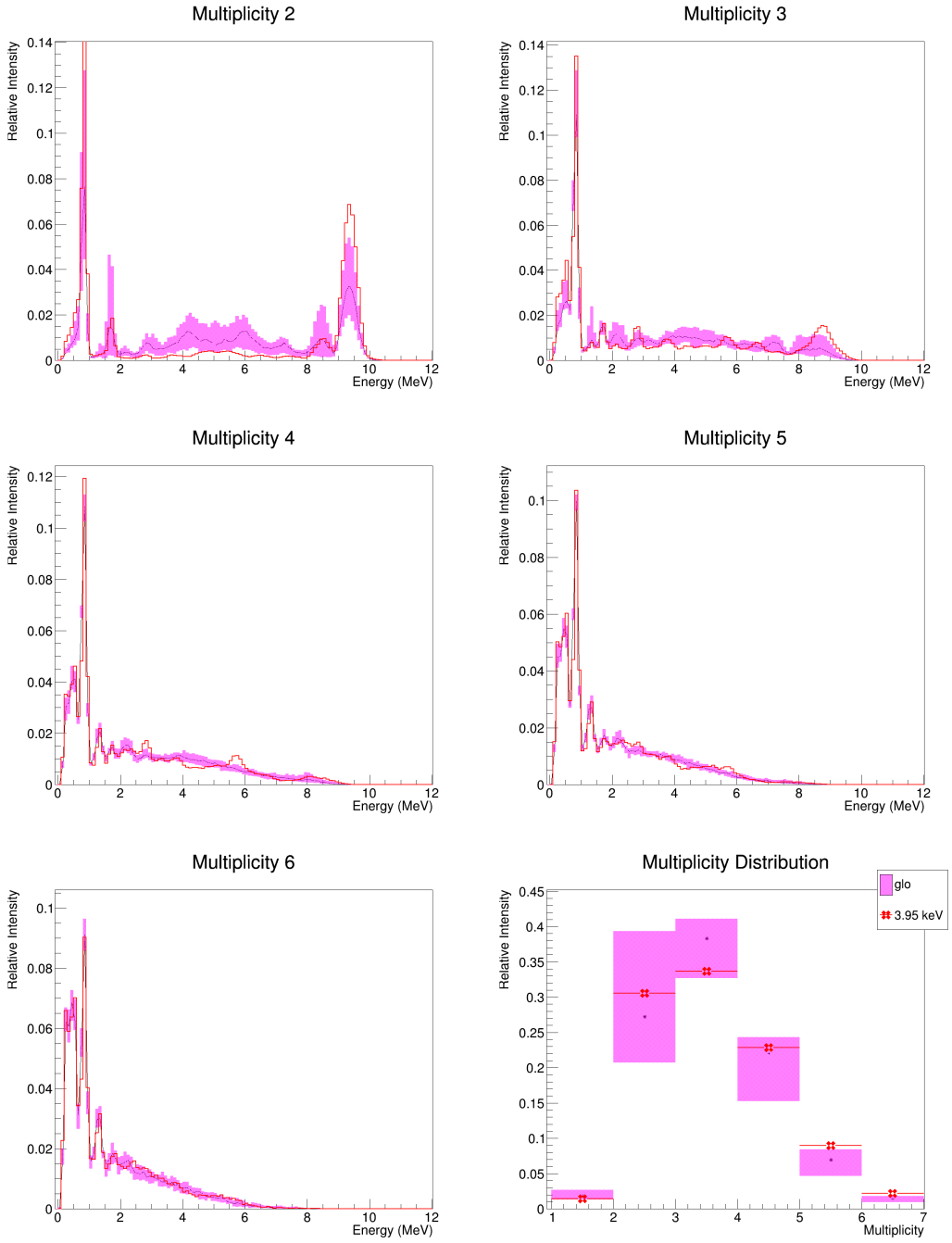

Figure A.30: Comparison of batched GLO simulations and 2^+ resonances. This plot shows batched multi-step gamma-cascades and multiplicity distributions of experimental and simulated 2^+ resonances. The simulations in this figure were produced using the GLO model of the photon strength function.

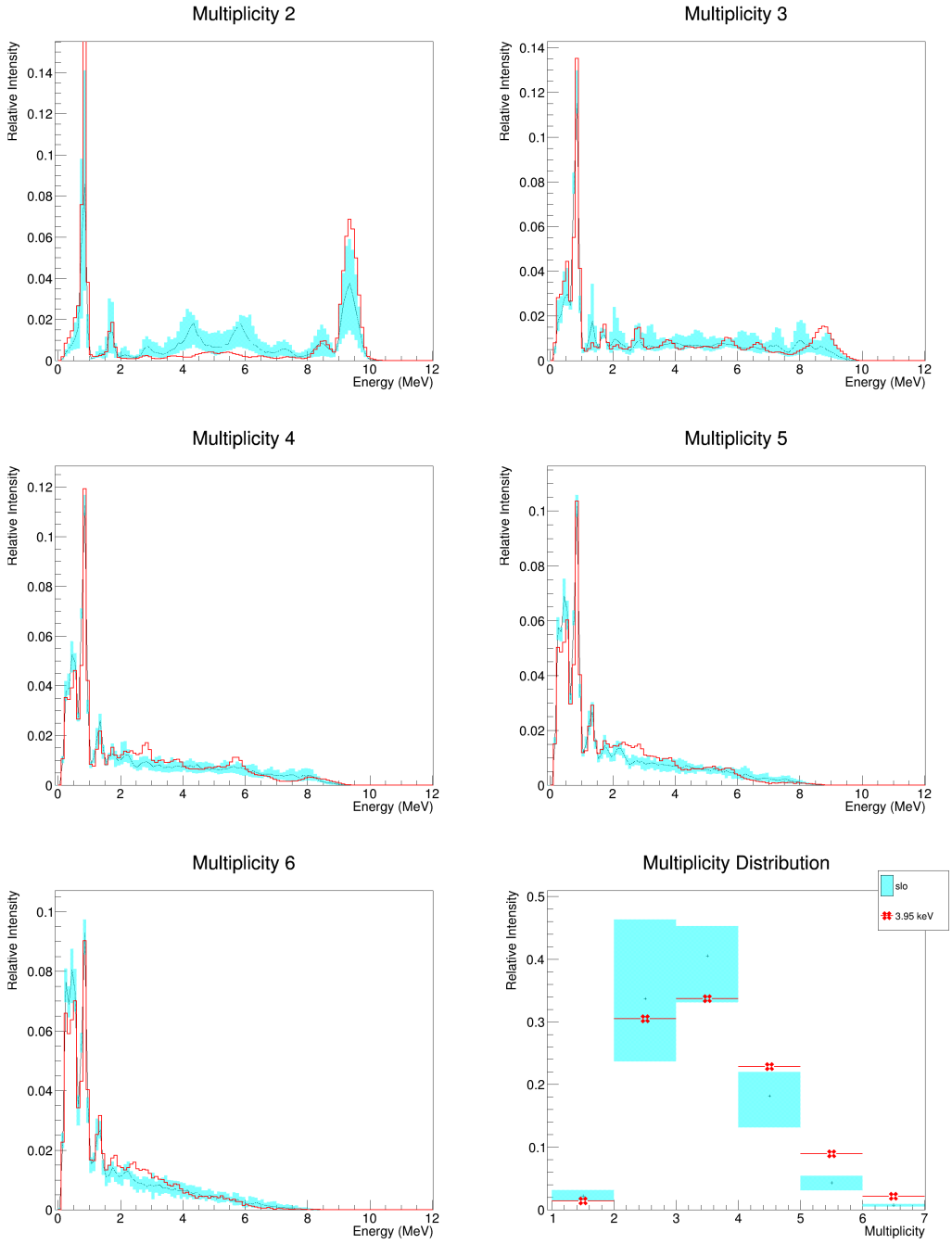

Figure A.31: Comparison of batched SLO simulations and 2^+ resonances. This plot shows batched multi-step gamma-cascades and multiplicity distributions of experimental and simulated 2^+ resonances. The simulations in this figure were produced using the SLO model of the photon strength function.

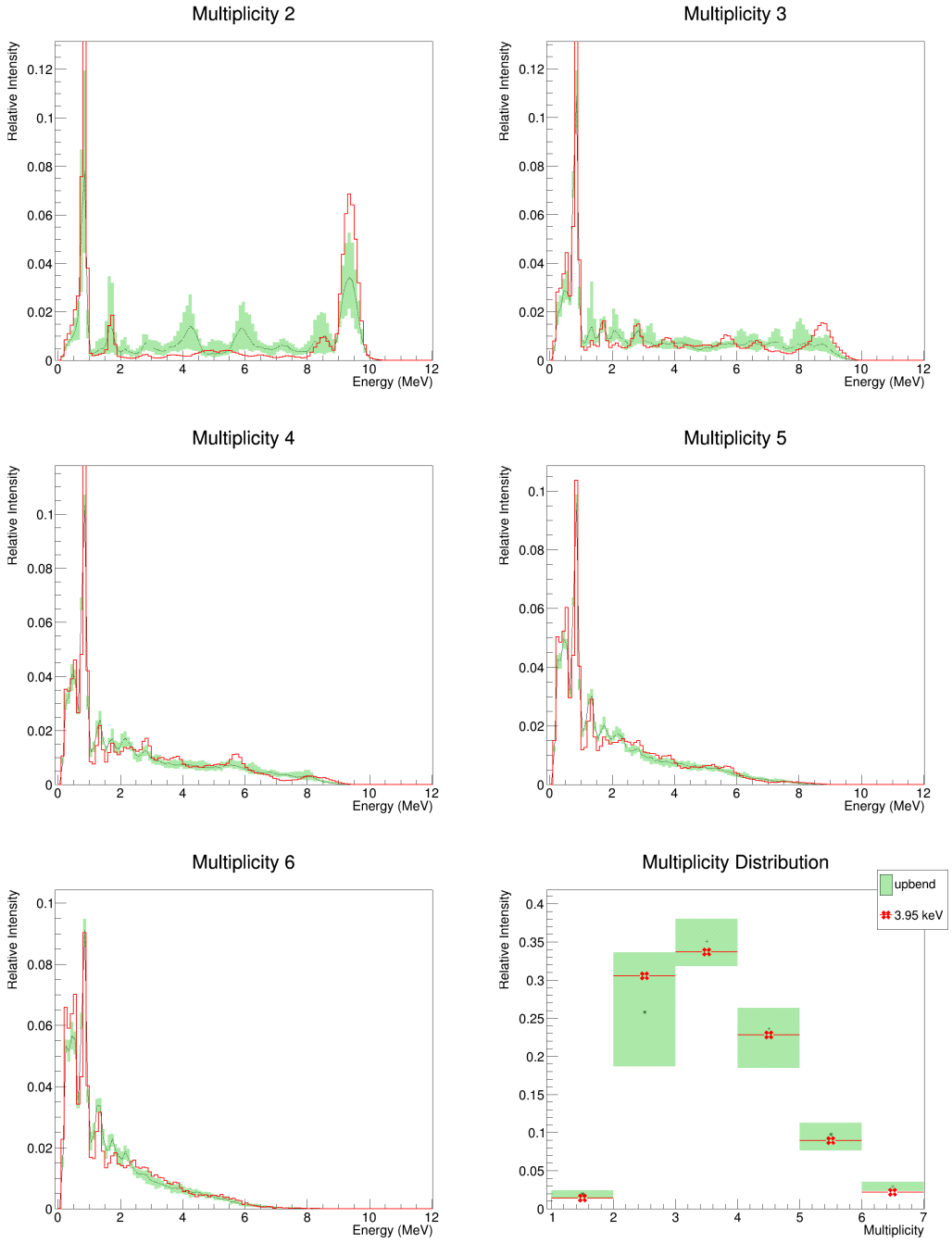

Figure A.32: Comparison of batched upbend simulations and 2^+ resonances. This plot shows batched multi-step gamma-cascades and multiplicity distributions of experimental and simulated 2^+ resonances. The simulations in this figure were produced using the upbend model of the photon strength function.

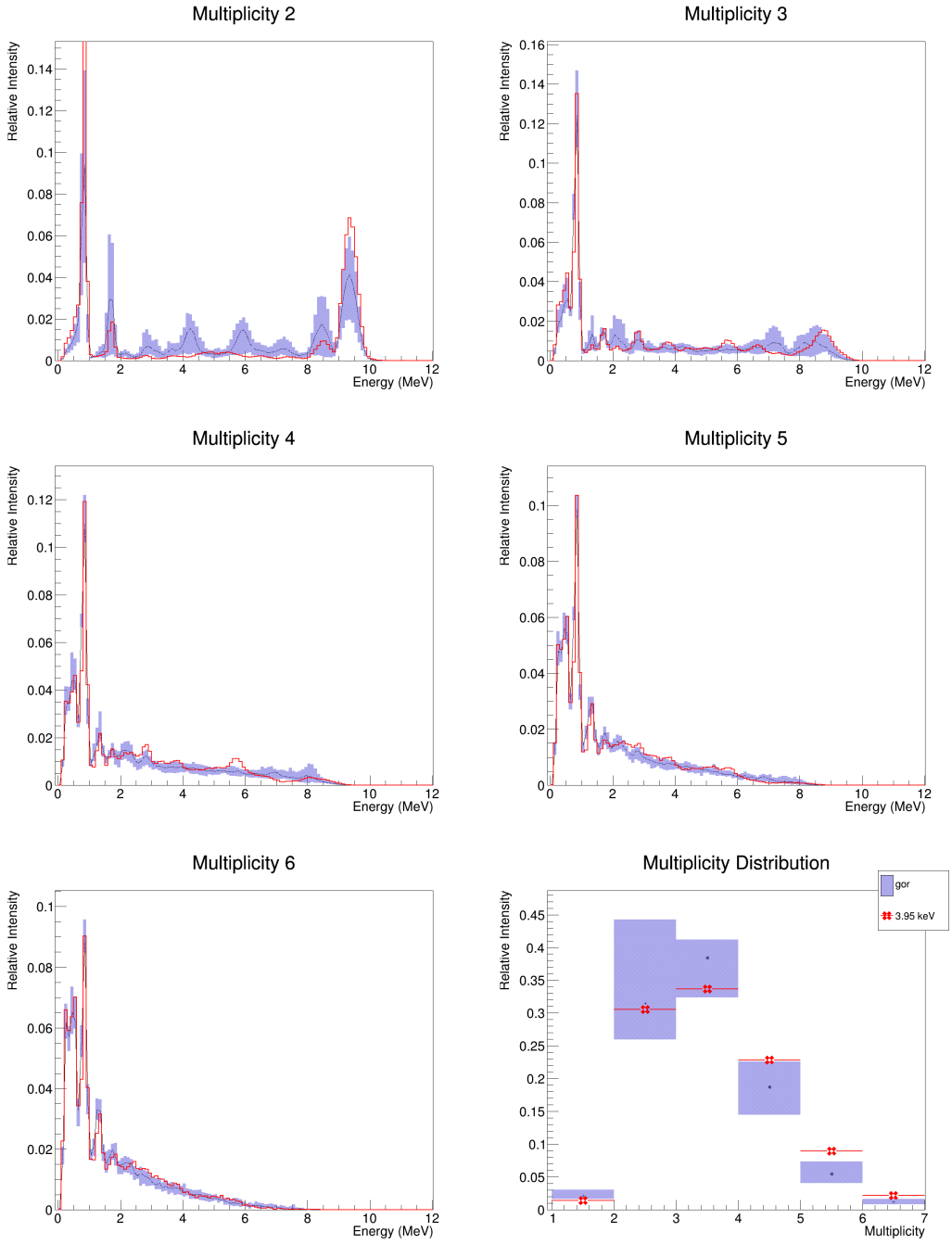

Figure A.33: Comparison of batched gor simulations and 2^+ resonances. This plot shows batched multi-step gamma-cascades and multiplicity distributions of experimental and simulated 2^+ resonances. The simulations in this figure were produced using the Goriely model of the photon strength function.